

INVESTIGATION OF TENSILE PLASTIC INSTABILITY AND NECKING FOR
AL2024T3 ALUMINUM AND S235JR STEEL ALLOYS

A THESIS SUBMITTED TO
THE GRADUATE SCHOOL OF NATURAL AND APPLIED SCIENCES
OF
MIDDLE EAST TECHNICAL UNIVERSITY

BY

VOLKAN İLİ

IN PARTIAL FULFILLMENT OF THE REQUIREMENTS
FOR
THE DEGREE OF MASTER OF SCIENCE
IN
MECHANICAL ENGINEERING

SEPTEMBER 2019

Approval of the thesis:

**INVESTIGATION OF TENSILE PLASTIC INSTABILITY AND NECKING
FOR AL2024T3 ALUMINUM AND S235JR STEEL ALLOYS**

submitted by Volkan İli in partial fulfillment of the requirements for the degree of
**Master of Science in Mechanical Engineering Department, Middle East
Technical University** by,

Prof. Dr. Halil Kalıpçılar
Dean, Graduate School of **Natural and Applied Sciences**

Prof. Dr. Sahir Arıkan
Head of Department, **Mechanical Engineering**

Prof. Dr. Haluk Darendeliler
Supervisor, **Mechanical Engineering, METU**

Examining Committee Members:

Prof. Dr. Süha Oral
Mechanical Engineering, METU

Prof. Dr. Haluk Darendeliler
Mechanical Engineering, METU

Prof. Dr. Suat Kadioğlu
Mechanical Engineering, METU

Assist. Prof. Dr. Orkun Özşahin
Mechanical Engineering, METU

Prof. Dr. Can Coğun
Mechatronics Engineering, Çankaya University

Date: 04.09.2019

I hereby declare that all information in this document has been obtained and presented in accordance with academic rules and ethical conduct. I also declare that, as required by these rules and conduct, I have fully cited and referenced all material and results that are not original to this work.

Name, Surname: Volkan İli

Signature:

ABSTRACT

INVESTIGATION OF TENSILE PLASTIC INSTABILITY AND NECKING FOR AL2024T3 ALUMINUM AND S235JR STEEL ALLOYS

İli, Volkan
Master of Science, Mechanical Engineering
Supervisor: Prof. Dr. Haluk Darendeliler

September 2019, 179 pages

Tensile plastic instability phenomenon is defined as the mode of deformation so that large amounts of deformation is localized in a certain region of a component during product life or testing procedure. Several studies have been published to assess the methods proposed to predict tensile plastic instability and necking behavior of materials. Although research has been done by using various specimens, comparative results on different specimen materials and geometries as well as different test methods have not been covered in most of these studies.

The purpose of this work is to investigate tensile plastic instability and necking prediction methods both experimentally and numerically. Two classical procedures have been selected: Uniaxial tensile test and deep drawing process, since they are still among the most common applications in the literature. To observe different material characteristics, Al2024T3 and S235JR specimens underwent several tensile tests. Both materials were used to manufacture cylindrical and sheet tensile test specimens. Furthermore, straight, tapered and notched forms of both cylindrical and sheet specimens have been tested and the results are compared. Further, Al2024T3 material specimens are used in cylindrical cup, round bottom cup and square cup deep drawing processes to review the applicability of the tensile test results.

The efficiency, precision and effectivity of tensile plastic instability and necking prediction methods have been discussed based on the finite element analysis results. The generalization of the methods so that they can be applied in any plastic deformation analysis is another focus point of this thesis.

Keywords: Tensile Plastic Instability, Prediction of Necking, Tensile Test, Deep Drawing Process, Finite Element Analysis

ÖZ

AL2024T3 ALÜMİNYUM VE S235JR ÇELİK ALAŞIMLARINDA GERİLME PLASTİK KARARSIZLIĞI VE BOYUN VERME İNCELEMESİ

İli, Volkan
Yüksek Lisans, Makina Mühendisliği
Tez Danışmanı: Prof. Dr. Haluk Darendeliler

Eylül 2019, 179 sayfa

Gerilme plastik kararsızlığı bir ürünün kullanım ömrü veya test edilmesi sırasında belirli bir bölgesinde büyük miktarlarda şekil değişimi meydana gelmesi sonucu oluşan deformasyon modu olarak tanımlanır. Malzemelerin gerilme plastik kararsızlığını ve boyun verme davranışını tahmin etmek için önerilen yöntemleri değerlendirmek üzere çeşitli çalışmalar yayınlanmıştır. Çeşitli numuneleri kıyaslamak için araştırmalar yapılmış olmasına rağmen, bu çalışmaların bir çoğu farklı numune malzemeleri, geometrileri ve test yöntemleri hakkında karşılaştırmalı sonuçları kapsamamaktadır.

Bu çalışmanın amacı deneysel ve sayısal olarak gerilme plastik kararsızlığı ve boyun verme tahmin yöntemlerini incelemektir. İki klasik yöntem olarak, tek eksenli çekme testi ve derin çekme işlemi literatürde yaygınca yer almaları sebebiyle seçilmişlerdir. Al2024T3 ve S235JR numuneleri değişik malzeme özellikleri arasındaki farkları gözlemlemek için çeşitli çekme testlerine tabi tutulmuşlardır. Her iki malzeme silindirik ve sac çekme testi numunelerini üretmek için kullanılmıştır. Hem silindirik hem de sac numunelerin düz, konik ve çentikli formları test edilmiş ve sonuçlar karşılaştırılmıştır. Ayrıca, Al2024T3 malzeme numuneleri çekme testi sonuçlarının uygulanabilirliğini gözden geçirmek için silindirik, yarı küresel ve kare kesitli derin çekme işlemlerinde kullanılmıştır.

Gerilme plastik kararsızlığı ve boyun verme tahmin yöntemlerinin verimi, doğruluğu ve etkinlikleri sonlu elemanlar analiz sonuçları kullanılarak tartışılmıştır. Yöntemlerin herhangi bir plastik şekillendirme analizinde uygulanabilecek şekilde genellenmesi bu tezin bir başka odak noktasıdır.

Anahtar Kelimeler: Gerilme Plastik Kararsızlığı, Boyun Verme Tahmini, Çekme Testi, Derin Çekme İşlemi, Sonlu Elemanlar Analizi

To The Keys That Move Mankind Forward, Perseverance And Hope

ACKNOWLEDGEMENTS

The author would like to express his earnest, heartfelt gratitude and appreciation to thesis supervisor Prof. Dr. Haluk Darendeliler for his patient guidance and advice he has provided throughout the thesis process.

The author wishes to thank Servet Şehirli and Burhan Aleessa Alam for their critical-thinking discussions, advises and suggestions. The significance of their role in experiment phase is beyond dispute.

The author is also grateful to his colleagues at Turkish Aerospace Industries Helicopter Group and TE Connectivity AD&M EMEA team for their technical assistance and encouragements.

Finally, the author would like to thank to his parents Alaaddin İli and Nefise Nesrin İli, brothers Sergen İli and Kutay İli and finally to his beloved wife Ezgi Gökpınar İli for their unwavering faith and support, limitless patience as well as everlasting care. This accomplishment would not have been possible without them.

TABLE OF CONTENTS

ABSTRACT	v
ÖZ	vii
ACKNOWLEDGEMENTS	x
TABLE OF CONTENTS	xi
LIST OF TABLES	xix
LIST OF FIGURES	xxi
LIST OF ABBREVIATIONS	xxxiv
LIST OF SYMBOLS	xxxv
CHAPTERS	
1. INTRODUCTION	1
1.1. Motivation	1
1.2. Background	2
1.2.1. Tensile Testing of Metals	2
1.2.2. Deep Drawing Processing of Metals	6
1.2.3. Methods to Predict the Onset of Instability	8
1.3. Objectives of the Research	8
1.4. Scope of the Thesis.....	9
1.5. Outline of the Thesis	10
2. LITERATURE REVIEW	11
3. THEORY	25
3.1. Introduction	25
3.2. Discussion about Instability Prediction Methods	27

3.3. Derivations for Determination of Onset of Instability/Necking	28
3.3.1. Equivalent Plastic Strain Rate Ratio	31
3.3.2. Criterion of Difference of Second Time Derivative of Equivalent Plastic Strain	32
3.3.3. Criterion of Second Time Derivative of Equivalent Plastic Strain	33
3.3.4. Criterion of Maximum Punch Force	34
4. EXPERIMENTS	35
4.1. Materials.....	35
4.2. Tensile Test Experiments.....	36
4.2.1. Experimental Set Up	36
4.2.2. Specimen Geometry and Material	37
4.2.3. Experimental Procedure	40
4.2.4. Experimental Results.....	41
4.2.4.1. Al2024T3 Sheet Specimen Tensile Test Results.....	42
4.2.4.2. Al2024T3 Round Specimen Tensile Test Results	43
4.2.4.3. Comments on the Graphs of Al2024T3 Specimen Tensile Tests	45
4.2.4.4. S235JR Sheet Specimen Tensile Test Results.....	46
4.2.4.5. S235JR Round Specimen Tensile Test Results	48
4.2.4.6. Comments on the Graphs of S235JR Specimen Tensile Tests.....	50
4.3. Deep Drawing Experiments	51
4.3.1. Experimental Set Up	52
4.3.2. Specimen Geometry and Material	53
4.3.3. Experimental Procedure	54
4.3.4. Experimental Results.....	55

4.3.4.1. Al2024T3 Cylindrical Cup Deep Drawing Process Results	55
4.3.4.2. Al2024T3 Round Bottom Cup Deep Drawing Process Results	57
4.3.4.3. Al2024T3 Square Cup Deep Drawing Process Results	59
5. FINITE ELEMENT MODELS	61
5.1. Introduction	61
5.2. Finite Element Analysis	62
5.3. FE Model Construction of Round Specimen Tensile Test	64
5.4. FE Model Construction of Flat Specimen Tensile Test	70
5.5. FE Model Construction for Deep Drawing Process	75
6. RESULTS AND DISCUSSION	81
6.1. FEA Results of Al2024T3 Sheet Specimen Tensile Tests	82
6.1.1. Straight Al2024T3 Sheet Specimen Analysis	82
6.1.1.1. Criterion of Equivalent Plastic Strain Increment Ratio (TT-She-Al-Str)	82
6.1.1.2. Criterion of Difference of Second Time Derivative of Equivalent Plastic Strain (TT-She-Al-Str)	84
6.1.1.3. Criterion of Maximum Second Time Derivative of Equivalent Plastic Strain (TT-She-Al-Str)	84
6.1.1.4. Criterion of Maximum Punch Force (TT-She-Al-Str)	86
6.1.2. Tapered Al2024T3 Sheet Specimen Analysis	87
6.1.2.1. Criterion of Equivalent Plastic Strain Increment Ratio (TT-She-Al- Tpr).....	87
6.1.2.2. Criterion of Difference of Second Time Derivative of Equivalent Plastic Strain (TT-She-Al-Tpr)	88

6.1.2.3. Criterion of Maximum Second Time Derivative of Equivalent Plastic Strain (TT-She-Al-Tpr)	89
6.1.2.4. Criterion of Maximum Punch Force (TT-She-Al-Tpr)	90
6.1.3. Notched Al2024T3 Sheet Specimen Analysis	91
6.1.3.1. Criterion of Equivalent Plastic Strain Increment Ratio (TT-She-Al-Ntc)	91
6.1.3.2. Criterion of Difference of Second Time Derivative of Equivalent Plastic Strain (TT-She-Al-Ntc).....	92
6.1.3.3. Criterion of Maximum Second Time Derivative of Equivalent Plastic Strain (TT-She-Al-Ntc)	93
6.1.3.4. Criterion of Maximum Punch Force (TT-She-Al-Ntc)	94
6.2. FEA Results of Al2024T3 Round Specimen Tensile Tests	95
6.2.1. Straight Al2024T3 Round Specimen Analysis	95
6.2.1.1. Criterion of Equivalent Plastic Strain Increment Ratio (TT-Ro-Al-Str)	95
6.2.1.2. Criterion of Difference of Second Time Derivative of Equivalent Plastic Strain (TT-Ro-Al-Str)	96
6.2.1.3. Criterion of Maximum Second Time Derivative of Equivalent Plastic Strain (TT-Ro-Al-Str).....	97
6.2.1.4. Criterion of Maximum Punch Force (TT-Ro-Al-Str).....	98
6.2.2. Tapered Al2024T3 Round Specimen Analysis	99
6.2.2.1. Criterion of Equivalent Plastic Strain Increment Ratio (TT-Ro-Al-Tpr)	99
6.2.2.2. Criterion of Difference of Second Time Derivative of Equivalent Plastic Strain (TT-Ro-Al-Tpr)	100

6.2.2.3. Criterion of Maximum Second Time Derivative of Equivalent Plastic Strain (TT-Ro-Al-Tpr)	100
6.2.2.4. Criterion of Maximum Punch Force (TT-Ro-Al-Tpr)	102
6.2.3. Notched Al2024T3 Round Specimen Analysis	103
6.2.3.1. Criterion of Equivalent Plastic Strain Increment Ratio (TT-Ro-Al-Ntc)	103
6.2.3.2. Criterion of Difference of Second Time Derivative of Equivalent Plastic Strain (TT-Ro-Al-Ntc).....	103
6.2.3.3. Criterion of Maximum Second Time Derivative of Equivalent Plastic Strain (TT-Ro-Al-Ntc)	104
6.2.3.4. Criterion of Maximum Punch Force (TT-Ro-Al-Ntc)	106
6.3. FEA Results of S235JR Sheet Specimen Tensile Tests	107
6.3.1. Straight S235JR Sheet Specimen Analysis.....	107
6.3.1.1. Criterion of Equivalent Plastic Strain Increment Ratio (TT-She-St-Str)	107
6.3.1.2. Criterion of Difference of Second Time Derivative of Equivalent Plastic Strain (TT-She-St-Str).....	107
6.3.1.3. Criterion of Maximum Second Time Derivative of Equivalent Plastic Strain (TT-She-St-Str).....	108
6.3.1.4. Criterion of Maximum Punch Force (TT-She-St-Str).....	110
6.3.2. Tapered S235JR Sheet Specimen Analysis	111
6.3.2.1. Criterion of Equivalent Plastic Strain Increment Ratio (TT-She-St-Tpr)	111
6.3.2.2. Criterion of Difference of Second Time Derivative of Equivalent Plastic Strain (TT-She-St-Tpr)	111

6.3.2.3. Criterion of Maximum Second Time Derivative of Equivalent Plastic Strain (TT-She-St-Tpr)	112
6.3.2.4. Criterion of Maximum Punch Force (TT-She-St-Tpr)	114
6.3.3. Notched S235JR Sheet Specimen Analysis	115
6.3.3.1. Criterion of Equivalent Plastic Strain Increment Ratio (TT-She-St-Ntc)	115
6.3.3.2. Criterion of Difference of Second Time Derivative of Equivalent Plastic Strain (TT-She-St-Ntc)	116
6.3.3.3. Criterion of Maximum Second Time Derivative of Equivalent Plastic Strain (TT-She-St-Ntc)	116
6.3.3.4. Criterion of Maximum Punch Force (TT-She-St-Ntc)	118
6.4. FEA Results of S235JR Round Specimen Tensile Tests	119
6.4.1. Straight S235JR Round Specimen Analysis	119
6.4.1.1. Criterion of Equivalent Plastic Strain Increment Ratio (TT-Ro-St-Str)	119
6.4.1.2. Criterion of Difference of Second Time Derivative of Equivalent Plastic Strain (TT-Ro-St-Str)	119
6.4.1.3. Criterion of Maximum Second Time Derivative of Equivalent Plastic Strain (TT-Ro-St-Str)	120
6.4.1.4. Criterion of Maximum Punch Force (TT-Ro-St-Str)	122
6.4.2. Tapered S235JR Round Specimen Analysis	123
6.4.2.1. Criterion of Equivalent Plastic Strain Increment Ratio (TT-Ro-St-Tpr)	123
6.4.2.2. Criterion of Difference of Second Time Derivative of Equivalent Plastic Strain (TT-Ro-St-Tpr)	123

6.4.2.3. Criterion of Maximum Second Time Derivative of Equivalent Plastic Strain (TT-Ro-St-Tpr).....	124
6.4.2.4. Criterion of Maximum Punch Force (TT-Ro-St-Tpr).....	126
6.4.3. Notched S235JR Round Specimen Analysis	127
6.4.3.1. Criterion of Equivalent Plastic Strain Increment Ratio (TT-Ro-St-Ntc)	127
6.4.3.2. Criterion of Difference of Second Time Derivative of Equivalent Plastic Strain (TT-Ro-St-Ntc)	127
6.4.3.3. Criterion of Maximum Second Time Derivative of Equivalent Plastic Strain (TT-Ro-St-Ntc).....	128
6.4.3.4. Criterion of Maximum Punch Force (TT-Ro-St-Ntc).....	130
6.5. Comparative Discussion for Tensile Test FEA Results	131
6.6. FEA Results of Al2024T3 Specimen Deep Drawing Process	138
6.6.1. Cylindrical Cup Deep Drawing Analysis	138
6.6.1.1. Criterion of Equivalent Plastic Strain Increment Ratio (DDP-CC-Al)	138
6.6.1.2. Criterion of Difference of Second Time Derivative of Equivalent Plastic Strain (DDP-CC-Al).....	139
6.6.1.3. Criterion of Maximum Second Time Derivative of Equivalent Plastic Strain (DDP-CC-Al)	140
6.6.1.4. Criterion of Maximum Punch Force (DDP-CC-Al).....	142
6.6.2. Round Bottom Cup Deep Drawing Analysis.....	143
6.6.2.1. Criterion of Equivalent Plastic Strain Increment Ratio (DDP-RB-Al)	143
6.6.2.2. Criterion of Difference of Second Time Derivative of Equivalent Plastic Strain (DDP-RB-Al).....	143

6.6.2.3. Criterion of Maximum Second Time Derivative of Equivalent Plastic Strain (DDP-RB-A1)	144
6.6.2.4. Criterion of Maximum Punch Force (DDP-RB-A1)	146
6.6.3. Square Cup Deep Drawing Analysis	147
6.6.3.1. Criterion of Equivalent Plastic Strain Increment Ratio (DDP-SC-A1)	147
6.6.3.2. Criterion of Difference of Second Time Derivative of Equivalent Plastic Strain (DDP-SC-A1)	147
6.6.3.3. Criterion of Maximum Second Time Derivative of Equivalent Plastic Strain (DDP-SC-A1)	148
6.6.3.4. Criterion of Maximum Punch Force (DDP-SC-A1)	150
6.7. Comparative Discussion for Deep Drawing FEA Results	151
6.8. Sources of Error	154
7. CONCLUSION AND FUTURE WORKS	157
7.1. Conclusion	157
7.2. Future Works	158
REFERENCES	159

LIST OF TABLES

TABLES

Table 4.1. Abbreviations for different experiment and analysis	36
Table 4.2. Tensile test sheet and round specimen number, name, material, type and defect information	38
Table 4.3. Cylindrical cup deep drawing process tooling dimensions.....	52
Table 4.4. Round bottom cup deep drawing process tooling dimensions.....	53
Table 4.5. Square cup deep drawing process tooling dimensions.....	53
Table 4.6. Deep drawing process sheet specimen number, name, material, thickness and type information	54
Table 6.1. Distances between elements in terms of percent of initial gauge length of tensile tests specimens.....	82
Table 6.2. Distances between elements in terms of initial diameter or initial edge dimension of deep drawing process specimens	82
Table 6.3. Equivalent plastic strain rate ratio method results of tensile test experiments and corresponding elongation at necking from experiment data	134
Table 6.4. Difference of second time derivative of equivalent plastic strain method results of tensile test experiments and corresponding elongation at necking from experiment data	135
Table 6.5. Maximum second time derivative of element strain and maximum punch force method results of tensile test analyses and corresponding elongations at necking from experiment data	136
Table 6.6. Equivalent plastic strain rate ratio method results of deep drawing processes and corresponding punch displacement at the onset of instability from experiment data	153

Table 6.7. Maximum Difference of second time derivative of equivalent plastic strain method results of deep drawing processes and corresponding punch displacement at the onset of instability from experiment data 153

Table 6.8. Maximum second time derivative of strain increment and maximum punch force method results of deep drawing processes and corresponding punch displacement at the onset of instability from experiment data 154

LIST OF FIGURES

FIGURES

Figure 1.1. (a)-(c) Consecutive stress conditions in a necked region in tension test, (d) Tension specimen and macroscopic tensile deformation behavior [3]	4
Figure 1.2. True and nominal stress–strain curve in which the work-hardening rate is plotted to indicate the onset of necking [3]	5
Figure 1.3. The typical load-displacement curve of a tensile test with flat specimen [4]	5
Figure 1.4. Development of (a) diffuse necking and (b) localized necking in tensile test of sheet metals [5].....	6
Figure 1.5. (a) Cross section view of a typical deep drawing process with forces exerted (b) Deformation zones and types of the blank during deep drawing [8].....	7
Figure 3.1. General algorithm to follow for the criteria to predict onset of necking .	29
Figure 4.1. MTS Servo-hydraulic testing machine and video extensometer	37
Figure 4.2. ASTM E8/E8M-16a Sheet specimen dimensions	37
Figure 4.3. ASTM E8/E8M-16a Round specimen dimensions	38
Figure 4.4. Flat specimens made of (a) S235JR steel (b) Al2024T3 aluminum alloy	39
Figure 4.5. All the round specimens prepared for the test including the spares (12 on the left hand-side are Al and 12 on the righthand- side are steel).....	39
Figure 4.6. (a) After-fracture tensile test specimen of flat material (b) Just-before-fracture tensile test specimen of circular material.....	40
Figure 4.7. Flat and cylindrical specimens after the completion of the tests	41
Figure 4.8. Average stress-strain curves for straight, Al2024T3, sheet specimen tensile test experiments.....	42
Figure 4.9. Average stress-strain curves for tapered, Al2024T3, sheet specimen tensile test experiments.....	42

Figure 4.10. Average stress-strain curves for notched, Al2024T3, sheet specimen tensile test experiments..... 43

Figure 4.11. Comparative engineering stress-strain curves of straight, tapered and notched Al2024T3 sheet specimen tensile test experiments 43

Figure 4.12. Average stress-strain curves for straight, Al2024T3, round specimen tensile test experiments..... 44

Figure 4.13. Average stress-strain curves for tapered, Al2024T3, round specimen tensile test experiments..... 44

Figure 4.14. Average stress-strain curves for notched, Al2024T3, round specimen tensile test experiments..... 45

Figure 4.15. Comparative engineering stress-strain curves of straight, tapered and notched Al2024T3 round specimen tensile test experiments 45

Figure 4.16. Average stress-strain curves for straight, S235JR, sheet specimen tensile test experiments 46

Figure 4.17. Average stress-strain curves for tapered, S235JR, sheet specimen tensile test experiments 47

Figure 4.18. Average stress-strain curves for notched, S235JR, sheet specimen tensile test experiments 47

Figure 4.19. Comparative engineering stress-strain curves of straight, tapered and notched S235JR sheet specimen tensile test experiments 48

Figure 4.20. Average stress-strain curves for straight, S235JR, round specimen tensile test experiments 49

Figure 4.21. Average stress-strain curves for tapered, S235JR, round specimen tensile test experiments 49

Figure 4.22. Average stress-strain curves for notched, S235JR, round specimen tensile test experiments 49

Figure 4.23. Comparative engineering stress-strain curves of straight, tapered and notched S235JR round specimen tensile test experiments 50

Figure 4.24. Tinius-Olsen Ductomatic A-40 Sheet Metal Tester 52

Figure 4.25. Specimen geometry for square cup test is on left-hand side. Specimen geometry for cylindrical and hemispherical specimens is on the right-hand side.	54
Figure 4.26. Deep drawing process specimens after completion of processes	55
Figure 4.27. Punch force vs. punch travel graph for Al2024T3 cylindrical cup deep drawing (C2) experiment	56
Figure 4.28. Punch force vs. punch travel graph for Al2024T3 cylindrical cup deep drawing (C3) experiment	56
Figure 4.29. Punch force vs. punch travel graph for Al2024T3 cylindrical cup deep drawing (C4) experiment	57
Figure 4.30. Punch force vs. punch travel graph for Al2024T3 round bottom cup deep drawing (R1) experiment	57
Figure 4.31. Punch force vs. punch travel graph for Al2024T3 round bottom cup deep drawing (R2) experiment	58
Figure 4.32. Punch force vs. punch travel graph for Al2024T3 round bottom cup deep drawing (R3) experiment	58
Figure 4.33. Punch force vs. punch travel graph for Al2024T3 square cup deep drawing (S3) experiment.....	59
Figure 4.34. Punch force vs. punch travel graph for Al2024T3 square cup deep drawing (S4) experiment.....	59
Figure 4.35. Punch force vs. punch travel graph for Al2024T3 square cup deep drawing (S5) experiment.....	60
Figure 5.1. (a) 3D view of a round tensile test specimen (b) half of the cross-section	65
Figure 5.2. Initial geometry coordinates of a quarter cross-section without head for (a) Cylindrical model (b) Tapered model (c) Notched model	66
Figure 5.3. Boundary conditions of (a) Cylindrical model (b) Tapered model (c) Notched model	67
Figure 5.4. Meshed domain covering $\frac{1}{4}$ of gauge cross-section.....	67

Figure 5.5. (a) Mesh domain for straight and tapered axisymmetric models (b) Some mesh element number and positions at upper section (c) Some mesh element numbers and positions at lower section.....	68
Figure 5.6. A closer view of notch location.....	68
Figure 5.7. New element numbers for meshes on notched domain.....	69
Figure 5.8. Upper and lower boundaries of axisymmetric model	69
Figure 5.9. (a) 3D view of a round tensile test specimen (b) half of the cross-section	70
Figure 5.10. Geometrical details of 3D sheet models (a) Isometric view (b) Straight strip (c) Tapered strip (d) Notched strip (e) A closer look at the notched strip.....	71
Figure 5.11. (a) Isometric view of the strip-type specimen (b) Boundary conditions of straight specimen (c) Boundary conditions of tapered specimen (d) Boundary conditions of notched specimen.....	72
Figure 5.12. Mesh domain covering $\frac{1}{4}$ of the specimen (a) Al2024T3 (b) S235JR..	72
Figure 5.13. (a) Isometric view and (b) Front view of mesh domain for straight and tapered 3D sheet models. Some mesh element number and positions at (c) upper section (d) lower section.....	73
Figure 5.14. A closer front view of notch location.....	74
Figure 5.15. (a) Isometric view and (b) Front view of mesh domain for notched 3D sheet models. Some mesh element number and positions at (c) upper section (d) lower section.....	74
Figure 5.16. (a) Displacement/velocity application region in FEA (b) Mesh elements at the bottom used to calculate punch force.....	75
Figure 5.17. (a) The holder (b) The die (c) The blank for both cylindrical cup and round bottom cup deep drawing FE analysis.....	76
Figure 5.18. Punch geometry of (a) Cylindrical cup (b) Round bottom cup for deep drawing FE analysis.....	76
Figure 5.19. Cylindrical cup deep drawing FE analysis (a) Assembly of the parts (b) Assembly of the meshed parts (c) Meshed sheet metal specimen.....	76

Figure 5.20. Round botom cup deep drawing FE analysis (a) Assembly of the parts (b) Assembly of the meshed parts (c) Meshed sheet metal specimen.....	77
Figure 5.21. (a) The die (b) The holder (c) The punch (d) The blank models of square cup deep drawing analysis	77
Figure 5.22. Square cup deep drawing FE analysis (a) Assembly of the parts (b) Assembly of the meshed parts (c) Meshed sheet metal specimen	77
Figure 5.23. Mesh elements and positions for cylindrical cup deep drawing specimen	78
Figure 5.24. Mesh elements and positions for hemispherical cup deep drawing specimen.....	79
Figure 5.25. Mesh elements and positions for square cup deep drawing specimen ..	79
Figure 6.1. Strain increment ratios of several mesh element couples vs. percent elongation of the gauge for straight cross-section, sheet, Al specimen	83
Figure 6.2. Difference of second time derivative of strain for several mesh element couples vs. percent elongation of the gauge for straight cross-section, sheet, Al specimen.....	84
Figure 6.3. Second time derivative of Element 1 strain vs. percent elongation of the gauge for straight cross-section, sheet, Al specimen (Necking at 18.52% total elongation).....	85
Figure 6.4. Plastic strain of Element 1 vs. percent elongation of the gauge for straight cross-section, sheet, Al specimen	86
Figure 6.5. First time derivative of Element 1 strain vs. percent elongation of the gauge for straight cross-section, sheet, Al specimen.....	86
Figure 6.6. Punch force vs. percent gauge elongation of Element 100 for tapered cross-section, sheet, Al specimen (Necking at 18.63% total elongation)	87
Figure 6.7. Strain increment ratios of several mesh element couples vs. percent elongation of the gauge for tapered cross-section, sheet, Al specimen	88
Figure 6.8. Difference of second time derivative of strain for several mesh element couples vs. percent elongation of the gauge for tapered cross-section, sheet, Al specimen.....	88

Figure 6.9. Second time derivative of Element 1 strain vs. percent elongation of the gauge for tapered cross-section, sheet, Al specimen (Necking at 16.42% total elongation)	89
Figure 6.10. Plastic strain of Element 1 vs. percent elongation of the gauge for tapered cross-section, sheet, Al specimen	90
Figure 6.11. First time derivative of Element 1 strain vs. percent elongation of the gauge for tapered cross-section, sheet, Al specimen	90
Figure 6.12. Punch force vs. percent gauge elongation of Element 100 for tapered cross-section, sheet, Al specimen (Necking at 16.17% total elongation).....	91
Figure 6.13. Strain increment ratios of several mesh element couples vs. percent elongation of the gauge for notched cross-section, sheet, Al specimen	91
Figure 6.14. Difference of second time derivative of strain for several mesh element couples vs. percent elongation of the gauge for notched cross-section, sheet, Al specimen	92
Figure 6.15. Second time derivative of Element 1 strain vs. percent elongation of the gauge for notched cross-section, sheet, Al specimen (Necking at 10.76% total elongation)	93
Figure 6.16. Plastic strain of Element 1 vs. percent elongation of the gauge for notched cross-section, sheet, Al specimen	94
Figure 6.17. First time derivative of Element 1 strain vs. percent elongation of the gauge for notched cross-section, sheet, Al specimen	94
Figure 6.18. Punch force vs. percent gauge elongation of Element 100 for notched cross-section, sheet, Al specimen (Necking a 10.21% total elongation).....	95
Figure 6.19. Strain increment ratios of several mesh element couples vs. percent elongation of the gauge for straight cross-section, round, Al specimen.....	96
Figure 6.20. Difference of second time derivative of strain for several mesh element couples vs. percent elongation of the gauge for straight cross-section, round, Al specimen	96

Figure 6.21. Second time derivative of Element 1 strain vs. percent elongation of the gauge for straight cross-section, round, Al specimen (Necking at 10.46% total elongation).....	97
Figure 6.22. Plastic strain of Element 1 vs. percent elongation of the gauge for straight cross-section, round, Al specimen	98
Figure 6.23. . First time derivative of Element 1 strain vs. percent elongation of the gauge for straight cross-section, round, Al specimen	98
Figure 6.24. Punch force vs. percent gauge elongation of Element 100 for straight cross-section, round, Al specimen (Necking at 11.06% total elongation).....	99
Figure 6.25. Strain increment ratios of several mesh element couples vs. percent elongation of the gauge for tapered cross-section, round, Al specimen	99
Figure 6.26. Difference of second time derivative of strain for several mesh element couples vs. percent elongation of the gauge for tapered cross-section, round, Al specimen.....	100
Figure 6.27. Second time derivative of Element 1 strain vs. percent elongation of the gauge for tapered cross-section, round, Al specimen (Necking 6.96% total elongation)	101
Figure 6.28. Plastic strain of Element 1 vs. percent elongation of the gauge for tapered cross-section, round, Al specimen	101
Figure 6.29. First time derivative of Element 1 strain vs. percent elongation of the gauge for tapered cross-section, round, Al specimen	102
Figure 6.30. Punch force vs. percent gauge elongation of Element 839 for tapered cross-section, round, Al specimen (Necking at 7.69% total elongation).....	102
Figure 6.31. . Strain increment ratios of several mesh element couples vs. percent elongation of the gauge for notched cross-section, round, Al specimen	103
Figure 6.32. Difference of second time derivative of strain for several mesh element couples vs. percent elongation of the gauge for notched cross-section, round, Al specimen.....	104

Figure 6.33. Second time derivative of Element 1 strain vs. percent elongation of the gauge for notched cross-section, round, Al specimen (Necking 3.51% elongation)	105
Figure 6.34. Plastic strain of Element 1 vs. percent elongation of the gauge for notched cross-section, round, Al specimen	105
Figure 6.35. First time derivative of Element 1 strain vs. percent elongation of the gauge for notched cross-section, round, Al specimen	106
Figure 6.36. Punch force vs. percent gauge elongation of Element 916 for notched cross-section, round, Al specimen (Necking at 3.66% total elongation).....	106
Figure 6.37. Strain increment ratios of several mesh element couples vs. percent elongation of the gauge for straight cross-section, sheet, steel specimen	107
Figure 6.38. Difference of second time derivative of strain for several mesh element couples vs. percent elongation of the gauge for straight cross-section, sheet, steel specimen	108
Figure 6.39. Second time derivative of Element 1 strain vs. percent elongation of the gauge for straight cross-section, sheet, steel specimen (Necking at 16.54% total elongation)	109
Figure 6.40. Plastic strain of Element 1 vs. percent elongation of the gauge for straight cross-section, sheet, steel specimen.....	109
Figure 6.41. First time derivative of Element 1 strain vs. percent elongation of the gauge for straight cross-section, sheet, steel specimen.....	110
Figure 6.42. Punch force vs. percent gauge elongation of Element 100 for straight cross-section, sheet, steel specimen (Necking at 17.34% total elongation)	110
Figure 6.43. Strain increment ratios of several mesh element couples vs. percent elongation of the gauge for tapered cross-section, sheet, steel specimen.....	111
Figure 6.44. Difference of second time derivative of strain for several mesh element couples vs. percent elongation of the gauge for tapered cross-section, sheet, steel specimen	112

Figure 6.45. Second time derivative of Element 1 strain vs. percent elongation of the gauge for tapered cross-section, sheet, steel specimen (Necking at 16.05% total elongation).....	113
Figure 6.46. Plastic strain of Element 1 vs. percent elongation of the gauge for tapered cross-section, sheet, steel specimen	113
Figure 6.47 First time derivative of Element 1 strain vs. percent elongation of the gauge for tapered cross-section, sheet, steel specimen.	114
Figure 6.48. Punch force vs. percent gauge elongation of Element 100 for tapered cross-section, sheet, steel specimen (Necking at 14.17% total elongation).....	114
Figure 6.49. Strain increment ratios of several mesh element couples vs. percent elongation of the gauge for notched cross-section, sheet, steel specimen	115
Figure 6.50. Difference of second time derivative of strain for several mesh element couples vs. percent elongation of the gauge for notched cross-section, sheet, steel specimen.....	116
Figure 6.51. Second time derivative of Element 1 strain vs. percent elongation of the gauge for notched cross-section, sheet, steel specimen (Necking at 14.55% total elongation).....	117
Figure 6.52. Plastic strain of Element 1 vs. percent elongation of the gauge for notched cross-section, sheet, steel specimen	117
Figure 6.53. First time derivative of Element 1 strain vs. percent elongation of the gauge for notched cross-section, sheet, steel specimen	118
Figure 6.54. Punch force over percent gauge elongation of Element 100 for notched cross-section, sheet, steel specimen (Necking at 13.12% total elongation).....	118
Figure 6.55. Strain increment ratios of several mesh element couples vs. percent elongation of the gauge for straight cross-section, round, steel specimen.....	119
Figure 6.56. Difference of second time derivative of strain for several mesh element couples vs. percent elongation of the gauge for straight cross-section, round, steel specimen.....	120

Figure 6.57. Second time derivative of Element 1 strain vs. percent elongation of the gauge for straight cross-section, round, steel specimen (Necking at 5.83% total elongation) 121

Figure 6.58. Plastic strain of Element 1 vs. percent elongation of the gauge for straight cross-section, round, steel specimen..... 121

Figure 6.59. First time derivative of Element 1 strain vs. percent elongation of the gauge for straight cross-section, round, steel specimen 122

Figure 6.60. Punch force vs. percent gauge elongation of Element 100 for straight cross-section, round, steel specimen (Necking at 6.71% total elongation) 122

Figure 6.61. Strain increment ratios of several mesh element couples vs. percent elongation of the gauge for tapered cross-section, round, steel specimen..... 123

Figure 6.62. Difference of second time derivative of strain for several mesh element couples vs. percent elongation of the gauge for tapered cross-section, round, steel specimen 124

Figure 6.63. Second time derivative of Element 1 strain vs. percent elongation of the gauge for tapered cross-section, round, steel specimen (Necking at 4.47% elongation) 125

Figure 6.64. Plastic strain of Element 1 vs. percent elongation of the gauge for tapered cross-section, round, steel specimen..... 125

Figure 6.65. First time derivative of Element 1 strain vs. percent elongation of the gauge for tapered cross-section, round, steel specimen..... 126

Figure 6.66. Punch force vs. percent gauge elongation of Element 100 for tapered cross-section, round, steel specimen (Necking a 5.32% total elongation) 126

Figure 6.67. Strain increment ratios of several mesh element couples vs. percent elongation of the gauge for notched cross-section, round, steel specimen..... 127

Figure 6.68. Difference of second time derivative of strain for several mesh element couples vs. percent elongation of the gauge for notched cross-section, round, steel specimen 128

Figure 6.69. Second time derivative of Element 1 strain vs. percent elongation of the gauge for notched cross-section, round, steel specimen (Necking at 3.85% elongation)	129
Figure 6.70. Plastic strain of Element 1 vs. percent elongation of the gauge for notched cross-section, round, steel specimen	129
Figure 6.71. First time derivative of Element 1 strain vs. percent elongation of the gauge for notched cross-section, round, steel specimen	130
Figure 6.72. Punch force vs. percent gauge elongation of Element 100 for notched cross-section, round, steel specimen (Necking a 4.55% elongation).....	130
Figure 6.73. Strain increment ratios of several mesh element couples vs. punch displacement for cylindrical cup deep drawing process with 110 mm diameter, sheet, Al specimen.....	139
Figure 6.74. Difference of second time derivative of strain for several mesh element couples vs. punch displacement for cylindrical cup deep drawing process with 110 mm diameter, sheet, Al specimen	140
Figure 6.75. Second time derivative of Element 1 strain vs. punch displacement for cylindrical cup deep drawing process with 110 mm diameter, sheet, Al specimen (Necking at 13.72 mm displacement)	141
Figure 6.76. Plastic strain of Element 1 vs. punch displacement for cylindrical cup deep drawing process with 110 mm diameter, sheet, Al specimen	141
Figure 6.77. First time derivative of Element 1 strain vs. punch displacement for cylindrical cup deep drawing process with 110 mm diameter, sheet, Al specimen.	142
Figure 6.78. Punch force vs. punch displacement for cylindrical cup deep drawing process with 110 mm diameter, sheet, Al specimen (Necking at 10.24 mm displacement)	142
Figure 6.79. Strain increment ratios of several mesh element couples vs. punch displacement for round bottom cup deep drawing process with 110 mm diameter, sheet, Al specimen	143

Figure 6.80. Difference of second time derivative of strain for several mesh element couples vs. punch displacement for round bottom cup deep drawing process with 110 mm diameter, sheet, Al specimen..... 144

Figure 6.81. Second time derivative of Element 1 strain vs. punch displacement for round bottom cup deep drawing process with 110 mm diameter, sheet, Al specimen (Necking at 19.28 mm displacement) 145

Figure 6.82. Plastic strain of Element 1 vs. punch displacement for round bottom cup deep drawing process with 110 mm diameter, sheet, Al specimen 145

Figure 6.83. First time derivative of Element 1 strain vs. punch displacement for round bottom cup deep drawing process with 110 mm diameter, sheet, Al specimen 146

Figure 6.84. Punch force vs. punch displacement for round bottom cup deep drawing process with 110 mm diameter, sheet, Al specimen (Necking at 18.62 mm displacement) 146

Figure 6.85. Strain increment ratios of several mesh element couples vs. punch displacement for square cup deep drawing process with 80x80 mm-square, sheet, Al specimen 147

Figure 6.86. Difference of second time derivative of strain for several mesh element couples vs. punch displacement for square cup deep drawing process with 80x80 mm-square, sheet, Al specimen..... 148

Figure 6.87. Second time derivative of Element 1 strain vs. punch displacement for square cup deep drawing process with 80x80 mm-square, sheet, Al specimen (Necking at 12.64 mm displacement)..... 149

Figure 6.88. Plastic strain of Element 1 vs. punch displacement for square cup deep drawing process with 80x80 mm-square, sheet, Al specimen..... 149

Figure 6.89. First time derivative of Element 1 strain vs. punch displacement for square cup deep drawing process with 80x80 mm-square, sheet, Al specimen 150

Figure 6.90. Punch force vs. punch displacement for round bottom cup deep drawing process with 110 mm diameter, sheet, Al specimen (Necking at 13.21 mm displacement)..... 150

Figure 0.1. FE view of equivalent plastic strain and stress for TT-She-Al-Str 171

Figure 0.2. FE view of equivalent plastic strain and stress for TT-She-Al-Tpr.....	171
Figure 0.3. FE view of equivalent plastic strain and stress for TT-She-Al-Ntc.....	172
Figure 0.4. FE view of equivalent plastic strain and stress for TT-Ro-Al-Str.....	172
Figure 0.5. FE view of equivalent plastic strain and stress for TT-Ro-Al-Tpr.....	173
Figure 0.6. FE view of equivalent plastic strain and stress for TT-Ro-Al-Ntc.....	173
Figure 0.7. FE view of equivalent plastic strain and stress for TT-She-St-Str	174
Figure 0.8. FE view of equivalent plastic strain and stress for TT-She-St-Tpr	174
Figure 0.9. FE view of equivalent plastic strain and stress for TT-She-St-Ntc	175
Figure 0.10. FE view of equivalent plastic strain and stress for TT-Ro-St-Str.....	175
Figure 0.11. FE view of equivalent plastic strain and stress for TT-Ro-St-Tpr.....	176
Figure 0.12. FE view of equivalent plastic strain and stress for TT-Ro-St-Ntc.....	176
Figure 0.13. FE view of equivalent plastic strain for DDP-CC-Al.....	177
Figure 0.14. FE view of equivalent stress for DDP-CC-Al	177
Figure 0.15. FE view of equivalent plastic strain for DDP-RB-Al.....	178
Figure 0.16. FE view of equivalent stress for DDP-RB-Al	178
Figure 0.17. FE view of equivalent plastic strain for DDP-SC-Al	179
Figure 0.18. FE view of equivalent stress for DDP-RB-Al	179

LIST OF ABBREVIATIONS

ABBREVIATIONS

2D	2 Dimensional
3D	3 Dimensional
BHF	Blank Holder Force
DIC	Digital Image Correlation
FE	Finite Element
FEA	Finite Element Analysis
PEEQ	Equivalent Plastic Strain
SMF	Sheet Metal Forming

LIST OF SYMBOLS

SYMBOLS

ρ	Density, ton/mm ³
σ	True Stress, MPa (N/mm ²)
σ_0	Nominal (Engineering) Stress, MPa (N/mm ²)
τ	Shear Stress, MPa (N/mm ²)
t	Time (s)
ε	True Strain, mm/mm
ϵ	Nominal (Engineering) Strain, mm/mm
ν	Poisson ratio
A	Area, mm ²
L	Length, mm
F	Force, N
E	Young's (Elastic) Modulus, GPa

SUBSCRIPTS / SUPERSSCRIPTS

u	Ultimate
f	Fracture
Y	Yield
l	Limit
0	Initial State / Condition

i	Any Certain State Between Initial and Final
p	Plastic
e	Elastic

CHAPTER 1

INTRODUCTION

1.1. Motivation

Tensile plastic instability in metals is a mode of unstable deformation caused by the imbalance between increase in mechanical strength due to hardening and increase in stress due to thinning. On the other hand, necking, as a tensile plastic instability, refers to the rapid thinning in long and narrow specimens. Thus, the localized thinning phenomenon is referred as tensile plastic instability in deep drawing process; whereas, it is attributed as necking in tensile tests in this thesis.

Since Considère published the basic criterion for necking in 1885, tensile plastic instability and necking in metal forming and testing operations have received an enormous amount of attention in scientific and engineering literature [1]. There are two main reasons behind: Necking is an important indicator of material properties and it usually points an incoming material failure. Until last decade, the main focus had been on representing the material deformation in plastic region precisely and accurately. As important as this, the time and the deformation stage at which uniform deformation of the specimen becomes concentrated into a certain region are of utmost interest for the proper description of material resistance under a given load. Many authors have simulated plastic instability of tensile test, deep drawing, Nakazima test, tube bending, bulge testing, dome stretching and hydroforming. However, researchers have recently focused more on the methods to predict it. Consequently, prediction of the plastic instability and necking formation of components remains an active research topic.

Because the outputs in this field is growing, it is important to have sound foundations for the methods applied. Are they only applicable to certain materials, specimen

geometries, test types or modeling approaches? Are they effective any time or do some requirements exist to employ these procedures? Which methods are more effective or practical than others?

These questions are still tough and need answers after having scientific evidence or proof. The starting points of this thesis are the aforementioned questions and curiosity.

1.2. Background

In engineering or material science, tensile plastic instability and necking phenomena occur during a deformation process when relatively large amount of strain is concentrated into a small region of specimen. In other words, tensile plastic instability occurs when the rate of work hardening is lower than the flow stress along a tested part under stress. Different materials and different application types reveal different tensile plastic instability characteristics; yet, the fundamental concepts are similar in most processes. Still, many different approaches have been derived to explain tensile plastic instability behavior of materials. Although several tensile plastic instability and necking criteria have been used in literature, some restrictions limit their implementations. This study aims to conduct experimental and numerical analysis to oversee universality, accuracy, precision of the methods as well as their restrictions.

Tensile and deep drawing processes are selected to apply the methods because they are widely used and accepted experiments; moreover, the results can easily be utilized in further studies.

1.2.1. Tensile Testing of Metals

Simple tension test (also known as uniaxial tensile test) is a classical method used to plot stress-strain curve of metallic materials. It is one of the most important tests in mechanical engineering technology since it provides detailed information on a material in a relatively inexpensive and practical/versatile procedure. This test elongates the material to its limits in one direction. During the test, some physical

properties of the material (such as shape) are changed as well as the internal structure. The results allow the researchers and engineers to compare different materials independent of the size and weight. Tensile test outputs reveal strength and ductility characteristics of a specimen. Some resulting mechanical properties such as modulus of elasticity, yield strength, ultimate tensile strength, and Poisson's ratio are used in material selection, quality control, material development and design under not only axial loading but also other types of load types such as torsion, bending and their combinations.

Tensile test specimen geometry can vary depending on the procedure and purpose of the test. Two types of tension test specimens are used; namely, round or cylindrical specimen and sheet or flat specimen.

Tension test methods and specimen dimensions are standardized by several organizations such as American Society for Testing and Materials International (ASTM), International Organization for Standardization (ISO) and Japanese Industrial Standards (JIS). In this work, ASTM E8/E8M-16a: Standard Test Methods for Tension Testing of Metallic Materials is to be taken as basis [2].

There are alternative tensile test machine types in use. In electro-mechanical machines, the displacement of one head is obtained by the rotation of spindles. On the other hand, in hydraulic machines, oil pressure is exploited to acquire the desired displacement. Lastly, the displacement is attained through linear electricity motors in electro-dynamic test machines.

The standard procedure of the tensile test is placing a sample between two fixtures and applying load to extend it until failure. The load is exerted to the material at one end while the other end is fixed. The load is kept increasing while the change in length and cross-section of the material is being recorded. In some cases, displacement of the moving fixture is controlled rather than the applied load. As the test commences, stress applied on the specimen is proportional to strain until proportional limit. In this region, the deformation is reversible.

If the specimen is loaded beyond elastic limit, plastic flow occurs, the curve deviates from the elastic linear line and the further deformation becomes permanent. Elastic limit is hard to detect for many materials; hence, 0.2% strain offset method is usually utilized to acquire yield point. If the load keeps increasing at yield point, the material hardens, and stress increases until ultimate strength. The plastic deformation strengthens the material, which is referred as work or strain hardening. If the load on the specimen is removed, elastic strain is recovered. After reaching ultimate load, an important phenomenon called necking takes place as in Figures 1.1(a)-(c) [3]. Thereafter, gradually decreasing load levels are sufficient to deform the specimen further.

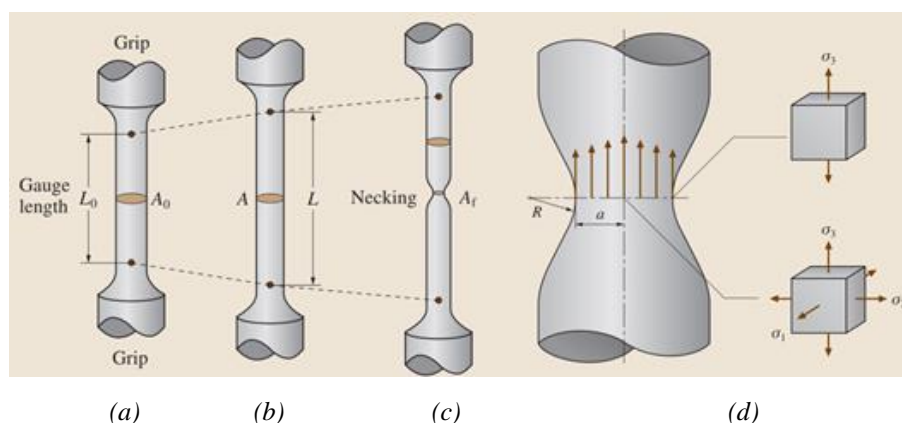


Figure 1.1. (a)-(c) Consecutive stress conditions in a necked region in tension test, (d) Tension specimen and macroscopic tensile deformation behavior [3]

Necking results from an instability during tensile deformation when a material's cross-sectional area decreases by a greater proportion than the material strain hardens. The complex stress-state resulting from the instability in the necking region is shown in Figure 1.1(d) [3]. Figure 1.2 illustrates true and nominal stress-strain curves, which are compared with work-hardening rate [3]. This plot indicates there is a balance between work-hardening and cross-sectional area reduction until onset of necking. Afterwards, cross-section reduction dominates the work-hardening, resulting in a rapid dimension change in a particular region. The intersection point of true stress and work-hardening rate curves remarks the onset of necking. Micro-voids are formed in

necked region, they grow and join each other. Finally, at fracture point, the specimen fails and breaks into two parts.

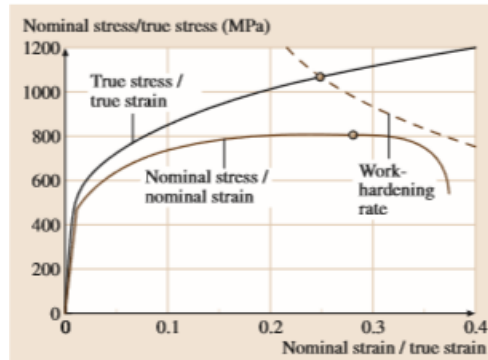


Figure 1.2. True and nominal stress–strain curve in which the work-hardening rate is plotted to indicate the onset of necking [3]

There are several factors that affect the stress-strain curve obtained from tensile tests. Material of the specimen is a factor, whose distinctive affect can be illustrated on tensile testing of low-carbon steel specimens such as mild steel. A phenomenon called Lüders band is detected in such tests. Geometry of the specimen is another important critical factor in tensile testing e.g. sheet specimens undergo different phases than rod specimens. The phenomenon occurring at ultimate strength is sometimes referred to as diffuse necking as shown in Figure 1.3 [4].

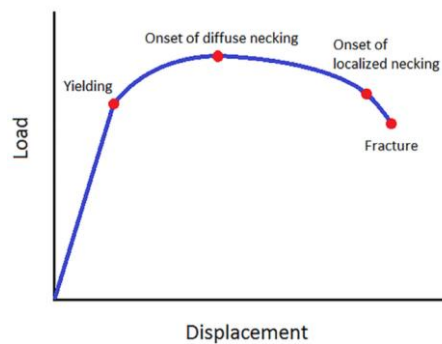


Figure 1.3. The typical load-displacement curve of a tensile test with flat specimen [4]

Although a complicated triaxial stress state is observed in diffuse necking, the neck spreads parallel to specimen cross section. Diffuse necking is common for both round specimens with circular cross-section and flat specimens with rectangular cross-

section. Flat specimens undergo localized necking shortly after diffuse necking is observed. In localized necking of sheets, neck propagation is concentrated in a band which is at a certain angle to specimen cross section as in Figure 1.4(b) [5].

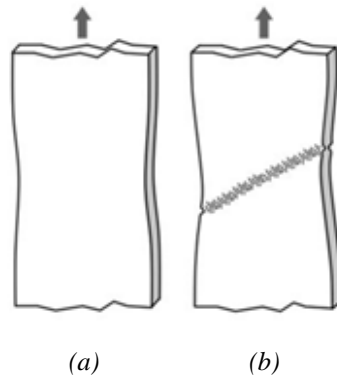


Figure 1.4. Development of (a) diffuse necking and (b) localized necking in tensile test of sheet metals [5]

Fracture of the material in flat specimens occurs within the same region as localized necking. The onset of localized necking is usually very close to fracture point (Figure 1.3) [4].

Isotropic material assumption is compatible with bar specimen experiment models, since the mentioned uniformity is a natural result of extrusion process during production stage. On the other hand, the strip specimens may have significantly different properties when cut along different directions on raw sheet.

1.2.2. Deep Drawing Processing of Metals

There are several metal forming operations utilized such forging, rolling, extrusion, drawing and deep drawing which is defined as [6],

“Deep drawing is a method of forming under compressive and tensile conditions whereby a sheet metal blank is transformed into a hollow cup, or a hollow cup is transformed into a similar part of smaller dimensions without any intention of altering the sheet thickness.”

Beverage cans, sinks, cooking pots, ammunition shell containers, pressure vessels, auto panels and parts are commonly fabricated with deep drawing.

Deep drawing is a compression-tension process. In deep drawing process, after the specimen is clamped between blank holder and die, the punch moves through those parts. The flange of sheet metal is compressed with blank holder throughout the operation to prevent wrinkling and control the process. The force and the feed rate of the punch are crucial to obtain the desired final cup shape with acceptable level of defects. Note that lubricants must be applied to prevent friction damages between punch and the specimen and other contact areas, as mentioned before. Fracture is the ultimate failure type and can be caused by excessive punch displacement or velocity, mal-practices such as no lubricant usage, and ill-applied blank holder position and force. Furthermore, the friction force caused by the blank holder and die surfaces restrains the undesired material flow. On the other hand, if the blank force is beyond certain limits, fracture might be observed before the necessary cup height is acquired [7].

The primary deformation zones can be identified as in Figure 1.5: Zones 1-2 refer to the flange which experience axial compression, radial tension, circumferential compression [8].

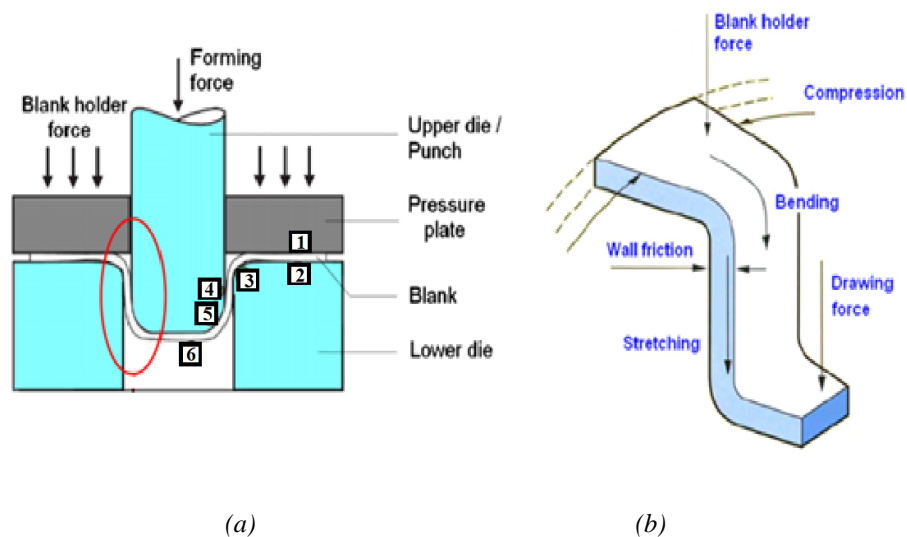


Figure 1.5. (a) Cross section view of a typical deep drawing process with forces exerted (b) Deformation zones and types of the blank during deep drawing [8]

Zone 3 is the die corner radius which is exposed to bending and friction. Zone 4 is the wall of the cup where tension is dominant and has high potential of fracture. Zone 5 is the punch corner radius which is affected by bending and friction. Lastly, Zone 6 touches to the flat circular bottom which is only enforced by friction and thus record near zero strain.

Since it is a commonly used sheet metal forming process, deep drawing is frequently used to evaluate the tensile plastic instability and fracture prediction methods.

1.2.3. Methods to Predict the Onset of Instability

In this thesis work, several criteria for necking/tensile plastic instability prediction will be utilized; namely:

- Equivalent plastic strain rate ratio
- Difference of second time derivative of equivalent plastic strain
- Maximum second time derivative of equivalent plastic strain
- Maximum punch force

1.3. Objectives of the Research

The primary objective of this thesis is to conduct a comprehensive study about tensile plastic instability and necking characteristics and their applications to the solid mechanics problems. Instability prediction phenomenon has been investigated a number of works; yet, this study aims to determine reliable, accurate and flexible methods with a series of experimental and numerical procedures.

Different test methods, different material and specimen shapes may require unique practices to predict the onset of instability. This thesis study involves numerical simulations and experiments of two operations; uniaxial tensile test and deep drawing process, two materials; Al2024T3 aluminum and S235JR steel, two specimen types; cylindrical and sheet and three cross-section geometries; straight, tapered and notched.

As a result, the onset of necking or tensile plastic instability for each case will be understood deeply and the predictions will be assessed on the basis of the outcomes.

The main reasons behind the choice of tensile test and deep drawing process are that they are traditional, widely used and the results can be applicable to many other applications. Obtaining a foresight on the necking/instability prediction will enlighten plastic deformation characteristics of metals further and material failure as well.

Lastly, this thesis aims to predict instability properties of specimens so that production and testing procedures in real-life can be optimized in terms of time, cost and quality.

1.4. Scope of the Thesis

First, an exhaustive literature survey is conducted so that the methods to predict necking and tensile plastic instability can be gathered and assessed along with the associated challenges, problems and results. According to the evaluations, some methods are chosen to apply in FEA.

Then, process details and results of the experiments will be presented. 12 different tensile test specimens are prepared. Similarly, sheet metal specimens of aluminum undergo cylindrical cup, square cup and round bottom drawing processes.

Next, finite element (FE) simulations are run for each case and all prediction methods are going to be employed. Note that the simulation processes are carried out in a commercial software. In those analysis, accuracy, validity and generality of the methods are investigated.

In the literature, there are few studies that implement methods to predict onset of necking. It is even rarer to find records comparing them. Lastly, almost all of the necking prediction works are limited to one material type, one specimen type or one testing type. To the author's best knowledge, none of the resources in literature utilizes and compares straight, tapered and notched specimens from necking prediction point of view.

1.5. Outline of the Thesis

This thesis consists of seven chapters.

In Chapter I, an introduction has been made. Motivation and background information for technical notions are given along with objectives, scope and outline of the thesis.

In Chapter II, an overview of the associated literature is written. Many sub-topics such as tests, materials, simulation and analysis techniques are touched and provided with researches and developments in academic world.

In Chapter III, theoretical formulation and constitutive models are explained. Some generic formulations are given; then, tensile plastic instability and necking prediction techniques have been constructed.

In Chapter IV, the experiments; namely, tensile test and deep drawing processes with different specimens are described and depicted step-by-step. Many figures have been generated so that different combinations of results can be compared and contrasted.

In Chapter V, FE model of both tensile test and deep drawing process on commercial software are expressed and portrayed.

In Chapter VI, results of FE analysis are put forward as well as some comments and discussions points.

In Chapter VII, a conclusion section is provided on the current study. In the other subsection, possible future work subjects are also presented.

As the last part, references and appendices are stated.

CHAPTER 2

LITERATURE REVIEW

Tensile testing is a mechanical test type receiving close review for long times. Since humanity settled in permanent structures in Neolithic age, the strength of materials such as softwoods, hardwoods, stones have been under close investigation. As a result, Greek, Egyptian, Roman and Norman civilizations had frankly comprehended material properties based on experience [9]. Nonetheless, the first documented evidence of tensile test dates to Leonardo Da Vinci, a famous scientist and artist of Renaissance period. His work “Testing the strength of iron wires of various lengths” displayed he used iron wires of different length and diameter to suspend a basket filled with sand [10].

First modern tensile test machines originate from 19th century, and the first standards for tensile test were published in first half of 20th century [9].

According to the literature survey, a large and growing body of literature has investigated tensile testing of metallic materials. Because this testing is widely accepted and very flexible so that the results can be employed in other tests; uniaxial tensile testing is to be the starting point for this work.

To begin with, material types to be tested must be discussed. The mechanical behavior of mostly used elements such as aluminum, iron, copper, zinc is of broad and current interest. Yet, alloys composed of these elements have exhibited higher performance than their pure forms. Consequently, the most common materials in the tensile test literature are alloys of steel, aluminum and copper. Steel is a significant alloy, it is consumed extensively in construction, transportation and machinery industries. In last decades, much more information has become available on steel specimen analysis due to the studies of Zhang [11] (BB503 steel), Le Van et al. [12] (XC48C steel), Cabezas

et al. [13] and Careglio et al. [14] (SAE 1045 steel), Mirone [15] (20MnMoNi55 steel), Tu et al. [16] (20MnMoNi55 steel, AISI 304 steel and FE 430 steel), Farahnak et al. [17] (DC01 mild steel), Lumelskyj et al. [18] (DC04 grade steel), Coppieters et al. [19] and Manopulo et al. [20] (DC05 mild steel), Kamaya et al. [21] (316L stainless steel), Ahn et al. [22] (409L stainless steel), Merklein et al. [23] (HX260 steel), Kim et al. [24] (A533B RPV steel), Kolasangiani et al. [25] (SS304L stainless steel), Galpin et al. [26] (DP450 steel), Min et al. [27] and Min et al. [28] (MP980 steel and DP600 steel), Li et al. [4] (DP780 steel), Abbassi et al. [29] (S360 steel, Bao et al. [30] (430 steel), Saboori et al. [31] (Grade 321 stainless steel), Morales-Palme et al. [32] (1008 AK steel), and Kweon et al. [33] (SA-508 low alloy steel). Such a diversity in material selection is owing to the fact that different industries and applications specialize in different material compositions. Indeed, scientific curiosity drives the researchers to work on as many different materials as possible.

Many construction products are being made of S235JR steel including beams, pipes, rods, plates used in bridges, towers, plants etc. Moreover, non-building structures such as bridges involve many parts made of S235JR, that is a mild, low-carbon steel [34].

In the second place, a considerable amount of literature has been published on aluminum alloys. Aluminum alloys are extensively utilized in aerospace, automotive, electrical and marine applications. Related studies include Zhang et al. [35] (5086 aluminum alloy), Banabic et al. [36] and Barata de Rocha et al. [37] and [38] (5182-O aluminum alloy), Drotleff et al. [39] (6014 aluminum alloy), Merklein et al. [23] and Galpin et al. [26] and Manopulo et al. [20] (6016 aluminum alloy), Hyun et al. [5] (6061 aluminum alloy), Butuc et al. [40] (6016-T4 aluminum alloy), Min et al. [4] and Min et al. [28] (6022 T4 aluminum alloy), Korsunsky et al. [41] and Garcia-Garino et al. [42] (6082 aluminum alloy), Duan et al. [43] (5754-O aluminum alloy), Reyes et al. [44] (2008 T4 and 6111 T4 aluminum alloys), Situ et al. [45] (6181 T4 and 6111 T4 aluminum alloys), Jaamialahmadi et al. [46] (6016 T4 and 6111 aluminum alloys), Abovyan et al. [47] (5182 and 5754 aluminum alloys), Martinez-Donaire et al. [48] (7075-O aluminum alloy), Yu et al. [49] (5456, 7017 and 2040 aluminum alloys),

Morales-Palme et al. [32] (6010 and 7075-O aluminum alloys), Elyasi et al. [50] (8112 aluminum alloy), Lokoschenko et al. [51] (D16T aluminum alloy) and lastly Pham et al. [52] (5052-O and 6016 T4 aluminum alloys). There are many different types of aluminum alloys investigated in the literature; still, majority of the experiments are conducted with steel specimens.

Widespread application areas of Al2024T3 include aircraft structural components, aircraft fittings, hardware, truck wheels and other parts in transportation industry. Some components that are made of Al2024T3 are hydraulic valve bodies, missile parts, munitions, nuts or pistons [53].

Although steel and aluminum alloys are the most sought-after materials in the tensile test resources, other materials do also exist. A notable example is copper alloys. This can be illustrated by Ling [54] (C51100, C52100, C26000, C10200, C17510 copper alloys), Sing et al. [55] (C260 copper alloy), Yuan et al. [56] (pure copper), and Sene et al. [57] (C194 copper alloy). Copper alloys are good electricity conductors and are also widely used in architecture, automotive, machined products and telecommunication applications.

From tensile plastic instability prediction point of view, there are several possible experiments to work on. In this regard, tensile test is one of the most prominent and prevailing methods. Tensile test experiments with round or cylindrical specimens had been conducted in following studies: Zhang [11], Brünig [58], Cabezas et al. [13], Mirone [15], García-Garino et al. [42], Joun et al. [59], Yuan et al. [56], Eom et al. [60], Tabourot et al. [61], Yu et al. [49], Murata et al. [62], Tu et al. [16], Kweon et al. [33], Lokoschenko et al. [51], and Hu et al. [63].

In the literature, many attempts have been made to examine sheet or strip specimens with rectangular cross section undergoing tensile testing. Researchers such as Rao et al. [65], Cabezas et al. [13], Dumoulin et al. [66], Tabourot et al. [67], Korsunsky et al. [41], Zhang et al. [35], Coppieters et al. [19], Kim et al. [24], Hyun et al. [5], Kolasangiani et al. [25], Abbassi et al. [29], Kamaya et al. [21], Bao et al. [30], Sene

et al. [57], Saboori et al. [31], Farahnak et al. [17], Li et al.[4], Pham et al. [52], Shimizu et al. [68], Hu et al. [63] and Drotleff et al. [39] has worked on tensile testing on flat specimens.

Sheet metals have widespread use in many areas like aerospace, ground vehicles, electronics enclosures, home appliances, medical equipments etc. In this connection, mechanical behaviors of sheet metals are investigated through not only tensile tests, but also Nakazima [17,18,28,47,48,52,63,69], Marciniak [27,28,35,70,71], deep drawing [22,37,39,45,57,72–75], stretch bending [48], dome stretching [76] and circular bulge tests [26]. One of the aims of this thesis is to apply the instability prediction results of tensile test in another test to validate, compare and contrast the performed approaches. In that sense, deep drawing process is selected since it is also very important and common process in metal forming operations.

Measurement and data collection methods in experiments are crucial. Until last decade, contact-type extensometers had been used more widely. However, in recent years visual or optical methods become more common because of some limitations of contact-type extensometers such as potential damage on the sensor during material fracture. Digital Image Correlation is an optical method that allows image-analysis by comparing images of test specimen throughout the experiment. Based on the tracking and registering the reference geometries on test specimen; this technique can be used in a variety of tests such as tensile, torsion, bending etc. to record numerous parameters like displacement, strain, vibration, contour, deformation. In the literature, one can notice visual methods such as DIC, thermograph, laser displacement mater, luminance distribution and electronics speckle pattern interferometry. The resources that they are utilized as [4,17,49,51,52,57,61,62,66,67,70,74,19,77,21,23,28,29,31,39,48]. On the other hand, some innovative approaches such as Electronic Speckle Pattern Interferometry (ESPI) or Digital Speckle Pattern Interferometry (DSPI) [30,78], Luminance Distribution Method [68] and Laser Displacement Mater [68] exist.

FE model of tensile test is another crucial subject to be touched.

Much of the current literature on FE analysis exploits commercial softwares to carry out FE analysis. The most common examples are ABAQUS™ [16,24,61,63,67,70,71,73,79–82,25,83,29,33,37,49,50,54,57] and ANSYS LS-DYNA™ [26,31,44,46,47,62,64,76]. FE analysis softwares provide virtual testing through model simulations. They allow the users to build flexible models which can be adjusted to different conditions easily. Furthermore, the FE models constructed through commercial softwares can be optimized according to many factors like computation time and degree of accuracy.

Next, researchers in the literature have performed different approaches to geometric configurations of tensile test specimen models to be solved with FE analysis. To reduce the time spent on the analysis, some specimens are modeled partially, i.e. only half or quarter of the specimen is represented within the simulation. This approach gives accurate and precise results only if the symmetry conditions are defined appropriately. Furthermore, many researchers preferred to include grip region of the specimen, where the jaws, clamps or vices of the tensile test machine hold the specimen at both ends. Nevertheless, a number of authors have reported to work only on gauge region of the specimen and represent the grip region effects through boundary conditions. They had to compromise between computation time and closeness of the model to real life experiment.

Axisymmetric FE models are very commonly used to build round specimens in digital environment. When compared to 3D models, axisymmetric 2D models provide a significant simplification resulting in reduction of time spent. Cylindrical cross-section tensile test specimens can be constructed in 2D as whole-body including grip region [58]. In some other instances, full-gauge zone [60], half-specimen covering only gauge region [84] and quarter-specimen covering only gauge region [11,12,87,13,16,42,59,62,79,85,86] have been examined. 3D models of quarter of the specimen with grip zone [33,83,88] are also commonly applied.

Several studies investigating 2D FE analysis of strip specimens undergoing tension test modeled have simulated only a half of the gauge region [89] or quarter of the gauge region [82,90]. Along with those, there are some cases in which a quarter of the specimen with grip region [54] have been focused. In addition, 3D FE structures have been modeled for whole-specimen including grip zone [5,29,31], whole-specimen gauge zone [61], quarter-specimen with grip region [66,67], one-eighth-specimen (half of the quarter) [24,88] as well as half of the gauge region in thickness [35] and one-eighth of the gauge region [13].

Another issue of FE model is the choice of geometrically perfect or imperfect specimen. The onset of necking occurs at a random position within the gauge zone if the specimen has ideally cylindrical or rectangular cross-section. There are three main styles for round bars; perfectly cylindrical or straight specimens [11,12,54,85,86,88,89], tapered specimens [45] and notched specimens [11,12,16,62,79]. Likewise, for the sheet specimens there are three main approaches; perfectly rectangular cross-section [88], tapered cross section [13] and specimen with artificial imperfection [35].

The yield point detection is another issue; in that regard von Mises criterion [11,15,91,17,40,59,60,62,66,84,85] and Tresca criterion [84,92,93] are utilized in majority of resources. On the other hand, in plastic region there are several approaches to describe the trend of work-hardening; or based on that, stress-strain relationship. Many constitutive relations have been derived to represent the behavior of the material in plastic region such as Hollomon, Swift, Voce, and Ludwik's Laws. Some related references are as follows: Hollomon's equation or power law [26,42,43,55,59,64,85,87,88], Swift's law [19,21,29,40,62,88,94], Ludwik's law [86], and Voce's law [43,62,82,92,95]. These constitutive models all define a homogeneous deformation and can cover both pre-necking and post-necking regions. As a deduction from the literature review, it can be said that the constitutive models are more accurate in pre-necking region than post-necking region. In addition, the

hardening models are generally coupled with a damage criterion to demonstrate the full behavior of the specimen from elastic region until fracture.

As explained previously, necking is an instability phenomenon observed during plastic deformation and has been investigated in numbers of works for its modeling and numerical computation. Although Considère determined the basic criteria for necking in 1885; many pioneering and currently valid papers related with necking geometry date back to the 1950's [1]. Bridgman published *Large Plastic Flow and Fracture* in 1952 where he developed a correction method to simplify the complex stress state in necking region of the rod-shaped tensile specimen [96].

A variety of methods have been developed to detect the onset of necking or instability in manufacturing, testing or product usage life. The main approaches can be categorized as spatial methods, temporal methods, spatio-temporal methods and analytical methods [28]. A method can also be classified as local if it is evaluating certain parameters in a specific portion of the component or as global if it is working on the whole part.

In spatial methods, the strain or another geometrical property over the specimen body is observed and some instability indicators are sought.

One approach under spatial method classification is to examine the number of unloaded or discharged elements. After the onset of plastic instability, strain increment is localized in critical zone and the remaining portions of the specimen experience a sudden drop in stress. Tabourot et al. [67] compared two consecutive stress state values of each element. They deducted that if the difference is greater than zero, the element is loaded; otherwise, it is unloaded. When there is a sharp increase in the number of unloaded elements, onset of tensile plastic instability is determined. The same application is also used in Tabourot et al. [61], where they worked on tensile test simulation with C68 steel sheet metal to detect the onset of necking. Since the load is uniaxial, only the stress values of selected elements along a line in the load direction are compared. Number of unloaded elements method has also been utilized by Sene

et al. [57] for simple tension and biaxial expansion tests. Next, dome-stretching tests has been studied in the paper of Li et al. [76]. It is indicated that if the major and minor strains of an element have no simultaneous change, the element is assumed to be outside of the necked or instability region. Zhang et al. [97] modeled Nakazima test and investigated the elongation quantity when the major strain is suddenly reduced to zero to detect onset of tensile plastic instability. Brünig [58] predicted the onset of necking of tensile test in terms of elongation; he also examined the effect of different boundary conditions on necking.

Bridgman proposed to measure some geometrical dimensions of the instability region (such as curvature radius) to detect necking during a tensile test experiment and several many authors applied similar techniques [27,51,96]. Shimizu et al. [68] utilized different visual techniques to detect necking; namely, measurement of surface shape by laser displacement meter, measurement of difference in strain between different gauge lengths and luminance distribution of specimen surface. There are also some methods that observe specimen parameters smaller than macro-level. Furushima et al. [98] and Romanova et al. [99] measured surface roughening behavior in experiment and modeled in FEA. That method is stated to detect necking earlier than macro-level observation methods. Some other researchers such as Boudeau et al. [100], Bettaieb et al. [101], Yoon et al. [79], Franz et al. [102] and Akpama et al. [103] defined and traced the mechanisms of material crystallography or slip systems.

Another spatial method is to determine a critical strain value for the onset of instability. In the work of Situ et al. [45], critical major strain is assumed to be the point where one of the two neighboring elements experience a rapid increase in its strain.

Calibration by experiments is also practiced to predict necking. Drotleff et al. [39] constructed a 3D surface corresponding to major strain, minor strain and equivalent strain by using data from 27 tensile test experiments. The curve is exploited to predict localized necking. In the article of Kim et al. [24], the predictions of force and

displacement are conducted iteratively by calculating the error between the experimental data and FE simulation data.

The plot of current to initial diameter ratio vs. engineering deformation has been used to detect onset of necking for round bar tensile test experiment [13]. The same figure is also exploited in the article of García-Garino et al. [42]. For sheet metal tensile tests, Cabezas et al. [13] plotted current to initial thickness ratio vs. engineering deformation and current to initial width ratio vs. engineering deformation curves. A sudden change of the curve trend is assumed to be onset of necking. Another analysis specific to flat and rectangular cross-section specimens is minor-to-major strain ratio that has been performed in the paper belongs to Zhang et al. [70]. In transition of strain path criterion, they compared minor-to-major strain ratio change curves of two elements on a Nakazima test specimen and detected a dissimilar evolution at the onset of tensile plastic instability. One element has converged to zero; yet, the other one has gone under instability condition. Hyun et al. [5] marked both diffuse and localized necking on minor-to-major strain ratio graphs. Lastly, aspect ratio approach has been adopted in the work of Niordson et al. [90]; the critical ratio of length and width of the strip-type specimen is taken as 10 in that report.

The second group of instability prediction methods is referred to as temporal or time-dependent methods. In these methods, first and second time derivatives of crucial parameters -other than spatial types- are perused. If the expected increase or a peak value is obtained, the onset of instability phenomenon is assumed to be recorded.

One of the earliest studies of this category belongs to Considère [1]; the resulting criterion states that diffuse necking occurs when the maximum force is reached during a uniaxial tension test. This method is also accredited as Maximum Force Criterion (MFC) in some resources and it is the most commonly performed approach in this category. Some studies plotted the force vs. time, force vs. strain or force vs. punch displacement graphs and looked for the peak point of force value to detect instability [16,17,42,43,66,70,86,106]; whereas, some other studies equated the derivative of

force to zero and benefited from this equation in further derivations [31,32,51,55,63,91,94,110,111]. In several resources, maximum value of stress instead of force is examined with the same purpose [33,49,56,112]. Le Van et al. [12] used MFC total Lagrangian FE formulation instead of Eulerian approach. Similarly, Careglio et al. [14] attained necking by embedding MFC into both updated and total Lagrangian FE formulations. The MFC method can also be utilized in power form [113]. Next, certain researchers worked on MFC for improvements. Swift [114] modified Considère criterion to cover biaxial loadings; then, Hill [115] modified it to predict localized necking in rigid-plastic models. Hora et al. [116,117] proposed Modified Maximum Force Criteria (MMFC) to detect localized necking for sheet metal applications. It is thoroughly utilized in various contributions [20,36,52,63]. Moreover, Enhanced Modified Maximum Force Criteria is also established to include the thickness effect in the formulation [77]. Aretz et al. [118] has applied a critical value to major force per unit width which is taken as onset of necking.

Some attempts have been made to predict the onset of tensile plastic instability through formulations which exploit critical shear stress value obtained from uniaxial or biaxial tests [44,77].

Several sound formulations in the media are based on the second time derivative of strain, also known as strain acceleration. Maximum value of the strain acceleration is assumed necessary and sufficient to observe necking on the specimen body [18,23,45,63,70,73,80,106,119]. These works have common characteristics; they applied strain acceleration method on either thickness strain or major principle strain of sheet metal forming processes. Furthermore, in those references second temporal evolution of strain is plotted against time (Except Zhang et al. [70] that used principal strains). An important note here is that Situ et al. [45] compared Bragard Criterion, critical major strain criterion and maximum strain acceleration criterion and found that the latter one provided more definite and physically meaningful onset of localization.

Abovyan et al. [47] has determined critical values for second time derivative of the major strain difference between two adjacent elements. Unlike the second time derivative of one mesh element, this method compares two separate elements' difference which continuously increase during an analysis. Thus, the resulting plot required a specific threshold to detect necking.

Not as common as strain acceleration, but strain rate or first derivative of strain with respect to time is also utilized in the literature [47,48]. Similarly, researchers look for a significant change in the slope of strain vs. time graph. Zhang et al. [70], Chalal et al. [73] and Lumelskyj et al. [119] have taken the thickness strain evolution as the tensile plastic instability indicator. Thickness strain vs. time plots of sheet metals have different courses before and after the initiation of tensile plastic instability phenomenon. Thus, they fitted two curves on these portions of the plot and the intersection of these curves are accepted to represent the onset of instability. Pepelnjack et al. [71] and Kolasangiani et al. [25] compared thickness strain vs. time, first time derivative of thickness strain vs. time and second time derivative of thickness strain vs. time plots; nevertheless, they did not apply a curve fitting procedure to find the necking initiation point. Recently, Zahedi et al. [120] worked on instability prediction of AA1050 aluminum and 1100 copper laminated sheets through maximum value of thickness strain rate as previously applied by Martínez-Donaire et al. [48].

In addition to aforementioned temporal methods, several other techniques are based on ratio of critical parameters. The most common example of is this approach is strain rate ratio of two separate elements. Marciniak-Kuczynski (M-K) analysis technique was first published in 1967 by Marciniak et al. [105] and there has been many studies which exploited strain rate ratio since then. Recently, the critical strain rate ratio for the onset of necking has been taken as 10 [37,38,40,106,107], 7 [35,36,70], and 5 [108] in different resources. Furthermore, Aretz [109] has compared plastic strain increment of one element with total thickness increment of another element; hence, the user-defined critical ratio is assumed to become 100. Elyasi et al. [50] could decide a ratio of approximately 2.5 is enough by experience on tube bending test. The

expressed ratio thresholds are mostly obtained directly from the literature and in some cases the analyst depends on his/her experience.

As a type of temporal methods, necking or tensile plastic instability time has been computed based on ductile fracture criteria; necking-to-fracture time ratios of the test processes have been researched [25,51].

In the report of Galpin et al. [26], they have performed an Experimental-Numerical Method (ENM) to predict necking. In this hybrid approach, the second time derivative of the ratio between the loads obtained from experiment and simulation is observed for a clear change in the plot trend.

The third class of necking prediction methods is spatio-temporal methods. As the name suggests, in these methods both spatial (position or displacement) and temporal changes in specimen are exploited to predict the onset of necking. For instance, Martínez-Donaire et al. [48] investigated temporal evolution of the displacement profile in a Nakazima experiment. They corroborated that when only a portion of the specimen undergoes to rapid thickness reduction, the displacement curves drawn at different elongation quantities will first flatten, and then have a well-like shape. Additionally, the shape of first spatial derivative of displacement at different elongation quantities changes its pattern. Another work which utilized regarded under spatio-temporal methods has been reported by Min et al. [27]. They predicted the dimples on specimen surface during Marciniak test, which is the indicator of localized necking. The position of the dimple initiation is calibrated by experimental data obtained by Digital Image Correlation (DIC) methods. Then, they improved the method to involve the out-of-plane deformations as in the case of Nakazima tests [28].

The last category to predict tensile plastic instability and necking phenomena can be referred to as analytical methods. Under this general name, there are sub-categories such as curve fitting, bifurcation approach and instability or perturbation approach. Physically, a system is considered stable if a small disturbance in initial conditions

does not amplify or diverge with increasing time. On the other hand, bifurcation refers to the loss of uniqueness of solutions of a given boundary problem [121].

In 1972, Bragard et al. [104] defined Bragard criterion, in which a quadratic curve fitting is applied to major and minor strains of selected points. The vertex of major strain and corresponding minor strain are taken as limit strains. This method is prone to errors since the curve formula can change with the selection of different points.

General bifurcation criterion has been investigated first by Drucker [122] and Hill [123]; they have studied on loss of uniqueness for the solution of the boundary value problem. Afterwards, limit-point bifurcation theory has been published by Valanis [124], which is less conservative than general bifurcation approach. It has also been shown that, for associative elasto-plasticity, limit-point bifurcation coincides with general bifurcation [95]. Bifurcation method has also been used by Rudnicki et al. [125] and Rice [126] to predict localized necking in strip samples which has been known as loss of ellipticity. Subsequently, Bigoni et al. [127] and Neilsen et al. [93] has assessed loss of strong ellipticity approach; while after Chalal et al. [106] carried out the same approach. Le Van et al. [12] performed bifurcation solution to round bar tensile test with a Lagrangian formulation. Zhang et al. [70] found two different trends in thickness evolution curve, and the intersection point of these bifurcation branches is taken as onset of necking. Recently, Bouktir et al. [82] used bifurcation criterion to obtain a lower bound for diffuse necking prediction and loss of ellipticity criterion to obtain upper bound for localized necking prediction. Four major types of bifurcation methods are well described by Bouktir and coworkers [82]. To begin with, loss of ellipticity and loss of strong ellipticity methods can only be used to predict localized necking which is not the main purpose of this study. Note that general bifurcation and limit point bifurcation methods can predict both diffuse and localized necking. General bifurcation theory generate more conservative results than its special case, limit point bifurcation method [82,128]. In addition, limit point bifurcation and Maximum Force Criterion are based on similar assumptions and their results agree well [128].

Finally, the next sub-category of analytical methods to predict necking is instability criteria or the associated perturbation analysis. In these methods, the users apply stability analysis on local equilibrium equations. The first reference to stability belongs to Lyapunov [129], the mathematical stability results can be applied to the evolution of a well defined perturbation on a mechanical system in time. Many researchers applied perturbation analysis [122,123,130–137] which is especially effective in the case of thermo-viscoplastic material modeling.

CHAPTER 3

THEORY

3.1. Introduction

It is a challenge to measure true stress-strain directly from tensile test experiments. However, one can calculate the engineering stress and strain from experimental force and elongation data and then reproduce the true stress and strain easily. Assuming the stress is distributed evenly over the cross-section,

$$\sigma_0 = \frac{F}{A_0} \quad (2.1)$$

where σ_0 is the nominal or engineering stress, F is the force and A_0 is the initial area. Instead of initial cross-section area, dividing the force by instantaneous cross-section area, A , the true stress value, σ , emerges as:

$$\sigma = \frac{F}{A} \quad (2.2)$$

Then, the average linear nominal or engineering strain, ε_0 , can be expressed as:

$$\varepsilon_0 = \frac{l - l_0}{l_0} \quad (2.3)$$

which can also be defined as division of change in the gauge length by the original gauge length. On the other hand, true strain, ε , is expressed in terms of instantaneous change in the length of specimen so that,

$$\varepsilon = \frac{dl}{l} \quad (2.4)$$

Integrating;

$$\varepsilon = \int_{l_0}^l \frac{dl}{l} = \ln \frac{L}{l_0} \quad (2.5)$$

true/logarithmic or natural strain can be attained for any specific time during the process. The logarithmic strain is additive while nominal strain is not. True strain values are obtained by

$$\varepsilon = \ln \frac{l}{l_0} = \ln(\varepsilon_0 + 1) \quad (2.6)$$

In plastic deformation, since volume is assumed to remain constant, the relation between the true and engineering stress then can be found as:

$$\sigma = \sigma_0 (\varepsilon_0 + 1) \quad (2.7)$$

For a process of deformation in a material under multiaxial states of stress, yield criteria define the condition for the limit of elastic state or the onset of plastic deformation. After that threshold, the material starts to flow plastically. The yield functions are generally expressed as follows:

$$f(\boldsymbol{\sigma}, \boldsymbol{\alpha}) = 0 \quad (2.8)$$

where $\boldsymbol{\sigma}$ is the stress tensor and $\boldsymbol{\alpha}$ defines hardening parameters. Thus, a yield function forms a surface in stress space. In this thesis, von Mises yield criterion is used:

$$\sigma_Y = \sqrt{\frac{1}{2} \{ (\sigma_1 - \sigma_2)^2 + (\sigma_2 - \sigma_3)^2 + (\sigma_3 - \sigma_1)^2 \}} \quad (2.9)$$

with isotropic hardening rule.

3.2. Discussion about Instability Prediction Methods

Several methods to predict the onset of necking or tensile plastic instability have been introduced and examined in Literature Review chapter. Some of them are selected and applied to analyses due to a variety of reasons.

Many researchers propose to utilize visual/optical methods to observe, record, analyze and predict stable-to-unstable transitions. Usually they are under spatial methods classification. Firstly, it is still very impractical or expensive to employ those methods, even though theoretically possible. Secondly, a significant part of the testing and forming processes, such as Nakazima, deep drawing, Erichsen tests, do not allow the specimens to be visually inspected or recorded by a camera. From the generality point of view, those methods became less attractive in this study.

An active area to predict instability uses thickness strain or major/minor strain evolution. One purpose of the current work is to acquire universally valid results from the analyses and methods. Equivalent plastic strain can be calculated for any material under plastic deformation; which is not specific to sheet samples. So, this general option is employed in this work, that is equivalent plastic strain and its derivatives.

Experimental-numerical methods or criteria involving calibration through experiments are also not chosen in this work. The idea has a merit that correction of finite element analysis and predictions through experiment outputs is practical in cases such as simple tension test. Yet, those methods are challenging to apply in the existence of multi-axial stress-strains during complicated loading and part geometry conditions. Moreover, from universality perspective, the calibration experiments may be impractical or cost-inefficient in some cases.

Prediction of plastic instability or necking methods is implemented with parameters on crystallographic structures of slip systems of metallic materials. These approaches are beyond the scope of this thesis.

Spatio-temporal methods generate reliable results; yet, they are inclined to be case-specific.

Recall that three analytical methods are commonly practiced in the instability or necking prediction literature: Curve fitting, bifurcation analysis and perturbation analysis. Curve techniques are highly dependent on the selected points and therefore inclined to produce errors depending on reference data. Secondly, bifurcation methods are limited to strain rate independent materials [82,95,128,138–140]. The methods tend to yield significantly overestimating results for strain rate dependent materials [103]. Bifurcation or loss of uniqueness methods are inappropriate in the current case since both Al2024T3 and S235JR are strain rate dependent materials [53,141–144].

Consequently, the following methods are to be applied in the current work:

- Equivalent plastic strain increment ratio (local and temporal)
- Difference of second time derivative of equivalent plastic strain (local and temporal)
- Maximum second time derivative of equivalent plastic strain (local and temporal)
- Maximum force criterion (global and temporal)

3.3. Derivations for Determination of Onset of Instability/Necking

The highest strain and deformation effects are localized in the region after the commencement of instability. Hence, any clear-cut change in the evolution of the criterion parameters reflects the occurrence of a change in certain characteristics of the metal, due to the onset of tensile plastic instability and necking. Generally, instability is detected with the observation of aberrantly high variable or parameter characteristics. In Figure 3.1, the general algorithm to follow for the applied criteria is illustrated.

In order to observe the change in variables of interest with respect to other independent variables, derivation relations must be established. Taylor series expansion can be properly used to derive forward, backward and central difference formulas of first and second order derivatives.

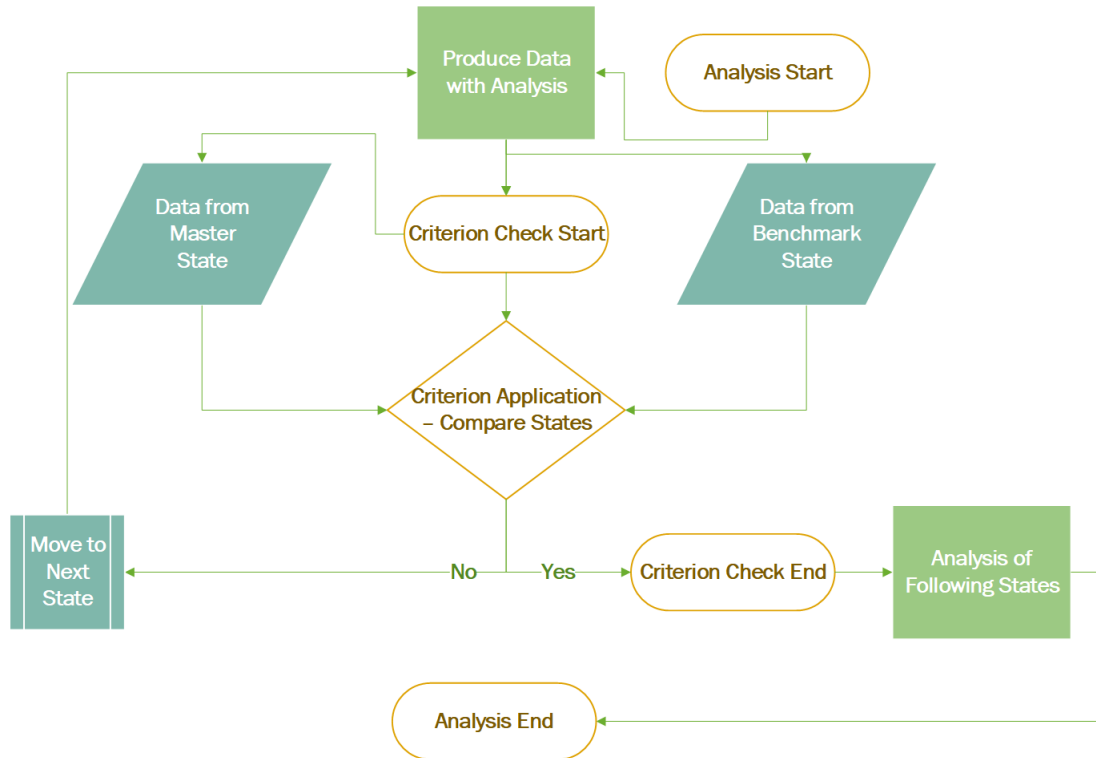


Figure 3.1. General algorithm to follow for the criteria to predict onset of necking

Sample formulation for exact Taylor series expansion of first order forward difference derivative of function $f(t)$:

$$\frac{df(t)}{dt} = \frac{f(t + \Delta t) - f(t)}{\Delta t} - O(\Delta t) \quad (2.10)$$

Approximation is achieved by omitting O term. Note that t is the point of interest and can be time or space variable. In addition, Δt states the order of truncation error after omitting. Then, the approximated form of above equation appears as:

$$\frac{df(t)}{dt} = \frac{f(t + \Delta t) - f(t)}{\Delta t} \quad (2.11)$$

Similarly, backward difference formulation of first order derivative is

$$\frac{df(t)}{dt} = \frac{f(t) - f(t - \Delta t)}{\Delta t} \quad (2.12)$$

By summing up the forward and backward difference formulas, one can get the central difference formula for the first order derivative

$$\frac{df(t)}{dt} = \frac{f(t + \Delta t) - f(t - \Delta t)}{2\Delta t} \quad (2.13)$$

Taylor series expansions of $f(t + \Delta t)$ and $f(t - \Delta t)$ omit the terms $O(\Delta t^2)$ and obtain the below equation

$$\frac{d^2f(t)}{dt^2} = \frac{f(t + \Delta t) - 2f(t) + f(t - \Delta t)}{\Delta t^2} \quad (2.14)$$

Then manipulations can be employed to derive second order forward difference relation:

$$\frac{d^2f(t)}{dt^2} = \frac{f(t + 2\Delta t) - 2f(t + \Delta t) + f(t)}{\Delta t^2} \quad (2.15)$$

and backward difference relation:

$$\frac{d^2f(t)}{dt^2} = \frac{f(t) - 2f(t - \Delta t) + f(t - 2\Delta t)}{\Delta t^2} \quad (2.16)$$

As a result, forward difference formulas are going to be used at first intervals and backward difference formulas are going to be used in last intervals of each analysis. In the corresponding calculations of the remaining intervals of those analysis, central

difference formulas will be used whenever possible since it provides less error than other two alternatives.

3.3.1. Criterion of Equivalent Plastic Strain Rate Ratio

The effective or equivalent plastic strain rate gives a measure of the amount of permanent strain in a body. For Mises plasticity, the definition of equivalent plastic strain rate is given as

$$\dot{\bar{\epsilon}}^p = \sqrt{\frac{2}{3} \dot{\epsilon}^p : \dot{\epsilon}^p} \quad (2.17)$$

In this criterion, two separate elements are compared in terms of their equivalent plastic strain rates as

$$k_r = \frac{(\dot{\bar{\epsilon}}_t^p)_A}{(\dot{\bar{\epsilon}}_t^p)_B} \quad (2.18)$$

where k_r is the ratio between equivalent plastic strain rates of Element A and Element B. This numerical method clarifies that if the strain rate ratio of two elements reach a certain critical level, instability occurs

$$k_c \geq k_r \quad (2.19)$$

where k_c is the critical threshold for necking to initiate. However, there are different approaches on how to select the two elements to be compared. Abovyan et al. takes the neighboring element, yet, Chalal et al. takes 5th element from the gauge center [47,106]. Recalling from the literature survey chapter, the critical ratio to predict the onset of necking is mostly taken as 10; even though there some instances of 7 and 5.

The formula of the method can be expressed explicitly for backward difference as follows:

$$k_r = \frac{\frac{(\bar{\varepsilon}_t^p - \bar{\varepsilon}_{t-1}^p)_A}{\Delta t}}{\frac{(\bar{\varepsilon}_t^p - \bar{\varepsilon}_{t-1}^p)_B}{\Delta t}} = \frac{(\bar{\varepsilon}_t^p - \bar{\varepsilon}_{t-1}^p)_A}{(\bar{\varepsilon}_t^p - \bar{\varepsilon}_{t-1}^p)_B} \quad (2.20)$$

Obviously, equivalent plastic strain rate ratio is a local criterion.

3.3.2. Criterion of Difference of Second Time Derivative of Equivalent Plastic Strain

In this approach the change in strain is calculated with respect to second derivative of time. Hence, the criterion parameter for strain acceleration in this method is obtained as:

$$k_d = (\ddot{\varepsilon}_t^p)_A - (\ddot{\varepsilon}_t^p)_B \quad (2.21)$$

or

$$k_d = \left(\frac{d^2 \varepsilon_t^p}{dt^2} \right)_A - \left(\frac{d^2 \varepsilon_t^p}{dt^2} \right)_B \quad (2.22)$$

where k_d is the difference between second time derivative of equivalent plastic strain of Element A and Element B. Note that the formula given by Abovyan et al. [47] is modified from second derivative of strain difference to difference of second derivative of strains because it is more proper to compare the change characteristics of the elements during the process evolution.

It is expected that the value is to vary with different materials and different process application procedures. This method can be used with a threshold level beyond which the specimen is to be assumed necked [47],

$$k_c \geq k_d \quad (2.23)$$

where k_c is the critical threshold for necking to initiate.

However, the algorithms used in this thesis employed a change because this formulation require strain value, k_c . Researchers usually select the threshold value based on their experiences or experiments. A threshold value can be weakness for a method unless selected appropriately. Instead, the algorithm in this thesis is seeking a point in the graphs where a significant change in slope is observed. Generally, if the slope of the graph increases 3 times or more in one step, that track the onset of instability. This moment is assumed to correspond the instability initiation by rapid thinning in the specimen.

Finally, the central difference approximation on this criterion gives

$$k_d = \left(\frac{\bar{\varepsilon}_{t+1}^p - 2\bar{\varepsilon}_t^p + \bar{\varepsilon}_{t-1}^p}{\Delta t^2} \right)_A - \left(\frac{\bar{\varepsilon}_{t+1}^p - 2\bar{\varepsilon}_t^p + \bar{\varepsilon}_{t-1}^p}{\Delta t^2} \right)_B \quad (2.24)$$

Note that if Element B is in critical region and Element A is not, the results are expected to increase in negative direction.

Similar to equivalent plastic strain rate ratio criterion; this criterion is local.

3.3.3. Criterion of Second Time Derivative of Equivalent Plastic Strain

Previous sections depict two criteria which compare strain values of two separate elements. On the contrary, criterion of maximum second time derivative of equivalent plastic strain works on the change in strain acceleration of a single element.

If instability commences, rapidly increasing deformations are observed in a small region of the analysis domain. This criterion checks the irregularly high changes in strain values at different time intervals. The method is applied on each element by inspecting the strain acceleration values at different time intervals:

$$k_a = \ddot{\bar{\varepsilon}}_t^p \quad (2.25)$$

where k_a is the second time derivative of equivalent plastic strain of an element. When k_a reaches its highest value for an element in instability region on the specimen, instability or necking is assumed to occur. Using forward difference:

$$k_a = \frac{\bar{\varepsilon}_{t+2}^p - 2\bar{\varepsilon}_{t+1}^p + \bar{\varepsilon}_t^p}{\Delta t^2} \quad (2.26)$$

This method is local. It is imperative that local criteria would be time-consuming if applied to all the elements in the mesh grid. To exploit the symmetry axes is quite important for optimization purposes; among the elements in close proximity, which are expected to exhibit similar characteristics under applied loads, only one element can be chosen that undergoes the criterion evaluation to use the resources effectively.

3.3.4. Criterion of Maximum Punch Force

Maximum reaction force or maximum punch-die force is generally obtained at the onset of necking/instability during a testing or forming process. The load value starts to drop which precedes the final fracture or failure. Therefore, the peak force can be utilized as a global criterion to predict instability or necking. Recall that

$$F = \sigma A \quad (2.27)$$

One of the first studies belongs to Considère stated that diffuse necking occurs when the maximum force is applied to the sample [1]; thus the criterion for instability is

$$dF = 0 \quad (2.28)$$

In order to detect maximum force, both force vs. time or force vs. displacement plots can be employed. Here, the variable is force value and the master and benchmark states are two consecutive total elongations. The next state will be evaluated as long as the condition (decrease in force) is not satisfied. When the peak value of force is reached, the criterion check process ends.

CHAPTER 4

EXPERIMENTS

4.1. Materials

Two different materials have been used in experimental and numerical processes; namely, Al2024T3 aluminum and S235JR steel.

Al 2024 series is a heat-treatable Al-Cu alloy and its T3 temper versions are known for their high strength, toughness and fatigue resistance. It is commonly used in structures and components where good strength-to-weight ratio is required. In the designation of Al2024T3, the first digit indicates the major alloying element (2 is for Copper), the second digit indicates alloy modification (0 is the original alloy), last two digits have no special purposes and T3 means solution heat-treated, then cold-worked.

Next, S235JR steel is used as the second material used in tensile test procedures. This steel has equivalents in European standards as EN 10025-2-2004, German Standards as R St 37-2 (old DIN 17100) and in many other countries the corresponding steel number is 1.0038. It is still known as St 37 in Turkey.

S235JR is a non-alloy structural steel. Toughness and weldability of the material is good. Although its strength capability is limited, S235JR has good cold-working properties. In the designation S indicates structural steel, 235 indicates minimum yield strength (MPa) for the thickness less than 16 mm and JR means quality grade related to Charpy impact test energy values (27J at room temperature).

Abbreviations used in order to represent experiment cases as well as FE analyses are indicated in Table 4.1. For example, the tensile test for tapered specimen of steel sheet and square cup aluminum specimen deep drawings tests are going to be referred as TT-She-St-Tpr and DDP-SC-Al, respectively.

Table 4.1. Abbreviations for different experiment and analysis

TT	Uniaxial tensile test
DDP	Deep drawing process
She	Sheet or strip-type specimen
Ro	Round or rod-type specimen
Al	Al2024T3 aluminum 1 mm thick sheet or 10 mm gauge cylinder
St	S235JR steel 2 mm thick sheet or 10 mm gauge cylinder
Str	Straight, meaning the cross-section width/radius of the specimen is constant throughout the gauge
Tpr	Tapered, meaning the cross-section width/radius is 100% at both gauge ends, but 99% at gauge center
Ntc	Notched, meaning the cross-section width/radius is constant except a semi-circular dent/notch of 1% at gauge center
CC	Cylindrical cup deep drawing
RB	Round bottom deep drawing
SC	Square cup deep drawing

4.2. Tensile Test Experiments

Time, displacement and force data have been obtained using tensile tests. By utilizing those data, percent elongation, yield strength, proportional limit, modulus of elasticity and ultimate tensile strength of each material has been recorded.

Approximately 100 data points were recorded in every second in the course of experiments. Furthermore, both the visual extensometer/camera elongation results and the mechanical crosshead data had been recorded during the experiments.

4.2.1. Experimental Set Up

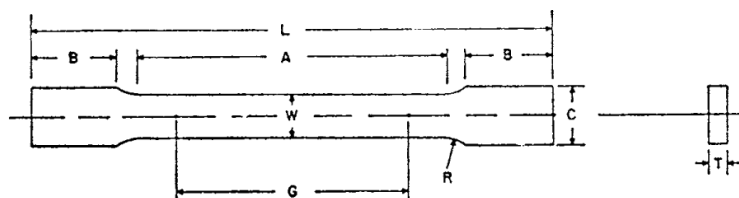
The experimental set up used for this thesis is the MTS Landmark[®] Servohydraulic Testing System shown in Figure 4.1 in Middle East Technical University Civil Engineering Department. This floor-standing model has a force range of 500 kN.



Figure 4.1. MTS Servo-hydraulic testing machine and video extensometer

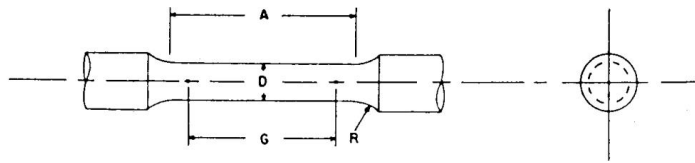
4.2.2. Specimen Geometry and Material

All specimens were prepared according to ASTM E8/E8M 16a for sheet and cylindrical specimens as shown in Figures 4.2 and 4.3, respectively [2]. For flat specimens, sheet-type specimen dimensions on Figure 4.2 are applied [2]. For cylindrical specimens, Specimen 3 of “Five times the diameter” specimen group on Figure 4.3 is utilized [2]. Note that the dimensions are changed for production and measurement purposes in permitted range (diameter is 10 mm and gauge is 55 mm).



	Dimensions
	Standard Specimens
	Sheet-Type, 12.5 mm [0.500 in.] Wide
	mm [in.]
G—Gauge length (Note 1 and Note 2)	50.0 ± 0.1 [2.000 ± 0.005]
W—Width (Note 3 and Note 4)	12.5 ± 0.2 [0.500 ± 0.010]
T—Thickness (Note 5)	thickness of material
R—Radius of fillet, min (Note 6)	12.5 [0.500]
L—Overall length, min (Note 2, Note 7, and Note 8)	200 [8]
A—Length of reduced section, min	57 [2.25]
B—Length of grip section, min (Note 9)	50 [2]
C—Width of grip section, approximate (Note 4 and Note 9)	20 [0.750]

Figure 4.2. ASTM E8/E8M-16a Sheet specimen dimensions



Dimensions, mm [in.]
For Test Specimens with Gauge Length Five times the Diameter [E8M]
 Small-Size Specimens Proportional to Standard

	Specimen 2
G—Gauge length	45.0 ± 0.1 [1.750 ± 0.005]
D—Diameter (Note 1)	9.0 ± 0.1 [0.350 ± 0.007]
R—Radius of fillet, min	8 [0.25]
A—Length of reduced section, min (Note 2)	54 [2.0]

Figure 4.3. ASTM E8/E8M-16a Round specimen dimensions

Round specimens had been worked with CNC turning machine and sheet specimens had been processed by using CNC laser cutting machines.

The designations defined for strip-type and rod-type specimens used in tensile test experiments are listed in Table 4.2.

Table 4.2. Tensile test sheet and round specimen number, name, material, type and defect information

Specimen Number	Specimen Names	Name of Average Data
3	DA1, DA2, DA3	TT-She-Al-Str
3	AA1, AA2, AA3	TT-She-Al-Tpr
3	CA1, CA2, CA3	TT-She-Al-Ntc
3	DA4, DA5, DA6	TT-Ro-Al-Str
3	AA4, AA5, AA6	TT-Ro-Al-Tpr
3	CA4, CA5, CA6	TT-Ro-Al-Ntc
3	DS1, DS2, DS3	TT-She-St-Str
3	AS1, AS2, AS3	TT-She-St-Tpr
3	CS1, CS2, CS3	TT-She-St-Ntc
3	DS5, DS6, DS7	TT-Ro-St-Str
3	AS4, AS5, AS6	TT-Ro-St-Tpr
3	CS4, CS5, CS6	TT-Ro-St-Ntc

18 different specimens have been tested for each category. In order to detect and compensate possible errors, three specimens of each type have been exposed to the

same test procedures. Sheet and cylindrical metals tabulated in Table 4.2 are made of two different materials. They can have straight rectangle cross-sections through the gauge, tapered cross-sections which has a minimum at gauge center (having a width value of 99% in length when compared two gauge ends) and notches at gauge center (semi-circles having a diameter of 1% or specimen width).

Figure 4.4 depicts the steel and aluminum specimens in part a and part b, respectively. Note that in Figure 4.4(a), all the main and spare steel specimens are shown; whereas, in Figure 4.4(b) only main aluminum flat specimens are provided.

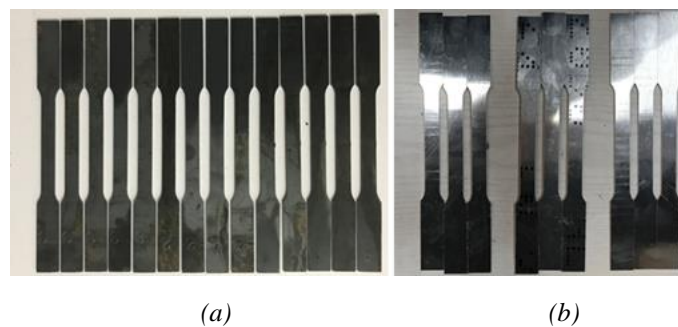


Figure 4.4. Flat specimens made of (a) S235JR steel (b) Al2024T3 aluminum alloy

Similarly, all the main and spare round specimens can be seen in Figure 4.5. The difference in color between aluminum (light gray) and steel (dark gray) can be noticed with ease. Lastly, all experiments have been conducted at room temperature.



Figure 4.5. All the round specimens prepared for the test including the spares (12 on the left hand-side are Al and 12 on the righthand- side are steel)

4.2.3. Experimental Procedure

Section 7 of ASTM E8/E8M 16a [2] clearly defines the test procedure to follow. All specimen types are manufactured and tested three times to increase the reliability of the results. First, dummy specimens are tested for trial and calibration purposes for both the test machine and the video extensometer. To check the dimensional tolerances, all the specimen gauges are measured just before each experiment. Then the specimens are marked with a board marker for video extensometer to detect the gauge. Adjustment on speed of testing is achieved through ASTM control methods in Section 7.6 [2]. Two control methods specified in Section 7.6.4.3 “Crosshead Speed Control Method for Determining Yield Properties” (Although the focus of this thesis is not elastic region) and Section 7.6.5. “Speed of Testing When Determining Tensile Strength” are utilized through all experiments. The applied speeds are 0.0333 mm/s in elastic region and 0.167 mm/s in plastic region, with a smooth transition. The tests are therefore considered quasi-static meaning that inertia effects are very small and can be neglected. Then, the data of load/force, elongation and time are recorded from two separate sources: Extensometer and load-cell in machine crosshead. The loading of the specimen continues so that the apparatus pulls on each end of the specimen until fracture occurs. After fracture, the machine stops automatically; and the specimen pieces (as in Figure 4.6) was removed from the machine by researchers.

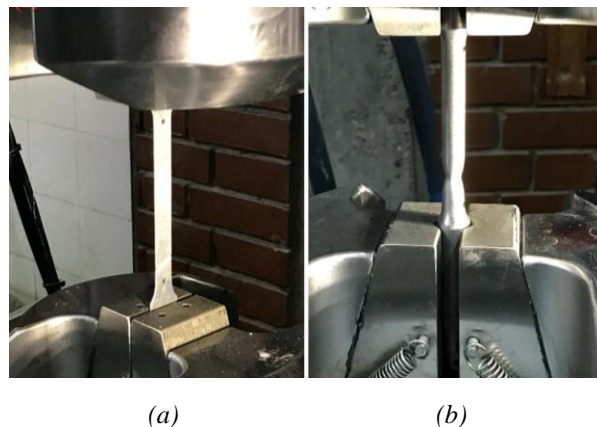


Figure 4.6. (a) After-fracture tensile test specimen of flat material (b) Just-before-fracture tensile test specimen of circular material

Determination of yield strength, yield point elongation, ultimate tensile strength and fracture points was then achieved. Measurement of elongation after fracture had also been done even though not to be used directly. Reduction in cross-sectional area had been saved. Also, the thickness and width data had been recorded for specimens with rectangular cross-sections.



Figure 4.7. Flat and cylindrical specimens after the completion of the tests

4.2.4. Experimental Results

Tensile test machines provide force and elongation data obtained throughout the process. Extensive approach is to use them by converting into engineering stress and engineering strain data by utilizing Equation 2.2 and Equation 2.4, respectively. Then engineering or nominal stress-strain curve can easily be plotted. The widespread method is to derive true stress-strain data from engineering stress-strain data rearranged through Equation 2.7 and Equation 2.9.

Note that the onset of necking is assumed to take place when the maximum value of punch force or stress is reached.

4.2.4.1. Al2024T3 Sheet Specimen Tensile Test Results

Firstly, the results for Al2024T3 sheet specimens are presented in Figures 4.8 - 4.10 for straight rectangular, tapered and notched specimens, respectively. Tapered and notched tensile specimens can be used to control the location of the diffuse necking.

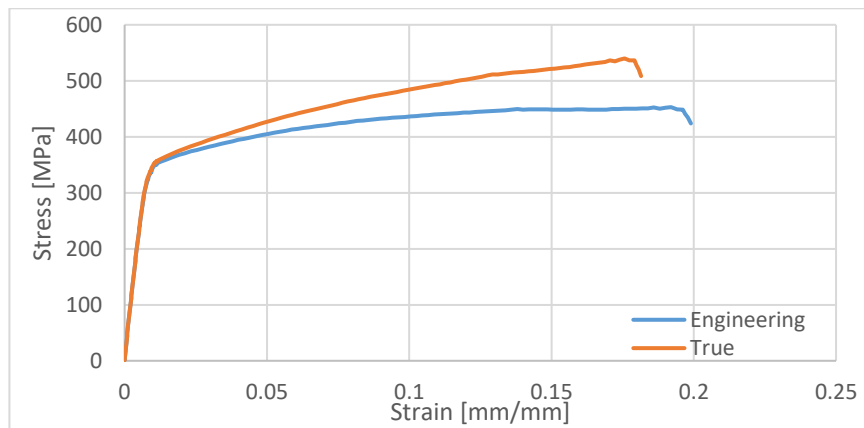


Figure 4.8. Average stress-strain curves for straight, Al2024T3, sheet specimen tensile test experiments

Next; tapered and notched analysis outputs are given in Figures 4.9 and 4.10, respectively.

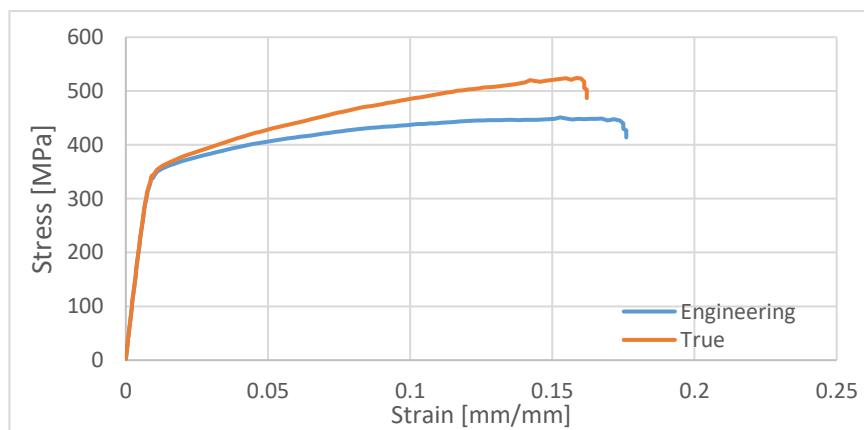


Figure 4.9. Average stress-strain curves for tapered, Al2024T3, sheet specimen tensile test experiments

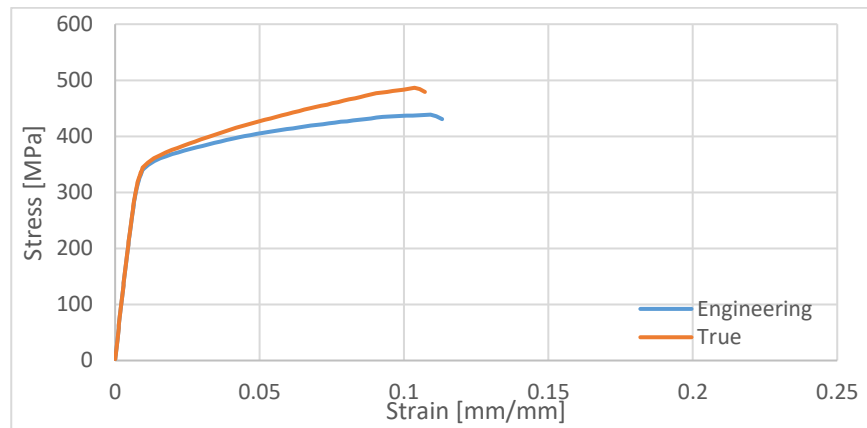


Figure 4.10. Average stress-strain curves for notched, Al2024T3, sheet specimen tensile test experiments

Figure 4.11 shows the comparison of engineering stress-strain curves acquired from rectangular, tapered and notched cross sectioned aluminum sheet metal experiments; namely, TT-She-Al-Str, TT-She-Al-Tpr and TT-She-Al-Ntc, respectively. The results are coherent. As anticipated, straight specimen has the highest strain value ($\epsilon_{axial} = 0.196$) and notched on has the lowest strain value ($\epsilon_{axial} = 0.11$).

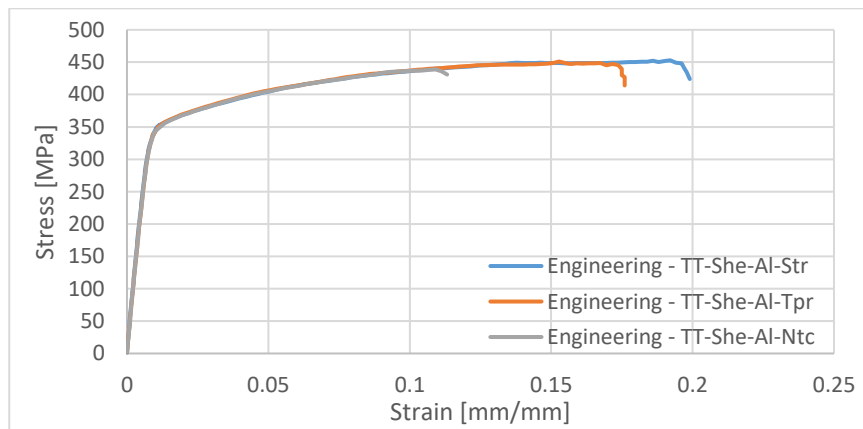


Figure 4.11. Comparative engineering stress-strain curves of straight, tapered and notched Al2024T3 sheet specimen tensile test experiments

4.2.4.2. Al2024T3 Round Specimen Tensile Test Results

Stress-strain curves for perfectly cylindrical, tapered and notched Al2024T3 round specimens are provided in Figures 4.12 - 4.14, respectively.

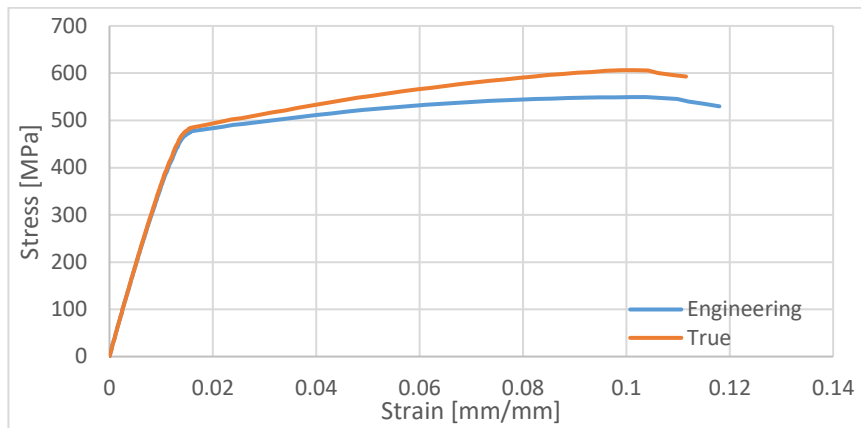


Figure 4.12. Average stress-strain curves for straight, Al2024T3, round specimen tensile test experiments

Aluminum specimens are observed to elongate less than steel specimens.

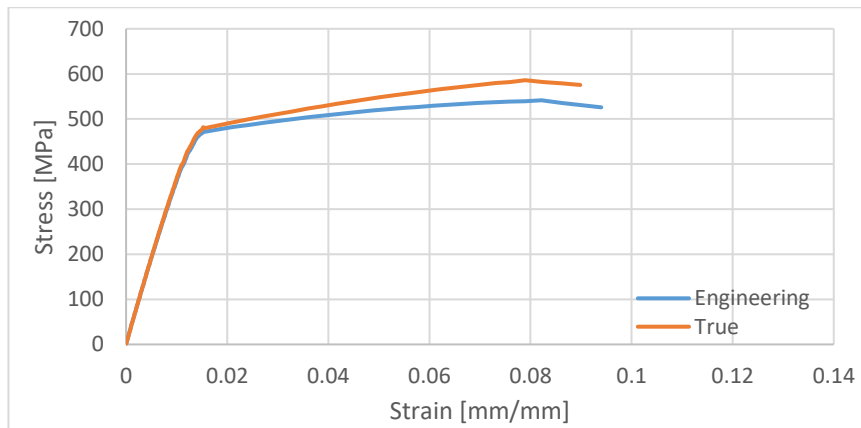


Figure 4.13. Average stress-strain curves for tapered, Al2024T3, round specimen tensile test experiments

Considering its low density, Al2024T3 has remarkably high ultimate tensile strength values. The related performance parameter is known as specific strength or strength-to-weight ratio and found by dividing the materials strength by its density. High specific strength of Al2024T3 also helps to explain why the materials is popular in aerospace structures. In Figure 4.15, engineering stress-strain curves for three cases are presented altogether.

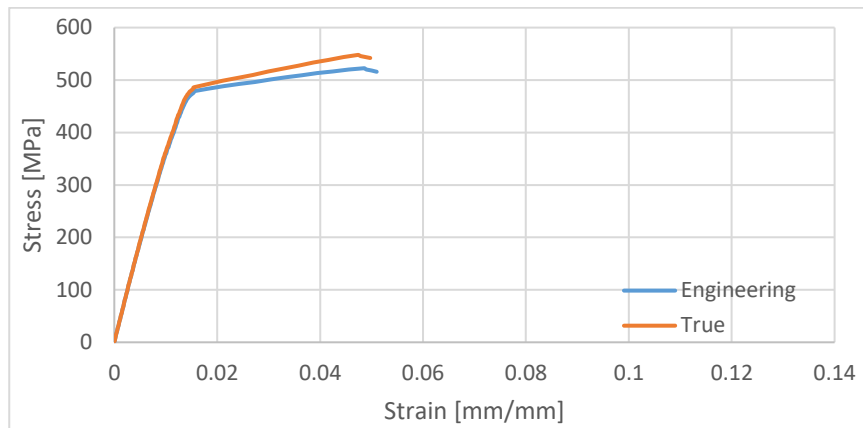


Figure 4.14. Average stress-strain curves for notched, Al2024T3, round specimen tensile test experiments

As in sheet metal specimens, imperfect round bars fail earlier when set against perfectly cylindrical specimens. Other than the failure times, the experiment outputs are quite consistent. Aluminum specimen experiment results are parallel with the literature survey [145].

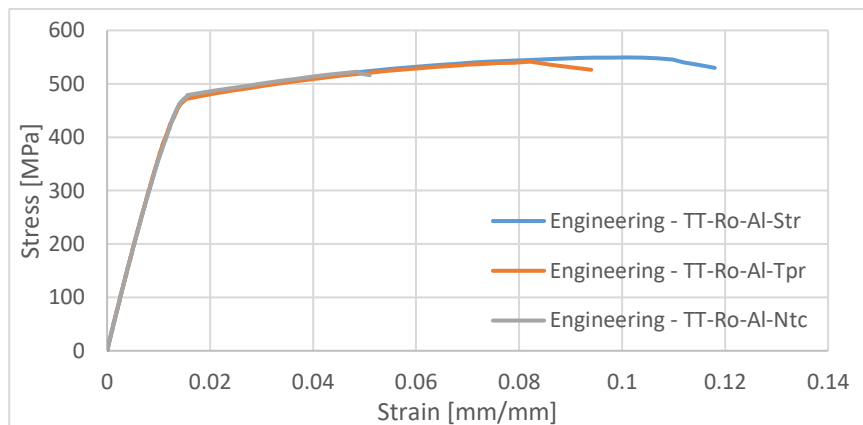


Figure 4.15. Comparative engineering stress-strain curves of straight, tapered and notched Al2024T3 round specimen tensile test experiments

4.2.4.3. Comments on the Graphs of Al2024T3 Specimen Tensile Tests

AL2024T3 specimen experiments clearly indicates that round specimens with 10mm diameter fail at a lower strain value than 1x12mm² rectangular cross section tensile test samples. This observation does not change with the defect, i.e. straight, tapered and notched specimens all exhibited similar behaviors in respective characteristics.

According to the manufacturer of raw aluminum pieces, Al2024T3 sheet metals with 1 mm thickness has tensile strength of 444-446 MPa, yield strength of 333-334 MPa and elongation of 18-19% in axial-direction. In straight specimen data (TT-She-Al-Str) the results are very close; ultimate tensile strength is 452 MPa and elongation is 19.6%. For round Al specimens, manufacturer statement for tensile strength, yield strength and elongation are 546.72 MPa, 476.66 MPa and 9%, respectively. The combined results of TT-Ro-Al-Str revealed the values of 549 MPa and 0.11% for tensile strength and elongation parameters, respectively. Hence the experiment results TT-She-Al-Str and TT-Ro-Al-Str represent the laboratory results of the manufacturer quite well.

4.2.4.4. S235JR Sheet Specimen Tensile Test Results

Steel sheet sample graphs are given in Figures 4.16 - 4.18. Catalogue maximum strain of S235JR is 0.26; yet, corresponding experiment result for straight sheet steel is 21% as in Figure 4.16. The experimented steel sheet is very thin (2 mm); on the other hand, the specification is given for sheet thickness lower than 16 mm; which is a major difference and can possibly cause such deviations. Another cause of deviation might be the markings of the specimens because they had been placed manually.

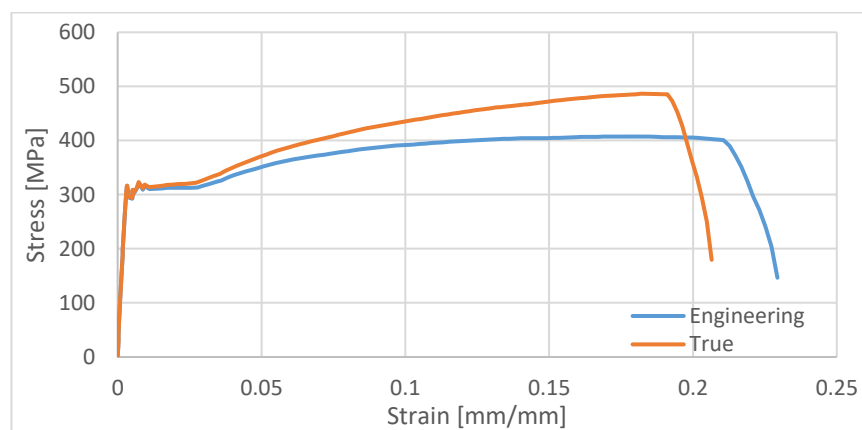


Figure 4.16. Average stress-strain curves for straight, S235JR, sheet specimen tensile test experiments

On the other hand, experiments revealed an expected decrease in strain values for tapered and notched specimens when compared to perfectly rectangular strip. The maximum (or fracture) strain values for tapered (Figure 4.17) and notched (Figure 4.18) S235JR sheet specimens are 18% and 15%, respectively. These are consistent and precise results.

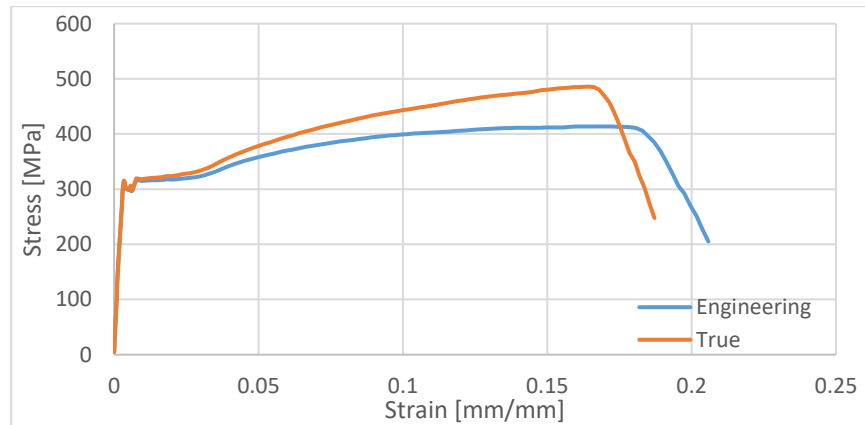


Figure 4.17. Average stress-strain curves for tapered, S235JR, sheet specimen tensile test experiments

Figures 4.17 and 4.18 point out that notched specimens lose their tensile strength and elongation (or ductility) abilities more than tapered specimens.

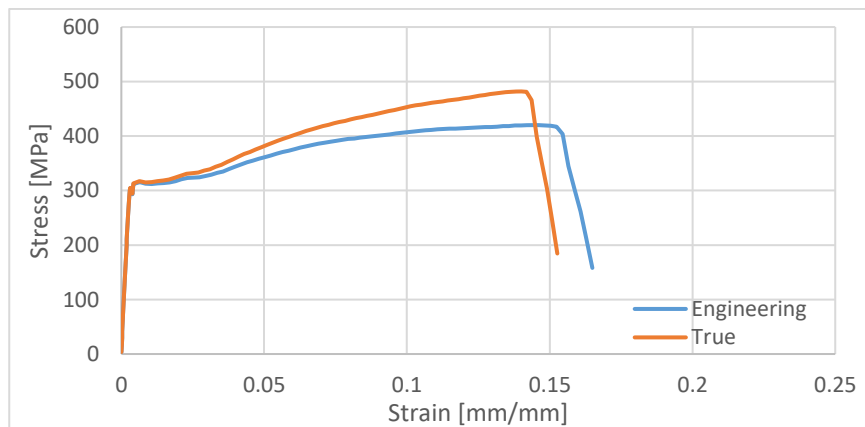


Figure 4.18. Average stress-strain curves for notched, S235JR, sheet specimen tensile test experiments

Engineering stress-strain curves for the three cases are plotted together in Figure 4.19 for comparison. An interesting deduction from Figure 4.19 is ultimate tensile strength

values of straight, tapered and notched specimens which are 407 MPa, 413 MPa and 419 MPa.

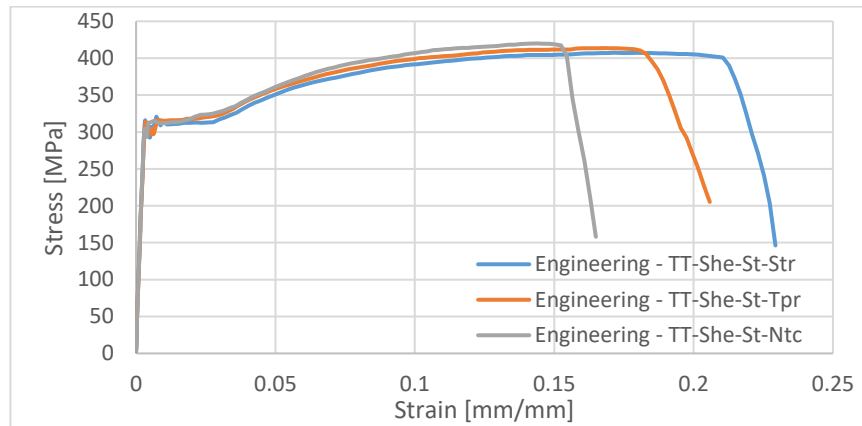


Figure 4.19. Comparative engineering stress-strain curves of straight, tapered and notched S235JR sheet specimen tensile test experiments

It is also noteworthy that S235JR is a mild or low-carbon steel. Thus, after yield point is reached, a plateau is formed in stress-strain curves. The phenomenon is known as Lüders band where the sample exhibits stable local deformation. This behavior is almost perfectly plastic, and no strain hardening occurs.

4.2.4.5. S235JR Round Specimen Tensile Test Results

The outputs from S235JR round specimen experiment are shown in Figures 4.20 -4.22 for straight, tapered and notched specimens, respectively. In those figures, the first important part is that Lüders bands are significantly less than sheet metal counterparts in Figures 4.16 - 4.18. According to literature survey, a factor behind it could be based on microscopic features. Smaller grain size results in less Lüders bands. The rod-shaped S235JR specimens may not be annealed well. This could cause more grain boundaries, smaller grain sizes and less bands to be formed [146].

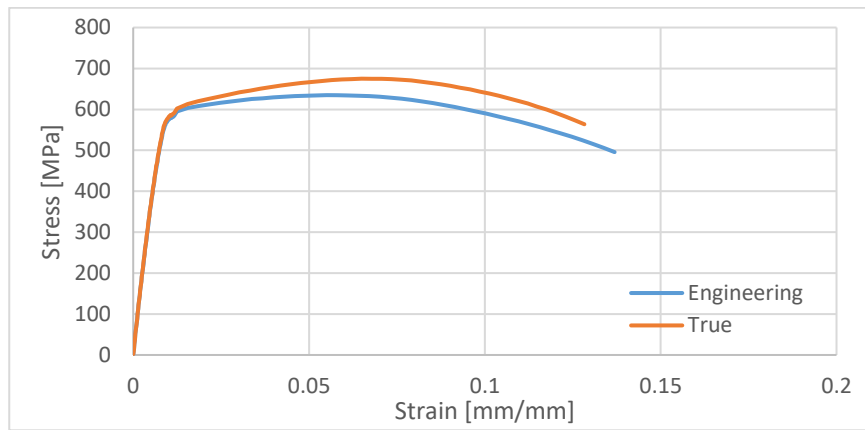


Figure 4.20. Average stress-strain curves for straight, S235JR, round specimen tensile test experiments

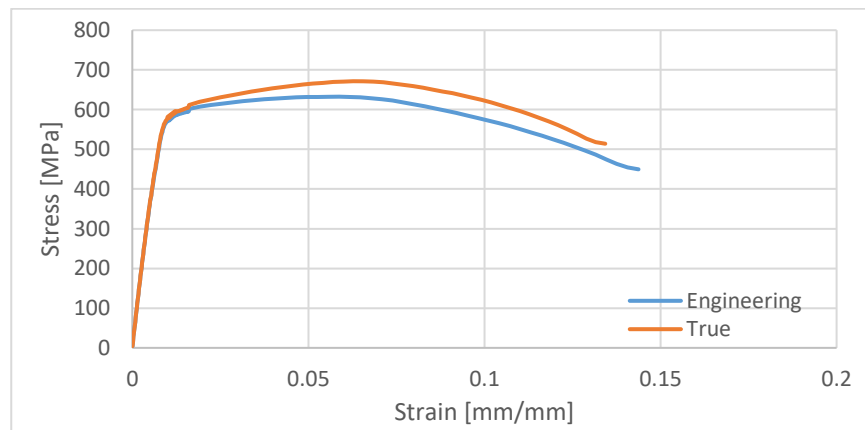


Figure 4.21. Average stress-strain curves for tapered, S235JR, round specimen tensile test experiments

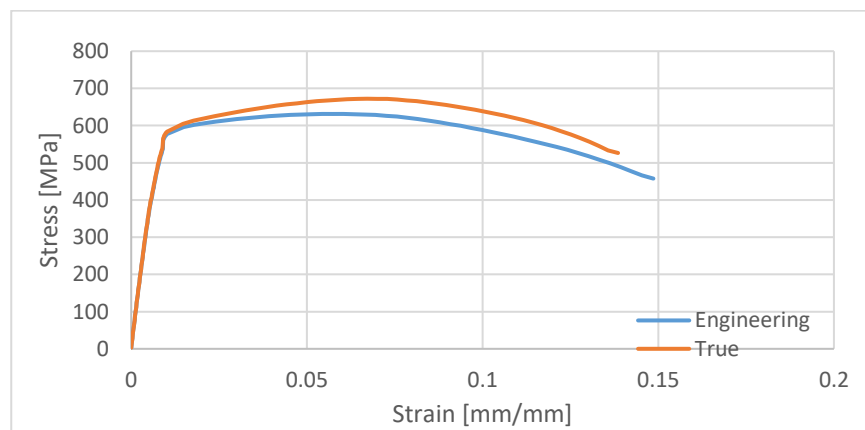


Figure 4.22. Average stress-strain curves for notched, S235JR, round specimen tensile test experiments

Engineering stress-strain curves for all cases are matched in Figure 4.23. The results from different geometries have the very close yield and ultimate tensile stress levels.

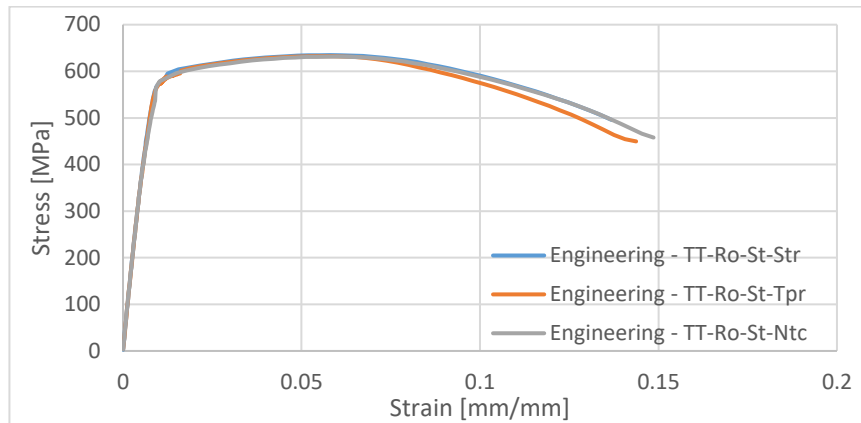


Figure 4.23. Comparative engineering stress-strain curves of straight, tapered and notched S235JR round specimen tensile test experiments

An interesting issue appears in fracture strain comparison in Figure 4.23. The fracture strain of straight specimen ($\epsilon_{axial} = 0.137$) is lower than both tapered ($\epsilon_{axial} = 0.144$) and notched ($\epsilon_{axial} = 0.149$) specimen averages. It is different than other experiment results. Yet, the differences are insignificant; thus, it is possible that experimental errors (such as operators manual marking of specimen gauge ends) might have led to that result.

4.2.4.6. Comments on the Graphs of S235JR Specimen Tensile Tests

S235JR specimen tensile test results have been represented previously. Extrusion parts have higher tensile strength but lower maximum strain values with respect to their rolled matches.

In addition, sheet metal versions have more Lüders bands in comparison to rod versions of specimens.

It is necessary to note that the trends of sheet and rod engineering stress-strain curves are differentiated. The strain value reached at ultimate tensile strength is closer to fracture stain for sheet metal specimens than round bars.

Those plots also explain why the manufacturers give a wide range to define S235JR and similar low-carbon mild steel properties. The properties can vary with processes applied.

As an overall conclusion from tensile test experiments, it is indicated that artificial imperfections such as tapered or notched specimens affect the material properties such as maximum punch force/ultimate tensile strength or maximum elongation/strain negatively.

4.3. Deep Drawing Experiments

In this thesis, the instability/necking prediction methods and their results are aimed to be universally validated. Thus, deep drawing process is chosen to apply the prediction methods in addition to tensile test. Deep drawing experiment has been selected because it has quite different nature than tensile test and very popular as a sheet metal forming (SMF) test.

At the end of a proper deep drawing application, the blank assumes the shape of punch. This divides the process into different categories depending on the shape of the punch.

The practical deep drawing experiment is differentiated from theory because there is a huge amount of details that should be taken care during the experiment. In fact, the aim of those efforts is to create ideal conditions for deep drawing process equipment and specimens.

The success of deep drawing operation is affected by many factors, including: type of material, size and thickness of the specimen, die clearance, clamping pressure (or blank holder force, BHF), forming speed and pressure/load, size and shape of the punch, and type of lubricant. Unless these factors are paid attention, failures and other types of undesired results tend to emerge.

4.3.1. Experimental Set Up

Deep drawing experiments have been carried out with Tinius-Olsen Ductomatic A-40 sheet metal testing machine (manufactured in 1971) in Figure 4.24. The machine can simulate many stresses and forces encountered in actual production processes.



Figure 4.24. Tinius-Olsen Ductomatic A-40 Sheet Metal Tester

Different male punches and female dies are going to be used; namely

- Cylindrical or flat-head deep drawing cup test (critical dimensions are given in Table 4.3)

Table 4.3. Cylindrical cup deep drawing process tooling dimensions

Parameter	Value [mm]
Punch Cylinder Diameter	50
Punch Bottom Shoulder Radius	5
Die Inner Diameter	53
Die Shoulder Radius	13.5

- Round bottom or hemispherical-head deep drawing cup test (critical dimensions are given in Table 4.4)

Table 4.4. Round bottom cup deep drawing process tooling dimensions

Parameter	Value [mm]
Punch Hemisphere Bottom Diameter	50
Die Inner Diameter	53
Die Outer Diameter	115
Die Shoulder Radius	13.5

- Square cup deep drawing process (critical dimensions are given in Table 4.5)

Table 4.5. Square cup deep drawing process tooling dimensions

Parameter	Value [mm]
Punch Edge Length	40
Punch Edge Radius	10
Punch Corner Radius	4.5
Die Inner Edge Length	42
Die Outer Edge Length	80
Die Shoulder Radius	13.5

As the lubricant, grease oil is used on the blanks, punches and dies to reduce friction between the machine and the workpiece. Lubricant selection is important because it can reduce forming energy, increase forming limit and tool life, and prevent surface damages on parts.

All experiments have been conducted approximately at 20°C temperature.

4.3.2. Specimen Geometry and Material

The experiments have been conducted with 1 mm thick Al2024T3 sheet specimens. There are two different specimen shapes; square sheet and circular sheet. The former is a square with edge length of 80 mm and the latter is a circle with diameter of 110 mm, which are picturized in Figure 4.25.

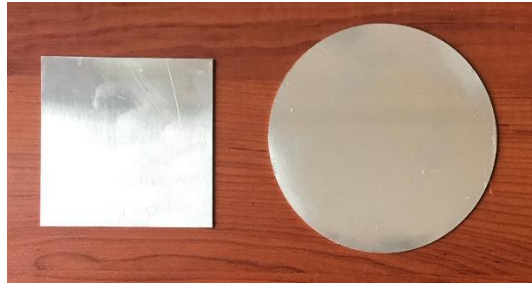


Figure 4.25. Specimen geometry for square cup test is on left-hand side. Specimen geometry for cylindrical and hemispherical specimens is on the right-hand side.

9 deep drawing experiments have been completed and related information is given in Table 4.6. Each type of deep drawing process is repeated three times to have reliable test data.

Table 4.6. Deep drawing process sheet specimen number, name, material, thickness and type information

Specimen Number	Specimen Names	Material	Thickness	Specimen Type
3	C2, C3, C4	Al2024T3	1 mm	Sheet, Circular
3	R1, R2, R3	Al2024T3	1 mm	Sheet, Circular
3	S2, S3, S4	Al2024T3	1 mm	Sheet, Square

4.3.3. Experimental Procedure

Grease oil is applied between punch-blank, die-blank and holder-blank for lubrication purposes.

Blank holder force (BHF) is selected for all deep drawing processes as 4903.325 N. This value has been considered as ideal for Al2024T3 specimen deep drawing processes after many trial experiments. Test speed is determined as 0.33 mm/s to have quasi-static experiment conditions.

The attempts in deep drawing processes are made to form cylindrical or rectangular cups from sheet metals. In summary, all the surfaces of die, punch and holder are cleaned and required surfaces are lubricated. Height stop limit switch is locked at the desired position. First BHF and then testing speed are set. Finally, the load and

displacement data are recorded. Figure 4.26 shows the fractured deep drawing process samples.



Figure 4.26. Deep drawing process specimens after completion of processes

4.3.4. Experimental Results

The main output of the tests is punch forces and punch displacement data. Unlike tensile test experiments, deep drawing results are not to be used in a FEA. Moreover, there are significantly less cases in deep drawing processes. As a result, the test results are not going to be averaged or combined; instead, they will be provided separately.

Note that the onset of tensile plastic instability is assumed to take place when the maximum value of punch force is reached. Punch travel value when the maximum punch force is acquired is essentially used in Results chapter.

4.3.4.1. Al2024T3 Cylindrical Cup Deep Drawing Process Results

Cylindrical cup results are given in Figures 4.27 - 4.29 for C2, C3 and C4 cases, respectively.

In case C2, the onset of tensile plastic instability is detected at 8.88 mm punch displacement and 5508.99 N punch force.

Tensile plastic instability of case C3 is marked at 13.83 mm punch stroke and 5904.81 N punch force which is also shown in Figure 4.28.

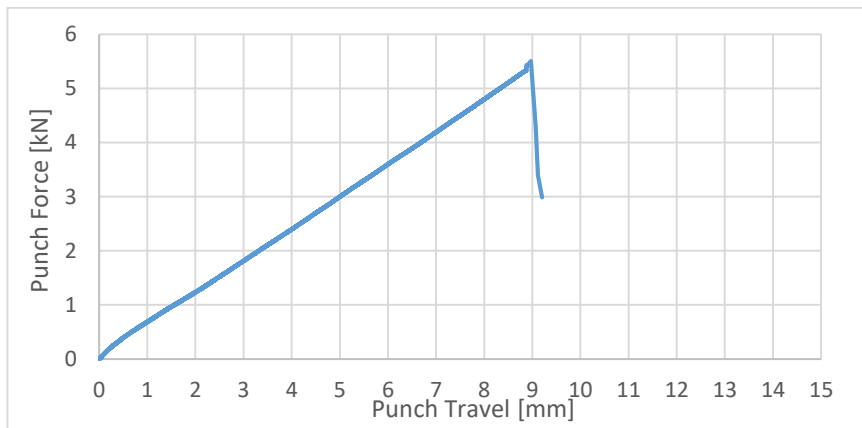


Figure 4.27. Punch force vs. punch travel graph for Al2024T3 cylindrical cup deep drawing (C2) experiment

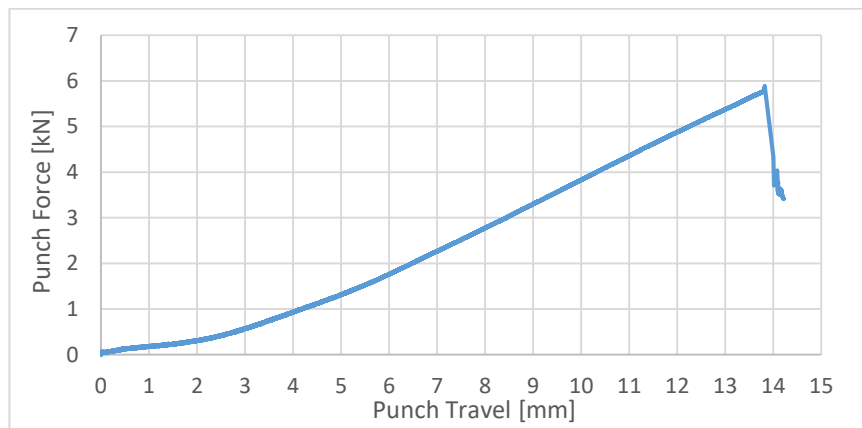


Figure 4.28. Punch force vs. punch travel graph for Al2024T3 cylindrical cup deep drawing (C3) experiment

Lastly, 8.77 mm and 5677.88 N values have been recorded as the punch displacement and load at the commencement of tensile plastic instability for experiment C4.

The figures have shown that when the punch and the blank get into contact, the force increases slowly. Then, the material resists since its flanges are fixed between the holder and die. A smoothly increasing trend maintained and followed by a sudden drop in all plots.

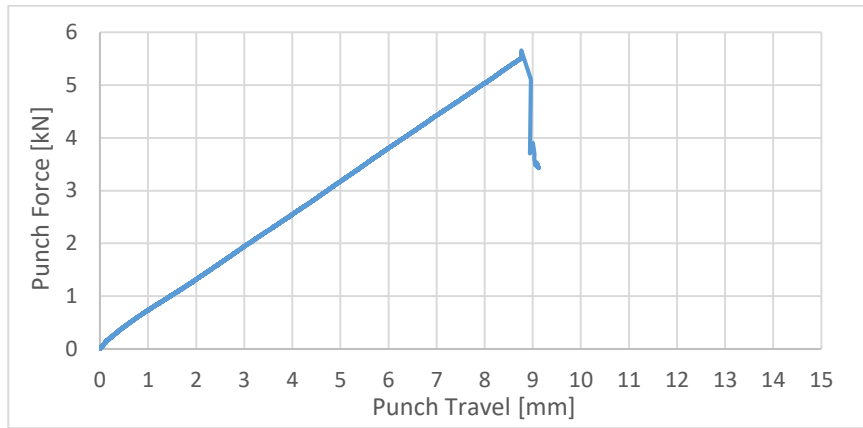


Figure 4.29. Punch force vs. punch travel graph for Al2024T3 cylindrical cup deep drawing (C4) experiment

4.3.4.2. Al2024T3 Round Bottom Cup Deep Drawing Process Results

Round bottom or hemispherical punch deep drawing process results are given in this subsection. Figures 4.30 - 4.32 illustrates the results of experiment cases R1, R2 and R3, respectively.

Experiment case R1 reached the instability condition at 20.05 mm punch travel and 3648.55 N punch force as shown in Figure 4.30.

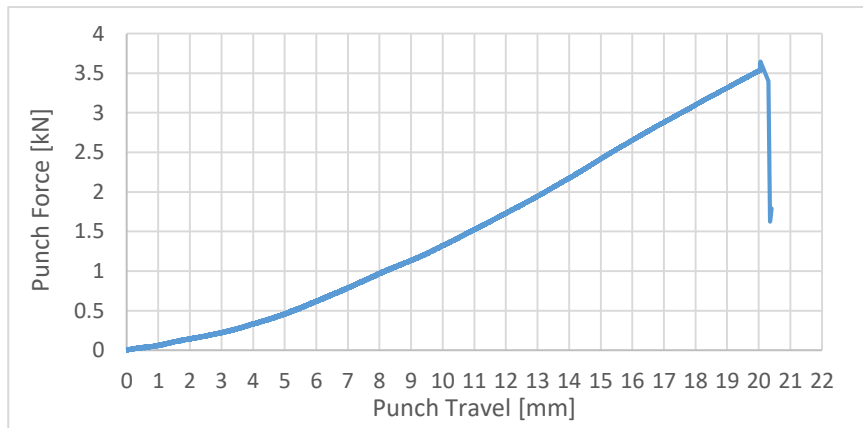


Figure 4.30. Punch force vs. punch travel graph for Al2024T3 round bottom cup deep drawing (R1) experiment

In Figure 4.31, tensile plastic instability is uncovered at a punch displacement of 17.22 mm and punch force of 3492.05 N. In the case of R3, corresponding displacement and force values are given as 14.83 mm and 3562.77 N, respectively.

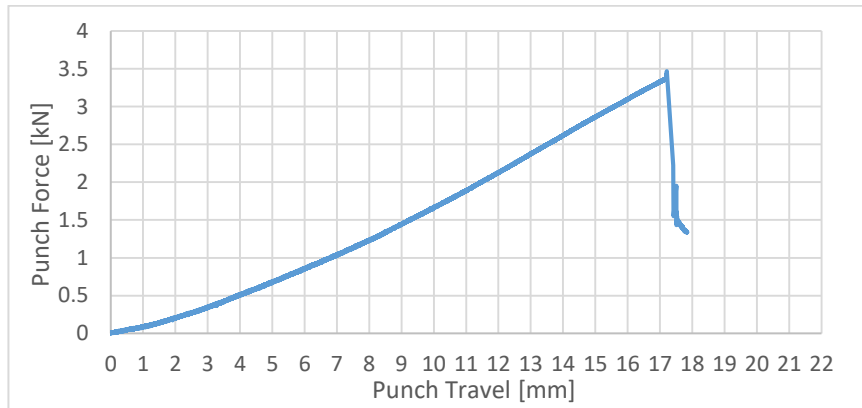


Figure 4.31. Punch force vs. punch travel graph for Al2024T3 round bottom cup deep drawing (R2) experiment

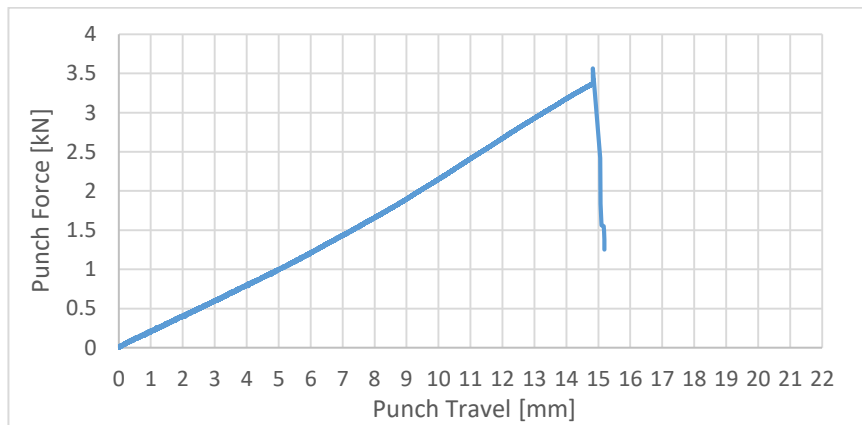


Figure 4.32. Punch force vs. punch travel graph for Al2024T3 round bottom cup deep drawing (R3) experiment

The curve trends of cylindrical cup and hemispherical cup deep drawing processes are alike. On the other hand, cylindrical cup tests require significantly higher magnitudes of force than round bottom counterparts.

4.3.4.3. Al2024T3 Square Cup Deep Drawing Process Results

Square cup deep drawing experimental results are presented in Figures 4.33 - 4.35. The corresponding cases are S3, S4 and S5, respectively, and they are described in Table 4.6.

In case S3, maximum force is enlisted at 15.78 mm displacement and 6015.42 N force. Figure 4.34 reveal the initiation of plastic instability at 15.87 mm punch travel and 5839.98 N punch force. On the other hand, tensile plastic instability occurred at 15.57 mm displacement and 5706.11 N load according to case S5 plotted in Figure 4.35.

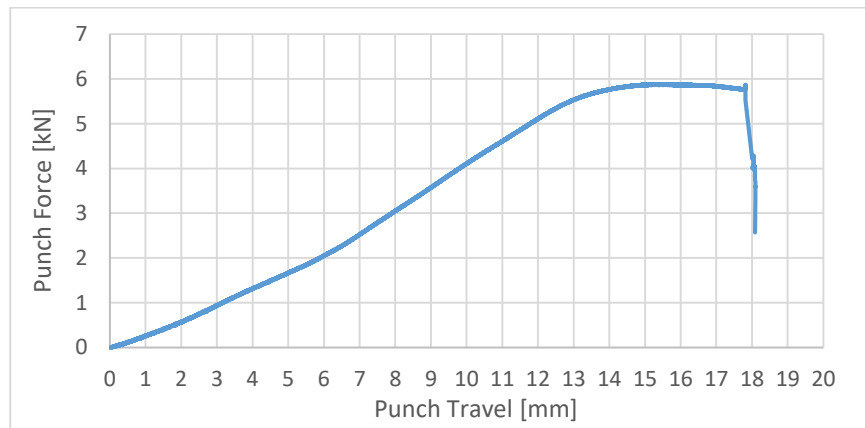


Figure 4.33. Punch force vs. punch travel graph for Al2024T3 square cup deep drawing (S3) experiment

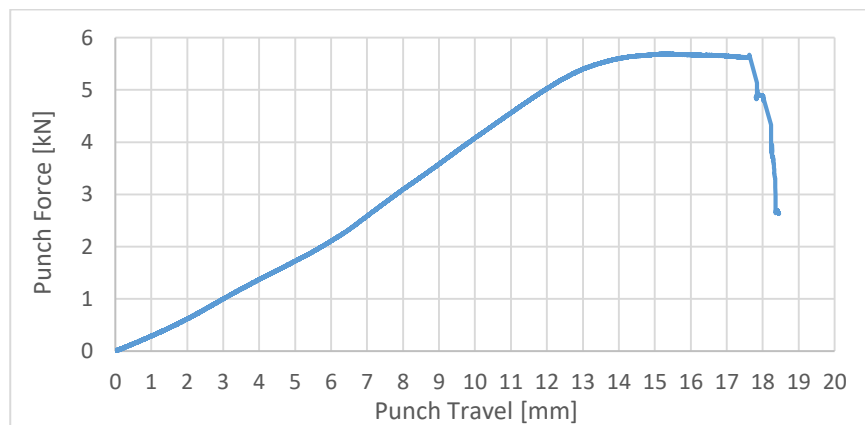


Figure 4.34. Punch force vs. punch travel graph for Al2024T3 square cup deep drawing (S4) experiment

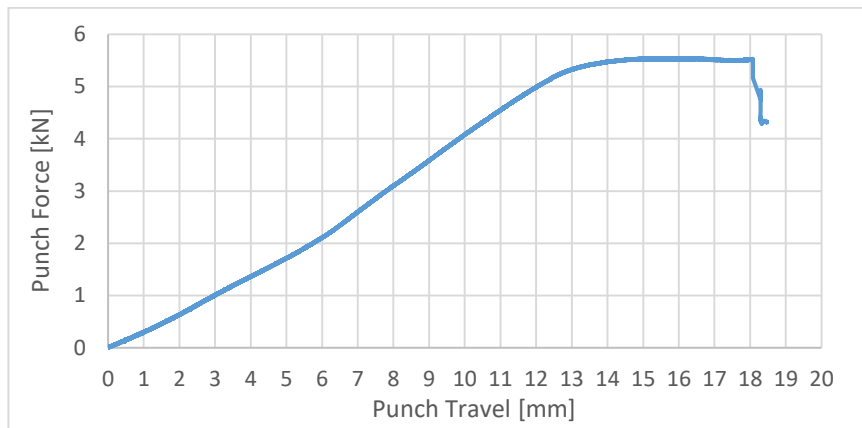


Figure 4.35. Punch force vs. punch travel graph for Al2024T3 square cup deep drawing (S5) experiment

Square cup deep drawing process have unique characteristics when compared to other deep drawing process. In cylindrical cup and round bottom cup deep drawing processes of Al2024T3 specimens, the tensile plastic instability is immediately followed by a sudden drop in force magnitude. However, the sudden reduction happens after the maximum force is smoothly decreased for a while.

CHAPTER 5

FINITE ELEMENT MODELS

5.1. Introduction

Present engineering applications require advanced and optimized products in terms of cost, strength, reliability, and durability. Hence; engineers create product models and analyze behavior of products by simulating the environmental effects during operation. Since the simulation processes are carried out in a systematical and controllable manner, they constitute significantly during the design phase. Due to cost and time concerns, engineering analyses through simulation models are mostly preferred to represent the physical system and surroundings adequately.

Engineering analysis can be mainly classified as classical methods and numerical methods.

The first sub-category of classical methods is analytical closed form solutions. Analytical solutions denote exact solutions for the behavior of a system with variable properties. However, there are few situations where a system can be represented analytically.

The other sub-category is approximate solutions such as Rayleigh-Ritz method. These methods can handle some situations where analytical approach does not work. For example, Rayleigh-Ritz method finds approximations to eigenvalue equations which are hard or impossible to solve analytically. On the other hand, classical methods can only be used simple structures (especially in terms of geometry) and simple load cases.

There are also numerical analysis types under engineering analysis; namely, finite difference method, boundary element method and finite element method. Finite difference method is a direct approach applied on differential equations, and mostly defined for geometries structured as regular grid. Therefore, it is not usually appropriate to use that technique on irregular geometries, complex boundary

conditions and inhomogeneities. Next, boundary element method also solves partial differential equations; yet, they are formulated as integral equations or in boundary integral form. Therefore, boundary element method discretizes the outer boundary of the analysis domain. Boundary element method application is effective to solve geometries with small surface-to-volume ratio, symmetrical problems with infinite domains, Laplace and Helmholtz problems etc. Nonetheless, it also has several disadvantages. Boundary element approaches have limitations under conditions with inhomogeneities and nonlinear differential equations [149]. Finite element method involves splitting the big system into small and “finite” number of elements.

It is important to note that numerical methods are always approximations. Consequently, results obtained from numerical solutions will inevitably deviate from real-life situations.

5.2. Finite Element Analysis

Finite element analyses have been conducted for several decades. The tools utilizing finite element methods are still reliable and widely used in aerospace, automotive, marine, consumer goods, industrial and life science technologies as well as construction, mining and energy applications.

Finite element models have been proven to be one of the most efficient and accurate techniques starting in 1950's [148]. In order to obtain finite element models, engineers divide the product model into basic units or elements, which are well-known from previous studies and experience. After re-constructing the physical model by assigning the elements, one can evaluate the behavior of the model under certain conditions [149].

In finite element models, interactions of physical systems are represented through partial differential equations which are derived from physical laws. Reducing partial differential equations into algebraic equations simplifies the complex problem. Next, numerical methods are employed to solve the system of algebraic equations.

Nowadays it is very common to complete this solution step by using computers owing to their high calculation capacity and speed.

Small simple structures, also known as subdomains, form the main domain of a finite element problem. The subdomains are the finite elements in the model; thus, finite element mesh is composed of the subdomains. The behavior of subdomains is well known by the researchers and engineers. Therefore, the real-life problem is distributed over each element, and the physical process is approximated by functions and algebraic equations relating physical quantities at selective points, called nodes, are developed. Finally, the element equations are assembled using continuity and balance of physical quantities and solved.

The basic principle of finite element analysis is to split the body of interest into small portions. The body is called domain and the portions are subdomains. This process of generating the subdomains is called discretization; thus, the subdomains are also referred as discrete elements. These elements are joined to each other via connection points or nodes. The response of a discrete system is described by finite number of points and lead to a set of algebraic equations. Depending on the system, there can be myriad of equations; which are hard or impossible to handle manually. Therefore, complex numerical analyses are solved with digital computers [149].

To summarize the steps of a finite element analysis, the structure is discretized into several elements by dividing the domain. The system is idealized through assumptions. Then, behavior of each element is described by a finite number of parameters so that material properties are defined. Next, element assemblage is achieved by connecting them together. Boundary conditions are applied, and system of equations is solved. Lastly, post-processing is implemented; quantities of interest are determined.

The most crucial advantage of finite element analysis is its adaptability to different and complex geometries. Moreover, arbitrary supports (boundary conditions) and arbitrary load are easily applied. The properties of elements can be changed practically

and results in any location can be interpreted separately. The external conditions (such as temperature) of the system are implemented simply. Lastly, many resources in the literature and many software packages on finite element analysis are available. Some disadvantages of finite element analysis are, the obtained results are not exact, and assumptions made before the process cause the results to vary significantly. In addition, the numerical result is unique to the problem. No closed form solution is obtained from finite element analysis. Lastly, complex finite element models are computationally expensive.

Since a complicated solid mechanics problem may contain parts with different dimensions, materials, openings etc.; finite element method is the most suitable to implement in this thesis. Yet, it is still an arduous task to build a reliable FE model; many research topics do still exist to construct and solve reliable, precise, accurate and optimized simulations.

5.3. FE Model Construction of Round Specimen Tensile Test

Axisymmetric, deformable and shell part options are chosen for 2D tension test specimen. In axisymmetric 2D analysis of round specimens, researchers used different portions of the specimen's cross section.

One can work on the cross-section of whole specimen, half of specimen or quarter of specimen. Moreover, researchers may prefer to include or exclude the specimen head or grip region in the analysis.

In this work, quarter of the specimen cross-section with head portion will be studied for axisymmetric 2D FEA which represents round tensile test specimens corresponding to Figure 5.1(b). The region illustrated in Figure 5.1(b) is the most appropriate approach to be utilized in this thesis because this configuration simplifies the model by exploiting symmetry axes and include end effects caused by the grip region properly.

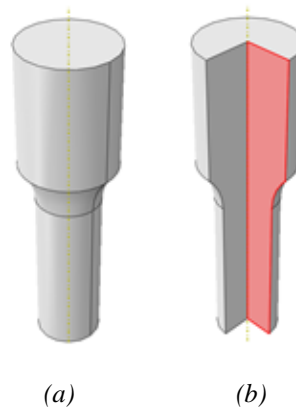


Figure 5.1. (a) 3D view of a round tensile test specimen (b) half of the cross-section

It is important that even with quarter portion of cross-section, there are three different models to be analyzed in this thesis. Recall that necking can occur at any section of the gauge region in a simple tension test with a cylindrical specimen. In order to monitor the position of the necking region, artificial defects are commonly introduced to concentrate the necking in the middle of gauge section. To achieve that purpose, either tapered or notched specimens are exploited in real-life experiments as in Figures 5.2(b) and (c). Note that grip region is excluded to reveal the coordinates clearly.

In all cases, the x-coordinates of the nodes at lower boundary are free to move (shear-free boundary condition), then the necking eventually occurs at the bottom which corresponds to gauge center of the specimen. Dirichlet or first-type boundary condition restricts the nodes to move in y-direction. As a result, the shear-free end at the bottom section is designed to cause stress concentration.

As a remark, the effect of the test machine fixture/clamp can be represented well with boundary conditions and loads instead of drawing another part instance. Therefore, the grips of a tensile test machine will not be simulated separately in tension test FE models.

In ABAQUS, steps are utilized to define and order the stages of the analysis process. In this thesis, the change of the properties with respect to time is investigated; hence dynamic analysis is required instead of static. After this selection, one must decide on standard (implicit) or explicit analysis.

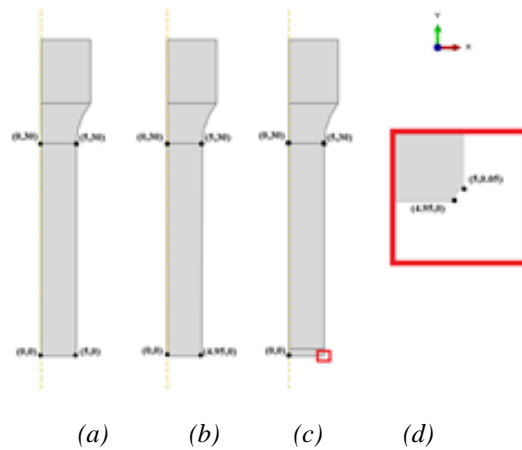


Figure 5.2. Initial geometry coordinates of a quarter cross-section without head for (a) Cylindrical model (b) Tapered model (c) Notched model

Although explicit analysis is conditionally stable, it is versatile, appropriate for large deformation analysis and effectively handle nonlinear behavior. Consequently, dynamic explicit analysis is selected as the step type. Then, Nlgeom is turned on to take nonlinear effects of large displacements (or strains) into account in subsequent solution steps.

In ABAQUS, field outputs (calculated for each element or node in the domain) like stress, strain, translation, rotation, velocity, acceleration, reaction forces, contact stresses are recorded at evenly spaced 20 time intervals by default. In this thesis, the number of intervals has been increased to 40 in order to increase the accuracy of results. Note that, the force plot is a history output (calculated for a certain geometry, node or element). Thus, the number of evenly spaced time intervals are defined as 200 for force values; which does not increase the calculation time significantly. Thereupon, equivalent plastic strain (PEEQ) and other field output variables will be calculated at 40 discretized time intervals.

Then boundary conditions applied for perfectly round, tapered and notched specimen models can be found in Figures 5.3(a) - (c), respectively. Note that in ABAQUS, “U” represents the displacements and “UR” represents the rotations. Directions x, y and z are denoted as 1, 2 and 3, respectively.

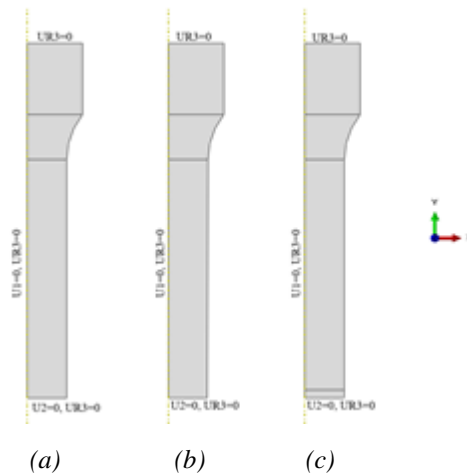


Figure 5.3. Boundary conditions of (a) Cylindrical model (b) Tapered model (c) Notched model

Next, upper boundary condition is applied as velocity (0.033 mm/s in elastic region and 0.167 mm/s in plastic region) to create the quasi-static analysis. Note that the bottom boundary condition allows only translation in x-direction.

Mesh size is determined to be $0.5 \times 0.5 \text{ mm}^2$ and part is meshed as in Figure 5.4. Finally, the model is compiled to create a job in the Job module and it can be submitted to obtain the solution.

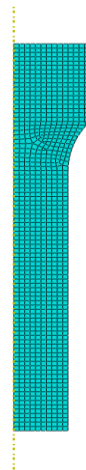


Figure 5.4. Meshed domain covering $\frac{1}{4}$ of gauge cross-section

For straight specimens, the diameter of cylindrical specimens is 10 mm; thus, axisymmetric 2D model is 5 mm wide in gauge region. Mesh elements of size 0.5×0.5

mm² are distributed as in Figure 5.5(a). Important elements and their numbers are provided in Figures 5.5(b) and (c).

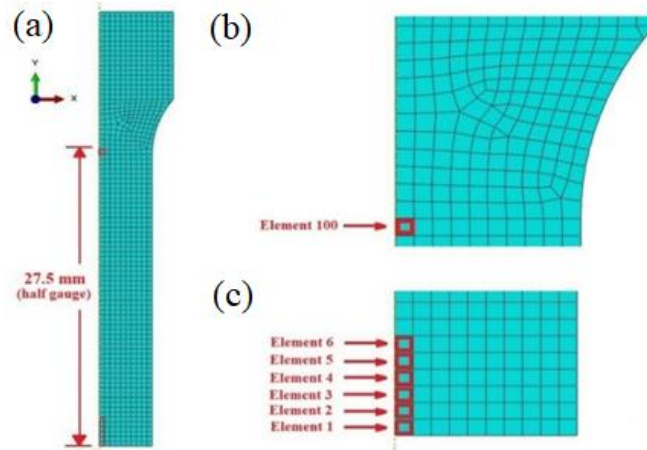


Figure 5.5. (a) Mesh domain for straight and tapered axisymmetric models (b) Some mesh element number and positions at upper section (c) Some mesh element numbers and positions at lower section

Tapered gauge regions have slightly larger diameter at both ends and slightly narrower at gauge center. The diameter is 10 mm at gauge extremes and 9.90 mm at the center. In the axisymmetric model, half of these length values are drawn. Similar to the sheet metal experiment case, the gradual change in cross section along the gauge in y-direction does not result in a significant difference in mesh distribution of round models. Thus, tapered models have the mesh distribution illustrated in Figure 5.5(a). Consequently, mesh element numbers in Figures 5.5(b) and (c) will be utilized in methods applied on tapered specimens.

As in the case of notched sheet metals, ABAQUS increases the number of elements around a notch since it is a stress concentration geometry. Figure 5.6 shows the additional elements when compared to Figure 5.5.

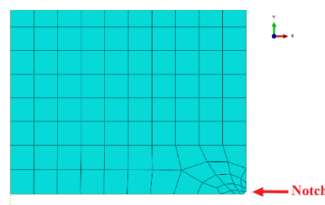


Figure 5.6. A closer view of notch location

However, same numbers are assigned to elements of interest for simplicity, as in Figure 5.7.

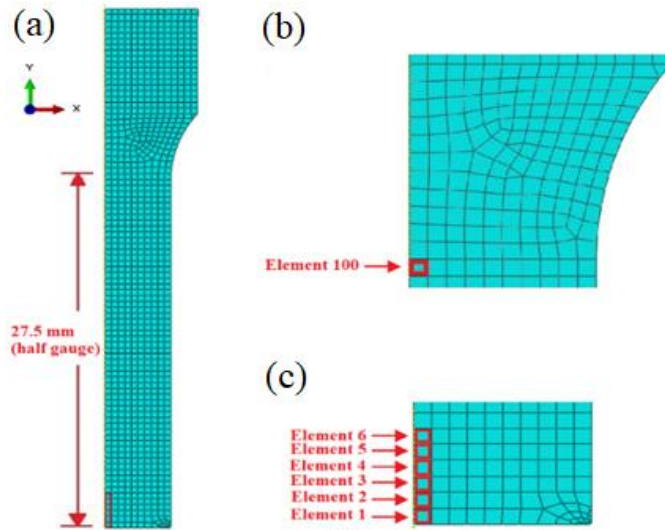


Figure 5.7. New element numbers for meshes on notched domain

The initial small geometrical defect is going to focus high stress and strain values around its territory. Yet, the same mesh elements are selected in order to compare the results of different methods and materials properly on the same basis.

Finally, in a uniaxial tensile test FEA, the velocity is applied on upper boundary of the domain of study in Figure 5.8. Axisymmetric models allow the punch force to be measured at lower boundary properly.

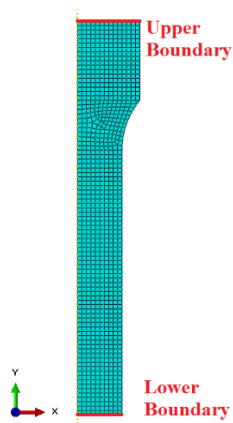


Figure 5.8. Upper and lower boundaries of axisymmetric model

5.4. FE Model Construction of Flat Specimen Tensile Test

In this section, FE modeling of tensile test with strip-type specimen will be prescribed. In previous section the steps and important details of contracting an axisymmetric 2D FE analysis described thoroughly; hence, only the differences will be underlined in the current section.

It is possible to construct a 2D model for sheet metal analysis; yet, necking of a sheet metal specimen has been proved to be more complicated than that of a round bar [150]. The stress distribution in necking region becomes non-uniform and strain distribution reveals varying characteristics with different aspect ratios [88]. On the other hand, 3D models allow the analyst to observe stress and strain effects along the thickness as well. Hence, the selected properties for the specimen part are 3D, deformable and solid.

There are several options to simulate the experiment specimen. In this work, a quarter of the specimen cross-section with head will be studied in 3D FE analysis for sheet metal tensile test specimens, which corresponds to Figure 5.9(b). The reason behind is to exploit the symmetry of upper half of the specimen in y-direction and to involve end effect of the head region in calculations. Some authors have used quarter of the sheet metal specimen with grip region in 3D finite element analysis similarly [24,66,67,88].

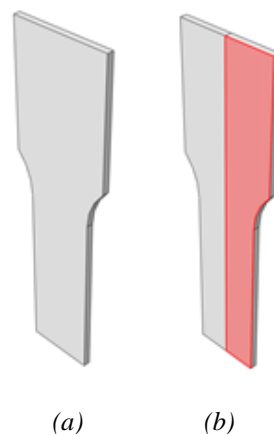


Figure 5.9. (a) 3D view of a round tensile test specimen (b) half of the cross-section

The sheets or plates are made by rolling process. The process affects the internal structure and overall characteristics of the part. Thereupon, properties of a sheet metals vary with the direction; which is defined as anisotropy. There are studies comparing isotropic and anisotropic material behaviors with experiments [17]. Anisotropic models are found to agree with the experimental results better than isotropic models. On the other hand, the main purpose of this thesis is to investigate the methods to predict the onset of necking. The deviations from anisotropic models have been assumed to be acceptable. Therefore, the anisotropic effects will be excluded in the analysis; the material will be assumed isotropic in sheet metal tensile test simulation (as well as deep drawing simulations). In fact, isotropic material model is stated as a good approximation for Al2024T3 sheet specimens in the literature [142].

Note that, the experiments are to be conducted with strips cut in rolling direction (length) which has better performance characteristics than transverse (width) and normal (thickness) directions.

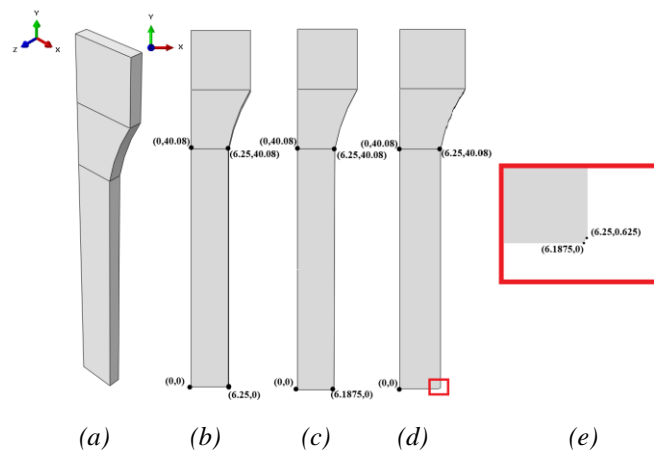


Figure 5.10. Geometrical details of 3D sheet models (a) Isometric view (b) Straight strip (c) Tapered strip (d) Notched strip (e) A closer look at the notched strip

In Figure 5.10, coordinates of straight, tapered and notched specimen gauge region are given in Figures 5.10(a) - (c), respectively. In Figure 5.10(a), isometric view of the 3D model is presented; and, the coordinates around notch region can be viewed in Figure 5.10(e).

The boundary conditions are revealed in Figure 5.11 for the three cases.

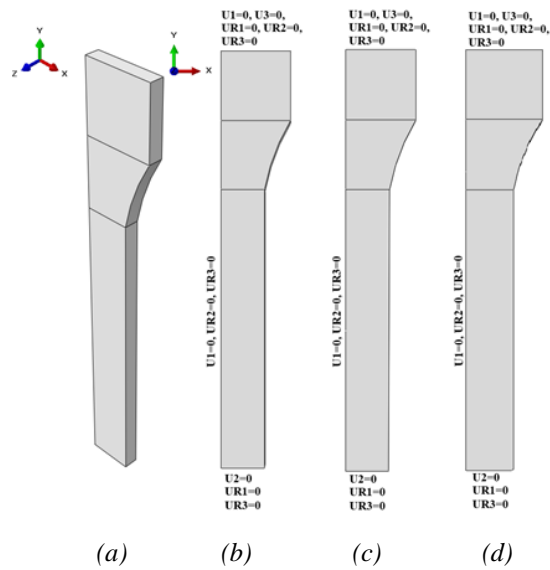


Figure 5.11. (a) Isometric view of the strip-type specimen (b) Boundary conditions of straight specimen (c) Boundary conditions of tapered specimen (d) Boundary conditions of notched specimen

Then, mesh size is determined to be $0.5 \times 0.5 \times 0.5 \text{ mm}^3$ and part is meshed as in Figure 5.12. Note that S235JR was not available for 1mm; hence 2mm thick sheet is used in experiments as well as numerical analysis. The rest of the analysis procedure is the same as round bar specimen analysis discussed in previous section.



Figure 5.12. Mesh domain covering $\frac{1}{4}$ of the specimen (a) Al2024T3 (b) S235JR

In straight cross section sheet metal tensile test analysis, the FE mesh is given in Figures 5.13(a) and (b). This includes a quarter of the specimen since the symmetry of x- and y-axes are exploited throughout the process. The portion included in analysis excludes the end effects on gauge section. In addition, Figure 5.13(b) points out the gauge portion of the specimen model, where the necking is expected to occur. Elongation of gauge region in y-direction is crucial while predicting the onset of necking.

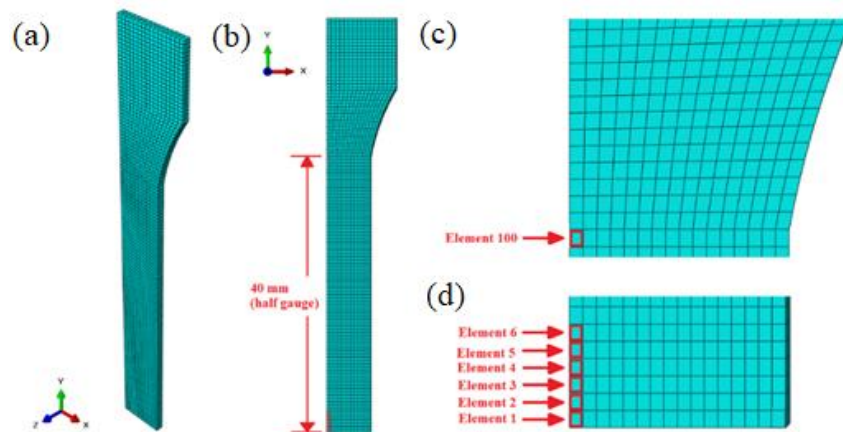


Figure 5.13. (a) Isometric view and (b) Front view of mesh domain for straight and tapered 3D sheet models. Some mesh element number and positions at (c) upper section (d) lower section

Figure 5.13(c) reveals the transition section between grip and gauge. Element 100 is at the cross section where gauge portion ends. Thus, Element 100's displacement is recorded during the analysis and compared with gauge elongation information obtained from experiments.

On the other hand, Figure 5.13(d) shows the gauge center and related elements. Both equivalent plastic strain rate ratio and difference of second time derivative of equivalent plastic strain methods yield different results by selecting different elements. Results from different pairs of elements shown in Figure 5.13(d) are going to be selected and compared.

Tapered gauge regions are slightly thicker at both ends and slightly thinner at center. This slight change does not cause a significant effect on mesh distribution shown in .

In sheet metal tensile test analyses, the domain of interest similar to Figures 5.13(a) and (b), that is the same as straight cross section analysis. The element numbers in Figures 5.13(c) and (d) are also valid in those sections.

The notch takes place at the gauge center on the perimeter of specimen cross-section, which can be observed in Figure 5.14.

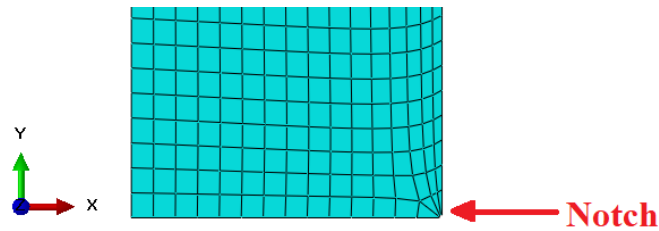


Figure 5.14. A closer front view of notch location

More mesh elements around critical region do not cause a change in element numbers to be worked on; the element numbers are shown in Figure 5.15.

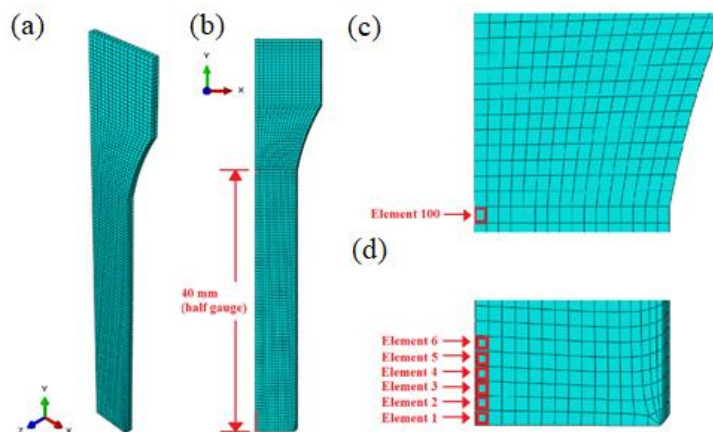


Figure 5.15. (a) Isometric view and (b) Front view of mesh domain for notched 3D sheet models. Some mesh element number and positions at (c) upper section (d) lower section

Even though the number of mesh elements through the sheet thickness in four instead of two shown in Figure 5.15(a), the mesh element numbers in Figures 5.15(b) and (c) are still suitable for notched cross-section studies of sheet S235JR specimen FEA.

Lastly, the region on top of grip on which the velocity is applied can be seen in Figure 5.16(a). As a result of this action, the punch force is calculated and plotted from nodes at the bottom section of the domain as in Figure 5.16(b).

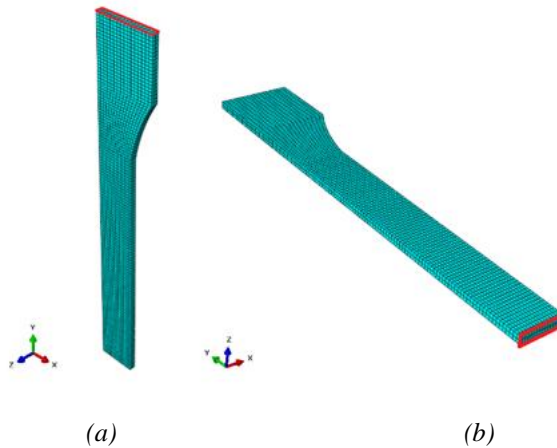


Figure 5.16. (a) Displacement/velocity application region in FEA (b) Mesh elements at the bottom used to calculate punch force

5.5. FE Model Construction for Deep Drawing Process

Modeling of deep drawing process is to be described in this part. The blank or sheet to be formed must be simulated with three other parts; namely, punch, holder and die. The interaction definitions and the friction play a major role in deep drawing process models.

In cylindrical cup and round bottom cup drawing analysis, the die, the holder and the punch are all defined with 3D, discrete rigid and shell properties.

As the material properties, straight sample sheet metal specimen data for Al2024T3 aluminum have been entered.

Models of die, holder and specimen in ABAQUS are given in Figure 5.17 for both cylindrical cup and round bottom cup deep drawing simulations.

On the other hand, the punch shapes for cylindrical cup and round bottom deep drawing processes are provided in Figures 5.18(a) and (b), respectively.

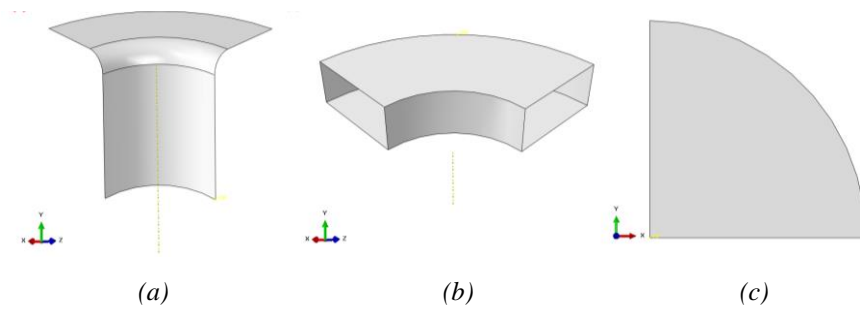


Figure 5.17. (a) The holder (b) The die (c) The blank for both cylindrical cup and round bottom cup deep drawing FE analysis

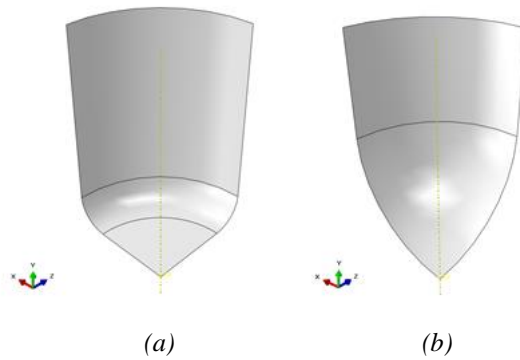


Figure 5.18. Punch geometry of (a) Cylindrical cup (b) Round bottom cup for deep drawing FE analysis

The assembly of cylindrical cup deep drawing parts emerges as in Figure 5.19(a). Besides, the meshed models of the assembly and specimen are appointed to Figures 5.19(b) and (c), respectively. Pictures from hemispherical punch deep drawing process can be found in Figure 5.20.

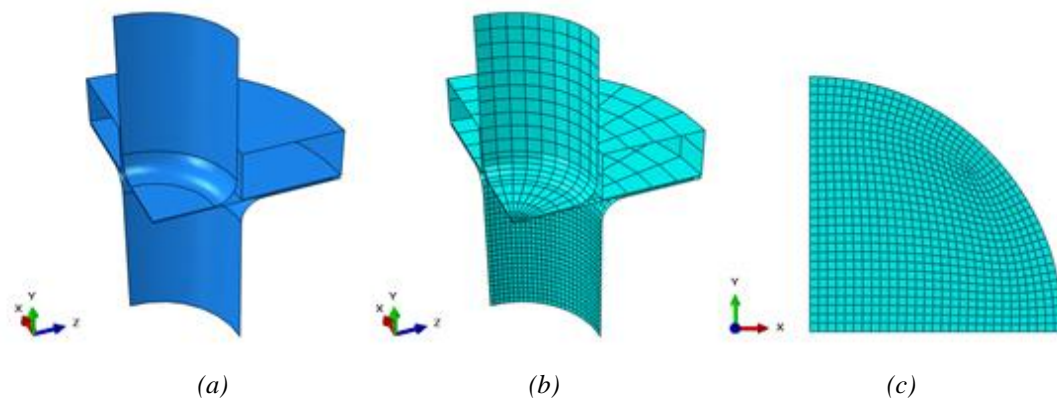


Figure 5.19. Cylindrical cup deep drawing FE analysis (a) Assembly of the parts (b) Assembly of the meshed parts (c) Meshed sheet metal specimen

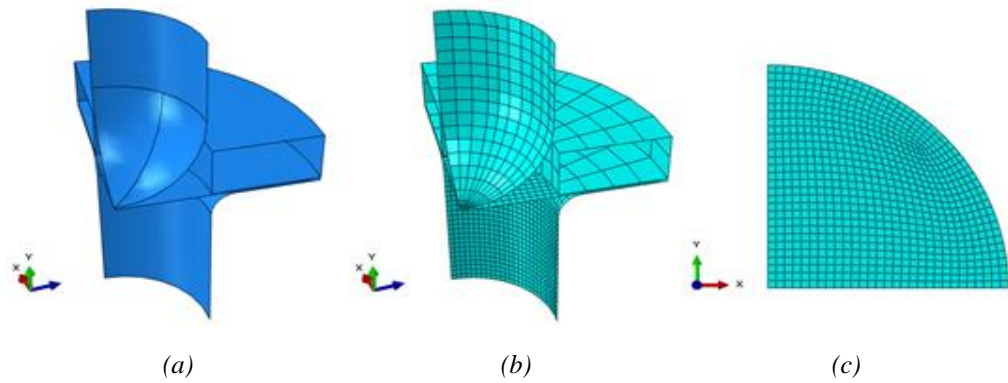


Figure 5.20. Round bottom cup deep drawing FE analysis (a) Assembly of the parts (b) Assembly of the meshed parts (c) Meshed sheet metal specimen

The shapes of die, holder, punch and blank used in square cup deep drawing are provided in Figure 5.21.

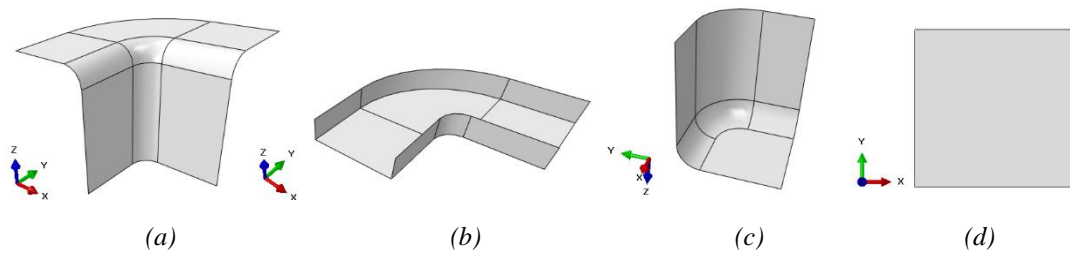


Figure 5.21. (a) The die (b) The holder (c) The punch (d) The blank models of square cup deep drawing analysis

Next, one can view the unmeshed and meshed assembly views of punch, die, blank holder and the blank for the square cup deep drawing in Figure 5.22.

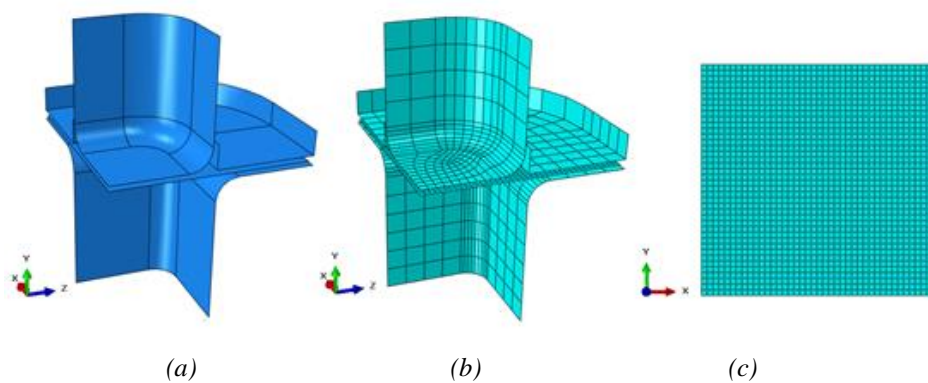


Figure 5.22. Square cup deep drawing FE analysis (a) Assembly of the parts (b) Assembly of the meshed parts (c) Meshed sheet metal specimen

Note that, $1 \times 1 \text{ mm}^2$ size mesh grids are constructed on the blank surface for all cases. The results are consistent with the experiments; thus, no finer mesh is necessary. In addition, it is important to have the same mesh size in all three processes to have a common basis for comparison because different mesh element sizes may yield different output from the same instability prediction criterion.

There are several parts in deep drawing process and their interaction characteristics must be defined in detail. Punch-blank, die-blank and blank holder-blank interactions are all defined as penalty contact method with Coulomb friction model. After investigating ABAQUS manual [151], Çoğun [152], Dizaji [153], and Altan et al. [7], the coefficient of friction for well-lubricated surface between and punch-blank is chosen as 0.06. Between die-blank and holder-blank, less grease oil is applied, and the coefficient is taken as 0.15. Symmetry axes are defined for two edges of the sheet metal blank; because the model contains $1/4^{\text{th}}$ of the experiment system. The die is fixed for all six degrees of freedom; yet, the punch and the holder are free to move only in y -direction. Similar to tensile test model, the punch's movement is described with displacement in y -direction. Yet, blank holder applies a uniform load in $-y$ -direction so that the specimen is hold between the die and the holder. Then the job is submitted, and results are harvested. Finally, some critical mesh elements on blank domains are to be illustrated in Figures 5.23 - 5.25 for cylindrical, round bottom and square cup deep drawing processes.

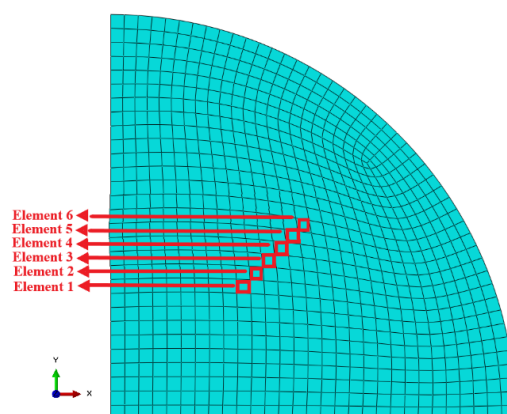


Figure 5.23. Mesh elements and positions for cylindrical cup deep drawing specimen

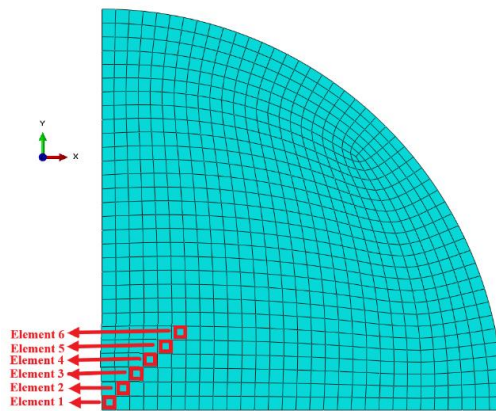


Figure 5.24. Mesh elements and positions for hemispherical cup deep drawing specimen

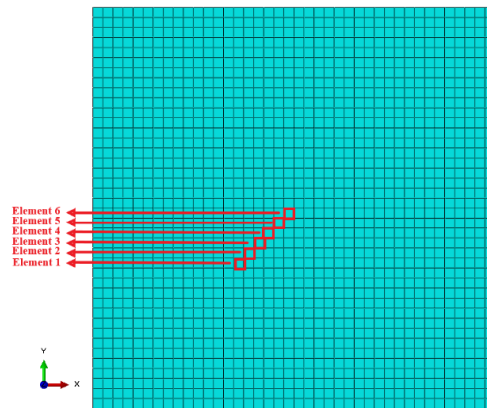


Figure 5.25. Mesh elements and positions for square cup deep drawing specimen

CHAPTER 6

RESULTS AND DISCUSSION

In this chapter, results from FE simulations of tensile and deep drawing processes are provided. Tensile plastic instability and necking prediction methods for tension and deep drawing processes are applied, presented, compared and discussed.

The numerical computations are performed on both Al2024T3 aluminum specimens and S235JR steel specimens. The results and related discussion for Al2024T3 aluminum and S235JR steel tensile tests have been divided into sub-sections according to the specimen shapes (cylindrical and sheet). Furthermore, there are straight, tapered and notched specimens under these sub-sections. The methods to predict the onset of necking are implemented in all cases.

Next, three types of deep drawing processes (cylindrical cup, round-bottom cup and square flange cup) for Al2024T3 are given under corresponding sub-sections and appropriate instability prediction methods are applied.

Note that, equivalent plastic strain rate ratio graphs are terminated as soon as the criterion threshold is exceeded meaning that necking/instability started. The rest of the figures represent the processes until the fracture point.

Criterion of equivalent plastic strain increment ratio and criterion of difference of second time derivative of equivalent plastic strain compare a critical element and a benchmark element. The ideal distance between these elements is an aim to be found in this study. Yet, different mesh sizes would give different ideal distance values for the same problem if the distance is based on number or elements. Therefore, it is more meaningful if the distance between those elements are expressed as a percentage of initial dimensions. For the tensile tests, the distance between element couples for cylindrical and sheet specimens are given in Table 6.1.

Table 6.1. Distances between elements in terms of percent of initial gauge length of tensile tests specimens

Percent of the gauge length	Sheet Specimens	Cylindrical Specimens
Elements 1 & 2	0.63	0.91
Elements 1 & 3	1.25	1.82
Elements 1 & 4	1.88	2.73
Elements 1 & 5	2.5	3.64
Elements 1 & 6	3.13	4.55

For deep drawing processes, initial specimen diameter or initial specimen edge dimensions can be utilized for generalization as in Table 6.2.

Table 6.2. Distances between elements in terms of initial diameter or initial edge dimension of deep drawing process specimens

	Cylindrical and Hemispherical Cup Specimens (percent of initial diameter)	Square Cup Specimens (percent of initial edge length)
Elements 1 & 2	1.29	1.77
Elements 1 & 3	2.57	3.54
Elements 1 & 4	3.86	5.30
Elements 1 & 5	5.14	7.07
Elements 1 & 6	6.43	8.84

6.1. FEA Results of Al2024T3 Sheet Specimen Tensile Tests

6.1.1. Straight Al2024T3 Sheet Specimen Analysis

Al2024T3 sheet specimens had three different geometries; namely, straight, tapered and notched. Methods are to be applied to all cases to predict onset of necking.

6.1.1.1. Criterion of Equivalent Plastic Strain Increment Ratio (TT-She-Al-Str)

Onset of necking for straight aluminum sheet tensile test is predicted through the strain rate ratio of two elements.

To investigate the effect and trend of the element selection, Figure 6.1 shows the strain rate ratios of Element 1 to Element 2, Element 3, Element 4, Element 5 and Element 6 shown in Figure 5.13 of Finite Element Models chapter. Figure 6.1 reveals that the critical ratio of 10 is exceeded at different elongation values. Note that the ratio values usually reach substantially higher levels in the further stages of the analysis; but, they are omitted in the plots for clarity purposes. Therefore, the plots of ratio method show the results between the analysis commencement and the surpassing of the critical limit for necking.

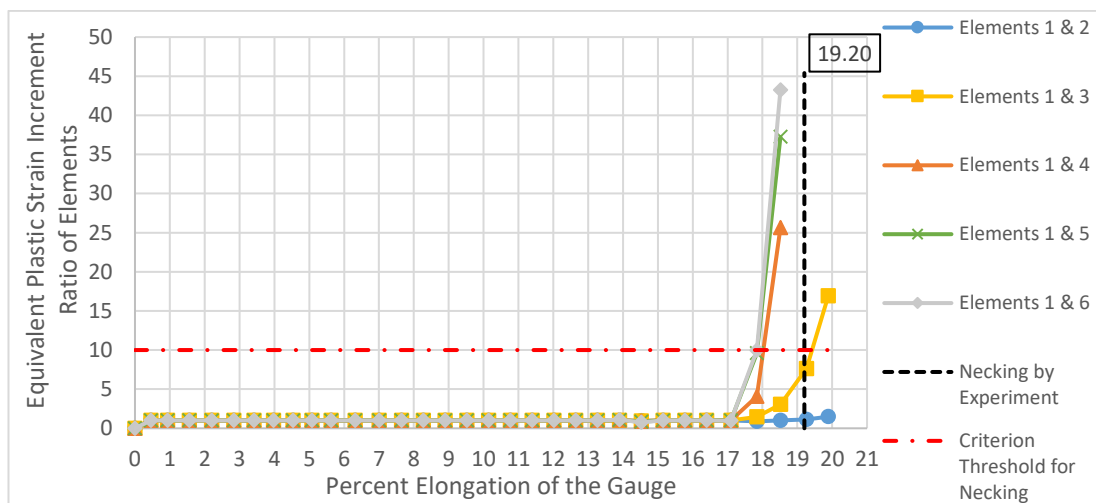


Figure 6.1. Strain increment ratios of several mesh element couples vs. percent elongation of the gauge for straight cross-section, sheet, Al specimen

The strain increment ratio of Elements 1 & 2 did not exceed 10 during the analysis; this means necking is not detected by employing these two mesh elements with a threshold of 10. For Elements 1 & 3, the total gauge elongation at necking onset is 15.54 mm which corresponds to 19.42% of the gauge. Yet, for Elements 1 & 4 elongation is 18.02%. Also note that Elements 1 & 5 and Elements 1 & 6 predicted necking at 17.85% and 17.84%, respectively. The most accurate prediction is from Element 1 & 3 when experiment result of 19.20% is considered. Furthermore, the results are precise since they vary in only 1.58% range.

6.1.1.2. Criterion of Difference of Second Time Derivative of Equivalent Plastic Strain (TT-She-Al-Str)

Difference of second time derivative of equivalent plastic strain criterion subtracts second time derivative of total equivalent plastic strain of two separate mesh elements. The plots acquired by current criterion are provided in Figure 6.2.

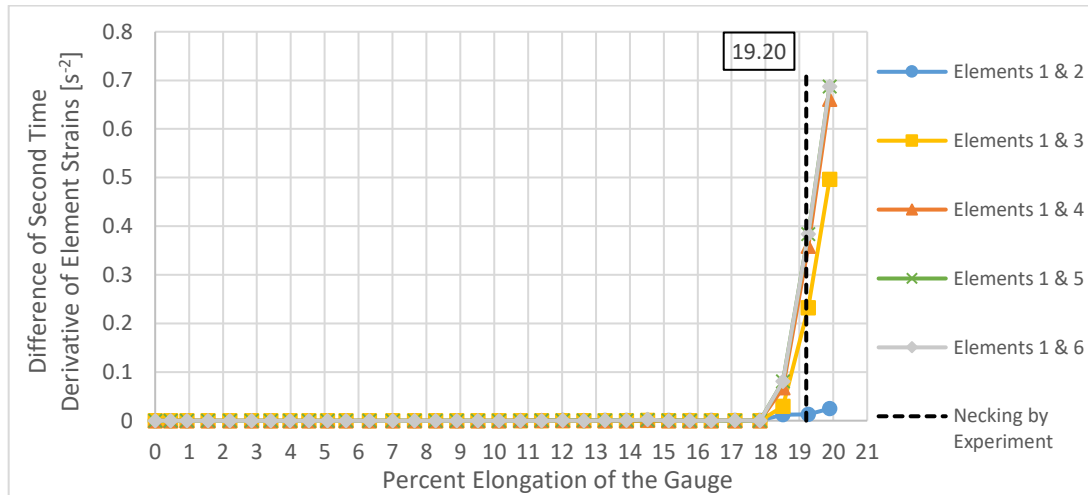


Figure 6.2. Difference of second time derivative of strain for several mesh element couples vs. percent elongation of the gauge for straight cross-section, sheet, Al specimen

The onset of necking is observed by Elements couples 1 & 2, 1 & 3, 1 & 4, 1 & 5 and 1 & 6 at 18.52% elongation although the slope of Elements 1 & 2 curve is very low compared to the rest of the plots.

6.1.1.3. Criterion of Maximum Second Time Derivative of Equivalent Plastic Strain (TT-She-Al-Str)

Maximum second time derivative of equivalent plastic strain for straight aluminum sheet tensile test is shown in Figure 6.3. It presents the change of second time derivate of equivalent plastic strain of Element 1, the critical element.

The maximum strain acceleration value is obtained at a total elongation of 14.81 mm, which corresponds to 18.52%. Yet, there are some oscillatory movements beginning

at 12.64% elongation, which might be deceiving the analyst. To be on the safe side, the analyst should have a rough idea on the acceleration levels expected to be reached.

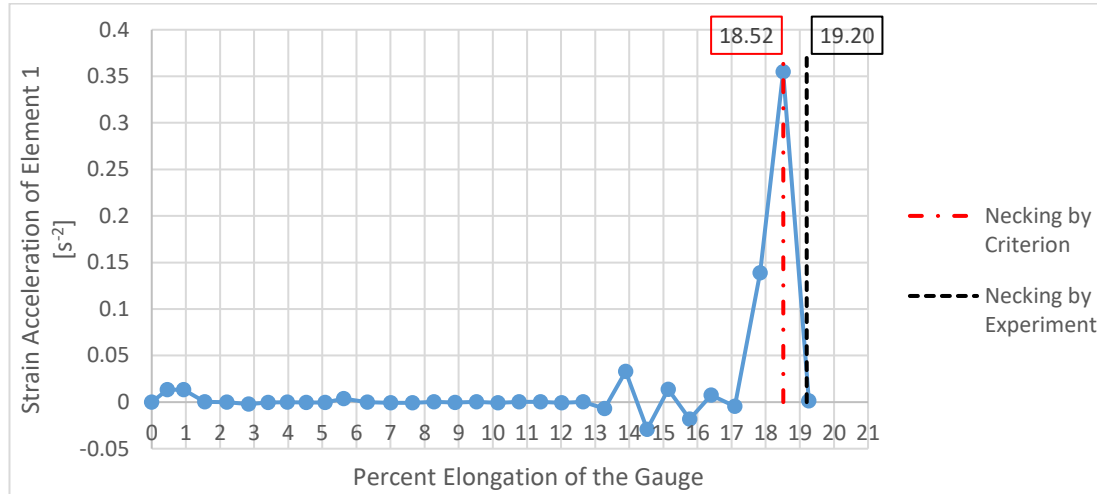


Figure 6.3. Second time derivative of Element 1 strain vs. percent elongation of the gauge for straight cross-section, sheet, Al specimen (Necking at 18.52% total elongation)

Equivalent plastic strain and equivalent plastic strain rate plots of Element 1 are given to provide a better understanding about the method. Note that the red dashed lines on these graphs are taken from equivalent plastic strain acceleration graph. It traces the total percent elongation of the gauge at which the acceleration has the peak value. Figure 6.4 clearly indicates that the change in strain increases drastically when necking occurs at elongation quantity 18.52%. Figure 6.5 also points out important information. The strain rate is nearly stable at the beginning; yet, it starts to fluctuate as necking approaches. Necking can be observed by checking the sharpest change in the strain rate; which is an indirect way of checking the strain acceleration.

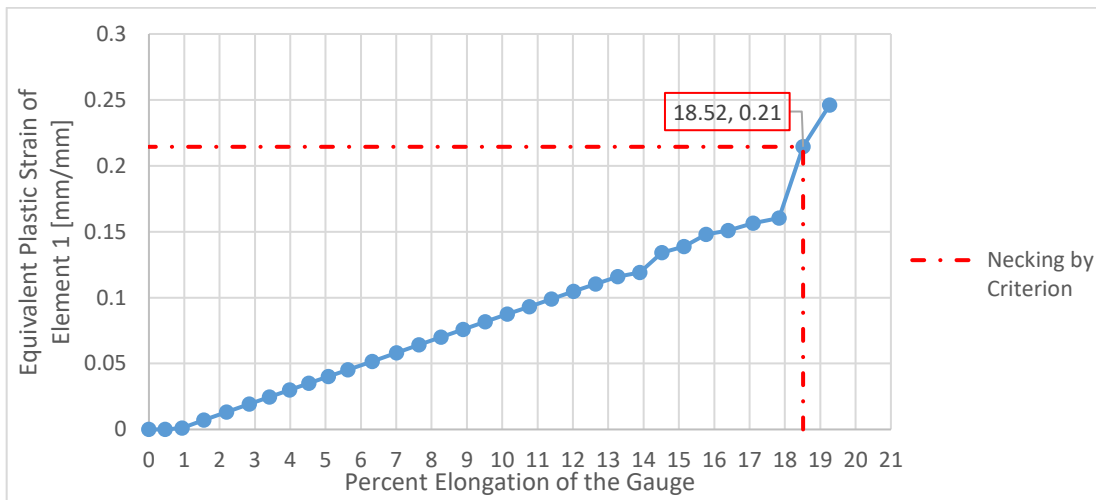


Figure 6.4. Plastic strain of Element 1 vs. percent elongation of the gauge for straight cross-section, sheet, Al specimen

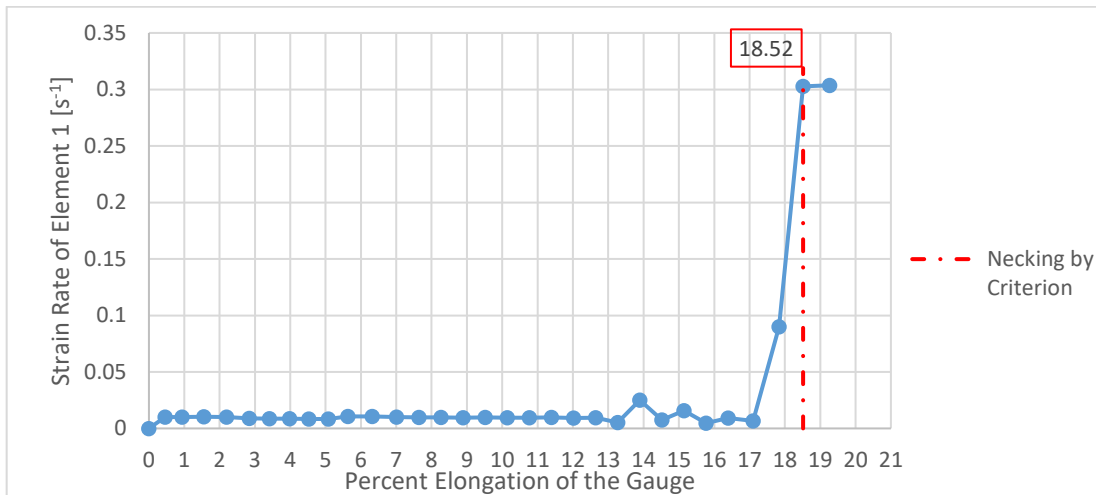


Figure 6.5. First time derivative of Element 1 strain vs. percent elongation of the gauge for straight cross-section, sheet, Al specimen

6.1.1.4. Criterion of Maximum Punch Force (TT-She-Al-Str)

Punch force vs. percent elongation of the gauge curve is plotted in this section. According to the maximum force method, the onset of necking is detected at 18.63% elongation; but, the onset of necking has been recorded at 19.20% elongation during the experiment. There is 0.57% difference in numerical and experimental results for

the same method. Consequently, maximum punch force method delivered more accurate results when compared to strain difference and strain acceleration methods.

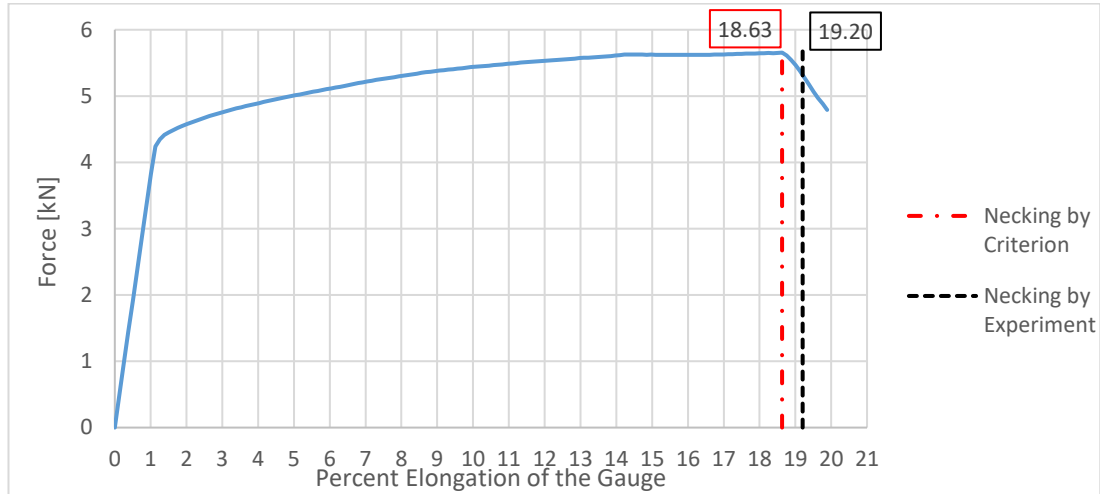


Figure 6.6. Punch force vs. percent gauge elongation of Element 100 for tapered cross-section, sheet, Al specimen (Necking at 18.63% total elongation)

6.1.2. Tapered Al2024T3 Sheet Specimen Analysis

6.1.2.1. Criterion of Equivalent Plastic Strain Increment Ratio (TT-She-Al-Tpr)

Equivalent plastic strain increment ratio method is applied on aluminum, sheet metal, tapered tensile test specimen. Several scenarios with different mesh element couples are analyzed, and they yielded quite distinguished results as depicted in Figure 6.7.

Critical ratio to remark necking is given as 10 with red dashed line. Accordingly, the onset of necking has been detected at 16.07%, 15.36%, 14.33%, 13.86% and 13.40% total percent elongations by using Elements 1 & 2, 1 & 3, 1 & 4, 1 & 5 and 1 & 6, respectively. Elements 1 & 3 presented the closest prediction to the experiment results for the onset of necking, which is at 15.28%.

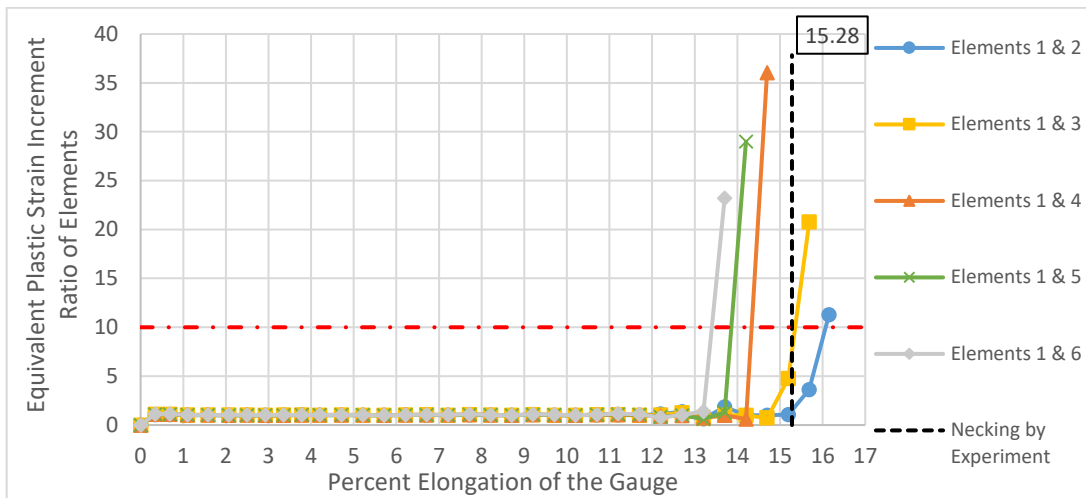


Figure 6.7. Strain increment ratios of several mesh element couples vs. percent elongation of the gauge for tapered cross-section, sheet, Al specimen

6.1.2.2. Criterion of Difference of Second Time Derivative of Equivalent Plastic Strain (TT-She-Al-Tpr)

Second temporal derivative of differences in strain for tapered aluminum sheet specimen tensile test are calculated and presented in Figure 6.8. The curves detected the onset of necking at three different elongation values, which was not the case in straight Al sheet metal specimen analysis.

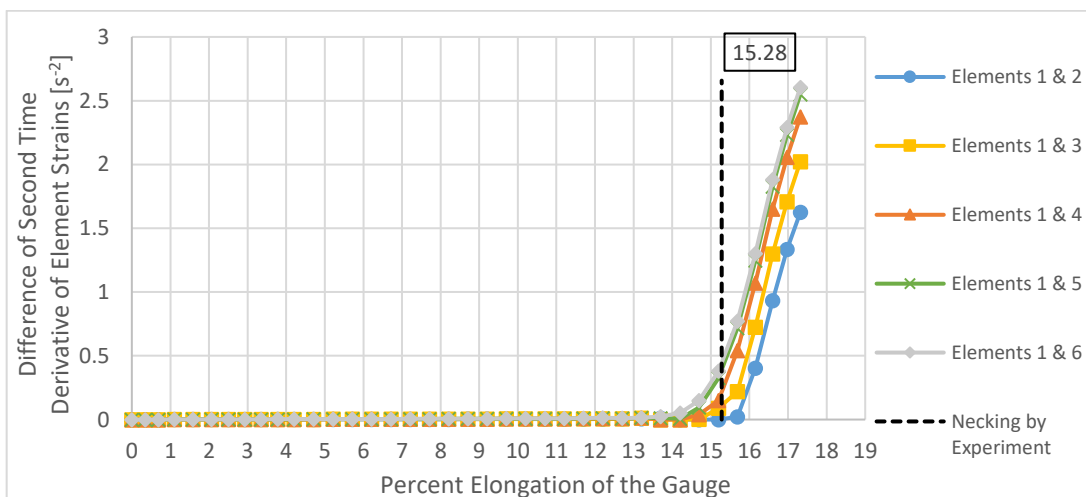


Figure 6.8. Difference of second time derivative of strain for several mesh element couples vs. percent elongation of the gauge for tapered cross-section, sheet, Al specimen

Elements 1 & 2, 1 & 3, 1 & 4, 1 & 5 and 1 & 6 predicted the onset of necking at 16.15%, 15.69%, 15.69%, 15.20% and 15.20% elongation in total gauge length in the same direction that the force applied. The most accurate predictions have been achieved by Elements 1 & 5 and 1 & 6 since the experimental result is 15.28% elongation.

6.1.2.3. Criterion of Maximum Second Time Derivative of Equivalent Plastic Strain (TT-She-Al-Tpr)

Results of strain acceleration method implemented on tapered aluminum sheet specimen tensile test is provided in Figure 6.9. This gives the onset of necking as 16.42% elongation in gauge. Experiment with the same specimen resulted in onset of necking at 15.28% elongation. Note that, some fluctuations before maximum strain acceleration point are noticed in Figure 6.9.

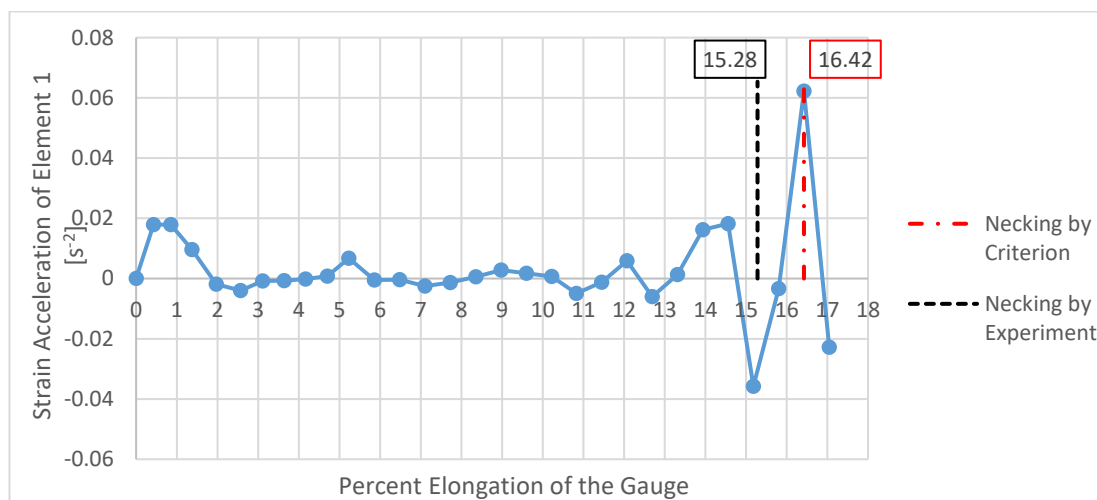


Figure 6.9. Second time derivative of Element 1 strain vs. percent elongation of the gauge for tapered cross-section, sheet, Al specimen (Necking at 16.42% total elongation)

Equivalent plastic strain and strain rate curves given in Figures 6.10 and 6.11, respectively. It is also possible to detect necking in those figures; but, the results are not as clear cut as strain acceleration graph. Thus, it is advised to guide strain acceleration plot to predict the necking instead of its different forms.

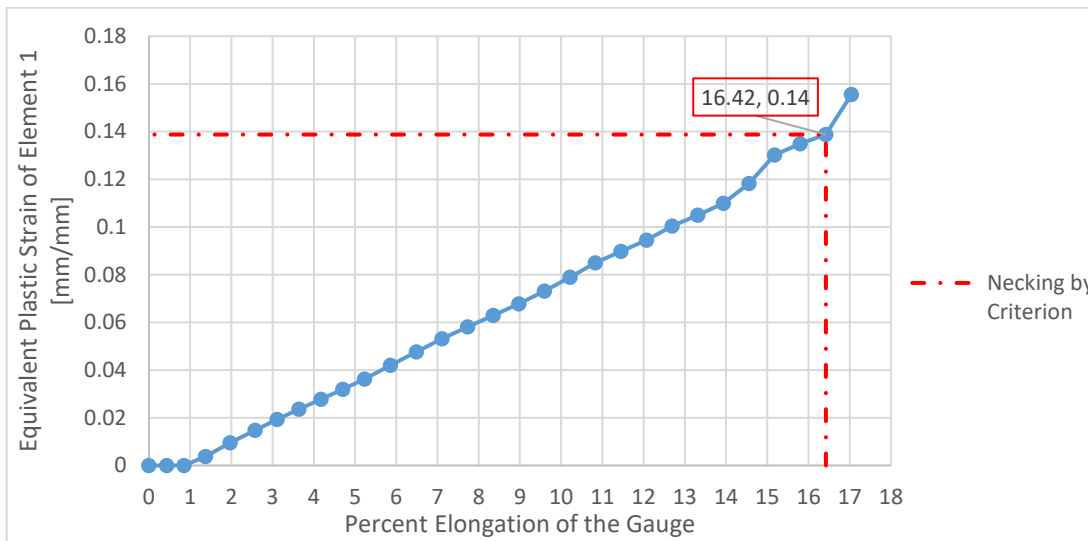


Figure 6.10. Plastic strain of Element 1 vs. percent elongation of the gauge for tapered cross-section, sheet, Al specimen

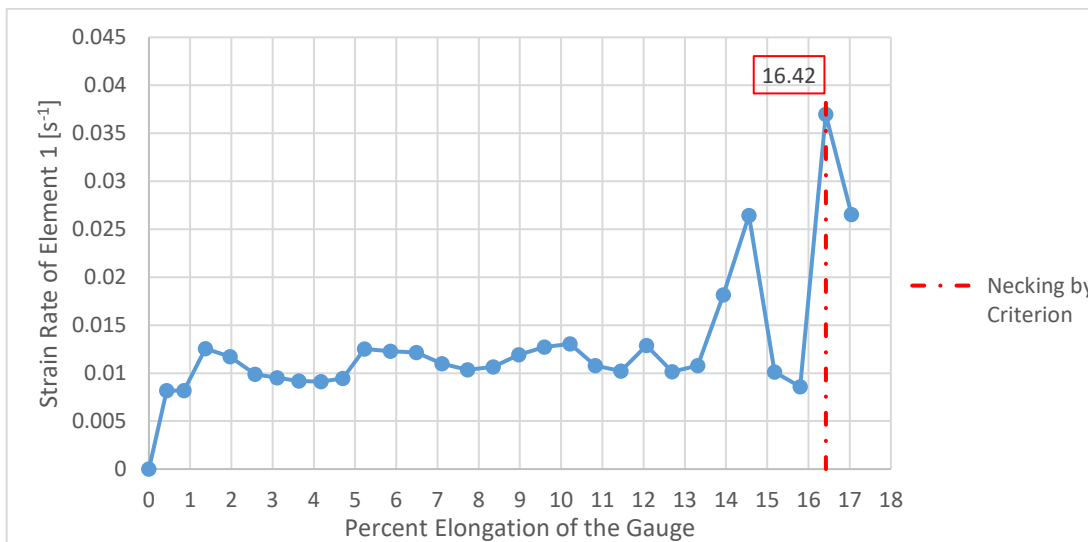


Figure 6.11. First time derivative of Element 1 strain vs. percent elongation of the gauge for tapered cross-section, sheet, Al specimen

6.1.2.4. Criterion of Maximum Punch Force (TT-She-Al-Tpr)

Punch force vs. percent elongation of the gauge data is shown in Figure 6.12. The necking obtained by the FEA and the experiment are at 16.17% and 15.28% elongation, respectively.

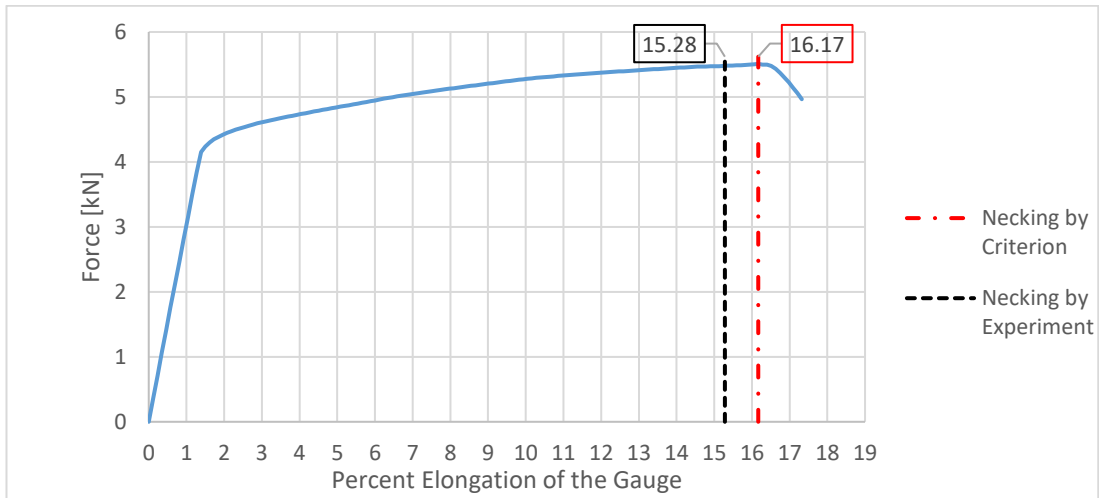


Figure 6.12. Punch force vs. percent gauge elongation of Element 100 for tapered cross-section, sheet, Al specimen (Necking at 16.17% total elongation)

Maximum force method dug out a result deviating within 1% from experimental studies, which is accepted as a good approximation.

6.1.3. Notched Al2024T3 Sheet Specimen Analysis

6.1.3.1. Criterion of Equivalent Plastic Strain Increment Ratio (TT-She-Al-Ntc)

As in straight and tapered versions, notched Al2024T3 sheet strain increment criterion for different elements delivered distinguished results as seen in Figure 6.13.

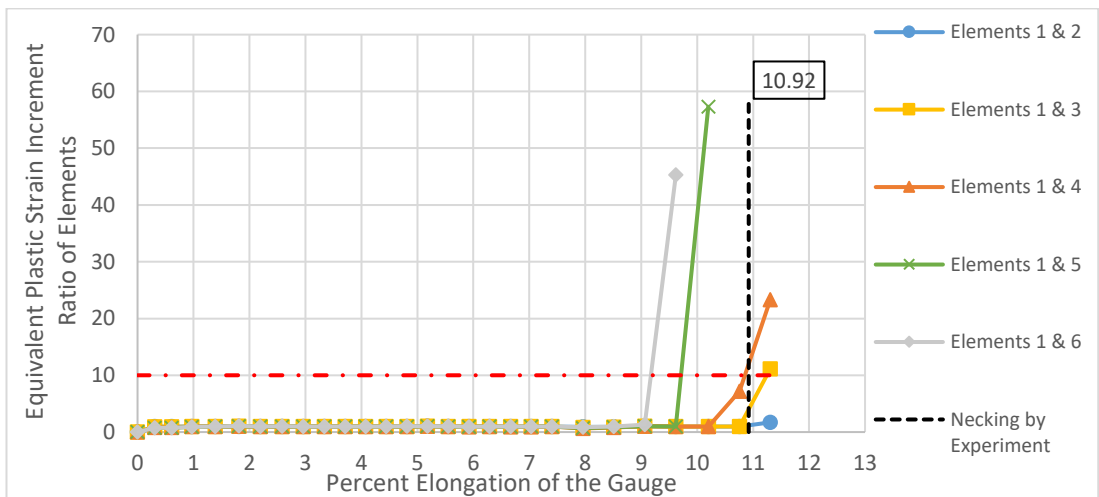


Figure 6.13. Strain increment ratios of several mesh element couples vs. percent elongation of the gauge for notched cross-section, sheet, Al specimen

The onset of necking is detected at 11.10%, 10.97%, 9.67% and 9.15% elongation by Elements 1 & 3, 1 & 4, 1 & 5 and 1 & 6, respectively. Elements 1 & 2 could not predict necking with a threshold value of 10. According to the corresponding experiment, necking commences at 10.92% elongation; thus, the most accurate prediction is performed by Elements 1 & 4.

6.1.3.2. Criterion of Difference of Second Time Derivative of Equivalent Plastic Strain (TT-She-Al-Ntc)

Quite interesting results are acquired from difference of second time derivative of equivalent plastic strain applied on sheet, Al2024T3, notched tensile test specimens. Although the curve trends are similar, all element combinations shown in Figure 6.14 perform an increase about 8.5% elongation even though the experiment points at 10.92% elongation for necking. Elements 1 & 2 does not have another significant increase trend; hence they could not determine necking initiation. On the other hand, Elements 1 & 3, 1 & 4, 1 & 5 and 1 & 6 detected the instability condition at the same value, 11.31 percent gauge elongation.

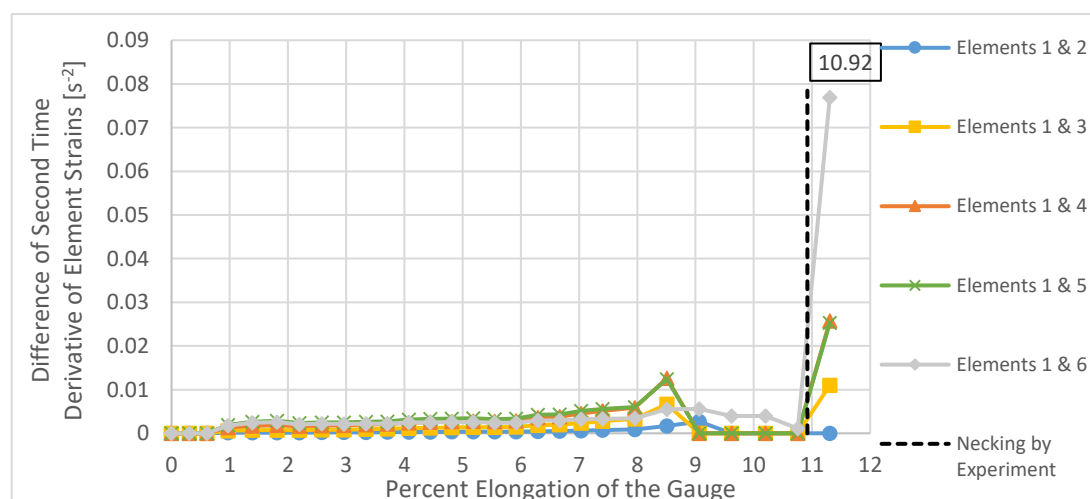


Figure 6.14. Difference of second time derivative of strain for several mesh element couples vs. percent elongation of the gauge for notched cross-section, sheet, Al specimen

6.1.3.3. Criterion of Maximum Second Time Derivative of Equivalent Plastic Strain (TT-She-Al-Ntc)

Second temporal derivative of strain plot has a peak value at 10.76% elongation. This is 0.716% close to the experimental data for necking in Figure 6.15. Moreover, the plot in Figure 6.15 has less fluctuations before the onset of necking than straight and tapered specimens of the same material. Following the onset of necking, a sharp decrease is observed.

One can also observe necking with red dashed line in Figures 6.16 and 6.17 which represent equivalent strain and equivalent strain increment rate plot, respectively. It is a coincidence that strain rate is at its maximum value when the strain acceleration is maximum (moment of necking initiation).

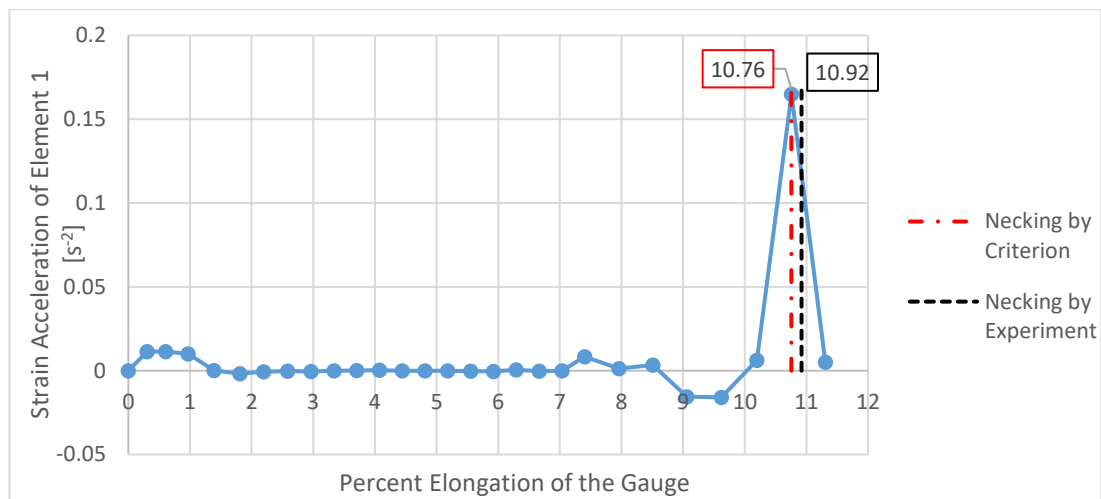


Figure 6.15. Second time derivative of Element 1 strain vs. percent elongation of the gauge for notched cross-section, sheet, Al specimen (Necking at 10.76% total elongation)

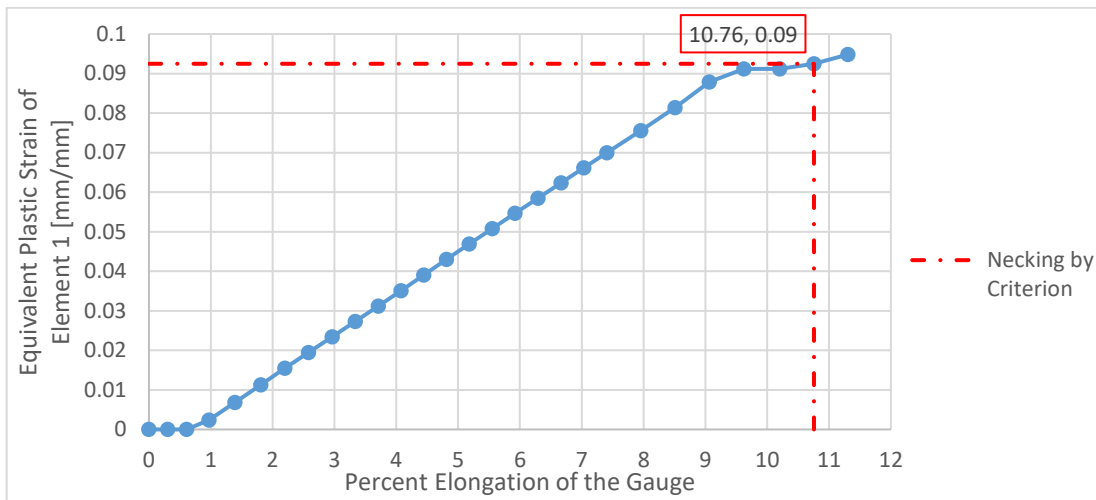


Figure 6.16. Plastic strain of Element 1 vs. percent elongation of the gauge for notched cross-section, sheet, Al specimen

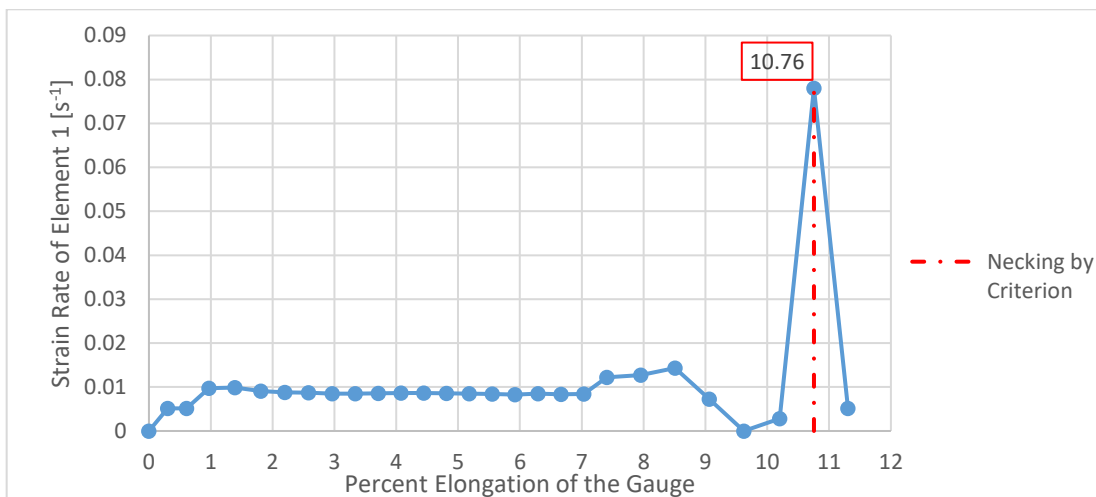


Figure 6.17. First time derivative of Element 1 strain vs. percent elongation of the gauge for notched cross-section, sheet, Al specimen

6.1.3.4. Criterion of Maximum Punch Force (TT-She-Al-Ntc)

According to punch force vs. total elongation plot illustrated in Figure 6.18, necking of tensile test experiment with Al2024T3 sheet specimen with notch occurs at 10.21% total elongation.

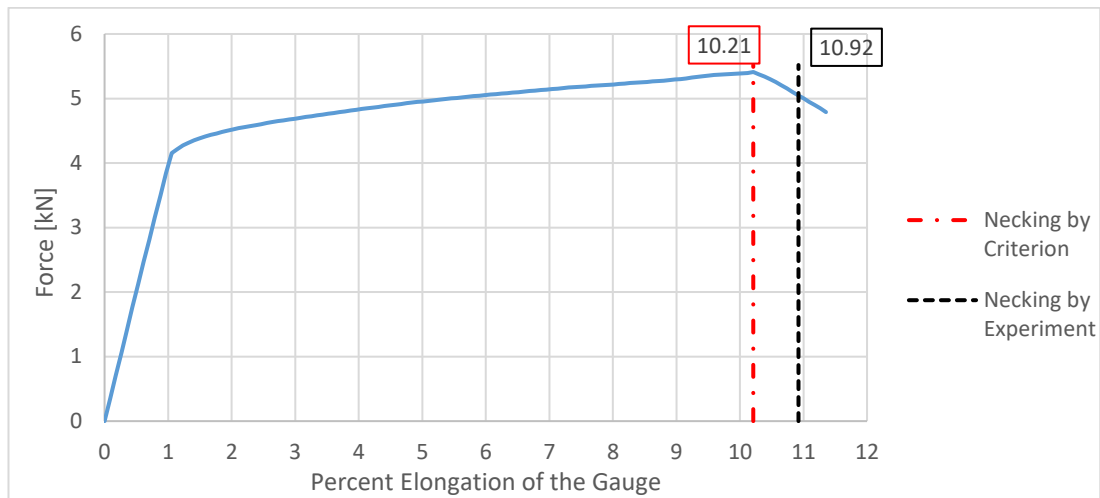


Figure 6.18. Punch force vs. percent gauge elongation of Element 100 for notched cross-section, sheet, Al specimen (Necking a 10.21% total elongation)

Note that, the specimen geometry is different due to the notch; however, the logic behind the calculation of punch force remains the same. As shown in Figure 5.15, actuation is applied on upper boundary of the domain and total punch force is calculated by summing the separate punch force values on nodes at lower boundary of the domain of interest.

6.2. FEA Results of Al2024T3 Round Specimen Tensile Tests

6.2.1. Straight Al2024T3 Round Specimen Analysis

Al2024T3 round specimens had three different geometries; namely, straight, tapered and notched. Methods are to be applied to all cases to predict onset of necking.

6.2.1.1. Criterion of Equivalent Plastic Strain Increment Ratio (TT-Ro-Al-Str)

The critical value for strain rate ratio of two separate elements is taken as 10 for cylindrical specimens, the same as in sheet metal analyses. Straight round specimen of Al2024T3 generated differentiated results for different element combinations in Figure 6.19. No element pairs could exceed the threshold of 10 and detect necking with this method. During the experiment with straight Al2024T3 round specimen, onset of necking has been recorded at 10.07% elongation.

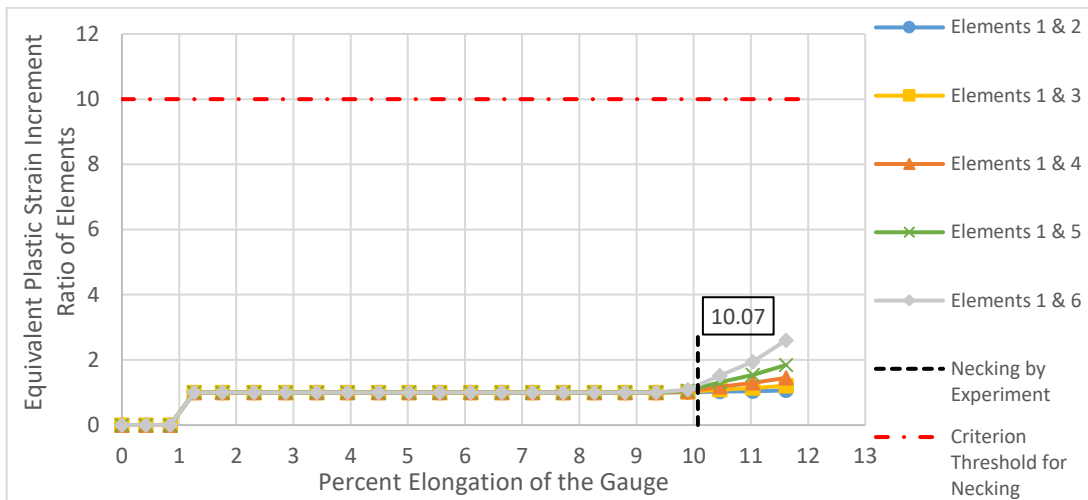


Figure 6.19. Strain increment ratios of several mesh element couples vs. percent elongation of the gauge for straight cross-section, round, Al specimen

6.2.1.2. Criterion of Difference of Second Time Derivative of Equivalent Plastic Strain (TT-Ro-Al-Str)

Difference of second time derivative of equivalent plastic strain criterion is applied to same elements as in previous method. Even though different element groups are assessed, the curves follow similar paths in Figure 6.20.

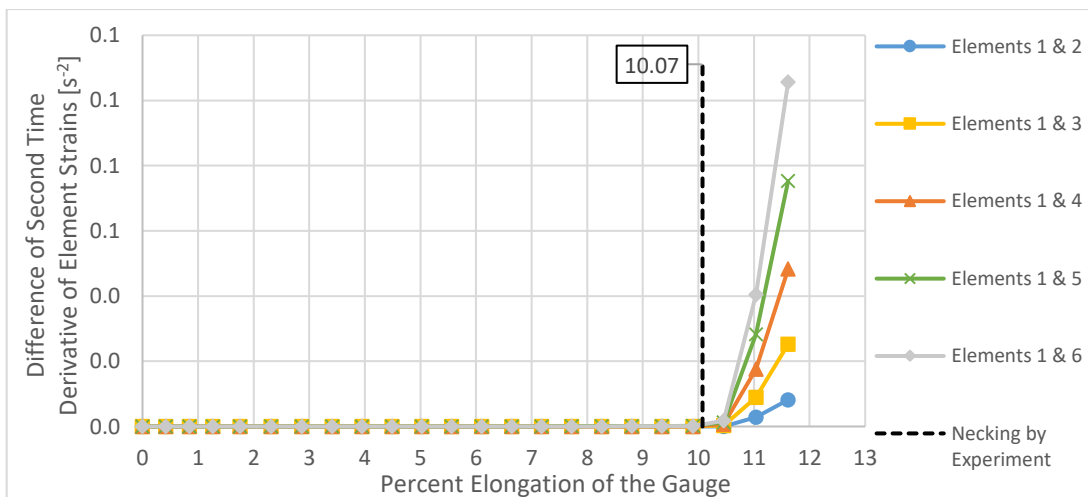


Figure 6.20. Difference of second time derivative of strain for several mesh element couples vs. percent elongation of the gauge for straight cross-section, round, Al specimen

The onset of necking is detected to be at 11.04% for all mesh element couples. Experiment results indicated that necking is recorded at 10.07%, hence, the predictions yielded by the method is within acceptable range.

6.2.1.3. Criterion of Maximum Second Time Derivative of Equivalent Plastic Strain (TT-Ro-Al-Str)

Maximum second time derivative of equivalent plastic strain criterion works on the change in strain acceleration of a single element, that is Element 1.

From Figure 6.21, necking is found to occur at 10.07% total elongation. Red dashed lines corresponding to necking are then placed at that position to investigate the behavior of the element's equivalent plastic strain and equivalent plastic strain rate graphs. Figure 6.21 starts with zero acceleration (except a small disruption at 1.26% elongation) then abruptly ascends and remarks necking.

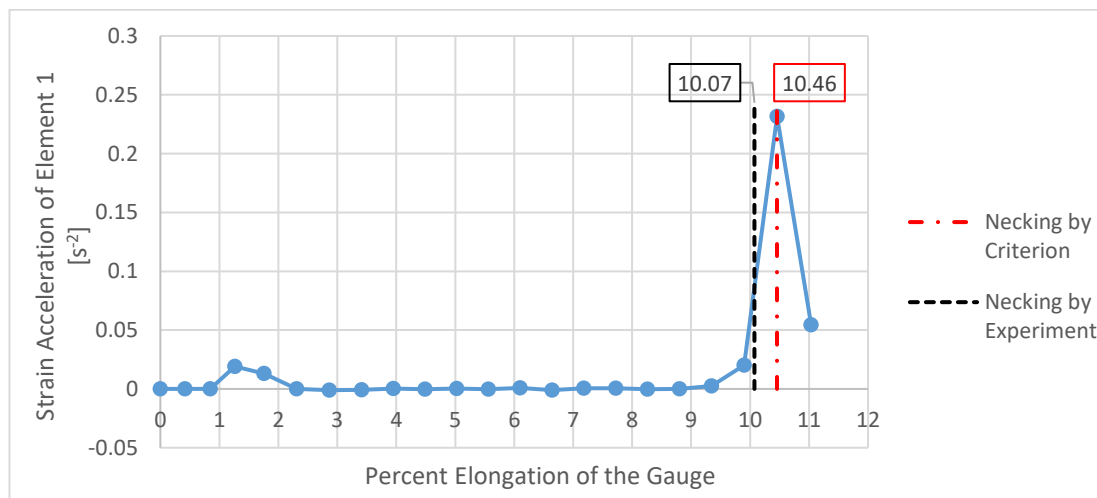


Figure 6.21. Second time derivative of Element 1 strain vs. percent elongation of the gauge for straight cross-section, round, Al specimen (Necking at 10.46% total elongation)

Strain values recorded along the process can be examined in Figure 6.22. Equivalent plastic strain value starts from zero in elastic region, then increases gradually until necking. Figure 6.23 reveals the necking with a relatively sharp change in the trend at 10.46% elongation. There is no other point where a more sudden change happens. Necking can also be observed with a sharp change in the strain rate curve trend.

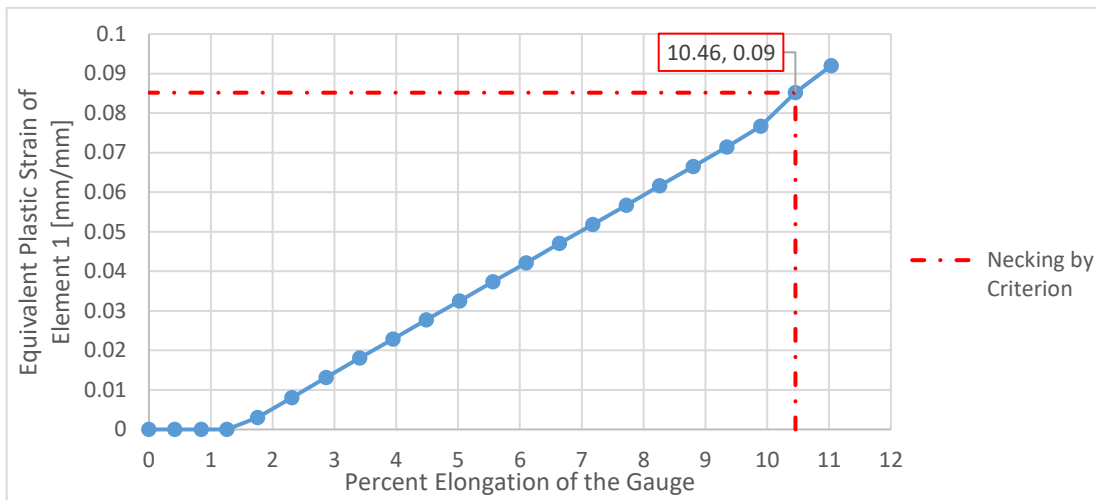


Figure 6.22. Plastic strain of Element 1 vs. percent elongation of the gauge for straight cross-section, round, Al specimen

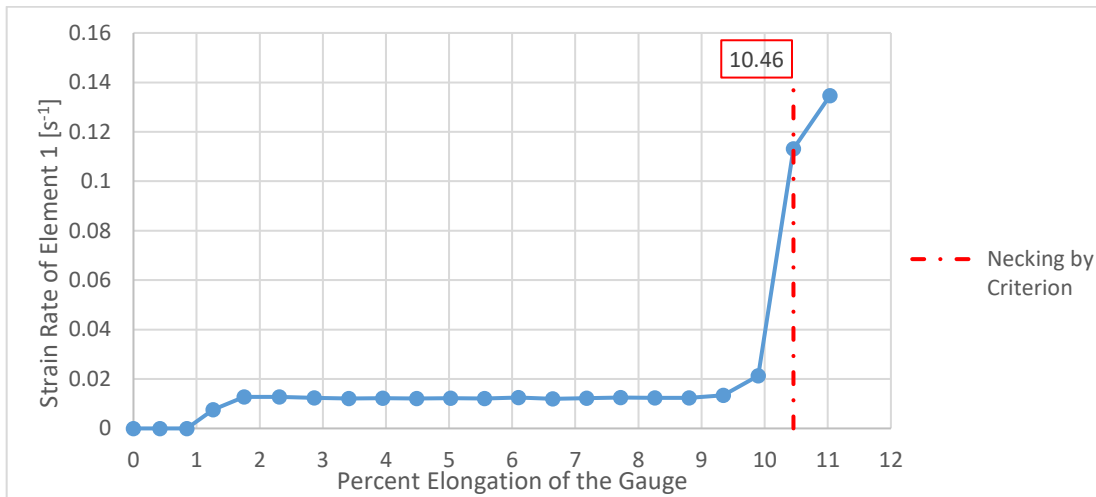


Figure 6.23. First time derivative of Element 1 strain vs. percent elongation of the gauge for straight cross-section, round, Al specimen

6.2.1.4. Criterion of Maximum Punch Force (TT-Ro-Al-Str)

Figure 6.24 depicts the change in punch force with respect to elongation quantities. The displacement is measured on Element 100 in Figure 5.5(b). Necking occurs at total elongation of 11.06% and 10.07% according to FEA and the experiment results, respectively. The accuracy of the method is good; but, overestimates the initiation of necking.

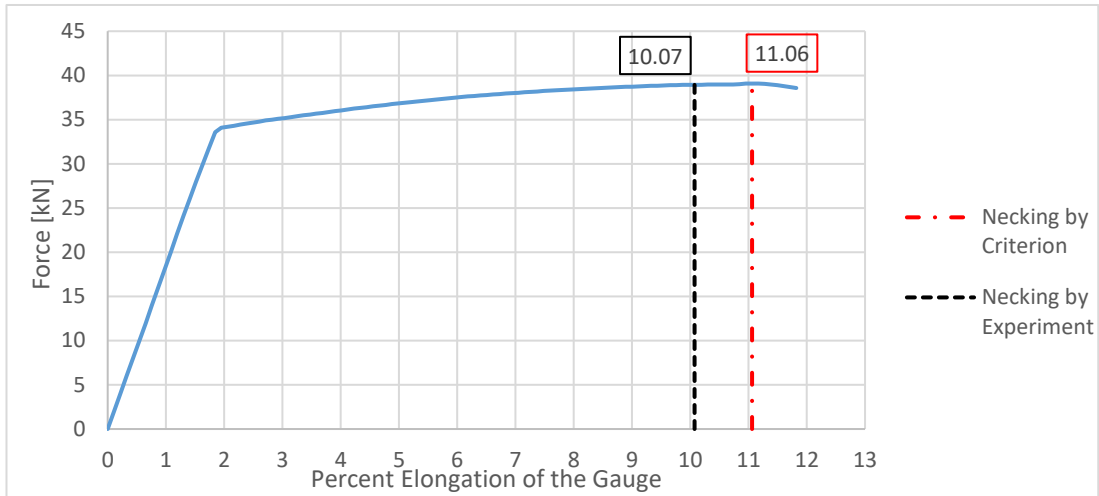


Figure 6.24. Punch force vs. percent gauge elongation of Element 100 for straight cross-section, round, Al specimen (Necking at 11.06% total elongation)

6.2.2. Tapered Al2024T3 Round Specimen Analysis

6.2.2.1. Criterion of Equivalent Plastic Strain Increment Ratio (TT-Ro-Al-Tpr)

Equivalent plastic strain rate ratio method is used on round, tapered, aluminum specimen and results are presented in Figure 6.25. The method could not detect necking by reaching the threshold 10 during FEA. Experiment result is 8.22%.

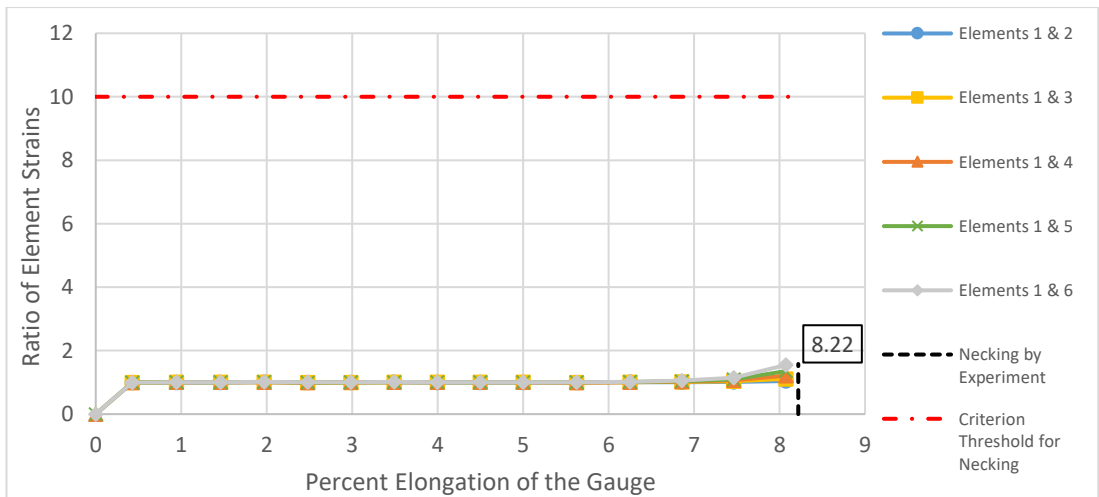


Figure 6.25. Strain increment ratios of several mesh element couples vs. percent elongation of the gauge for tapered cross-section, round, Al specimen

6.2.2.2. Criterion of Difference of Second Time Derivative of Equivalent Plastic Strain (TT-Ro-Al-Tpr)

The curves comparing the differences of equivalent plastic strain accelerations of separate elements follow consistent courses as can be seen in Figure 6.26.

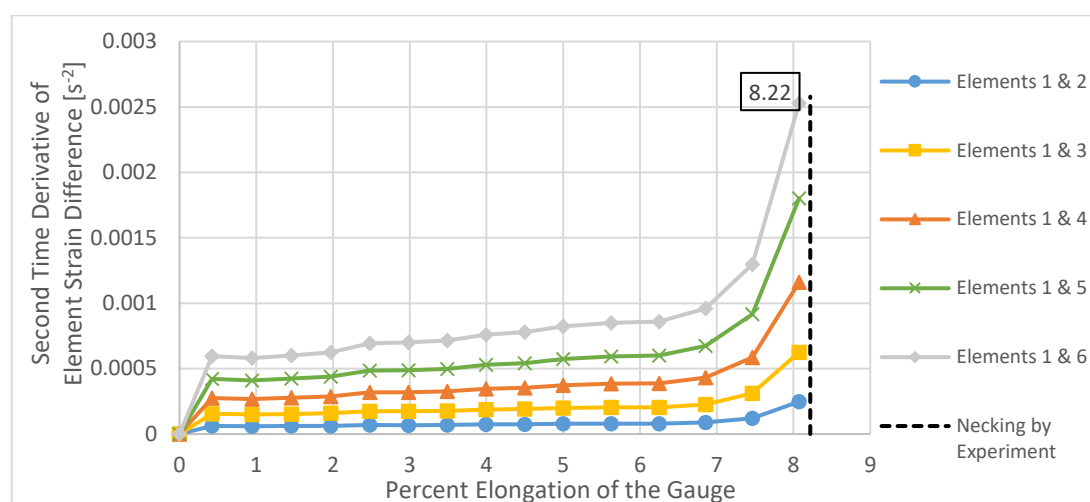


Figure 6.26. Difference of second time derivative of strain for several mesh element couples vs. percent elongation of the gauge for tapered cross-section, round, Al specimen

All the element couples predict the onset of necking at 7.46% elongation of the gauge length. Necking elongation determined by experiment is 8.22.

6.2.2.3. Criterion of Maximum Second Time Derivative of Equivalent Plastic Strain (TT-Ro-Al-Tpr)

Maximum strain acceleration value is achieved at total elongation of 6.96% in Figure 6.27. That value is remarked in element equivalent plastic strain (Figure 6.28) and first temporal derivative of equivalent plastic strain (Figure 6.29) graphs.

Element equivalent plastic strain acceleration method substantially underestimates necking when the corresponding experimental result is taken into consideration in Figure 6.27.

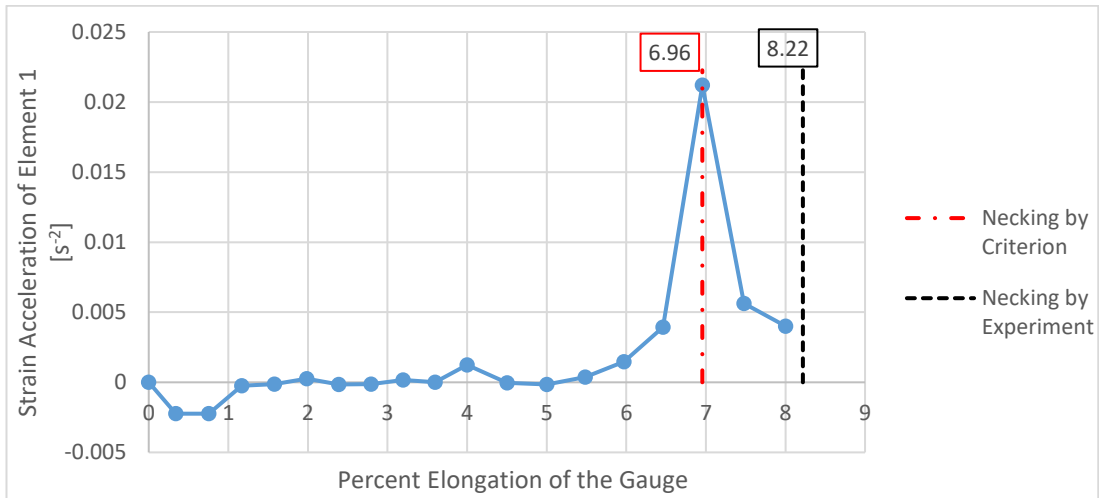


Figure 6.27. Second time derivative of Element 1 strain vs. percent elongation of the gauge for tapered cross-section, round, Al specimen (Necking 6.96% total elongation)

The sudden changes in plot trends are clearly observed in Figures 6.28 and 6.29.

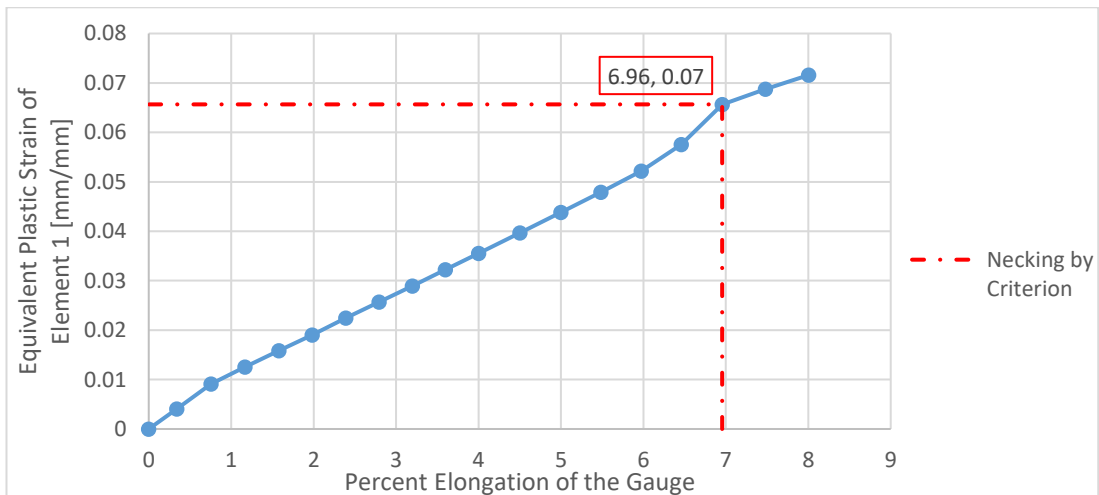


Figure 6.28. Plastic strain of Element 1 vs. percent elongation of the gauge for tapered cross-section, round, Al specimen

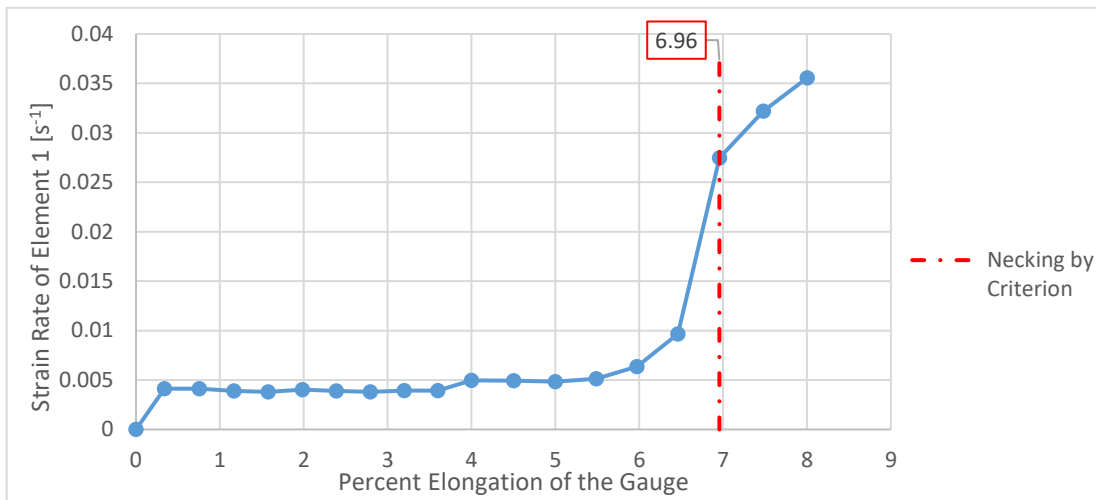


Figure 6.29. First time derivative of Element 1 strain vs. percent elongation of the gauge for tapered cross-section, round, Al specimen

6.2.2.4. Criterion of Maximum Punch Force (TT-Ro-Al-Tpr)

Punch force vs. percent elongation data are presented in Figure 6.30. The method confirms that necking occurs at 7.69% total elongation.

The onset of necking has been detected by experiment at 8.22% elongation value. FEA results of maximum force method accurately estimated the necking initiation.

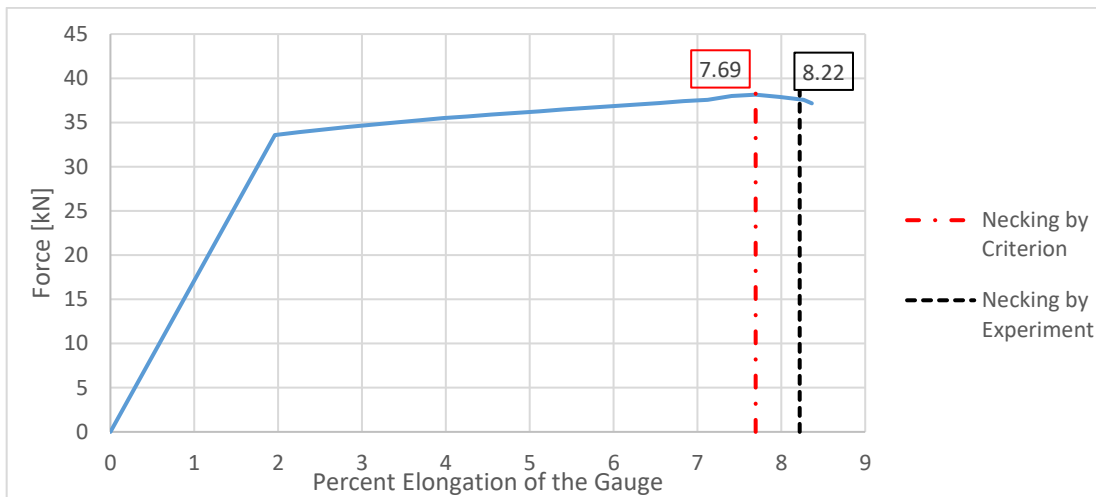


Figure 6.30. Punch force vs. percent gauge elongation of Element 839 for tapered cross-section, round, Al specimen (Necking at 7.69% total elongation)

6.2.3. Notched Al2024T3 Round Specimen Analysis

6.2.3.1. Criterion of Equivalent Plastic Strain Increment Ratio (TT-Ro-Al-Ntc)

Elements 1 & 2, 1 & 3, 1 & 4, 1 & 5 and 1 & 6 fail to recognize onset of necking for tensile test of notched aluminum rod-type specimen for strain rate ratio method. This can also be seen in Figure 6.29. Experiment result for necking is at 4.86% elongation.

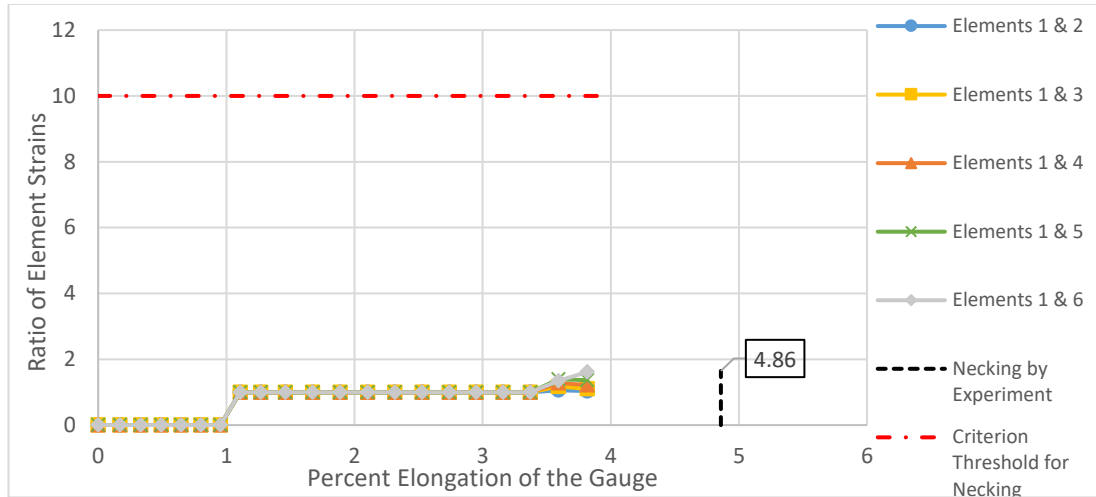


Figure 6.31. . Strain increment ratios of several mesh element couples vs. percent elongation of the gauge for notched cross-section, round, Al specimen

6.2.3.2. Criterion of Difference of Second Time Derivative of Equivalent Plastic Strain (TT-Ro-Al-Ntc)

Difference of second time derivative of equivalent plastic strain method curves follow a route depicted in Figure 6.32. Percent elongation values are realized at 3.59 by all element pairs employed for the method. The results from the experiment is 4.86%.

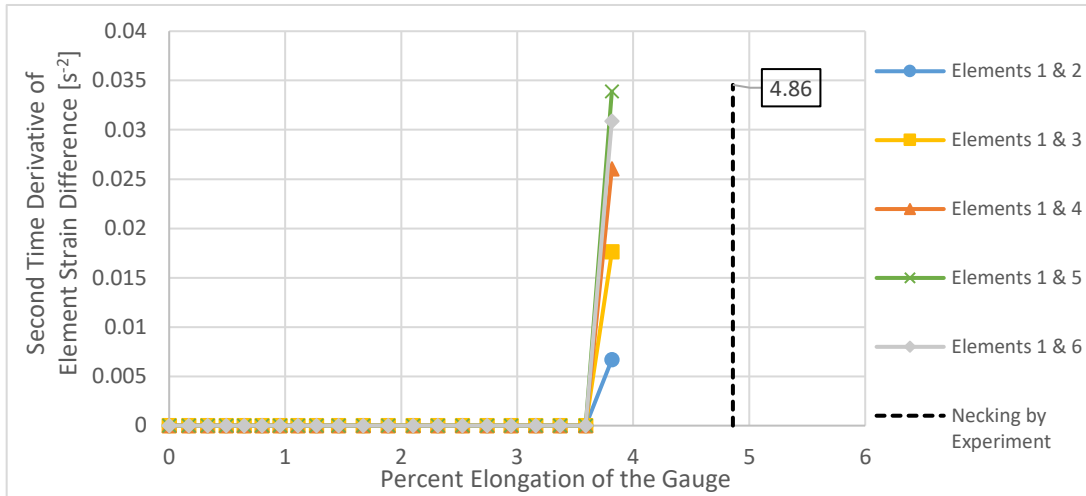


Figure 6.32. Difference of second time derivative of strain for several mesh element couples vs. percent elongation of the gauge for notched cross-section, round, Al specimen

6.2.3.3. Criterion of Maximum Second Time Derivative of Equivalent Plastic Strain (TT-Ro-Al-Ntc)

Maximum second temporal derivative of strain is utilized to predict necking in Figure 6.33. Commencement of necking is determined to be at elongation quantity of 3.51%. This value is marked with red dashed lines in equivalent plastic strain vs. total elongation (Figure 6.34) and equivalent plastic strain rate vs. total elongation (Figure 6.35) plots. Difference between the FEA and experiment predictions is 1.35%.

Plastic strain curve in Figure 6.34 exhibits similar trends that has been encountered in previous section.

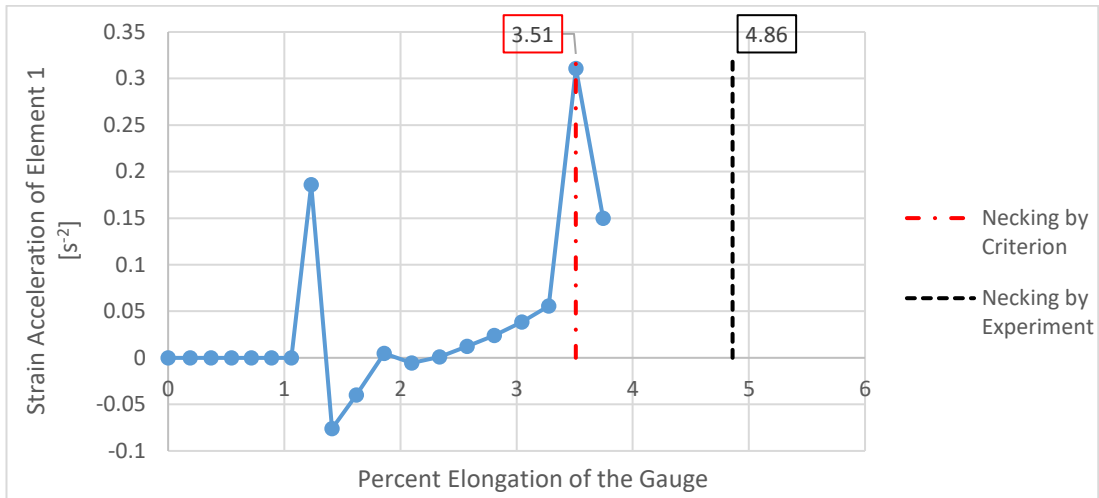


Figure 6.33. Second time derivative of Element 1 strain vs. percent elongation of the gauge for notched cross-section, round, Al specimen (Necking 3.51% elongation)

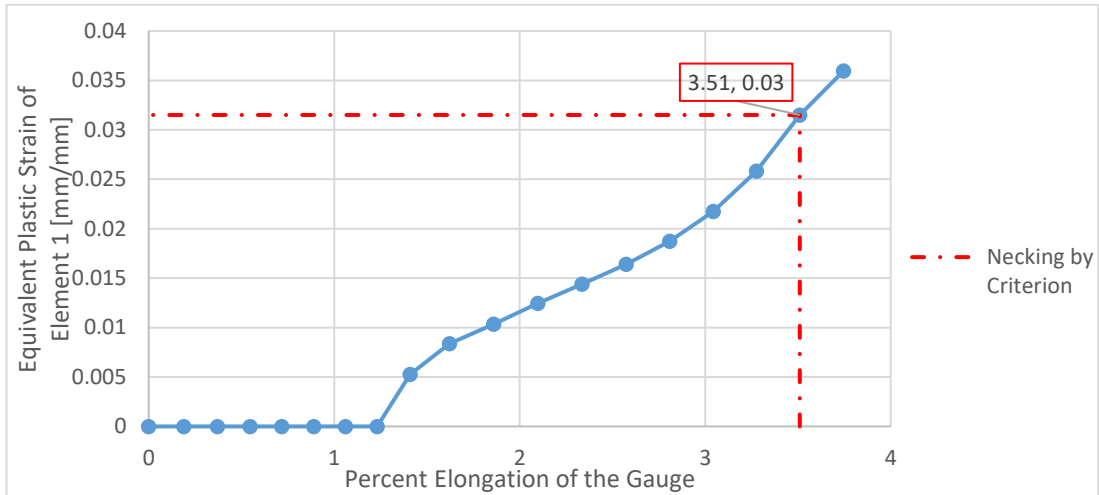


Figure 6.34. Plastic strain of Element 1 vs. percent elongation of the gauge for notched cross-section, round, Al specimen

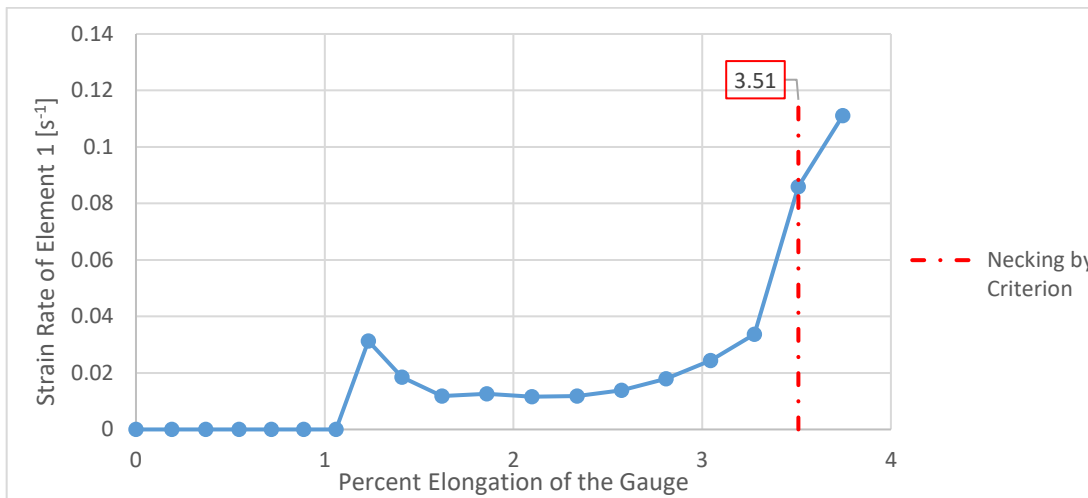


Figure 6.35. First time derivative of Element 1 strain vs. percent elongation of the gauge for notched cross-section, round, Al specimen

6.2.3.4. Criterion of Maximum Punch Force (TT-Ro-Al-Ntc)

Punch force vs. total elongation plot for notched specimen analysis of round aluminum tensile test specimen is presented in Figure 6.36. Considering the experiment gave the necking at 4.86%, FEA results for maximum force criterion are not at desired accuracy level.

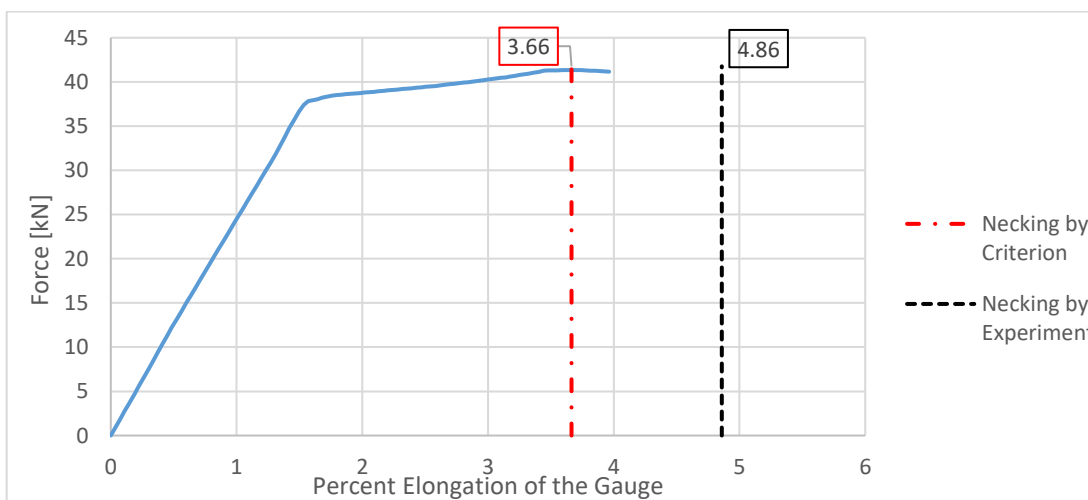


Figure 6.36. Punch force vs. percent gauge elongation of Element 916 for notched cross-section, round, Al specimen (Necking at 3.66% total elongation)

6.3. FEA Results of S235JR Sheet Specimen Tensile Tests

6.3.1. Straight S235JR Sheet Specimen Analysis

S235JR sheet specimens had three different geometries; namely, straight, tapered and notched. Methods are to be applied to all cases to predict onset of necking.

6.3.1.1. Criterion of Equivalent Plastic Strain Increment Ratio (TT-She-St-Str)

Equivalent plastic strain rate ratio method on straight S235JR sheet specimen tensile test FEA gives consistent results in Figure 6.37. Elements of 1 & 2, 1 & 3, 1 & 4, 1 & 5 and 1 & 6 identified necking at 16.74%, 16.60%, 16.41%, 16.20% and 16.09% total gauge elongation, respectively.

All the element pairs underestimated the necking as the experiment remarked it at 18.00% elongation of the gauge.

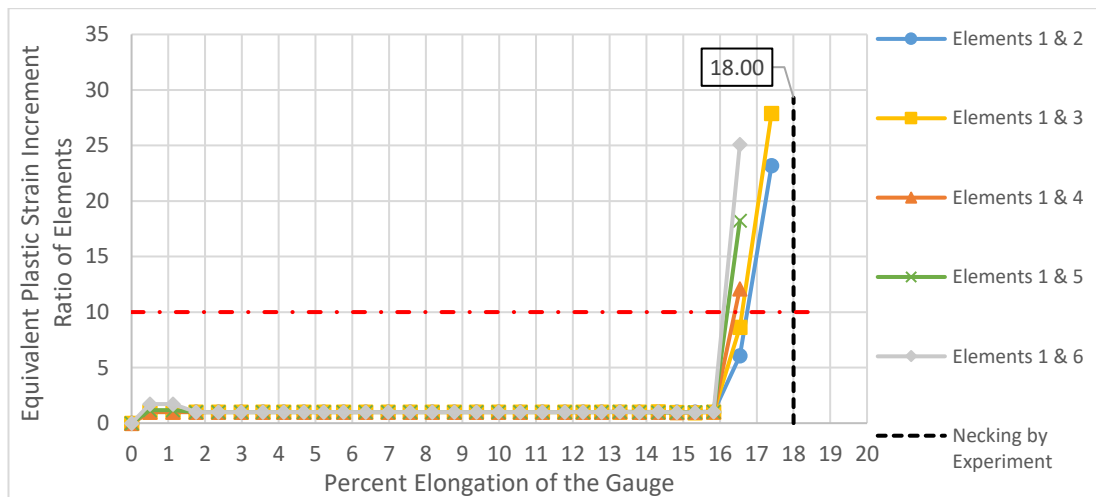


Figure 6.37. Strain increment ratios of several mesh element couples vs. percent elongation of the gauge for straight cross-section, sheet, steel specimen

6.3.1.2. Criterion of Difference of Second Time Derivative of Equivalent Plastic Strain (TT-She-St-Str)

Difference of second time derivative of equivalent plastic strain criterion generates the same result with all element combinations shown in Figure 6.38. The necking is predicted to start at 17.40% for all cases and the plots are highly consistent and

precise. The experimental value for necking is 18.00%; so, a good approximation is succeeded by using this method.

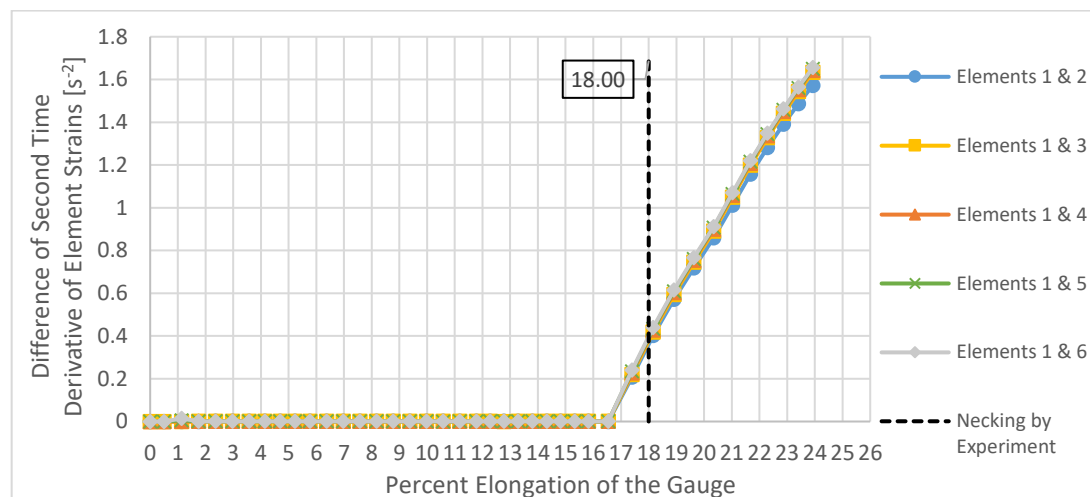


Figure 6.38. Difference of second time derivative of strain for several mesh element couples vs. percent elongation of the gauge for straight cross-section, sheet, steel specimen

6.3.1.3. Criterion of Maximum Second Time Derivative of Equivalent Plastic Strain (TT-She-St-Str)

Maximum second time derivative of equivalent plastic strain criterion is based on the total elongation value obtained when second temporal derivative of equivalent strain change is the highest.

The onset of necking is found to be at 16.54% total gauge elongation in Figure 6.39 and marked in Figures 6.40 and 6.41 with red dashed line for comparison purposes. Also note that necking measured during the experiment is marked at 18.00% elongation.

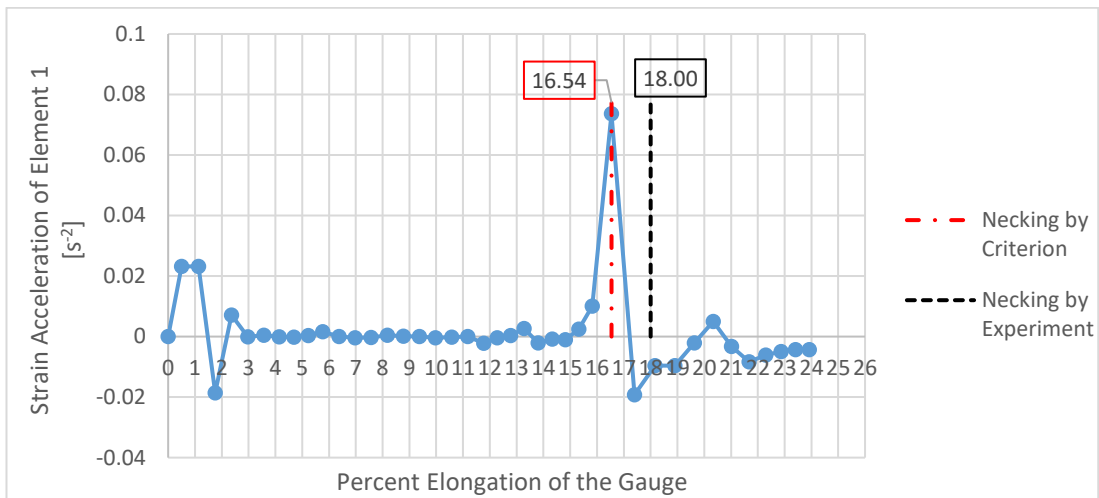


Figure 6.39. Second time derivative of Element 1 strain vs. percent elongation of the gauge for straight cross-section, sheet, steel specimen (Necking at 16.54% total elongation)

The course of equivalent plastic strain graph demonstrated in Figure 6.40 is also similar to the previous outputs. Nonetheless, another abrupt drop is observed in Figure 6.41 after highest value of strain rate is attained.

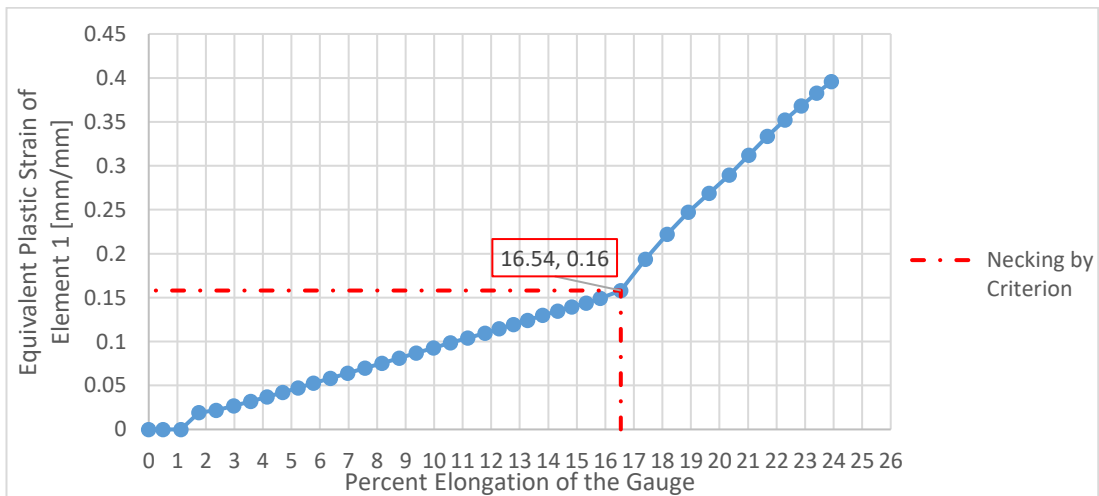


Figure 6.40. Plastic strain of Element 1 vs. percent elongation of the gauge for straight cross-section, sheet, steel specimen

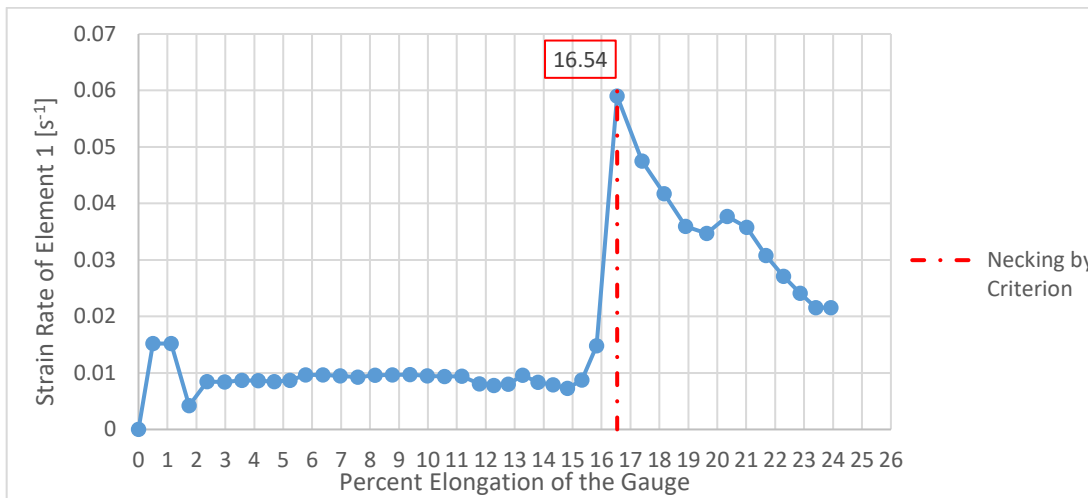


Figure 6.41. First time derivative of Element 1 strain vs. percent elongation of the gauge for straight cross-section, sheet, steel specimen

6.3.1.4. Criterion of Maximum Punch Force (TT-She-St-Str)

The curve in Figure 6.42 depicts the force vs. percent elongation behavior of straight round S235JR specimen tensile test. The onset of necking is detected at 17.34% total elongation. Elongation of 18.00% is obtained by experiment; thus, force method approximation is accurate.

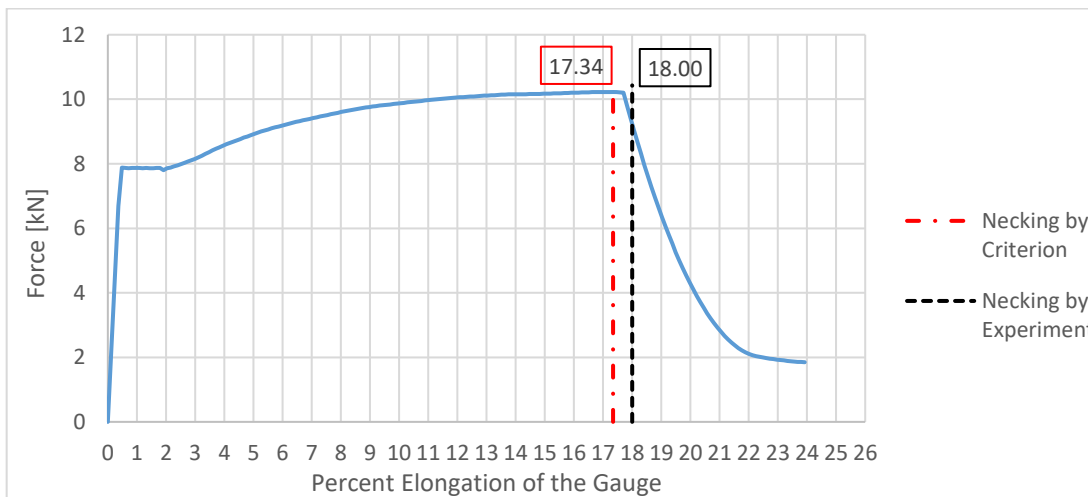


Figure 6.42. Punch force vs. percent gauge elongation of Element 100 for straight cross-section, sheet, steel specimen (Necking at 17.34% total elongation)

6.3.2. Tapered S235JR Sheet Specimen Analysis

6.3.2.1. Criterion of Equivalent Plastic Strain Increment Ratio (TT-She-St-Tpr)

Steel tapered sheet specimens yielded highly consistent results, which are presented in Figure 6.43. Ratio analysis on Elements 1 & 2, 1 & 3, 1 & 4, 1 & 5 and 1 & 6 uncovered necking at 13.94, 13.25, 13.23, 13.19 and 13.18 elongation for the threshold of 10, respectively. However, the result underestimate the necking since the experiment records specify necking at 16.83% elongation.

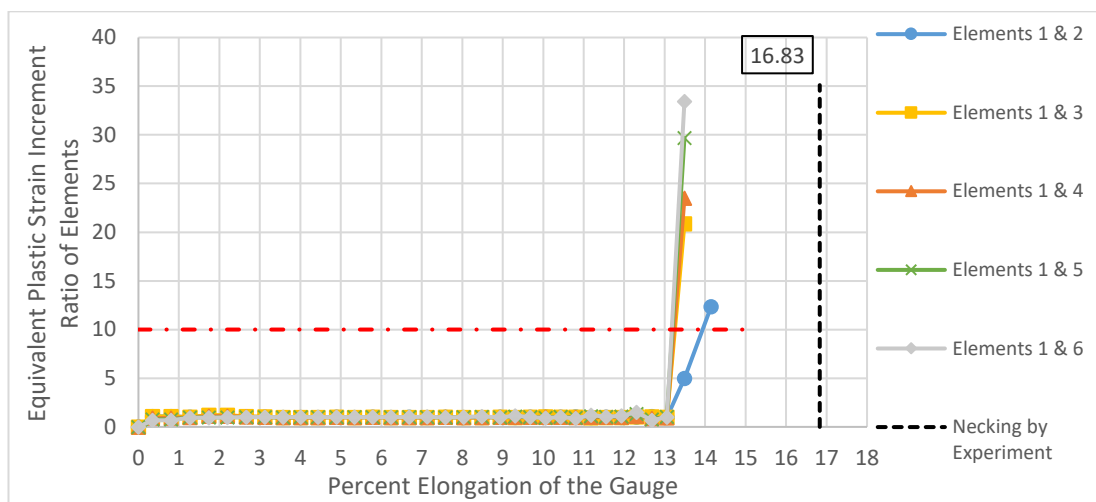


Figure 6.43. Strain increment ratios of several mesh element couples vs. percent elongation of the gauge for tapered cross-section, sheet, steel specimen

6.3.2.2. Criterion of Difference of Second Time Derivative of Equivalent Plastic Strain (TT-She-St-Tpr)

In Figure 6.44, analysis by difference of strain acceleration displayed similar trends as in previous sections.

The plot kept insignificantly low values at the start and then after an abrupt increase is followed. The experiment result for the onset of necking is 16.83%. The prediction of 14.15 percent elongation belongs to all pairs of mesh elements.

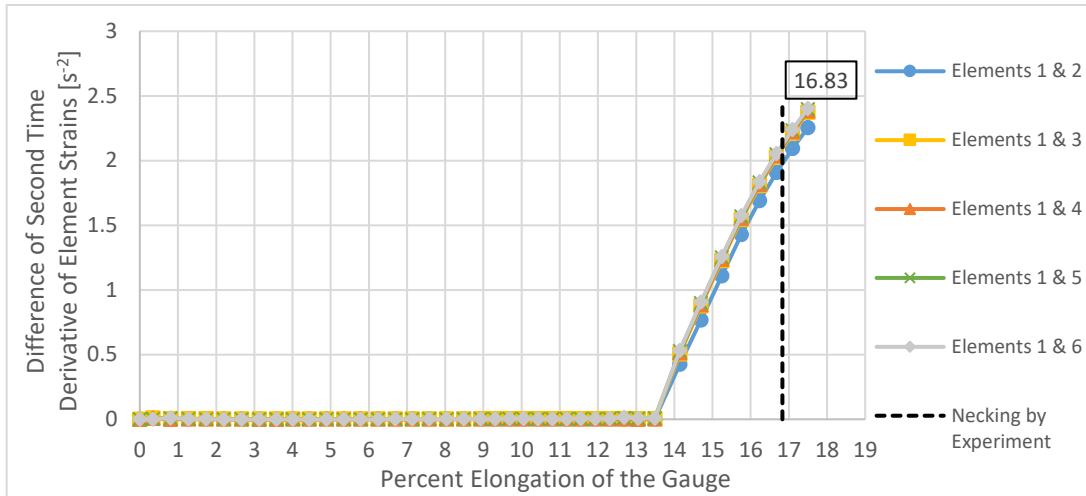


Figure 6.44. Difference of second time derivative of strain for several mesh element couples vs. percent elongation of the gauge for tapered cross-section, sheet, steel specimen

6.3.2.3. Criterion of Maximum Second Time Derivative of Equivalent Plastic Strain (TT-She-St-Tpr)

Second temporal derivative of strain increment on Element 1 is highest at 16.05% total elongation as indicated in Figure 6.45. This value is also traced in other figures of this subsection with red dashed line. Note that experiment result is 16.83%, that means the deviation is 3.34%. and the method made a poor prediction.

It can be stated that strain vs. total elongation (Figure 6.46), strain rate vs. total elongation (Figure 6.47) and strain acceleration vs. total elongation (Figure 6.45) exhibited similar traits like those of straight specimen analyses.

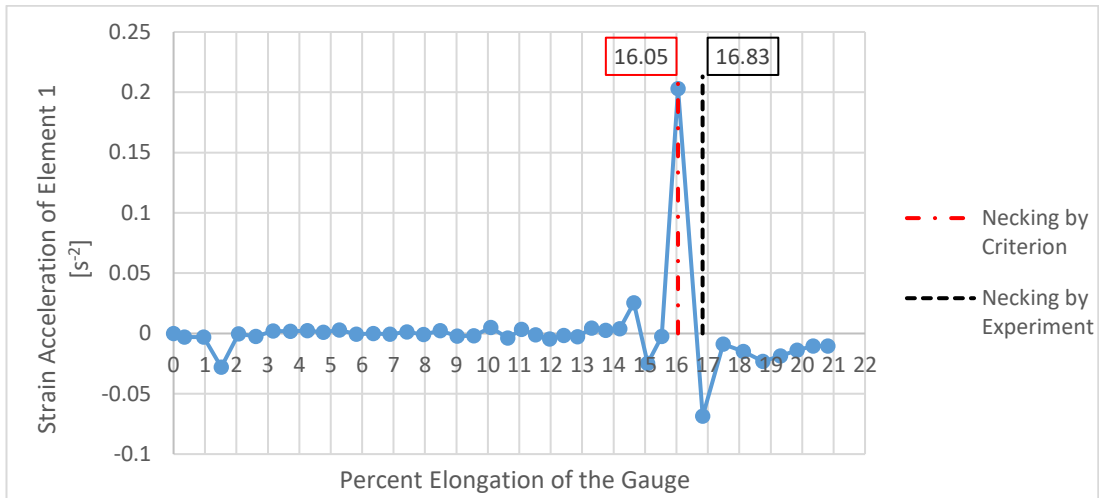


Figure 6.45. Second time derivative of Element 1 strain vs. percent elongation of the gauge for tapered cross-section, sheet, steel specimen (Necking at 16.05% total elongation)

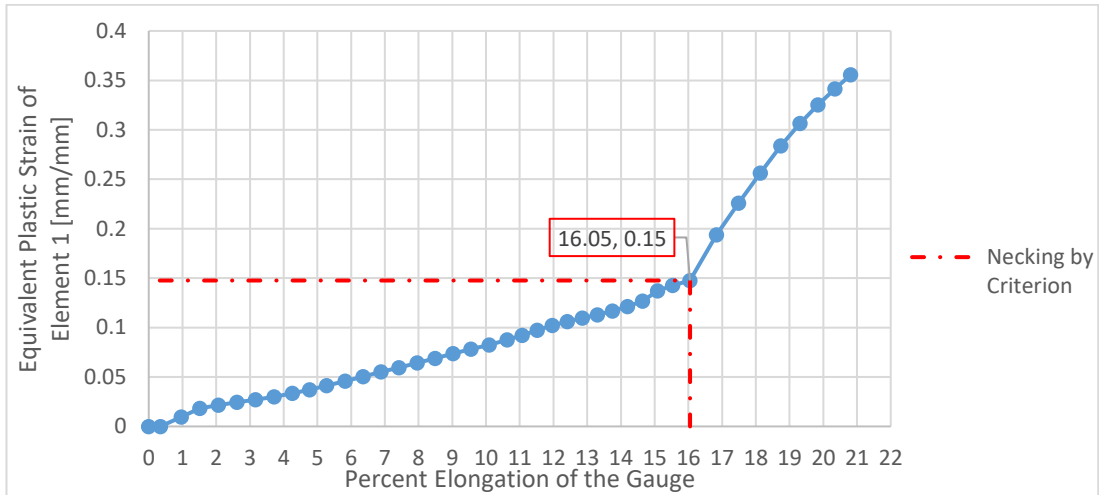


Figure 6.46. Plastic strain of Element 1 vs. percent elongation of the gauge for tapered cross-section, sheet, steel specimen

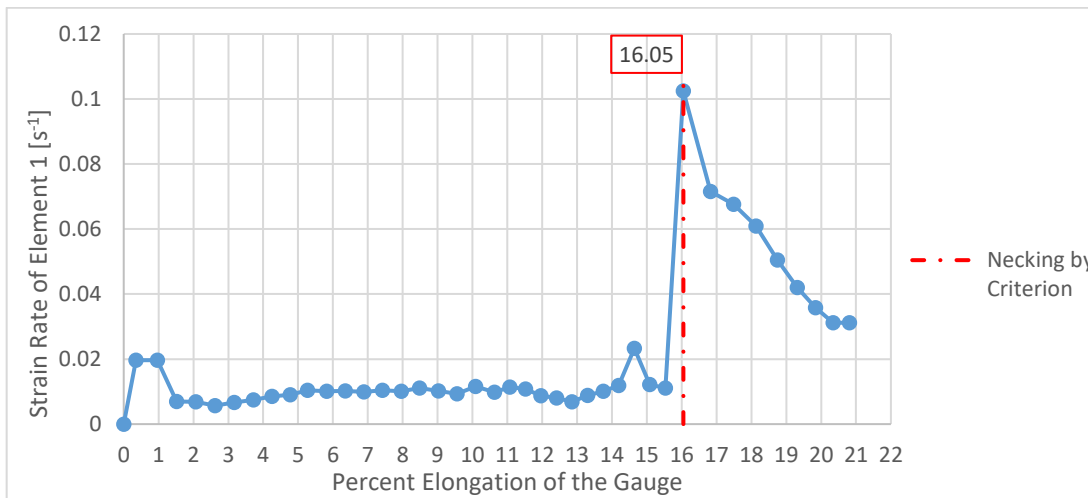


Figure 6.47 First time derivative of Element 1 strain vs. percent elongation of the gauge for tapered cross-section, sheet, steel specimen.

6.3.2.4. Criterion of Maximum Punch Force (TT-She-St-Tpr)

Punch force over percent elongation of the gauge for tapered cross-section, sheet, S235JR specimen reached its peak at 14.17% elongation in Figure 6.48.

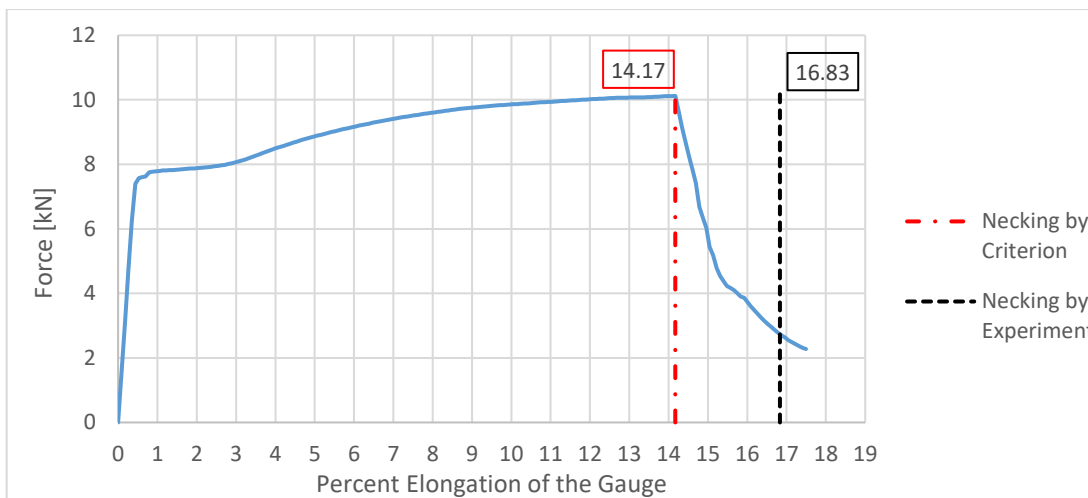


Figure 6.48. Punch force vs. percent gauge elongation of Element 100 for tapered cross-section, sheet, steel specimen (Necking at 14.17% total elongation)

The prediction value is 2.66% below the experimental output.

6.3.3. Notched S235JR Sheet Specimen Analysis

6.3.3.1. Criterion of Equivalent Plastic Strain Increment Ratio (TT-She-St-Ntc)

Equivalent plastic strain rate ratio analysis displayed quite interesting outputs in Figure 6.49. Elements 1 & 5 reached 9.4 ratio at the beginning of the process, a gauge elongation of 0.34%.

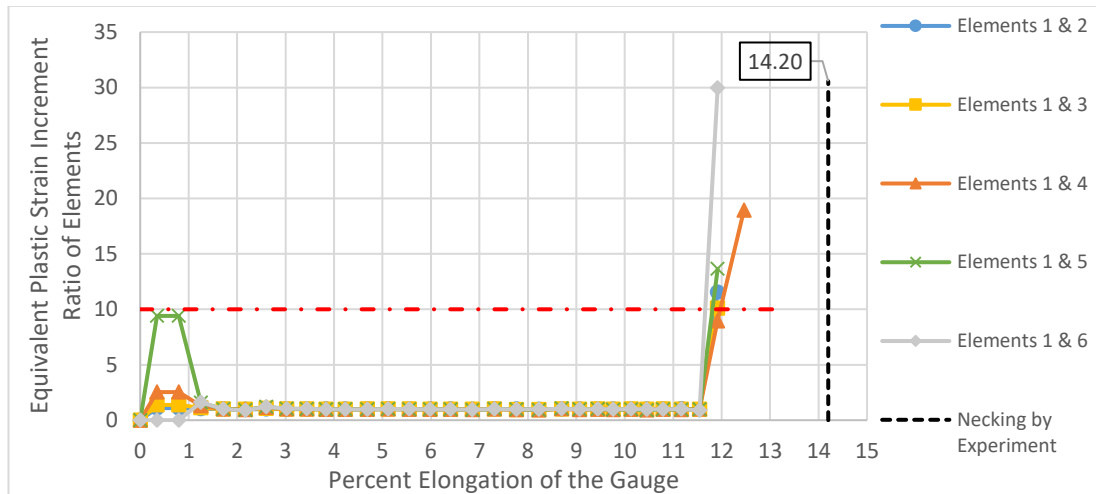


Figure 6.49. Strain increment ratios of several mesh element couples vs. percent elongation of the gauge for notched cross-section, sheet, steel specimen

Numerical methods such as the current case can imply unusual results at boundaries. The strains are very small at this moment as can be seen in Figure 6.52. Even though the absolute values are very low, the ratios can be high. Analysts should treat the boundaries with special focus.

Ratio of equivalent plastic strain increment method applied on Elements 1 & 2, 1 & 3, 1 & 4, 1 & 5 and 1 & 6 resulted in necking at 11.86%, 11.91%, 11.97%, 11.81% and 11.66%, respectively. The results underestimated necking since the experiment marked it at 14.20% total gauge elongation. Elements 1 & 4 gave the closest approximation.

6.3.3.2. Criterion of Difference of Second Time Derivative of Equivalent Plastic Strain (TT-She-St-Ntc)

Figure 6.50 shows the second temporal derivative of strain difference of separate elements. Different element pairs are yielded very close results as in straight and notched counterparts. Percent elongation value of 12.46% has been obtained by Elements 1 & 2, 1 & 3, 1 & 4, 1 & 5 and 1 & 6. Since the experiment result marks necking at 14.20%, strain difference method has acquired poor results.

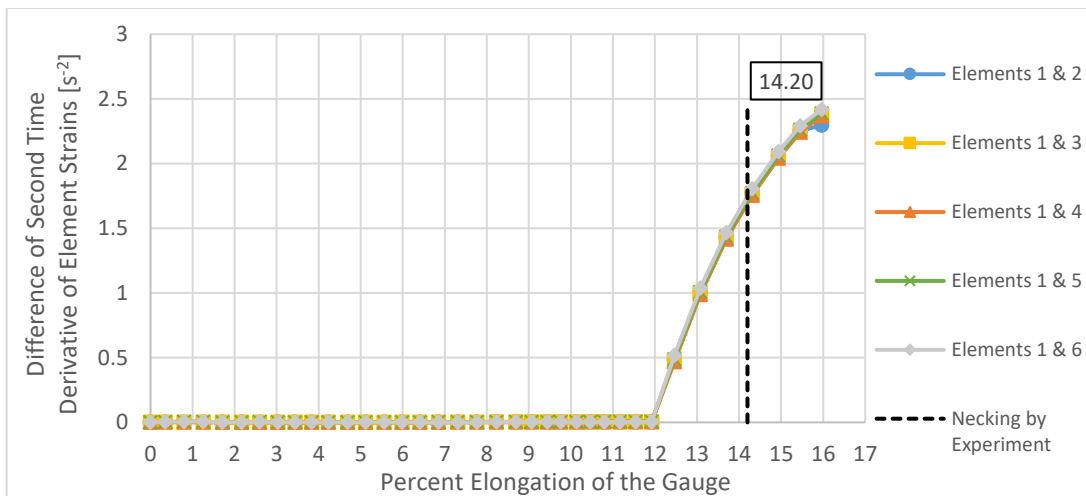


Figure 6.50. Difference of second time derivative of strain for several mesh element couples vs. percent elongation of the gauge for notched cross-section, sheet, steel specimen

6.3.3.3. Criterion of Maximum Second Time Derivative of Equivalent Plastic Strain (TT-She-St-Ntc)

Figure 6.51 illustrates strain acceleration vs. elongation graph of Element 1 and states that necking is observed at 14.55% elongation. Necking occurs at 14.20% elongation according to the experiment data; thus, the prediction is ineffective.

The elongation of 14.55% is shown in strain vs. elongation (Figure 6.52) and strain rate vs. elongation (Figure 6.53) graphs.

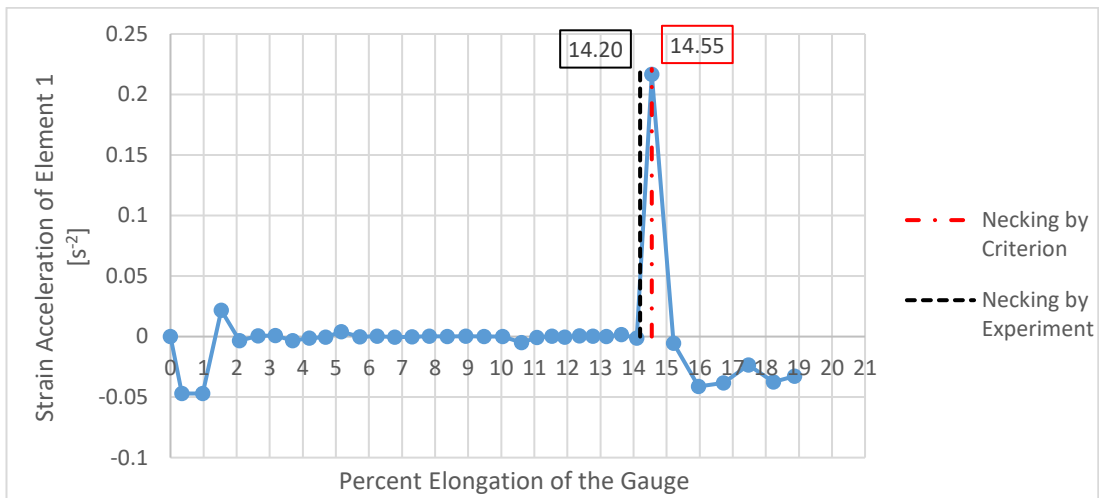


Figure 6.51. Second time derivative of Element 1 strain vs. percent elongation of the gauge for notched cross-section, sheet, steel specimen (Necking at 14.55% total elongation)

Equivalent plastic strain curve in Figure 6.52 performs similar trends as in straight and tapered cases.

Strain rate plot of Figure 6.53 is also similar to Figure 6.47; both of them increases sharply near necking and descends more smoothly.

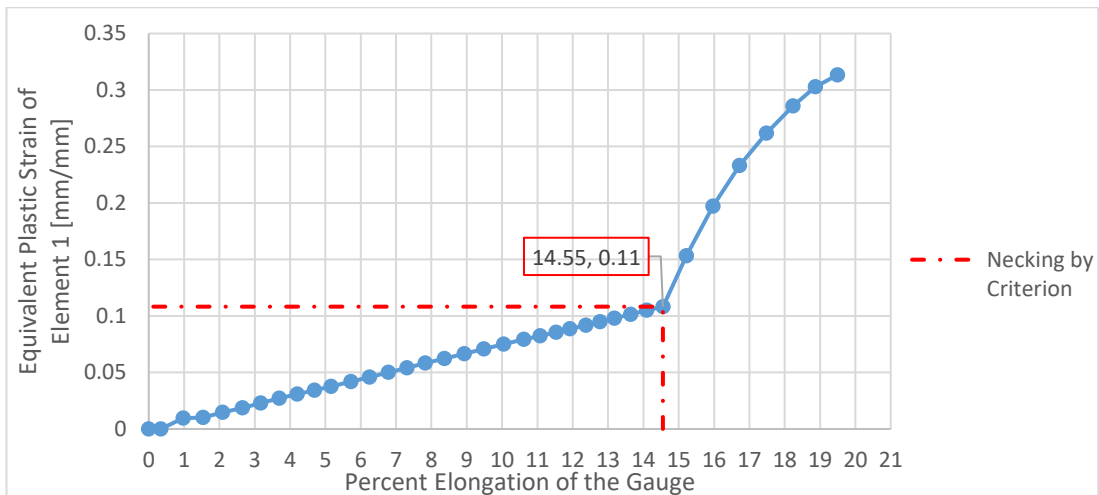


Figure 6.52. Plastic strain of Element 1 vs. percent elongation of the gauge for notched cross-section, sheet, steel specimen

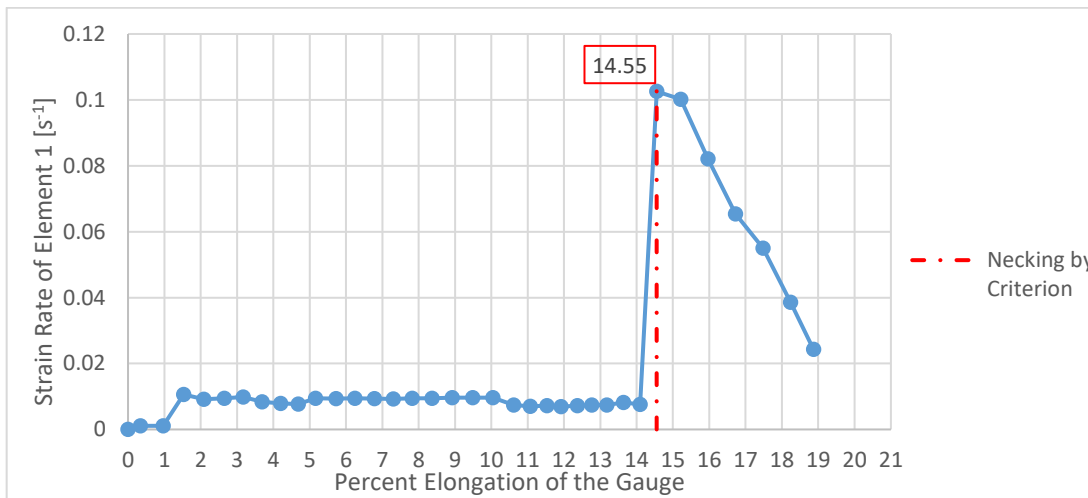


Figure 6.53. First time derivative of Element 1 strain vs. percent elongation of the gauge for notched cross-section, sheet, steel specimen

6.3.3.4. Criterion of Maximum Punch Force (TT-She-St-Ntc)

Figure 6.54 reveals that necking occurs at 13.12% total elongation in FEA; on the other hand, it is recognized at 14.20% elongation by the experiment. The method and the experiment results are consistent. Also, maximum force method predicts necking at underestimated value which is preferred.

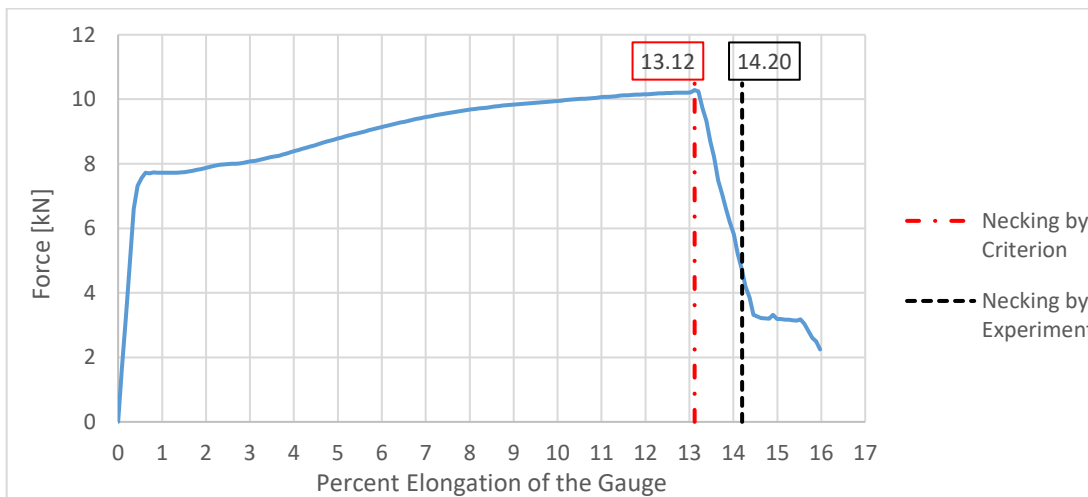


Figure 6.54. Punch force over percent gauge elongation of Element 100 for notched cross-section, sheet, steel specimen (Necking at 13.12% total elongation)

6.4. FEA Results of S235JR Round Specimen Tensile Tests

6.4.1. Straight S235JR Round Specimen Analysis

S235JR round specimens had three different geometries; namely, straight, tapered and notched. Methods are to be applied to all cases to predict onset of necking.

6.4.1.1. Criterion of Equivalent Plastic Strain Increment Ratio (TT-Ro-St-Str)

In Figure 6.55, equivalent plastic strain rate ratio method exhibited results for different element groups in a wide interval. The range to recognize necking varies between 6.35% and 12.83%.

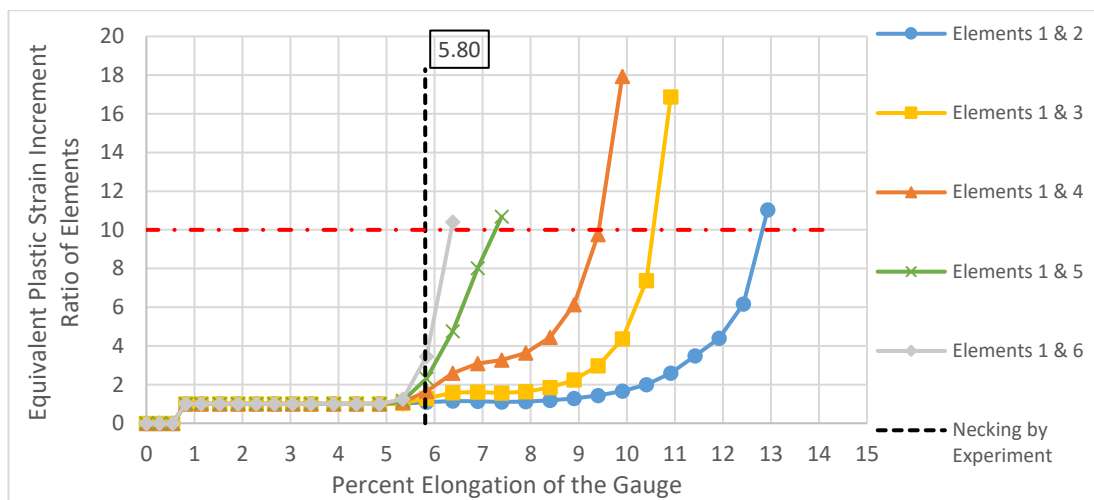


Figure 6.55. Strain increment ratios of several mesh element couples vs. percent elongation of the gauge for straight cross-section, round, steel specimen

Elements 1 & 2, 1 & 3, 1 & 4, 1 & 5 and 1 & 6 detected onset of necking at 12.83%, 10.55%, 9.42%, 7.27% and 6.35%, respectively. Elements 1 & 6 approached most to the experiment necking elongation value, which is 5.80%.

6.4.1.2. Criterion of Difference of Second Time Derivative of Equivalent Plastic Strain (TT-Ro-St-Str)

Difference of second time derivative of strain method implemented on round steel straight tensile test specimens displayed intriguing results provided in Figure 6.56. Elements 1 & 2 detected the onset of necking at 6.89% elongation. Elements 1 & 3, 1

& 4, 1 & 5 and 1 & 6 detected the necking at 6.38%. This value is closer to the experimental data which gives the necking at 5.80% elongation of the gauge.

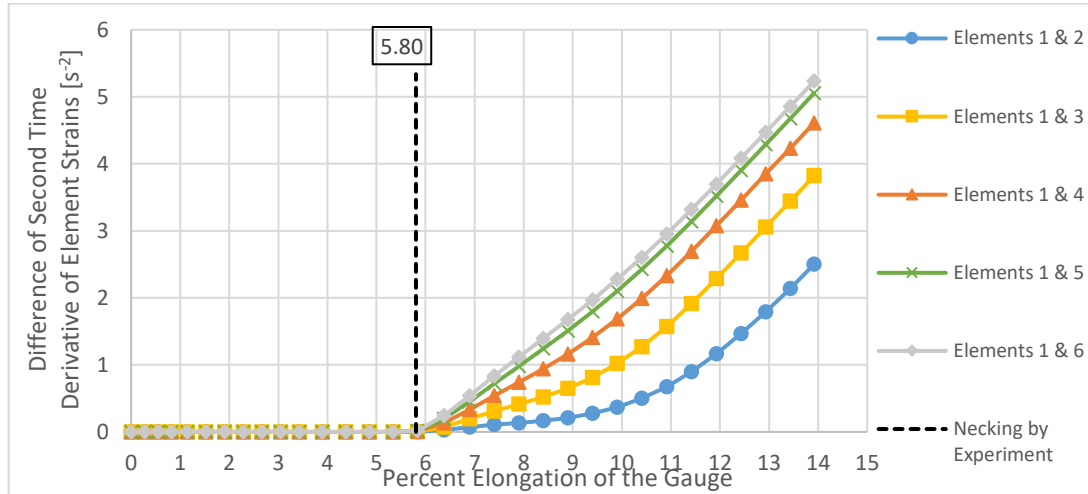


Figure 6.56. Difference of second time derivative of strain for several mesh element couples vs. percent elongation of the gauge for straight cross-section, round, steel specimen

6.4.1.3. Criterion of Maximum Second Time Derivative of Equivalent Plastic Strain (TT-Ro-St-Str)

Predicting the onset of necking through maximum strain acceleration of a critical element is to be performed in this section for axisymmetric model of straight steel specimen. Equivalent strain acceleration trajectory is plotted in Figure 6.57 which has a maximum value at 5.83% total gauge elongation. Negligible values at first and sudden increase followed by a decrease and some oscillatory motions until final minor values are reached.

Second time derivative of element strain graph in Figure 6.57 also yields results very close to experiment, which is 5.80% elongation.

The total percent elongation value of 5.83 is also shown in remaining graphs of this section; namely, strain vs. total elongation (Figure 6.58) and strain rate vs. total elongation (Figure 6.59).

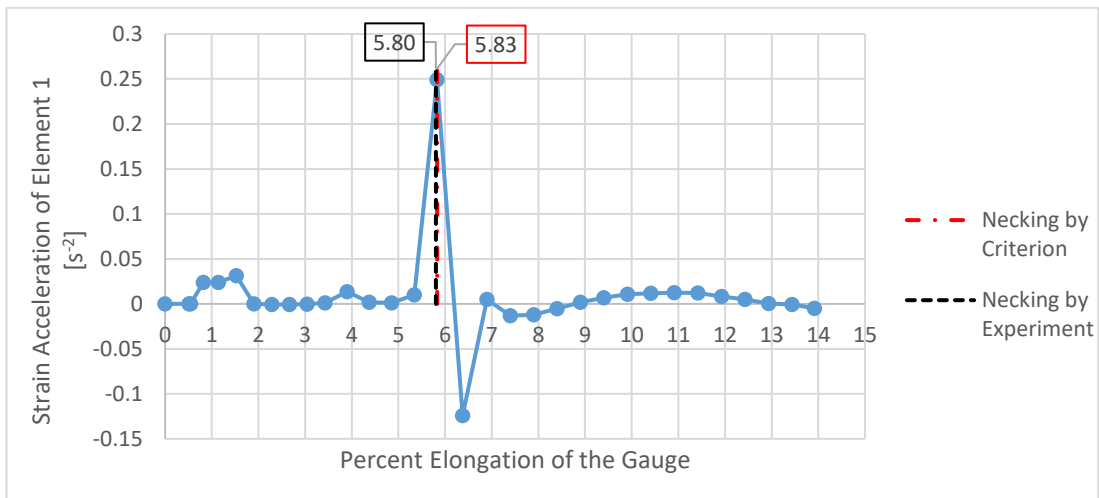


Figure 6.57. Second time derivative of Element 1 strain vs. percent elongation of the gauge for straight cross-section, round, steel specimen (Necking at 5.83% total elongation)

Figure 6.57 has trivial values at the beginning and increases gradually after necking until the end of the process. Those traits are similar to the previous discussions.

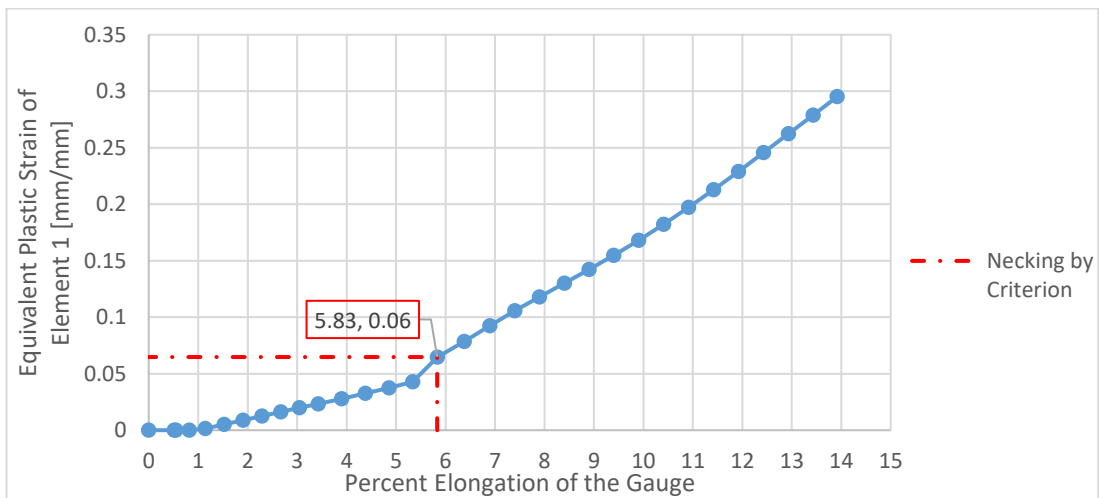


Figure 6.58. Plastic strain of Element 1 vs. percent elongation of the gauge for straight cross-section, round, steel specimen

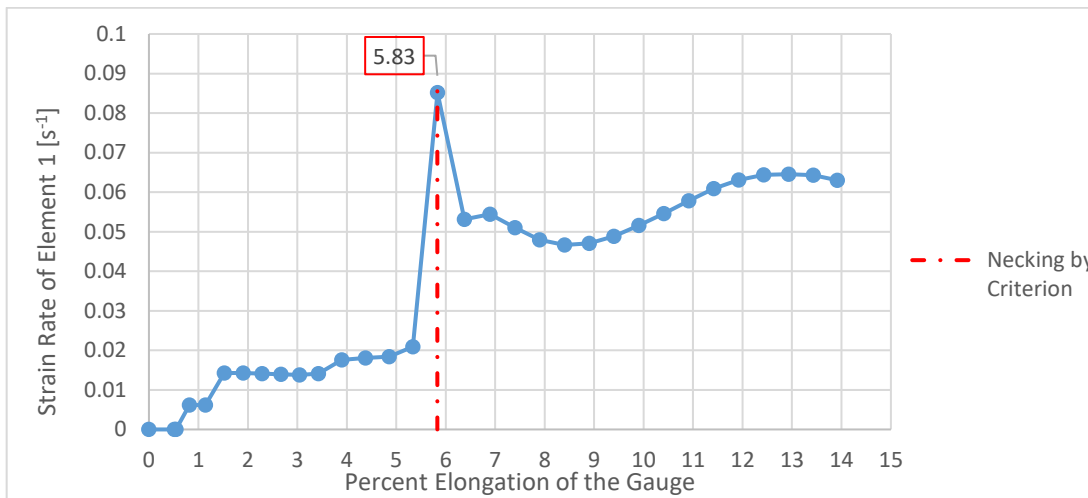


Figure 6.59. First time derivative of Element 1 strain vs. percent elongation of the gauge for straight cross-section, round, steel specimen

6.4.1.4. Criterion of Maximum Punch Force (TT-Ro-St-Str)

Punch force vs. total elongation chart for the FEA of TT-Ro-St-Str is given in Figure 6.60. The results brought out that necking occurs at 6.71% total elongation in FEA by measuring displacement of uppermost element (Element 100) in grip region. The onset of necking traced by experimental data expresses it to occur at 5.80% elongation, which is approximated reasonably.

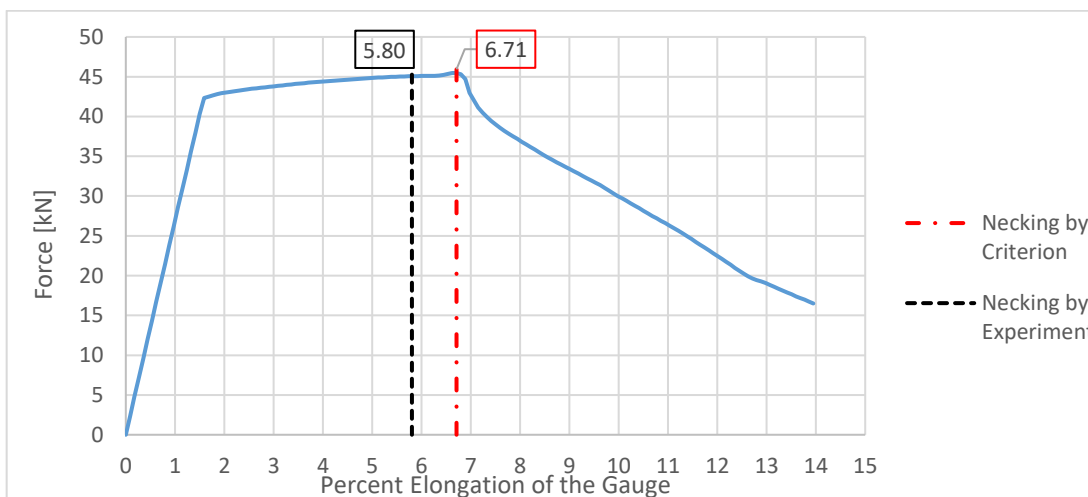


Figure 6.60. Punch force vs. percent gauge elongation of Element 100 for straight cross-section, round, steel specimen (Necking at 6.71% total elongation)

6.4.2. Tapered S235JR Round Specimen Analysis

6.4.2.1. Criterion of Equivalent Plastic Strain Increment Ratio (TT-Ro-St-Tpr)

As with the straight rod-shaped S235JR specimens, tapered specimens predict necking at quite different values shown in Figure 6.61.

Elements 1 & 2, 1 & 3, 1 & 4, 1 & 5 and 1 & 6 realized the onset of necking at 12.07%, 9.84%, 5.65%, 4.95% and 4.67%, respectively. Comparing with the corresponding experiment, necking occurs at 5.57% elongation. Thus, Elements 1 & 4 yield the most accurate result with respect to the corresponding experiments.

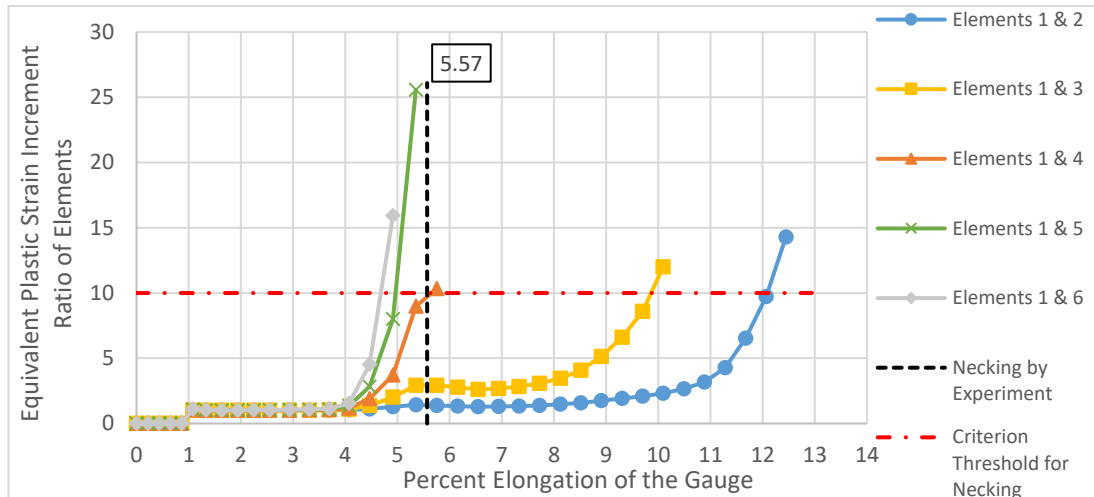


Figure 6.61. Strain increment ratios of several mesh element couples vs. percent elongation of the gauge for tapered cross-section, round, steel specimen

6.4.2.2. Criterion of Difference of Second Time Derivative of Equivalent Plastic Strain (TT-Ro-St-Tpr)

Figure 6.62 displays the difference of second time derivative of element strains. Elements 1 & 3, 1 & 4, 1 & 5 and 1 & 6 detect the onset of necking at 4.92% gauge elongation. On the other hand, Elements 1 & 2 predicted the onset of necking at 5.35%.

Elements 1 & 2 obtained the most accurate result when experiment prediction of necking at 5.57% elongation taken into consideration.

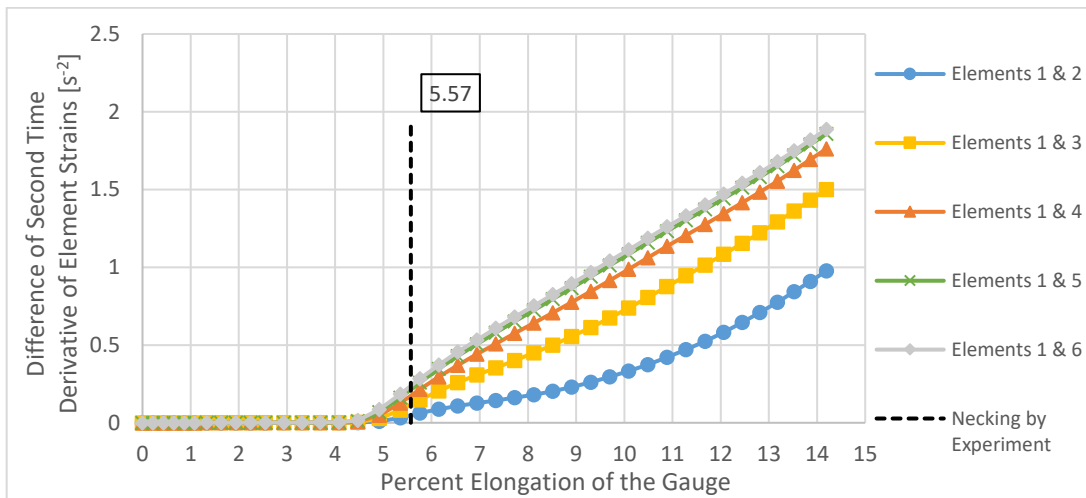


Figure 6.62. Difference of second time derivative of strain for several mesh element couples vs. percent elongation of the gauge for tapered cross-section, round, steel specimen

6.4.2.3. Criterion of Maximum Second Time Derivative of Equivalent Plastic Strain (TT-Ro-St-Tpr)

Figure 6.63 depicts the strain acceleration plot of S235JR round tapered specimen analysis. Strain acceleration curve reveals its common characteristics. Some fluctuations are observed before necking initiation; and, after maximum value is acquired the curve tend to decrease and converge. Necking is predicted to be at total elongation of 4.47% in Figure 6.63. This result underestimated the onset of necking when experimental necking of 5.57% is taken into account.

Equivalent plastic strain graph in Figure 6.64 is consistent with its counterparts in other sections. Note that the strain rate graph in Figure 6.65 has reached to a final stable value like straight round specimen. Yet, this was not the case in previous sections.

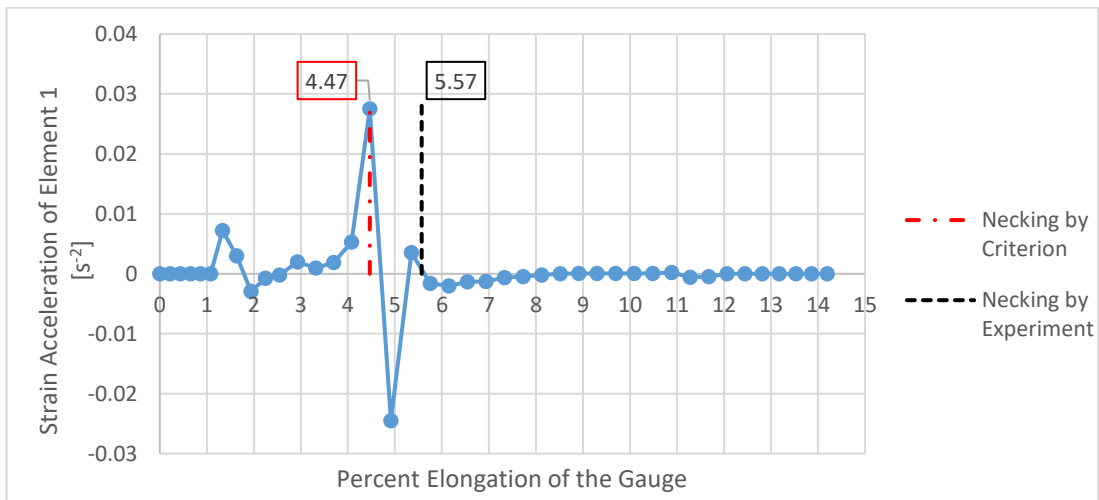


Figure 6.63. Second time derivative of Element 1 strain vs. percent elongation of the gauge for tapered cross-section, round, steel specimen (Necking at 4.47% elongation)

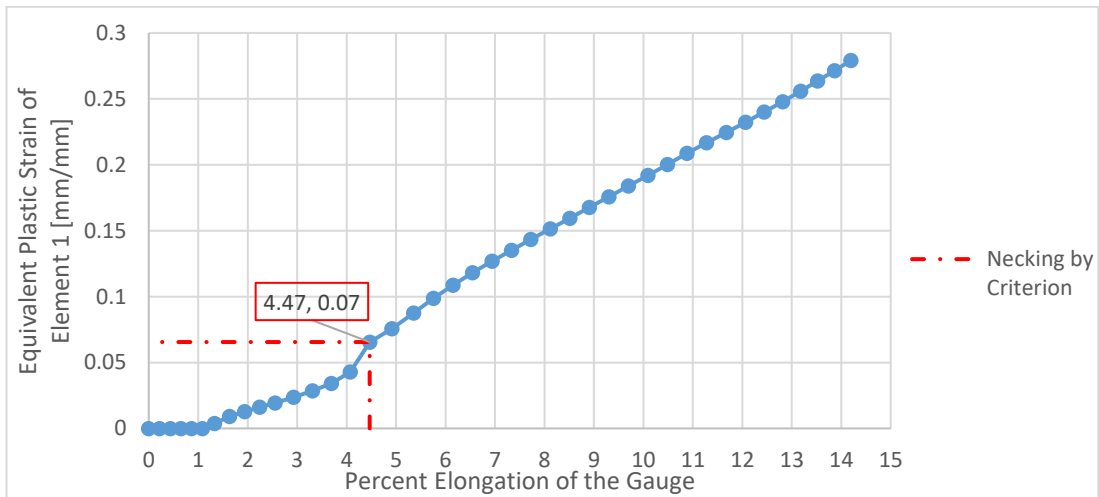


Figure 6.64. Plastic strain of Element 1 vs. percent elongation of the gauge for tapered cross-section, round, steel specimen

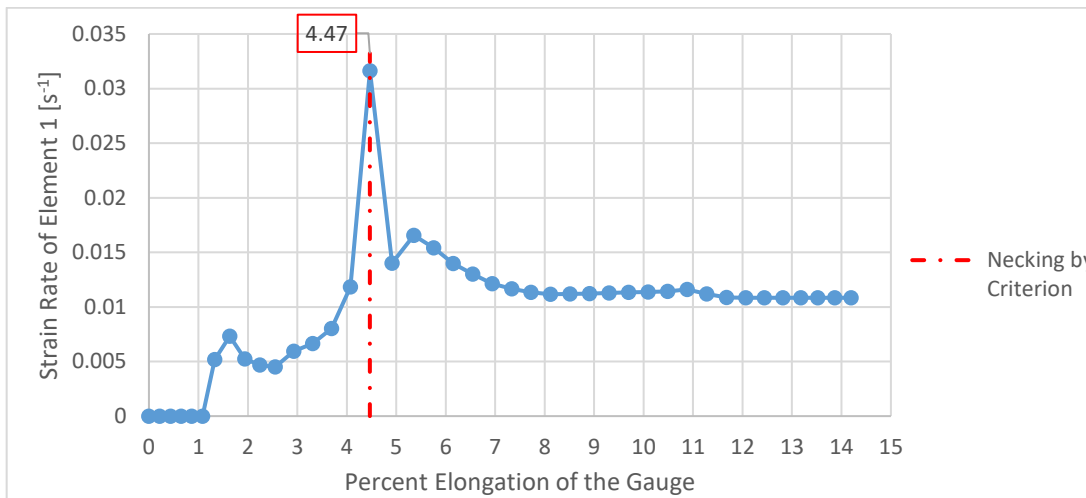


Figure 6.65. First time derivative of Element 1 strain vs. percent elongation of the gauge for tapered cross-section, round, steel specimen

6.4.2.4. Criterion of Maximum Punch Force (TT-Ro-St-Tpr)

Maximum force method in Figure 6.66 states that necking occurs at 5.32% total gauge elongation. Experiment gives 5.57% elongation for necking under same conditions. The approximation of the force method can be regarded as accurate.

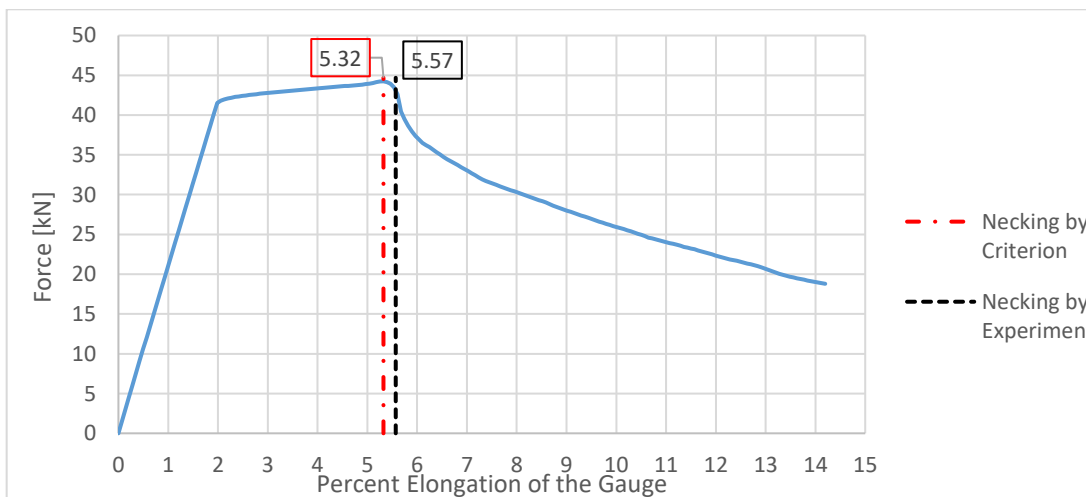


Figure 6.66. Punch force vs. percent gauge elongation of Element 100 for tapered cross-section, round, steel specimen (Necking a 5.32% total elongation)

6.4.3. Notched S235JR Round Specimen Analysis

6.4.3.1. Criterion of Equivalent Plastic Strain Increment Ratio (TT-Ro-St-Ntc)

Parallel with ratio method figures of steel cylindrical specimens, Figure 6.67 demonstrates different element pairs resulting in considerably distinguished outputs. Elements 1 & 2 predicts necking to occur at 10.70% elongation; whereas, Elements 1 & 6 estimates it as 4.65%; thus, a wide range of results are generated. To specify further, Elements 1 & 3, 1 & 4 and 1 & 5 detect the onset of necking at 9.61%, 8.17% and 5.72%, respectively.

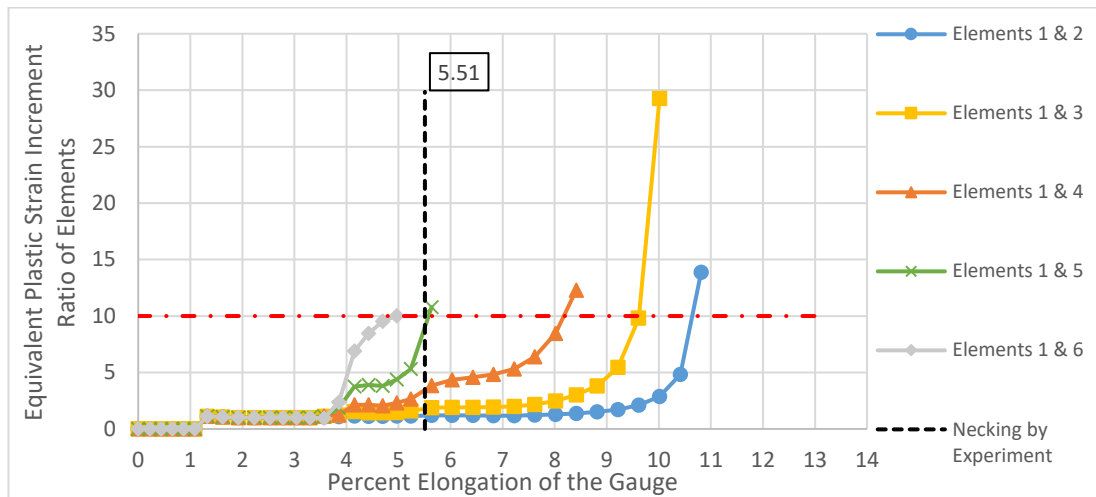


Figure 6.67. Strain increment ratios of several mesh element couples vs. percent elongation of the gauge for notched cross-section, round, steel specimen

Elements 1 & 5 brought out the closest result to that of the experiment that is 5.51% elongation.

6.4.3.2. Criterion of Difference of Second Time Derivative of Equivalent Plastic Strain (TT-Ro-St-Ntc)

Strain increment acceleration method yields Figure 6.68. The curves belonging to different element couples reveal similar trend as in cases investigated previously. Total gauge percentage elongation value of 4.15 is recorded as necking

commencement value by Elements 1 & 3, 1 & 4, 1 & 5 and 1 & 6. On another hand, Elements 1 & 2 is slightly delayed and detected necking at 4.43% gauge elongation.

The current method underestimated the necking as the experiment results state that necking occurs at 5.51% elongation.

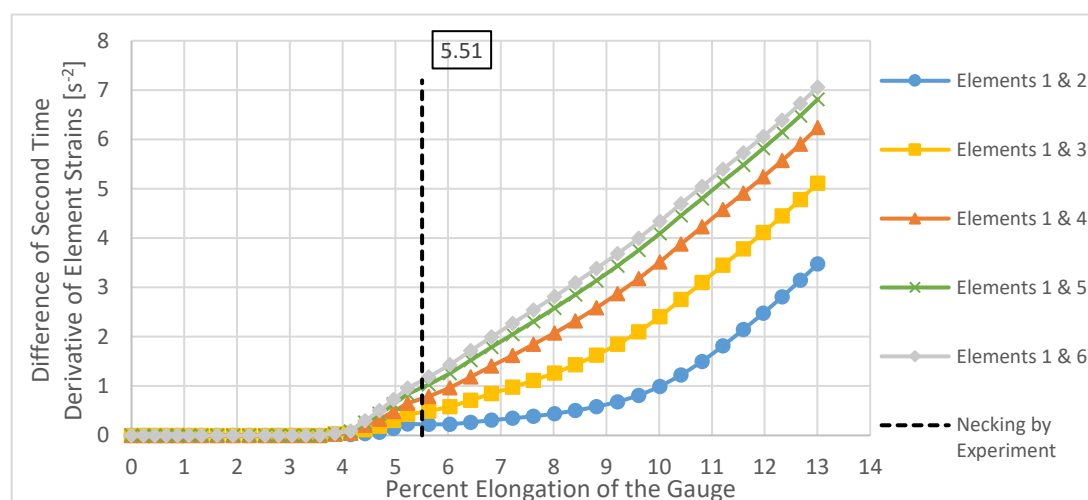


Figure 6.68. Difference of second time derivative of strain for several mesh element couples vs. percent elongation of the gauge for notched cross-section, round, steel specimen

6.4.3.3. Criterion of Maximum Second Time Derivative of Equivalent Plastic Strain (TT-Ro-St-Ntc)

Second time derivative data of strain increments of Element 1 are calculated and presented in Figure 6.69. The trend of strain acceleration curve in Figure 6.69 is rather stable before necking; yet, it is irregularly oscillatory after commencement of necking.

The necking is detected to occur at total elongation of 3.85% by FEA. However, experiment data yields the onset of necking at 5.51% elongation which is prominently underestimated.

In Figure 6.70, equivalent plastic strain graphs trend is similar to all previous cases. In Figure 6.71, the most abrupt change in the trend can easily be pointed out at 3.85% elongation when necking initiates.

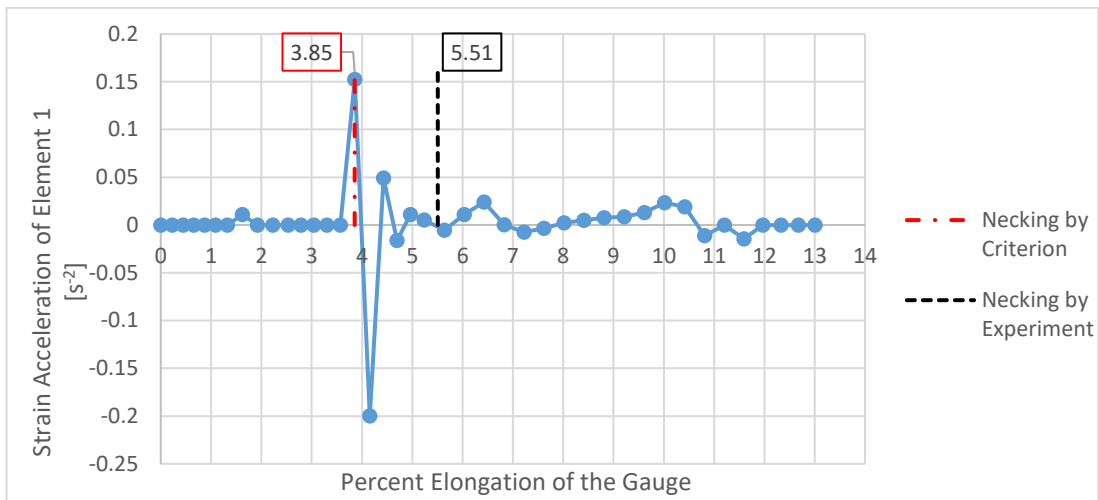


Figure 6.69. Second time derivative of Element 1 strain vs. percent elongation of the gauge for notched cross-section, round, steel specimen (Necking at 3.85% elongation)

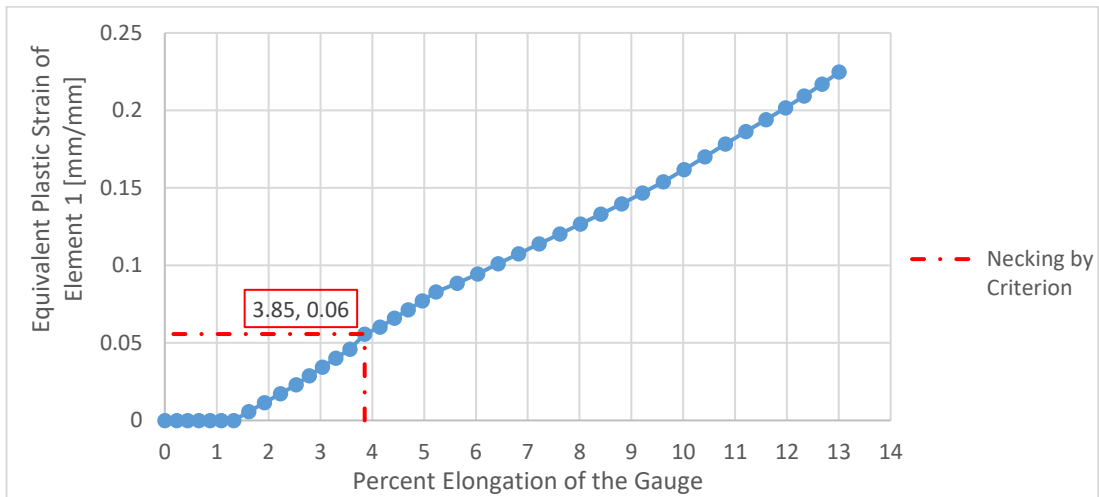


Figure 6.70. Plastic strain of Element 1 vs. percent elongation of the gauge for notched cross-section, round, steel specimen

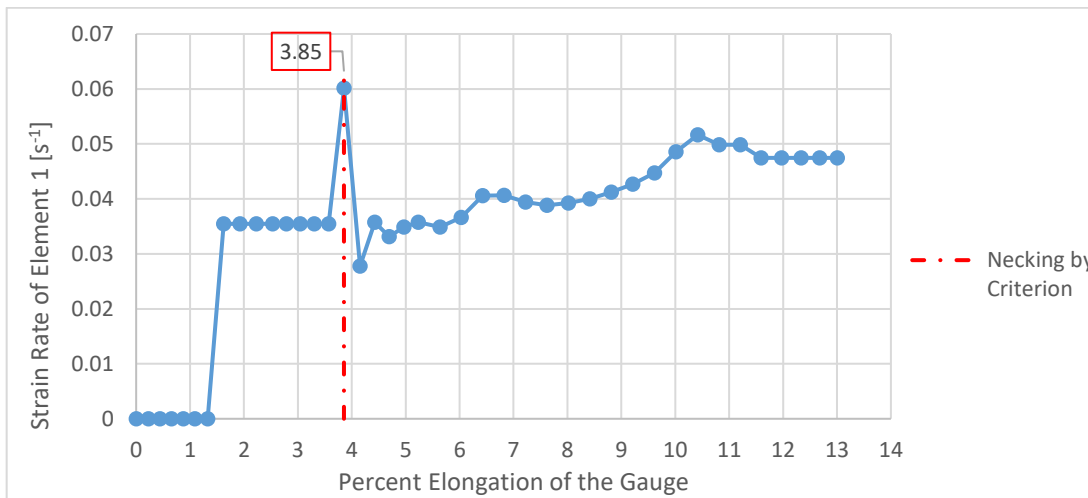


Figure 6.71. First time derivative of Element 1 strain vs. percent elongation of the gauge for notched cross-section, round, steel specimen

6.4.3.4. Criterion of Maximum Punch Force (TT-Ro-St-Ntc)

At 4.55% total elongation, necking is predicted as in Figure 6.72. The corresponding value obtained during the experiment is 5.51%. Force method underestimates the necking when compared to experiment, yet it yielded better results than strain difference and maximum strain acceleration methods.

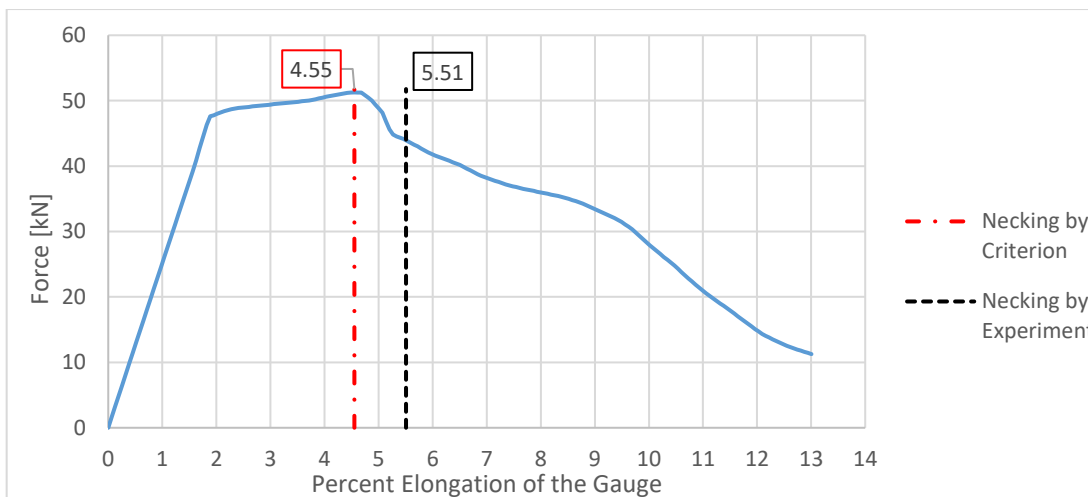


Figure 6.72. Punch force vs. percent gauge elongation of Element 100 for notched cross-section, round, steel specimen (Necking a 4.55% elongation)

6.5. Comparative Discussion for Tensile Test FEA Results

Combinations of different specimen materials and geometries of tensile tests resulted in many graphs. The applicability of several necking prediction methods is exemplarily shown for twelve different cases.

Degree of accuracy or the closeness of the FEA results to the corresponding experimental results is an important criterion while assessing the outputs.

Prediction of the onset of necking methods applied on different tensile tests with or without artificial imperfection. Commonly, authors have chosen one type and applied the criteria on it. This thesis allowed to extend the comparison of the methods by employing different necking location control practices.

Equivalent plastic strain vs. percent gauge elongation graphs are illustrated in Figures 6.4, 6.10, 6.16, 6.22, 6.28, 6.34, 6.40, 6.46, 6.52, 6.58, 6.64 and 6.70. In twelve tensile test analysis, the equivalent strain vs. percent elongation plots have similar characteristics. Initially, they increase at a slow pace until commencement of necking. After the onset of necking, they rise steeply. Note that Al2024T3 specimens experience fracture shortly after necking; but, steel specimen elongate significantly after the onset of necking.

Equivalent strain rate data is plotted in Figures 6.5, 6.11, 6.17, 6.23, 6.29, 6.35, 6.41, 6.47, 6.53, 6.59, 6.65 and 6.71 with respect to percent elongation of the specimen gauge length. It is hard to generalize strain rate curves as they indicate different traits in different types of analysis. In sheet specimen analysis, strain rate vs. elongation plots commence with low values and exhibit abrupt increase near necking initiation following an abrupt decrease in the case of steel specimens. For round specimens; there are no clear peaks in most cases.

At this point supplementary figures are finished and prediction of onset of necking figures are to be discussed. Ratio of equivalent plastic strain rate changes with respect to two different elements are given in Figures 6.1, 6.7, 6.13, 6.19, 6.25, 6.31, 6.37,

6.43, 6.49, 6.55, 6.61 and 6.67. Strain ratio plots have similar properties, starting with approximately unity and increasing with ununiform deformation or instability situation. First interesting observation in this case is sheet specimens increase quite sharply when compared to round specimens. This is because sheets are thin, localization occurs more swiftly than round specimens. On the other hand, cylindrical tensile test simulations significantly differentiated results with selection of different element pairs.

Difference of second time derivative of equivalent plastic strain method results can be investigated from Figures 6.2, 6.8, 6.14, 6.20, 6.26, 6.32, 6.38, 6.44, 6.50, 6.56, 6.62 and 6.68. Strain difference plots start and maintain almost zero value and display an increase. Similar to ratio method graphs, strain difference vs. percent gauge elongation graphs increase sharply in strip-type specimen analysis and more smoothly in rod-type specimens. Lastly, recall that difference of strain acceleration formula is rearranged in this thesis with a new definition to have a more suitable physical representation for the formula. In addition, difference of second time derivative of equivalent plastic strain method is used without a threshold value, which is an original contribution to the literature. The aim is to prevent possible errors by improper selection of a user-defined parameter. On the other hand, the criterion is based on a significant increase in the slope of the curve, which is taken as 3 times of the slope in the previous step. This can be taken as a condition rather than a threshold.

Second temporal derivative of strain changes on critical elements are depicted in Figures 6.3, 6.9, 6.15, 6.21, 6.27, 6.33, 6.39, 6.45, 6.51, 6.57, 6.63 and 6.69. The figures have common attributes. Until the onset of necking, they maintain naught or minor values. Necking is realized when rapid increase is observed, followed by a steep decrease. In some cases, small fluctuations can be monitored before or after necking initiation. Then, according to the author's best knowledge, prediction of onset of necking through maximum strain acceleration method is only applied to sheet metal forming or testing processes. In this work, the method is extended to all metal forming processes by employing equivalent plastic strain instead of principle strains.

Furthermore, the curves are plotted with respect to elongation instead of time; proving higher universal validity.

Examining sheet and round specimen results from both equivalent plastic strain rate ratio and difference of second time derivative of equivalent plastic strain, one can state that strain localization takes place very rapidly (high slope) in strip-type specimens compared to rod-type specimens. Note that the sheet metal specimens are in the smallest thickness category according to the standards [2].

Maximum force criterion analyses are presented in Figures 6.6, 6.12, 6.18, 6.24, 6.30, 6.36, 6.42, 6.48, 6.54, 6.60, 6.66 and 6.72. Punch force vs. percent elongation of the gauge graphs obtained numerically are compared with experiment results directly. That comparison brings out that corresponding graphs agree with each other in terms of plot trends and magnitudes. For example, FEA graphs of steel sheet tests clearly indicate the Lüders Bands as in experiment plots. Moreover, aluminum specimen processes are exposed to necking shortly before fracture; whilst, steel specimen plots continue to deform.

Among all tensile test experiments, equivalent plastic strain vs. percent elongation of the gauge, second time derivative of element strain vs. percent elongation of the gauge and punch force vs. percent elongation of the gauge graphs share the most common characteristics. These plots become proper candidates if general rules are to be studied to predict the onset of necking.

Some key points from those analyses are given in Tables 6.3 - 6.5 for integrative evaluation purposes.

Table 6.3 tabulates the data of equivalent plastic strain rate ratio method results for all tensile test FEA along with experiment results. Recall that the threshold for this analysis is commonly accepted as 10 in literature; therefore, this value is used in the analyses. The analyses results that cannot reach 10 are shown with a hyphen.

Table 6.3. Equivalent plastic strain rate ratio method results of tensile test experiments and corresponding elongation at necking from experiment data

All numbers are percent elongation	Experiment	Equivalent Plastic Strain Increment Ratio				
		Elements 1 & 2	Elements 1 & 3	Elements 1 & 4	Elements 1 & 5	Elements 1 & 6
TT-She-Al-Str	19.20	-	19.42	18.02	17.85	17.84
TT-She-Al-Tpr	15.28	16.07	15.36	14.33	13.86	13.40
TT-She-Al-Ntc	10.92	-	11.10	10.97	9.67	9.15
TT-Ro-Al-Str	10.07	-	-	-	-	-
TT-Ro-Al-Tpr	8.22	-	-	-	-	-
TT-Ro-Al-Ntc	4.86	-	-	-	-	-
TT-She-St-Str	18.00	16.74	16.60	16.41	16.20	16.09
TT-She-St-Tpr	16.83	13.94	13.25	13.23	13.19	13.18
TT-She-St-Ntc	14.20	11.86	11.91	11.97	11.81	11.66
TT-Ro-St-Str	5.80	12.83	10.55	9.42	7.27	6.35
TT-Ro-St-Tpr	5.57	12.07	9.84	5.65	4.95	4.67
TT-Ro-St-Ntc	5.51	10.70	9.61	6.59	5.50	4.65

First conclusion from Table 6.3 is that there is no general rule for the most accurate element pair or distance in terms of percent of the initial gauge lengths given in Table 6.1. Different element couples make the most accurate prediction in different analysis cases. when compared to the experiment data.

In terms of accuracy, Elements 1 & 4 have given the best results in most cases. Hence, that pair of mesh elements is advised to be utilized while conducting equivalent plastic strain rate ratio method.

An important observation from Table 6.3 is hyphen or dash warnings. Two hyphens belong to aluminum sheet specimen analysis. On the other hand, all 15 results of cylindrical specimen analysis could not detect the onset of necking with the threshold of 10. No hyphen warning appears in steel specimen tensile tests.

Al2024T3 is less ductile than S235JR; the difference in strain between necking and fracture points is much less. As a result, specimens fail before the ratio of different element strains can reach to 10. According to Table 6.3, the threshold value of 10 is suitable for S235JR steel specimens; yet, it is not suitable for Al2024T3 round specimens and Al2024T3 sheet specimens in some cases. As a result, materials which

reveal necking shortly before fracture may require a lower threshold level for equivalent plastic strain rate ratio method. By examination of the analysis results, the threshold value for tensile tests of Al2024T3 round specimens is determined as 1.6 instead of 10. This allows Elements 1 & 6 to predict necking. Consequently, cylindrical aluminum specimen tensile test predictions can be improved by applying a more appropriate threshold in ratio method.

In Table 6.4, difference of second time derivative of equivalent plastic strain method results of all tensile test specimens are exhibited.

Table 6.4. Difference of second time derivative of equivalent plastic strain method results of tensile test experiments and corresponding elongation at necking from experiment data

All numbers are percent elongation	Experiment	Difference of Second Time Derivative of Equivalent Plastic Strain				
		Elements 1 & 2	Elements 1 & 3	Elements 1 & 4	Elements 1 & 5	Elements 1 & 6
		TT-She-Al-Str	19.20	18.52	18.52	18.52
TT-She-Al-Tpr	15.28	16.15	15.69	15.69	15.20	15.20
TT-She-Al-Ntc	10.92	-	11.31	11.31	11.31	11.31
TT-Ro-Al-Str	10.07	11.04	11.04	11.04	11.04	11.04
TT-Ro-Al-Tpr	8.22	7.46	7.46	7.46	7.46	7.46
TT-Ro-Al-Ntc	4.86	3.59	3.59	3.59	3.59	3.59
TT-She-St-Str	18.00	17.40	17.40	17.40	17.40	17.40
TT-She-St-Tpr	16.83	14.15	14.15	14.15	14.15	14.15
TT-She-St-Ntc	14.20	12.46	12.46	12.46	12.46	12.46
TT-Ro-St-Str	5.80	6.89	6.38	6.38	6.38	6.38
TT-Ro-St-Tpr	5.57	5.35	4.92	4.92	4.92	4.92
TT-Ro-St-Ntc	5.51	4.43	4.15	4.15	4.15	4.15

Table 6.4 indicates difference of second time derivative method is almost insensitive to element pair selection within the range given in Table 6.1. In most cases, all element couples made the same prediction for the onset of necking. This is an advantage of difference method over ratio method. This advantage is obtained by the novel contribution made in this thesis (using the slope change instead of a materials threshold to detect necking).

In Table 6.4, in most cases Elements 1 & 5 and Elements 1 & 6 yielded the most accurate results. Selection of any of the mesh element couples is appropriate.

Table 6.5. Maximum second time derivative of element strain and maximum punch force method results of tensile test analyses and corresponding elongations at necking from experiment data

All numbers are percent elongation	Experiment	Maximum Second Time Derivative of Element Strain Increment	Maximum Punch Force
TT-She-Al-Str	19.20	18.52	18.63
TT-She-Al-Tpr	15.28	16.42	16.17
TT-She-Al-Ntc	10.92	10.76	10.21
TT-Ro-Al-Str	10.07	10.46	11.06
TT-Ro-Al-Tpr	8.22	6.96	7.69
TT-Ro-Al-Ntc	4.86	3.51	3.66
TT-She-St-Str	18.00	16.54	17.34
TT-She-St-Tpr	16.83	16.05	14.17
TT-She-St-Ntc	14.20	14.55	13.12
TT-Ro-St-Str	5.80	5.83	6.71
TT-Ro-St-Tpr	5.57	4.47	5.32
TT-Ro-St-Ntc	5.51	3.85	4.55

Table 6.5 provides data for the prediction of onset of necking by experiment, maximum second time derivative of strain increment and maximum punch force methods. Strain acceleration method has tendency to underestimate the necking elongation value more than maximum punch force method. On the other hand, maximum force method results are slightly more accurate. The reason is expected to be the fact that maximum force method had been used to detect the onset of necking from the experiment data. Since the methods are matching, they tend to generate compatible results.

In general, methods to predict necking tend to predict necking elongation of straight specimens with higher accuracy than other methods which can be deduced from Table 6.3 - Table 6.5. The predicted elongation values for the onset of necking deviates more when tapered and notched specimens are used.

An important observation from Table 6.5 is that both maximum strain acceleration and maximum punch force methods predict the necking of tapered and notched round specimens at lower values than the experiment. In general, the axisymmetric 2D

cylindrical models tend to underestimate the necking of imperfect specimens in tension testing.

It is also useful to assess the results from Table 6.3 - Table 6.5. Note that Elements 1 & 4 from Table 6.3 and Elements 1 & 3 from Table 6.4 are selected as the most appropriate pairs to apply the corresponding methods. To make the results more universal, the corresponding percent distance between the elements in terms of initial gauge length must be taken from Table 6.1.

An important dimension of this discussion is utilization of user-defined parameters. Throughout the analysis, the difference between the concepts of threshold and peak value has been clearly evidenced. In equivalent plastic strain rate ratio results, selection of the threshold directly affected the results. In this thesis, difference of second time derivative of equivalent plastic strain method is used without a threshold; but, the algorithm still needs a numerical indicator (change in slope is more than three times in one increment). In fact, user-defined parameter is a weakness for those methods, since a mis-selection of those values can substantially change the prediction values. Maximum force and maximum acceleration methods have an advantage since these criteria do not require introduction of user-defined parameters. These methods seek a maximum value to track necking in contrast to strain difference and strain ratio methods.

In terms of accuracy, maximum strain acceleration and maximum force methods applied on steel sheet specimens are the most successful methods. On the other hand, in tensile test results for aluminum specimens, maximum punch force method has slightly better predictions. It is important that the results from experiments are obtained through maximum force criterion; thus, it is expected the best-matching results are obtained from maximum punch force criteria of FEA. Also note that, maximum force criterion is a global method while others are local. Global criteria do not provide information about the region of the instability; only the general system information such as time, elongation, diameter or thickness can be tracked. Thus,

maximum strain acceleration method comes up as the best method among local criteria. To conclude, equivalent plastic strain acceleration of critical element method and maximum punch force method should be used together to have the most practical prediction of necking analyses results according to tensile test results.

Lastly, prediction of onset of necking methods can be utilized successfully to check instability conditions of other tensile test specimens with different specimen geometry and materials. Only true stress-strain data from the literature is sufficient for that purpose; experiments can be avoided to save cost and time.

6.6. FEA Results of Al2024T3 Specimen Deep Drawing Process

Al2024T3 sheet specimens had undergone three different processes; namely, cylindrical cup, round-bottom cup and square cup deep drawing processes. Methods are to be applied to all cases to predict the onset of tensile plastic instability. The critical mesh element names and positions are given in Finite Element Models chapter.

6.6.1. Cylindrical Cup Deep Drawing Analysis

6.6.1.1. Criterion of Equivalent Plastic Strain Increment Ratio (DDP-CC-AI)

Equivalent plastic strain increment ratio method exhibited quite irregular results for deep drawing process of Al2024T3 cylindrical cup as shown in Figure 6.73. Main deformation region is moved continuously; hence, a steady increase in ratio values is not shown. Note that Elements 1 & 6 exceed the criterion threshold 10 at 3.51% punch displacement because it is the transition step of the numerical method; thus, it is ignored.

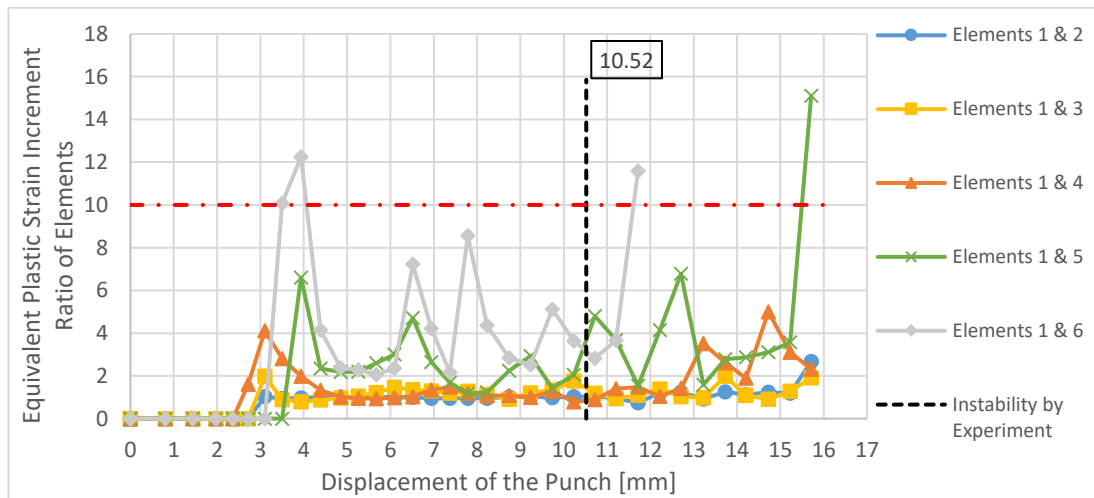


Figure 6.73. Strain increment ratios of several mesh element couples vs. punch displacement for cylindrical cup deep drawing process with 110 mm diameter, sheet, Al specimen

Punch displacement values at the onset of tensile plastic instability are 15.53 mm and 11.68 mm for Elements 1 & 5 and 1 & 6, respectively. Other element couples could not detect the instability with the utilized threshold value.

6.6.1.2. Criterion of Difference of Second Time Derivative of Equivalent Plastic Strain (DDP-CC-AI)

Difference of second time derivative of equivalent plastic strain method results for cylindrical cup deep drawing process is picturized in Figure 6.74. Elements 1 & 2, 1 & 3 and 1 & 4 detected the tensile plastic instability at 6.94 mm punch travel for which the corresponding experimental value is 10.52 mm. Elements 1 & 5 and Elements 1 & 6 achieved more accurate results; the instability condition has been recognized at 8.74 mm and 7.79 mm, respectively.

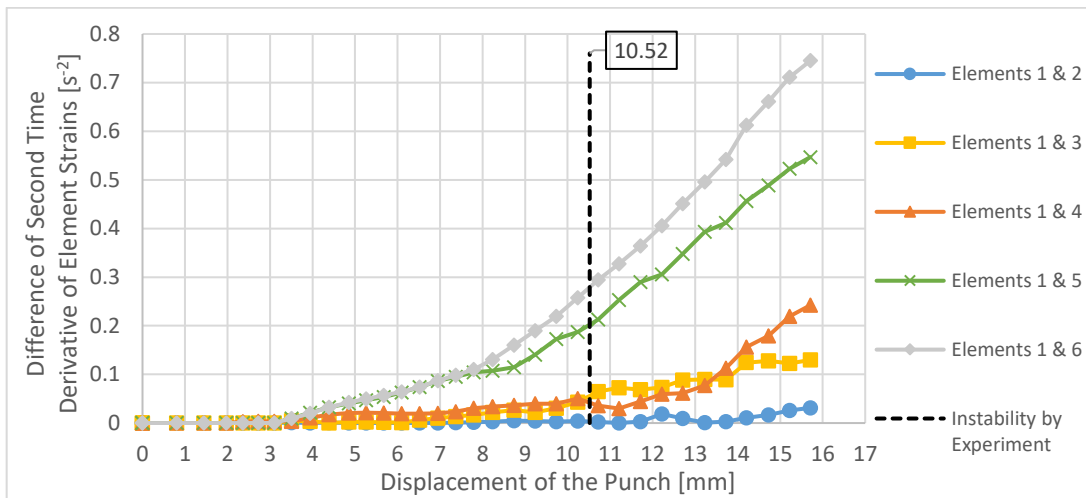


Figure 6.74. Difference of second time derivative of strain for several mesh element couples vs. punch displacement for cylindrical cup deep drawing process with 110 mm diameter, sheet, Al specimen

6.6.1.3. Criterion of Maximum Second Time Derivative of Equivalent Plastic Strain (DDP-CC-Al)

Maximum second time derivative of equivalent plastic strain method applied on Al2024T3 specimen is given in Figure 6.75. The tensile plastic instability is overestimated at 13.72 mm punch movement; yet, the experimental results is 10.52 mm. The plot has many fluctuations, especially when compare to its tensile test counterparts.

Equivalent plastic strain plot in Figure 6.76 is similar to tensile test analysis results; yet, in deep drawing process the material is able to reach higher strain levels. In Figure 6.76, equivalent plastic strain value from tensile test of Al2024T3 straight sheet FEA also marked. A very important result emerges: A material can experience higher strains at instability initiation in different processes. In the current case, Al2024T3 material revealed instability behavior at 0.18 true strain in uniaxial tensile test; yet, similar phenomenon appeared at 0.57 equivalent plastic strain value. Therefore, the maximum strain values obtained from tensile test experiments emerges as not appropriate to use in complex forming procedures. Although not investigated in this work, this conclusion can be extended to fracture failure as well.

In Figure 6.77, the strain rate characteristics of the cylindrical cup deep drawing analysis is depicted, which is very irregular as strain acceleration plot.

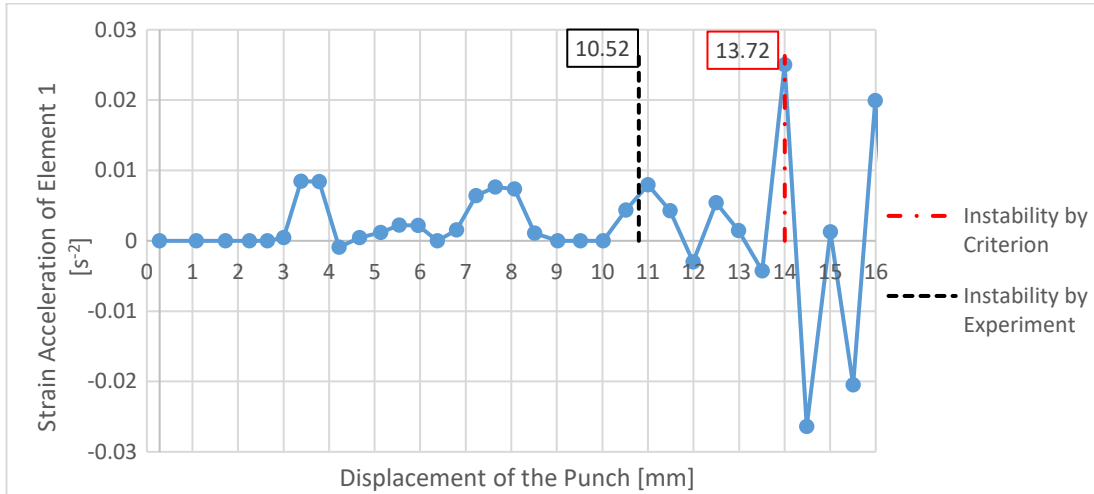


Figure 6.75. Second time derivative of Element 1 strain vs. punch displacement for cylindrical cup deep drawing process with 110 mm diameter, sheet, Al specimen (Necking at 13.72 mm displacement)

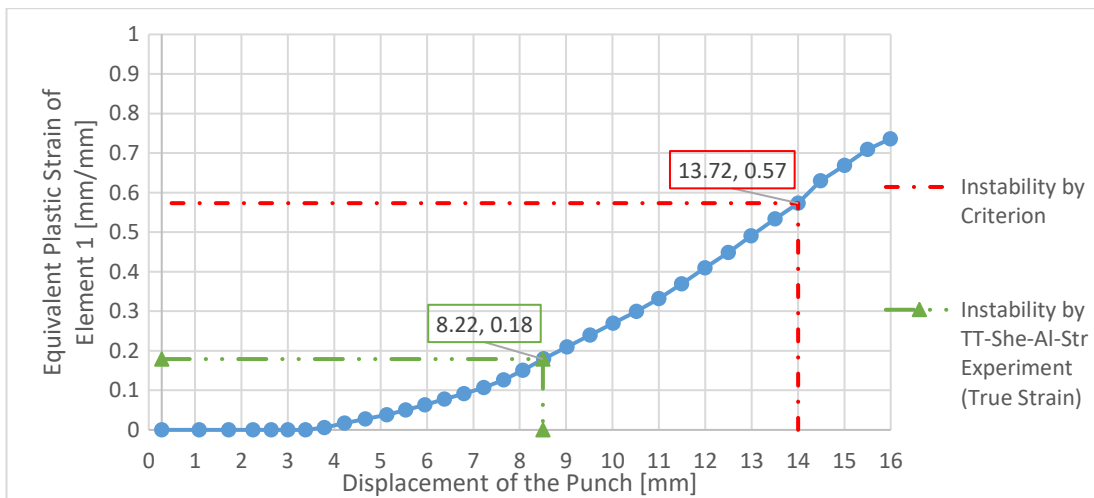


Figure 6.76. Plastic strain of Element 1 vs. punch displacement for cylindrical cup deep drawing process with 110 mm diameter, sheet, Al specimen

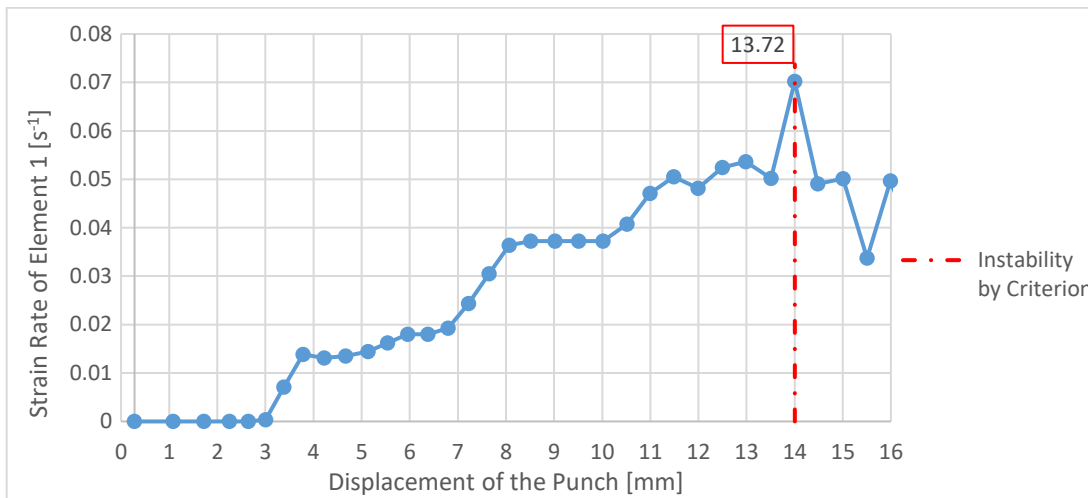


Figure 6.77. First time derivative of Element 1 strain vs. punch displacement for cylindrical cup deep drawing process with 110 mm diameter, sheet, Al specimen

6.6.1.4. Criterion of Maximum Punch Force (DDP-CC-Al)

Punch force vs. punch displacement graph obtained from FEA is provided in Figure 6.78. The analysis prediction for tensile plastic instability commencement is 10.24 mm punch translation; whereas, the experiment prediction is at 10.52 mm displacement. Maximum force method achieved the most accurate prediction.

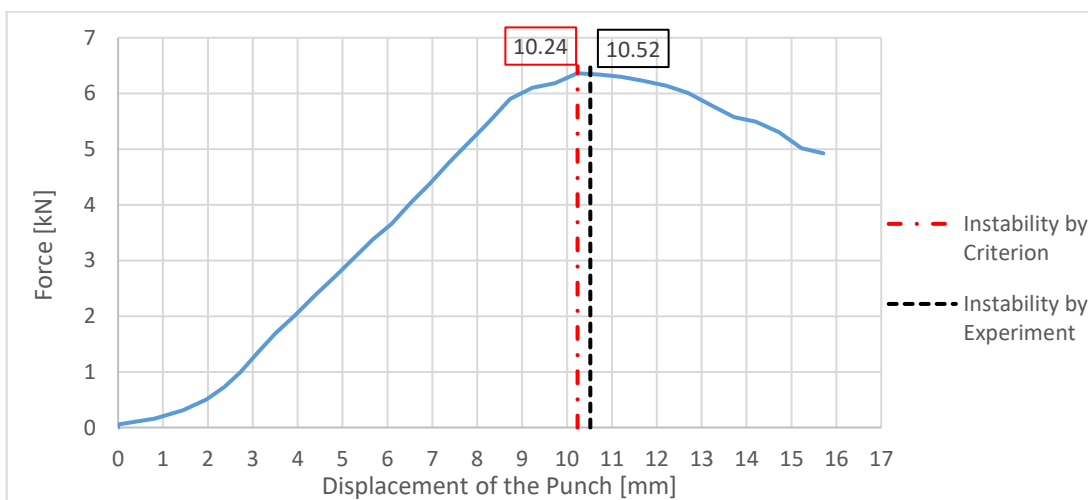


Figure 6.78. Punch force vs. punch displacement for cylindrical cup deep drawing process with 110 mm diameter, sheet, Al specimen (Necking at 10.24 mm displacement)

6.6.2. Round Bottom Cup Deep Drawing Analysis

6.6.2.1. Criterion of Equivalent Plastic Strain Increment Ratio (DDP-RB-AI)

Equivalent plastic strain increment ratio method in hemispherical cup deep drawing case yielded more stable results than cylindrical cup. The related plots are given in Figure 6.79. Elements 1 & 2 could not detect tensile plastic instability. Elements 1 & 3, 1 & 4, 1 & 5 and 1 & 6 detected it at 18.85 mm, 19.62 mm, 18.93 mm and 18.88 mm punch displacement, respectively. The experimental results for instability initiation is 17.32 mm displacement; the methods tend to overestimate necking in this case.

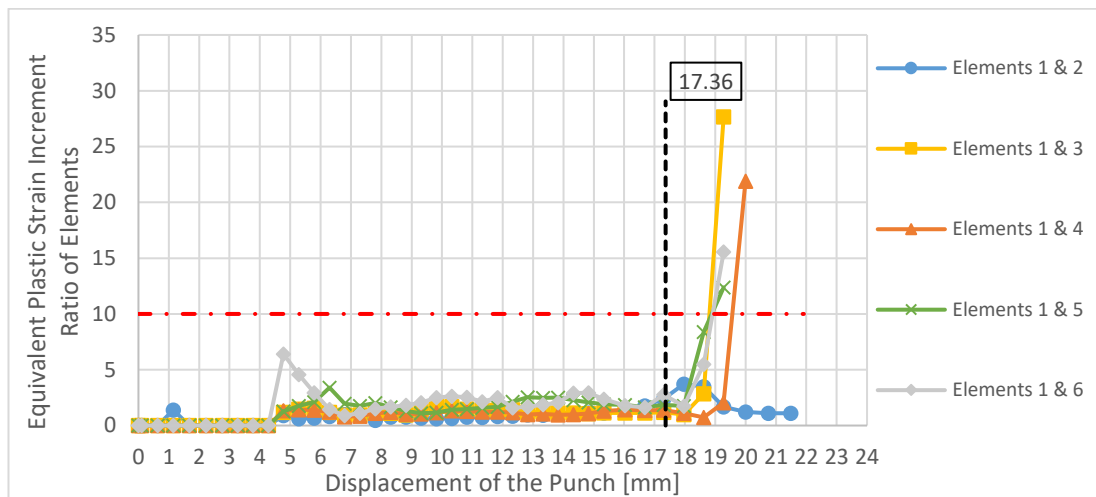


Figure 6.79. Strain increment ratios of several mesh element couples vs. punch displacement for round bottom cup deep drawing process with 110 mm diameter, sheet, Al specimen

6.6.2.2. Criterion of Difference of Second Time Derivative of Equivalent Plastic Strain (DDP-RB-AI)

Difference of strain acceleration plots of round bottom cup deep drawing analysis generated more consistent results than its cylindrical cup counterpart. In Figure 6.80, tensile plastic instability is recognized at 19.28 mm punch travel by all element pairs. This method also overestimates plastic instability as the experimental result is 17.36 mm displacement.

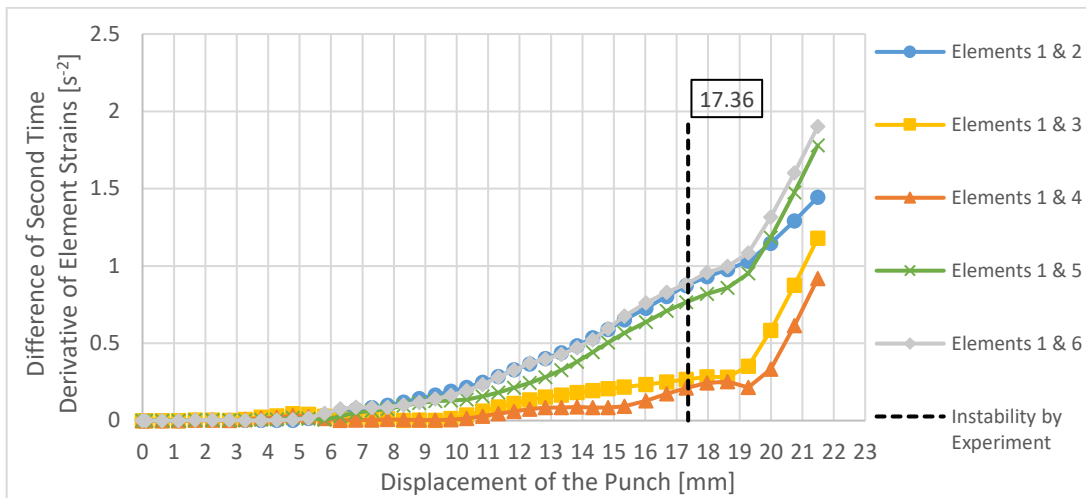


Figure 6.80. Difference of second time derivative of strain for several mesh element couples vs. punch displacement for round bottom cup deep drawing process with 110 mm diameter, sheet, Al specimen

6.6.2.3. Criterion of Maximum Second Time Derivative of Equivalent Plastic Strain (DDP-RB-Al)

Strain acceleration plot of Element 1 in round bottom cup deep drawing case is given in Figure 6.81, which show the determined instability is at 19.28 mm punch movement. Similar to previous cases, maximum strain acceleration value over-predicts the instability commencement. This plot is also fluctuating significantly.

Punch displacement value at tensile plastic instability is also shown in element equivalent plastic strain (Figure 6.82) and element equivalent strain rate (Figure 6.83) plots.

In Figure 6.82, strain at the onset of necking from straight, Al2024T3, sheet specimen tensile test analysis is shown along with deep drawing analysis tensile plastic instability prediction. Similar to the cylindrical cup case, the critical element in round bottom deep drawing process can have strain value significantly higher than its counterpart in tensile test analysis (0.77 versus 0.18).

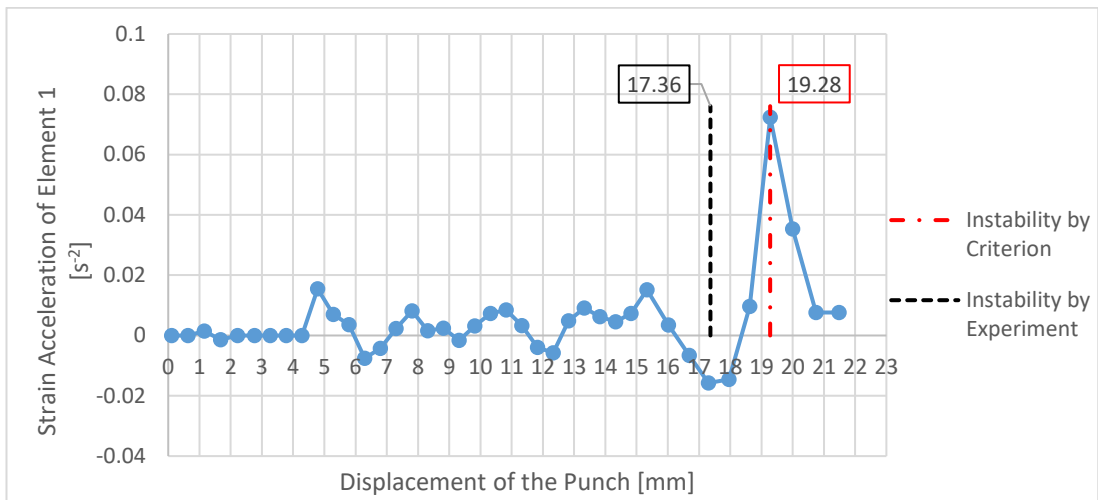


Figure 6.81. Second time derivative of Element 1 strain vs. punch displacement for round bottom cup deep drawing process with 110 mm diameter, sheet, Al specimen (Necking at 19.28 mm displacement)

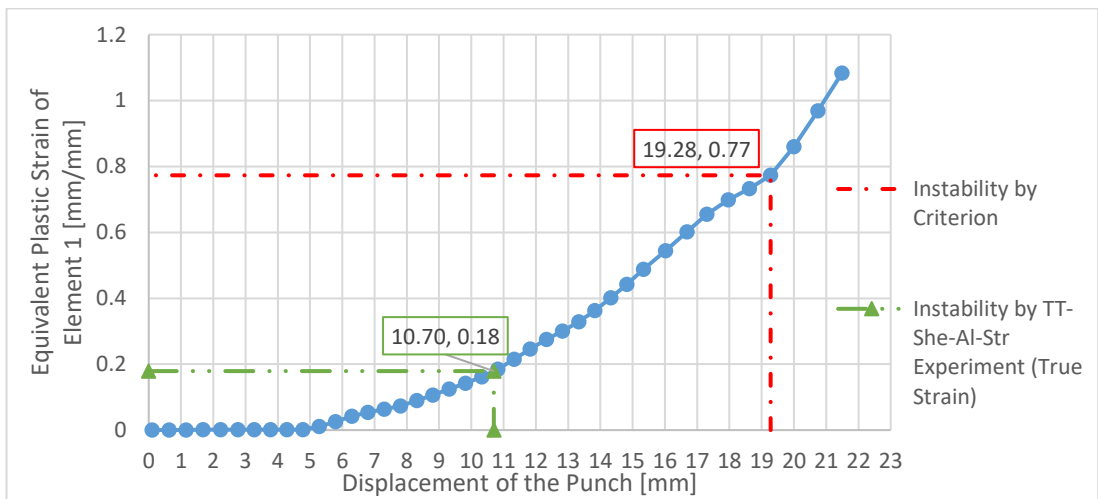


Figure 6.82. Plastic strain of Element 1 vs. punch displacement for round bottom cup deep drawing process with 110 mm diameter, sheet, Al specimen

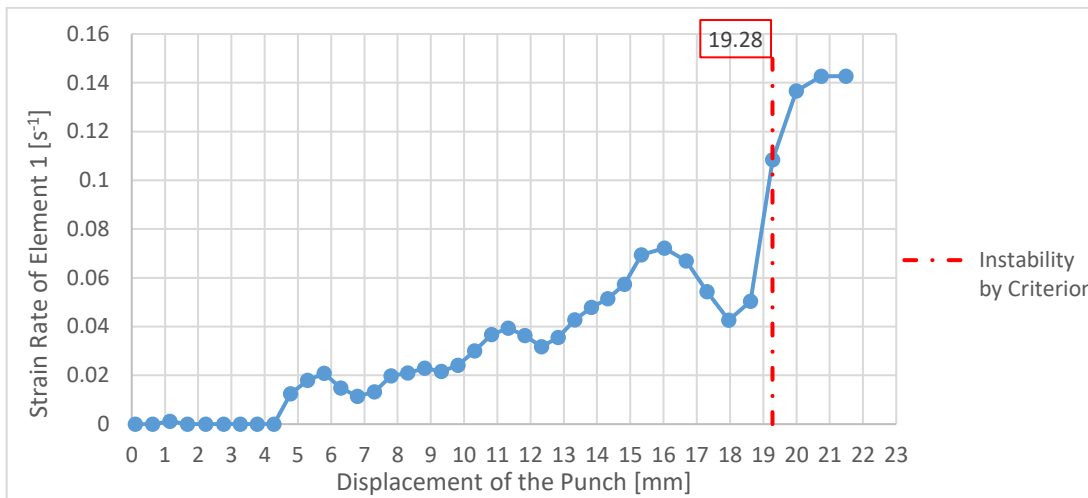


Figure 6.83. First time derivative of Element 1 strain vs. punch displacement for round bottom cup deep drawing process with 110 mm diameter, sheet, Al specimen

6.6.2.4. Criterion of Maximum Punch Force (DDP-RB-Al)

Maximum punch force method predict the onset of tensile plastic instability at 18.62 mm punch travel, revealed in Figure 6.84. The method also overestimated instability start; yet, it has the highest accuracy.

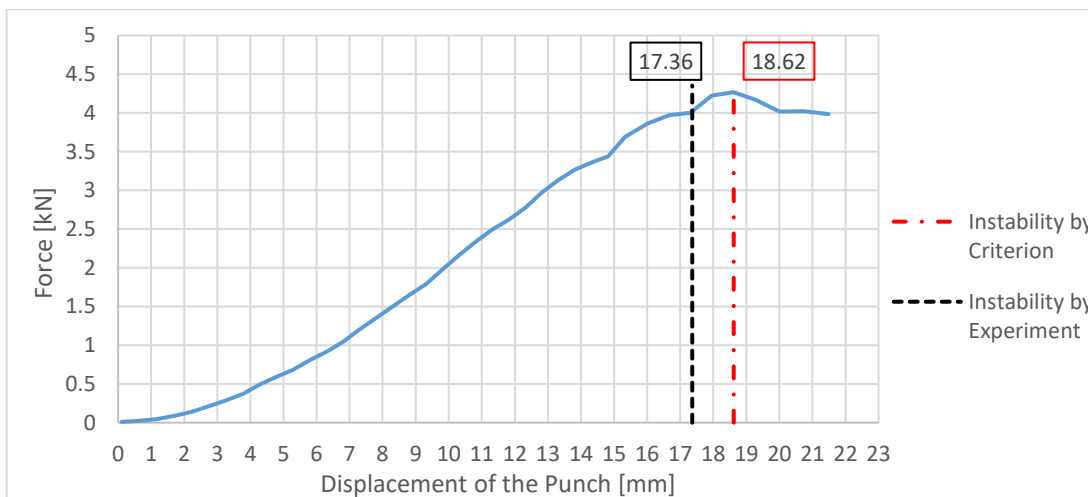


Figure 6.84. Punch force vs. punch displacement for round bottom cup deep drawing process with 110 mm diameter, sheet, Al specimen (Necking at 18.62 mm displacement)

6.6.3. Square Cup Deep Drawing Analysis

6.6.3.1. Criterion of Equivalent Plastic Strain Increment Ratio (DDP-SC-AI)

In Figure 6.85, the criterion threshold 10 has been exceeded several times before the actual prediction is made. Square cup deep drawing process produced fluctuating graphs as a result of equivalent plastic strain increment ratio method. Ignoring the misleading calculations, Elements 1 & 2, 1 & 3, 1 & 4, 1 & 5 and 1 & 6 predicted the onset of tensile plastic instability at 12.18 mm, 12.21 mm, 12.16 mm, 12.25 mm and 12.22 mm, respectively. The method underestimated the corresponding experimental value; which is 15.41 mm.

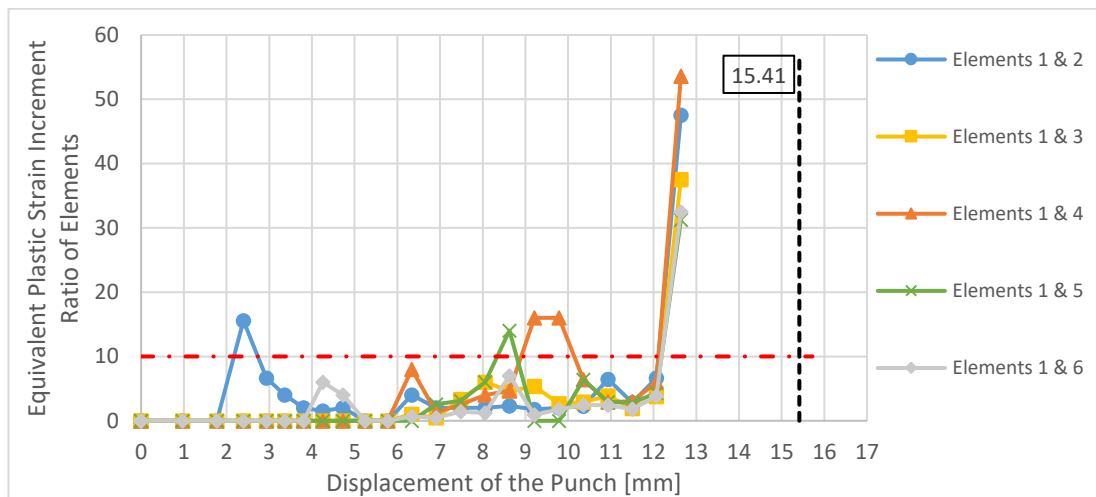


Figure 6.85. Strain increment ratios of several mesh element couples vs. punch displacement for square cup deep drawing process with 80x80 mm-square, sheet, Al specimen

6.6.3.2. Criterion of Difference of Second Time Derivative of Equivalent Plastic Strain (DDP-SC-AI)

Difference of second time derivative of equivalent plastic strain method applied on square cup deep drawing process with Al2024T3 specimen is shown in Figure 6.86 for different element couples. The results are consistent, all plots predicted the instability initiation at 13.21 mm punch movement. Recall that the experiment detected instability at 15.41 mm punch displacement.

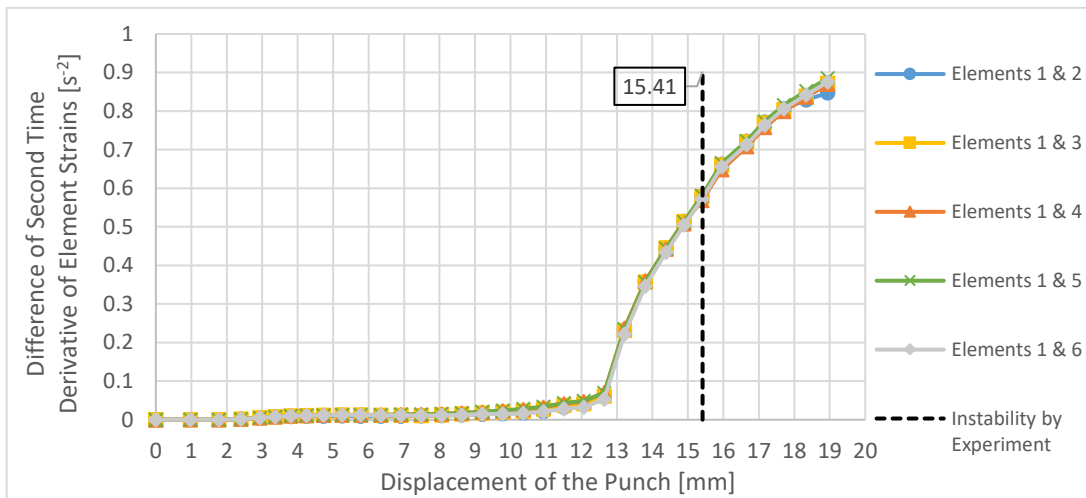


Figure 6.86 Difference of second time derivative of strain for several mesh element couples vs. punch displacement for square cup deep drawing process with 80x80 mm-square, sheet, Al specimen

6.6.3.3. Criterion of Maximum Second Time Derivative of Equivalent Plastic Strain (DDP-SC-AI)

Second time derivative of equivalent plastic strain of Element 1 is depicted in Figure 6.87. Tensile plastic instability is predicted to start at 12.64 mm punch displacement and that value is also shown in supporting plots of the method, i.e. strain vs. punch displacement (Figure 6.88) and strain rate vs punch displacement (Figure 6.89). The experiment recognized plastic instability at 15.41 mm punch travel.

The strain value of critical element in Al2024T3, straight, sheet specimen tensile test is plotted in Figure 6.88. Similar to other deep drawing analyses, critical mesh element can reach much larger strain values in deep drawing process. Strain values at the onset of instability are 0.18 and 0.69 for critical elements of tensile test and deep drawing process, respectively.

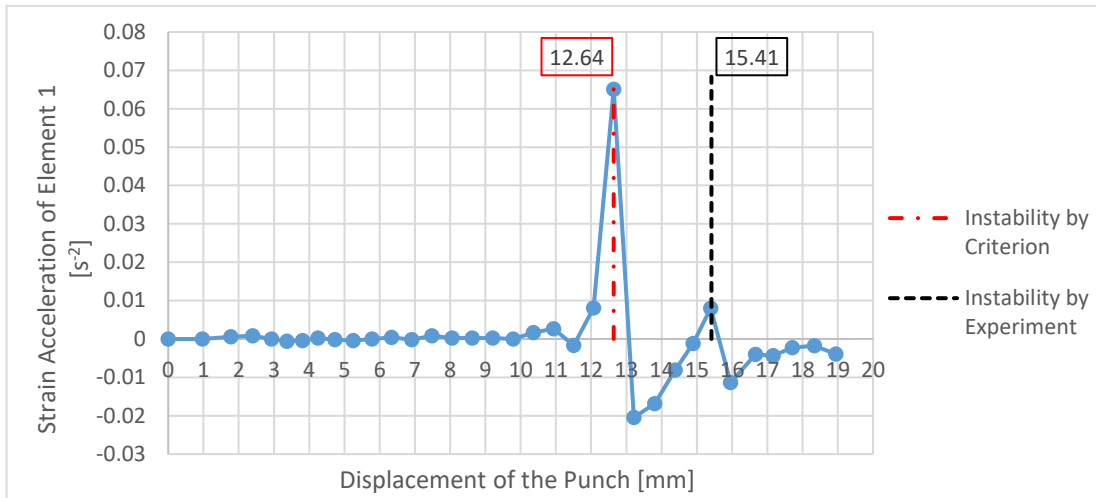


Figure 6.87. Second time derivative of Element 1 strain vs. punch displacement for square cup deep drawing process with 80x80 mm-square, sheet, Al specimen (Necking at 12.64 mm displacement)

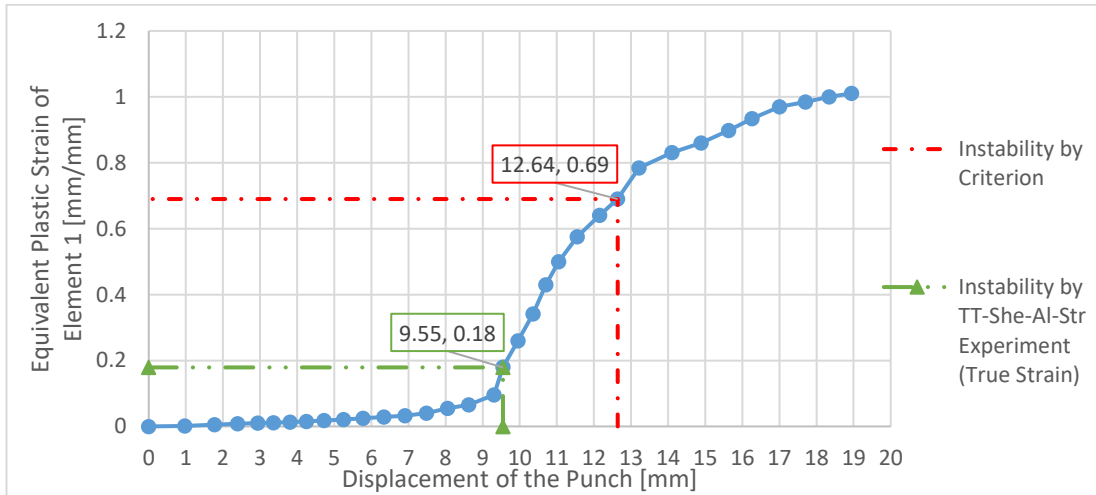


Figure 6.88. Plastic strain of Element 1 vs. punch displacement for square cup deep drawing process with 80x80 mm-square, sheet, Al specimen

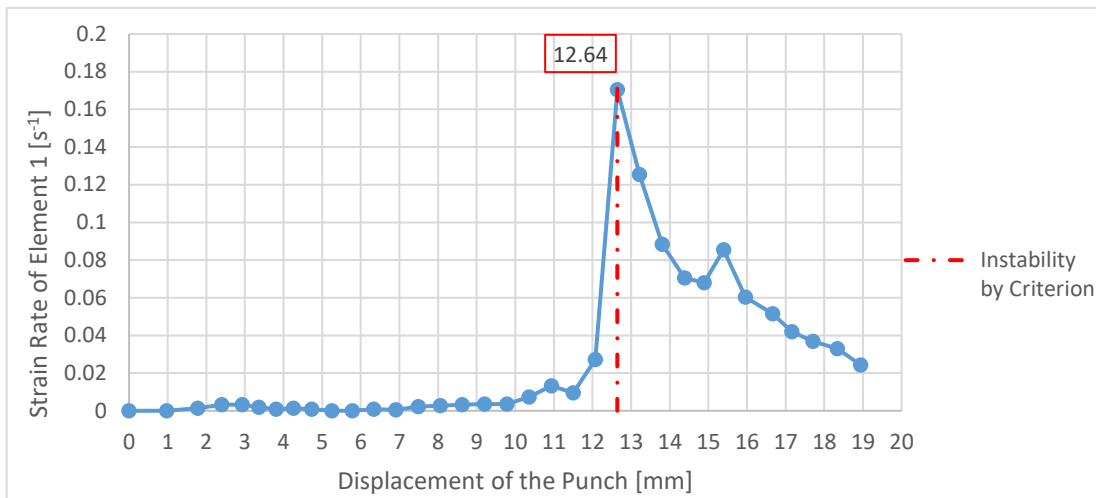


Figure 6.89. First time derivative of Element 1 strain vs. punch displacement for square cup deep drawing process with 80x80 mm-square, sheet, Al specimen

6.6.3.4. Criterion of Maximum Punch Force (DDP-SC-Al)

Figure 6.90 illustrates the punch travel data for square cup deep drawing process FEA. The method predicts the commencement of instability at 13.21 mm; yet, the experimental value is 15.41 mm.

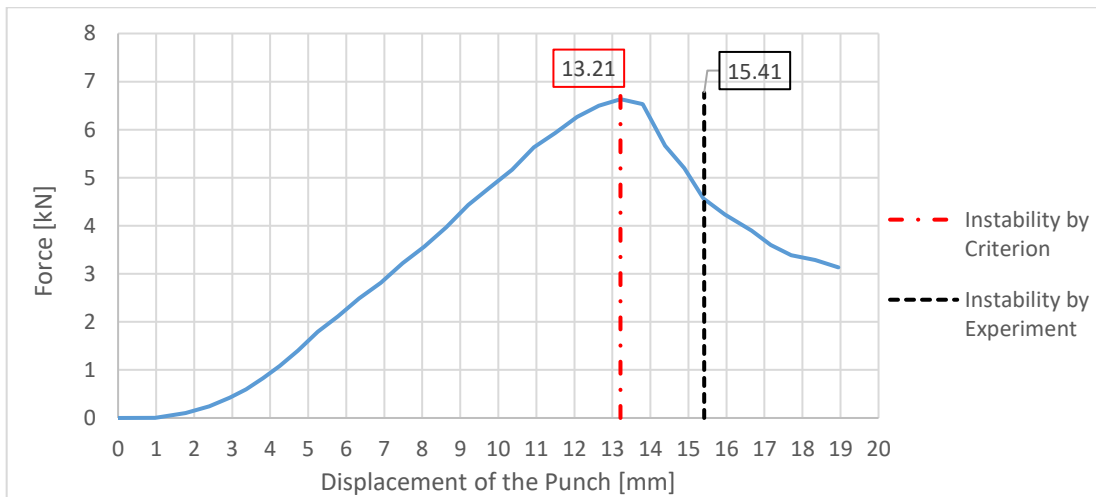


Figure 6.90. Punch force vs. punch displacement for round bottom cup deep drawing process with 110 mm diameter, sheet, Al specimen (Necking at 13.21 mm displacement)

6.7. Comparative Discussion for Deep Drawing FEA Results

Deep drawing analyses results are to be discussed in this section. Then, those results are compared to tensile test results.

To begin with, an important aspect of this work is to predict necking with respect to percent elongation of the specimen gauge in tensile tests and punch displacement in deep drawing processes. Majority of resources in the literature predict necking with respect to time. Prediction of necking in terms of time might be useful for specific cases; yet, that concept cannot be generalized because the results would change depending on the punch velocity in experiments and numerical analysis. On the other hand, percent elongation of the gauge can simply be generalized for materials as long as standard punch velocities (quasi-static in this thesis) and specimen shapes are followed. Punch displacement can also be used as a reference as long as a blank with the same thickness is utilized. In some other references, necking or instability conditions are plotted against element of major strains. To measure strain values can be challenging during experiments such as deep drawing. On the other hand, gauge elongation or punch travel can be directly measured both during the experiments and FE analysis which makes the current analysis more general.

Next, equivalent plastic strain vs. punch displacement plots given in Figures 6.76, 6.82 and 6.88. The characteristics of the plots are similar to each other; the curves start with smoothly increasing and continuous rapidly increasing manner. One important note here is that higher equivalent plastic strain magnitudes have been achieved with deep drawing processes than tensile test processes.

Equivalent plastic strain rate vs. punch displacement figures are picturized in Figures 6.77, 6.83 and 6.89. These graphs show dissimilar trends; yet, the highest increase which remarks the acceleration can easily be noticed in all cases.

Ratio of equivalent plastic strain rate changes with respect to two different elements are given Figures 6.73, 6.79 and 6.85. The graphs of this method fluctuated frequently

in cylindrical and square cup cases. Thus, this method with a threshold of 10 only worked on hemispherical deep drawing process properly.

Difference of second time derivative of equivalent plastic strain method results can be investigated from Figures 6.74, 6.80 and 6.86. Round bottom and square cup deep drawing analysis yielded consistent results for all element couples. Some irregular characteristics emerged in cylindrical cup process.

Second temporal derivative of strain changes on critical elements are depicted in Figures 6.75, 6.81 and 6.87. When compared to tensile test plots, more oscillations are observed in those graphs except the square cup case.

Maximum force criterion analyses are presented in Figures 6.78, 6.84 and 6.90. These figures represent the experimental results until instability initiation well. Yet, they follow dissimilar paths afterwards. Rapid decreases in test machine are due to manual switch-off. Thus, FEA results are more reliable for post-instability portion of the curves.

Next, the method results are to be compared for deep drawing analyses results.

Note that, equivalent plastic strain rate ratio and difference of second time derivative of equivalent plastic strain criteria elements must be considered with their percentage of related initial dimensions, given in Table 6.2.

In Table 6.6, equivalent plastic strain rate ratio predictions for onset of tensile plastic instability are tabulated. With the criterion threshold value of 10, Elements 1 & 2 fails in 2 cases to predict instability commencement. Elements 1 & 3 and 1 & 4 also fails to predict results in one case for each. The remaining element pairs are compared and Elements 1 & 6 predictions appeared to have higher accuracy than that of Elements 1 & 5. Recall that Elements 1 & 5 and 1 & 6 also emerged as the most accurate element pairs in tensile test analysis. This output has been confirmed by deep drawing process analyses. Note that, square cup analysis results for strain increment ratio exceeded the

threshold although the magnitudes of the strains are insignificant. This underlines the proper selection of the threshold. In that case, the threshold can be increased up to 20.

Table 6.6. Equivalent plastic strain rate ratio method results of deep drawing processes and corresponding punch displacement at the onset of instability from experiment data

All numbers are punch displacement [mm]	Experiment	Equivalent Plastic Strain Increment Ratio				
		Elements 1 & 2	Elements 1 & 3	Elements 1 & 4	Elements 1 & 5	Elements 1 & 6
DDP-CC-AI	10.52	-	-	-	15.53	11.68
DDP-RB-AI	17.36	-	18.85	19.62	18.93	18.88
DDP-SC-AI	15.41	12.18	12.21	12.16	12.25	12.22

Difference of second time derivative of equivalent plastic strain method results for different element pairs are enlisted in Table 6.7. For the same element couples, this method gives more precise results than strain increment ratio method, which had also been the case for tensile test analyses. In this method, Elements 1 & 5 and 1 & 6 perform the most accurate outputs; Elements 1 & 5 being slightly better.

Deep drawing processes analyses verified that difference of second time derivative of equivalent plastic strain method results are more aligned within themselves. Furthermore, choice of different element couples affect the method output to a smaller extent in that method.

Table 6.7. Maximum Difference of second time derivative of equivalent plastic strain method results of deep drawing processes and corresponding punch displacement at the onset of instability from experiment data

All numbers are punch displacement [mm]	Experiment	Difference of Second Time Derivative of Equivalent Plastic Strain				
		Elements 1 & 2	Elements 1 & 3	Elements 1 & 4	Elements 1 & 5	Elements 1 & 6
DDP-CC-AI	10.52	6.94	6.94	6.94	8.74	7.79
DDP-RB-AI	17.36	19.28	19.28	19.28	19.28	19.28
DDP-SC-AI	15.41	13.21	13.21	13.21	13.21	13.21

Maximum element strain acceleration and maximum punch force methods are summarized in Table 6.8. As in the case of tensile test analyses, maximum punch force method has achieved more accurate tensile plastic instability predictions benchmarked to experiment results.

Table 6.8. Maximum second time derivative of strain increment and maximum punch force method results of deep drawing processes and corresponding punch displacement at the onset of instability from experiment data

All numbers are punch displacement [mm]	Experiment	Maximum Second Time Derivative of Element Strain Increment	Maximum Reaction Force
DDP-Cc-AI	10.52	13.72	10.24
DDP-Rb-AI	17.36	19.28	18.62
DDP-Sc-AI	15.41	12.64	13.21

A very important deduction from the analysis is that all the methods have achieved less accurate prediction when compared to their respective counterparts in tensile test analysis. Deep drawing analysis involve complex loadings. Furthermore, the specimen is divided into different zones where the complex loading states vary. This reduces the effectivity of the methods in deep drawing analysis case.

6.8. Sources of Error

Considering all deviations in results between FEA and experiments, there can be some errors in the works done throughout the thesis. Four types of error do always affect the accuracy of the calculations; namely, experimental, human, modeling and numerical errors.

Experimental errors arise from the setup or specimens. For instance, ambient conditions such as temperature and light, production errors such as residual stresses, scratches on specimens, variations in cold work or grain size and device measurement errors can be sources of experimental errors.

Human error means unintentional lack of validity, precision or accuracy because of the acting person such as poor positioning of specimens, marking different points as gauge ends, making poor assumptions etc.

Modeling error concept is related to the analysis part of the work. Some examples of this type of error are assumptions such as isotropic material, model approximations such as Hooke's Law and von Mises yield criterion, analysis and mesh type, boundary conditions, and material data.

Lastly, numeric error is owing to the inefficient mathematical approaches in calculations. Finite number of calculation steps, using insufficient significant digits in calculation, round-off errors, limited number of mesh elements can be considered to illustrate numerical error concept.

CHAPTER 7

CONCLUSION AND FUTURE WORKS

7.1. Conclusion

In this thesis, four different methods to predict the onset of tensile plastic instability and necking are considered in tensile tests and deep drawing processes. Tensile tests have been carried out with two materials; Al2024T3 and S235JR, two different specimen types; cylindrical and rectangular cross section and three different specimen geometries; straight, tapered and notched. Cylindrical cup, round bottom cup and square cup deep drawing processes are conducted with Al2024T3 specimens.

From the experimental and finite element model analyses results, the following conclusions can be drawn:

- Usage of artificial imperfection methods such as tapered or notched tensile test specimens cause deviations from actual stress-strain values both in experiments and simulations. Moreover, necking prediction methods work on them less efficiently. Such strain concentration methods may cause significant deviations from actual results.
- In criterion of equivalent plastic strain rate ratio, the user-defined parameter used should be tailored specifically for the process type, material and specimen geometry. It is a challenge to obtain a specific value to predict onset of tensile plastic instability and necking well in all cases.
- Instability is predicted by the criterion of difference of second time derivative of equivalent plastic strain method when a sudden change in equivalent plastic strain value is observed.
- Both criterion of equivalent plastic strain increment ratio and criterion of difference of second time derivative of equivalent plastic strain are based on

the value between two points on the material, one having the highest strain value. The latter is less sensitive to the selection of points than the former.

- Criterion of maximum second time derivative of equivalent plastic strain is used instead of principle strains which is a common practice in the literature, and satisfactory and universal results are obtained.
- For tensile test experiments, maximum second time derivative of equivalent plastic strain and maximum punch force criteria generated the most accurate results. Deep drawing process results confirmed this output.
- None of the instability prediction methods performed well deep drawing analysis compared with tensile test experiments and this situation is attributed complex stress-strain state.

It is observed that the failure criteria emerged from tensile test experiments cannot be applied in complex forming operations such as deep drawing process.

7.2. Future Works

Some interesting future works would be:

- Sheet metal analyses can take anisotropy effects in consideration for more accurate reflection of the real-world problems.
- Analytical methods can be used to predict necking/instability to compare the results with the numerical methods.
- Results of ductile fracture criteria and instability prediction can be compared.

REFERENCES

1. Considère M. *Memoire sur l'emploi du fer et de l'acier dans les constructions*. Dunod; 1885.
2. Testing AAS for, *Materials*. Standard test methods for tension testing of metallic materials. ASTM international; 2009.
3. Czichos H, Saito T, Smith L. *Springer handbook of materials measurement methods*. Vol. 978. Springer Berlin; 2006.
4. Li J, Yang G, Siebert T, Shi MF, Yang L. A method of the direct measurement of the true stress–strain curve over a large strain range using multi-camera digital image correlation. *Opt Lasers Eng*. 2018;107:194–201.
5. Hyun HC, Kim M, Bang S, Lee H. On acquiring true stress–strain curves for sheet specimens using tensile test and FE analysis based on a local necking criterion. *J Mater Res*. 2014;29(05):695–707.
6. Handbook MF, Heidelberg SB. *Metal Forming Handbook*. Metal Forming. 1998.
7. Altan T, Tekkaya AE. *Sheet metal forming, Processes and applications*. Materials & Design. 2012.
8. Cora ÖN, Agcayaz A, Namiki K, Sofuoğlu H, Koç M. Die wear in stamping of advanced high strength steels - Investigations on the effects of substrate material and hard-coatings. *Tribol Int*. 2012;
9. Loveday MS, Gray T, Aegerter J. *Tensile testing of metallic materials: A review*. Final Rep TENSTAND Proj Work Packag. 2004;1.
10. Lund JR, Byrne JP. Leonardo Da Vinci's tensile strength tests: Implications for the discovery of engineering mechanics. *Civ Eng Syst*. 2001;18(3):243–50.
11. Zhang KS. Fracture prediction and necking analysis. *Eng Fract Mech*. 1995;52(3):575–82.
12. Le Van A, Le Grogneç P. Modeling and computation of necking instability in round bars using a total lagrangian elastoplastic formulation. In: *European Congress on Computational Methods in Applied Sciences and Engineering*. 2000.
13. Cabezas EE, Celentano DJ. Experimental and numerical analysis of the tensile test using sheet specimens. *Finite Elem Anal Des*. 2004;40(5–6):555–75.
14. Careglio CA, Celentano DJ, García Garino CG, Mirasso AE. *Global and Local*

- Mechanical Responses for Necking of Rectangular Bars Using Updated and Total Lagrangian Finite Element Formulations. *Math Probl Eng.* 2016;2016.
15. Mirone G. A new model for the elastoplastic characterization and the stress–strain determination on the necking section of a tensile specimen. *Int J Solids Struct.* 2004;41(13):3545–64.
 16. Tu S, Ren X, He J, Zhang Z. A method for determining material’s equivalent stress-strain curve with any axisymmetric notched tensile specimens without Bridgman correction. *Int J Mech Sci.* 2018;135:656–67.
 17. Farahnak P, Prantl A, Dzugan J, Konopik P, Prochazka R. Sheet necking prediction in forming limit diagrams with the anisotropy influence incorporation. In: *IOP Conference Series: Materials Science and Engineering.* IOP Publishing; 2017. p. 12023.
 18. Lumelskyj D, Rojek J, Banabic D, Lazarescu L. Detection of strain localization in Nakazima formability test-experimental research and numerical simulation. *Procedia Eng.* 2017;183:89–94.
 19. Coppieters S, Cooreman S, Sol H, Van Houtte P, Debruyne D. Identification of the post-necking hardening behaviour of sheet metal by comparison of the internal and external work in the necking zone. *J Mater Process Technol.* 2011;211(3):545–52.
 20. Manopulo N, Hora P, Peters P, Gorji M, Barlat F. An extended modified maximum force criterion for the prediction of localized necking under non-proportional loading. *Int J Plast.* 2015;75:189–203.
 21. Kamaya M, Kitsunai Y, Koshiishi M. True stress–strain curve acquisition for irradiated stainless steel including the range exceeding necking strain. *J Nucl Mater.* 2015;465:316–25.
 22. Ahn DC, Chung YJ, Won SY, Kim KY. Prediction of the Localized Necking under Non-Proportional Strain Paths by M-K Theory and FE Analyses. In: *AIP Conference Proceedings.* AIP; 2010. p. 1316–9.
 23. Merklein M, Kuppert A, Geiger M. Time dependent determination of forming limit diagrams. *CIRP Ann.* 2010;59(1):295–8.
 24. Kim JW, Byun TS. Analysis of necking deformation and fracture characteristics of irradiated A533B RPV steel. *Nucl Eng Technol.* 2012;44(8):953–60.
 25. Kolasangiani K, Shariati M, Farhangdoost K. Prediction of forming limit curves (FLD, MSFLD and FLSD) and necking time for SS304L sheet using finite element method and ductile fracture criteria. *J Comput Appl Res Mech Eng.* 2015;4.

26. Galpin B, Grolleau V, Penin A, Rio G. A hybrid method for detecting the onset of local necking by monitoring the bulge forming load. *Int J Mater Form*. 2016;9(2):161–73.
27. Min J, Stoughton TB, Carsley JE, Lin J. A method of detecting the onset of localized necking based on surface geometry measurements. *Exp Mech*. 2017;57(4):521–35.
28. Min J, Stoughton TB, Carsley JE, Lin J. An improved curvature method of detecting the onset of localized necking in Marciniak tests and its extension to Nakazima tests. *Int J Mech Sci*. 2017;123:238–52.
29. Abbassi F, Mistou S, Pantalé O, Zghal A. FE simulation and full-field strain measurements to evaluate the necking phenomena. *Procedia Manuf*. 2015;2:500–4.
30. Bao C, Francois M, Le Joncour L. A Closer Look at the Diffuse and Localised Necking of A Metallic Thin Sheet: Evolution of the Two Bands Pattern. *Strain*. 2016;52(3):244–60.
31. Saboori M, Champliand H, Gholipour J, Gakwaya A, Savoie J, Wanjara P. Extension of flow stress–strain curves of aerospace alloys after necking. *Int J Adv Manuf Technol*. 2016;83(1–4):313–23.
32. Morales-Palma D, Martínez-Donaire AJ, Vallellano C. On the Use of Maximum Force Criteria to Predict Localised Necking in Metal Sheets under Stretch-Bending. *Metals (Basel)*. 2017;7(11):469.
33. Do Kweon H, Heo EJ, Lee DH, Kim JW. A methodology for determining the true stress-strain curve of SA-508 low alloy steel from a tensile test with finite element analysis. *J Mech Sci Technol*. 2018;32(7):3137–43.
34. Kossakowski PG. Prediction of Ductile Fracture for S235JR Steel Using the Stress Modified Critical Strain and Gurson-Tvergaard-Needleman Models. 2012;(December):1492–500.
35. Zhang C, Leotoing L, Zhao G, Guines D, Ragneau E. A methodology for evaluating sheet formability combining the tensile test with the M–K model. *Mater Sci Eng A*. 2010;528(1):480–5.
36. Banabic D, Aretz H, Paraianu L, Jurco P. Application of various FLD modelling approaches. *Model Simul Mater Sci Eng*. 2005;13(5):759.
37. Barata da Rocha A, Santos AD, Teixeira P. Prediction on localized necking in sheet metal forming: finite element simulation and plastic instability in complex industrial strain paths. In: *Key Engineering Materials*. Trans Tech Publ; 2007. p. 825–32.
38. Barata da Rocha A, Santos AD, Teixeira P, Butuc MC. Plastic instability in

- complex strain paths and finite element simulation for localised necking prediction in sheet metal forming technology. *Int J Mater Prod Technol.* 2008;32(4):434–46.
39. Drotleff K, Liewald M. Novel Approach for Prediction of Localized Necking in Case of Nonlinear Strain Paths. In: *Journal of Physics: Conference Series.* IOP Publishing; 2017. p. 12113.
 40. Butuc MC, Gracio JJ, Da Rocha AB. A theoretical study on forming limit diagrams prediction. *J Mater Process Technol.* 2003;142(3):714–24.
 41. Korsunsky AM, Kyungmok KIM. Determination of essential work of necking and tearing from a single tensile test. *Int J Fract.* 2005;132(3):37–44.
 42. García-Garino C, Gabaldón F, Goicolea JM. Finite element simulation of the simple tension test in metals. *Finite Elem Anal Des.* 2006;42(13):1187–97.
 43. Duan X, Jain M, Metzger D, Kang J, Wilkinson DS, Embury JD. Prediction of shear localization during large deformation of a continuous cast Al–Mg sheet. *Mater Sci Eng A.* 2005;394(1–2):192–203.
 44. Reyes A, Hopperstad OS, Berstad T, Lademo O-G. Prediction of necking for two aluminum alloys under non-proportional loading by using an FE-based approach. *Int J Mater Form.* 2008;1(4):211–32.
 45. Situ Q, Jain MK, Metzger DR. Determination of forming limit diagrams of sheet materials with a hybrid experimental–numerical approach. *Int J Mech Sci.* 2011;53(9):707–19.
 46. Jaamialahmadi A, Kadkhodayan M. Necking prediction in tube hydroforming by stress-based forming limit diagrams. In: *Key Engineering Materials.* Trans Tech Publ; 2011. p. 284–8.
 47. Abovyan T, Kridli GT, Friedman PA, Ayoub G. Formability prediction of aluminum sheet alloys under isothermal forming conditions. *J Manuf Process.* 2015;20:406–13.
 48. Martínez-Donaire AJ, García-Lomas FJ, Vallengano C. New approaches to detect the onset of localised necking in sheets under through-thickness strain gradients. *Mater Des.* 2014;57:135–45.
 49. Yu JH, McWilliams BA, Kaste RP. Digital Image Correlation Analysis and Numerical Simulation of Aluminum Alloys under Quasi-static Tension after Necking Using the Bridgman’s Correction Method. *Exp Tech.* 2016;40(5):1359–67.
 50. Elyasi M, Paluch M, Hosseinzadeh M. Predicting the bending limit of AA8112 tubes using necking criterion in manufacturing of bent tubes. *Int J Adv Manuf Technol.* 2017;88(9–12):3307–18.

51. Lokoshchenko A, Teraud W. Determination of necking time in tensile test specimens, under high-temperature creep conditions, subjected to distribution of stresses over the cross-section. In: *Journal of Physics: Conference Series*. IOP Publishing; 2018. p. 12052.
52. Pham Q-T, Lee B-H, Park K-C, Kim Y-S. Influence of the post-necking prediction of hardening law on the theoretical forming limit curve of aluminium sheets. *Int J Mech Sci*. 2018;140:521–36.
53. Rodríguez-Martínez JA, Rusinek A, Arias A. Thermo-viscoplastic behaviour of 2024-T3 aluminium sheets subjected to low velocity perforation at different temperatures. *Thin-Walled Struct*. 2011;49(7):819–32.
54. Ling Y. Uniaxial true stress-strain after necking. *AMP J Technol*. 1996;5(1):37–48.
55. Sing WM, Rao KP. Role of strain-hardening laws in the prediction of forming limit curves. *J Mater Process Technol*. 1997;63(1–3):105–10.
56. Yuan WJ, Zhou F, Zhang ZL, Su YJ, Qiao LJ, Chu WY. An analysis on necking effect and stress distribution in round cross-section specimens of pure copper with different diameters. *Mater Sci Eng A*. 2013;561:183–90.
57. Sene NA, Balland P, Tabourot L, Vautrot M, Ksiksi N. An original prediction of localisation during tensile and biaxial expansion tests on copper by the compartmentalized model. In: *AIP Conference Proceedings*. AIP Publishing; 2016. p. 160010.
58. Brüning M. Numerical analysis and modeling of large deformation and necking behavior of tensile specimens. *Finite Elem Anal Des*. 1998;28(4):303–19.
59. Joun M, Eom JG, Lee MC. A new method for acquiring true stress–strain curves over a large range of strains using a tensile test and finite element method. *Mech Mater*. 2008;40(7):586–93.
60. Eom J, Chung W, Joun M. Comparison of rigid-plastic and elastoplastic finite element predictions of a tensile test of cylindrical specimens. *Key Eng Mater*. 2014;622:611–6.
61. Tabourot L, Balland P, Sène NA, Vautrot M, Ksiksi N, Maati A. Numerical study of the impact of constitutive modelling on the evolution of necking in the case of a tensile test on C68 grade steel. In: *Key Engineering Materials*. Trans Tech Publ; 2014. p. 521–8.
62. Murata M, Yoshida Y, Nishiwaki T. Stress correction method for flow stress identification by tensile test using notched round bar. *J Mater Process Technol*. 2018;251:65–72.
63. Hu Q, Zhang F, Li X, Chen J. Overview on the Prediction Models for Sheet

- Metal Forming Failure: Necking and Ductile Fracture. *Acta Mech Solida Sin.* 2018;1–31.
64. Hashemi R, Abrinia K, Assempour A. The strain gradient approach to predict necking in tube hydroforming. *J Manuf Process.* 2013;15(1):51–5.
 65. Rao KP, Mohan EVR. A unified test for evaluating material parameters for use in the modelling of sheet metal forming. *J Mater Process Technol.* 2001;113(1–3):725–31.
 66. Dumoulin S, Tabourot L, Chappuis C, Vacher P, Arrieux R. Determination of the equivalent stress–equivalent strain relationship of a copper sample under tensile loading. *J Mater Process Technol.* 2003;133(1–2):79–83.
 67. Tabourot L, Vacher P, Coudert T, Toussaint F, Arrieux R. Numerical determination of strain localisation during finite element simulation of deep-drawing operations. *J Mater Process Technol.* 2005;159(2):152–8.
 68. Shimizu D, Takahashi S, Sunaga H, Takamura M, Mihara S, Oohashi E. Measurement of local necking in tensile test of mild steel sheet for forming numerical simulation. In: *Journal of Physics: Conference Series.* IOP Publishing; 2018. p. 12154.
 69. Lumelskyj D, Lazarescu L, Banabic D, Rojek J. Comparison of two methods for detection of strain localization in sheet forming. In: *AIP Conference Proceedings.* 2018.
 70. Zhang C, Leotoing L, Zhao G, Guines D, Ragneau E. A comparative study of different necking criteria for numerical and experimental prediction of FLCs. *J Mater Eng Perform.* 2011;20(6):1036–42.
 71. Pepelnjak T, Petek A, Kuzman K. Analyses of the forming limit diagram in digital environment. Vol. 6. *Trans Tech Publ;* 2005.
 72. Boudeau N, Gelin JC. Post-processing of finite element results and prediction of the localized necking in sheet metal forming. *J Mater Process Technol.* 1996;60(1–4):325–30.
 73. Chalal H, Abed-Meraim F. Numerical Predictions of the Occurrence of Necking in Deep Drawing Processes. *Metals (Basel).* 2017;7(11):455.
 74. Drotleff K, Liewald M. Phenomenological model for prediction of localised necking in multi-step sheet metal forming processes. In: *Journal of Physics: Conference Series.* IOP Publishing; 2018. p. 12062.
 75. Drotleff K, Liewald M. Application of an advanced necking criterion for nonlinear strain paths to a complex sheet metal forming component. In: *IOP Conference Series: Materials Science and Engineering.* 2018.
 76. Li B, Nye TJ, Wu PD. Predicting the forming limit diagram of AA 5182-O. *J*

strain Anal Eng Des. 2010;45(4):255–73.

77. Brunet M, Clerc P. Predictions of necking with analytical criteria and comparisons with experimental results. In: AIP Conference Proceedings. AIP; 2007. p. 81–6.
78. Bao C, François M, Le Joncour L. Influence of Specimen Geometry on Strain Localization Phenomena in Steel Sheets. *Appl Mech Mater*. 2015;
79. Yoon J, Cazacu O, Lee JH. Localized Necking in a Round Tensile Bar with HCP Material Considering Tension-Compression Asymmetry in Plastic Flow. In: *Key Engineering Materials*. Trans Tech Publ; 2013. p. 164–7.
80. Karajibani E, Hashemi R, Sedighi M. Forming limit diagram of aluminum-copper two-layer sheets: Numerical simulations and experimental verifications. *Int J Adv Manuf Technol*. 2017;90(9–12):2713–22.
81. Pack K, Mohr D. Combined necking & fracture model to predict ductile failure with shell finite elements. *Eng Fract Mech*. 2017;182:32–51.
82. Bouktir Y, Chalal H, Abed-Meraim F. Prediction of necking in thin sheet metals using an elastic–plastic model coupled with ductile damage and bifurcation criteria. *Int J Damage Mech*. 2018;27(6):801–39.
83. Matic P, Kirby GC, Jolles MI. The Relation of Tensile Specimen Size and Geometry Effects to Unique Constitutive Parameters for Ductile Materials. *Proc R Soc A Math Phys Eng Sci*. 2006;
84. Gromada M, Mishuris G, Ochsner A. Necking in the tensile test. Correction formulae and related error estimation. *Arch Metall Mater*. 2007;52(2):231.
85. Datta TK, Banerjee D. A numerical analysis of neck formation in tensile specimens. *J Mater Process Technol*. 1995;54(1–4):309–13.
86. Kim HS, Kim SH, Ryu W-S. Finite element analysis of the onset of necking and the post-necking behaviour during uniaxial tensile testing. *Mater Trans*. 2005;46(10):2159–63.
87. Joun M, Choi I, Eom J, Lee M. Finite element analysis of tensile testing with emphasis on necking. *Comput Mater Sci*. 2007;41(1):63–9.
88. Wang Y, Xu S, Ren S, Wang H. An experimental-numerical combined method to determine the true constitutive relation of tensile specimens after necking. *Adv Mater Sci Eng*. 2016;2016.
89. Boudeau N, Gelin JC. Prediction of the localized necking in 3D sheet metal forming processes from FE simulations. *J Mater Process Technol*. 1994;45(1–4):229–35.
90. Niordson CF, Redanz P. Size-effects in plane strain sheet-necking. *J Mech Phys*

- Solids. 2004;52(11):2431–54.
91. Jouve D. Analytic study of plastic necking instabilities during plane tension tests. *Eur J Mech.* 2013;39:180–96.
 92. Morin D, Hopperstad OS, Benallal A. On the description of ductile fracture in metals by the strain localization theory. *Int J Fract.* 2018;
 93. Neilsen MK, Schreyer HL. Bifurcations in elastic-plastic materials. *Int J Solids Struct.* 1993;30(4):521–44.
 94. Abed-Meraim F, Peerlings R, Geers M. Comparison of bifurcation analysis and maximum force criteria in the prediction of necking in stretched metal sheets. 2015;
 95. Abed-Meraim F, Peerlings RHJ, Geers MGD. Bifurcation analysis versus maximum force criteria in formability limit assessment of stretched metal sheets. *Int J Appl Mech.* 2014;6(06):1450064.
 96. Bridgman PW. *Studies in Large Plastic Flow and Fracture: With Special Emphasis on the Effects of Hydrostatic Pressure.* Science. 1952.
 97. Zhang L, Lin J, Sun L, Wang C, Wang L. A new method for determination of forming limit diagram based on digital image correlation. *SAE Technical Paper*; 2013.
 98. Furushima T, Tsunozaki H, Nakayama T, Manabe KI, Alexandrov S. Prediction of surface roughening and necking behavior for metal foils by inhomogeneous FE material modeling. In: *Key Engineering Materials.* 2013.
 99. Romanova V, Balokhonov R, Emelianova E, Sinyakova E, Kazachenok M. Early prediction of macroscale plastic strain localization in titanium from observation of mesoscale surface roughening. *Int J Mech Sci* [Internet]. 2019;161–162(March):105047. Available from: <https://linkinghub.elsevier.com/retrieve/pii/S0020740319309348>
 100. Boudeau N, Gelin JC, Salhi S. Computational prediction of the localized necking in sheet forming based on microstructural material aspects. *Comput Mater Sci.* 1998;
 101. Ben Bettaieb M, Abed-Meraim F. Strain localization analysis for planar polycrystals based on bifurcation theory. *Comptes Rendus - Mecanique.* 2018.
 102. Franz G, Abed-Meraim F, Lorrain JP, Ben Zineb T, Lemoine X, Berveiller M. Ellipticity loss analysis for tangent moduli deduced from a large strain elastic-plastic self-consistent model. *Int J Plast.* 2009;
 103. Akpama HK, Ben Bettaieb M, Abed-Meraim F. Localized necking predictions based on rate-independent self-consistent polycrystal plasticity: Bifurcation analysis versus imperfection approach. *Int J Plast.* 2017;

104. Bragard A, Baret J-C, Bonnarens H. Simplified Technique to Determine the FLD on the Onset of Necking. *C R M.* 1972;(33):53–63.
105. Marciniak Z, Kuczyński K. Limit strains in the processes of stretch-forming sheet metal. *Int J Mech Sci.* 1967;9(9):609–20.
106. Chalal H, Abed-Meraim F. Determination of Forming Limit Diagrams Based on Ductile Damage Models and Necking Criteria. *Lat Am J Solids Struct.* 2017;14(10):1872–92.
107. Narasimhan K, Wagoner RH. Finite element modeling simulation of in-plane forming limit diagrams of sheets containing finite defects. *Metall Trans A.* 1991;
108. van den Boogaard AH, Huetink J. Prediction of sheet necking with shell finite element models. In: *Proc 6th ESAFORM Conference on Material Forming, Salerno.* 2003. p. 191–4.
109. Aretz H. A comparison between geometrical and material imperfections in localized necking prediction. In: *AIP Conference Proceedings.* AIP; 2007. p. 287–92.
110. Ramaekers JAH. A criterion for local necking. *J Mater Process Technol.* 2000;103(1):165–71.
111. Arutyunyan AR, Arutyunyan RA. The condition of transition to unstable state (necking) of a compressible elastic-plastic medium. *Mater Phys Mech.* 2017;31(1/2):89–92.
112. Audoly B, Hutchinson JW. Analysis of necking based on a one-dimensional model. *J Mech Phys Solids.* 2016;97:68–91.
113. Xue L. Localization conditions and diffused necking for damage plastic solids. *Eng Fract Mech.* 2010;77(8):1275–97.
114. Swift H. Plastic instability under plane stress. *J Mech Phys Solids.* 1952;1(1):1–18.
115. Hill RT. On discontinuous plastic states, with special reference to localized necking in thin sheets. *J Mech Phys Solids.* 1952;1(1):19–30.
116. Hora P, Tong L, Berisha B. Modified maximum force criterion, a model for the theoretical prediction of forming limit curves. *Int J Mater Form.* 2013;6(2):267–79.
117. Hora P, Tong L, Reissner J. A prediction method for ductile sheet metal failure in FE-simulation. In: *Proceedings of NUMISHEET.* 1996. p. 252–6.
118. Aretz H, Engler O. Efficient and robust prediction of localized necking in sheet metals. In: *AIP Conference Proceedings.* AIP; 2011. p. 453–60.

119. Lumelskyj D, Lazarescu L, Banabic D, Rojek J. Experimental and numerical investigations on determination of strain localization in sheet forming. In: *Journal of Physics: Conference Series*. 2018.
120. Zahedi A, Mollaei Dariani B, Mirnia MJ. Experimental determination and numerical prediction of necking and fracture forming limit curves of laminated Al/Cu sheets using a damage plasticity model. *Int J Mech Sci*. 2019;
121. Sulem J. Bifurcation theory and localization phenomena. *Eur J Environ Civ Eng*. 2010;14(8–9):989–1009.
122. Drucker DC. On uniqueness in the theory of plasticity. *Q Appl Math*. 1956;14(1):35–42.
123. Hill R. A general theory of uniqueness and stability in elastic-plastic solids. *J Mech Phys Solids*. 1958;6(3):236–49.
124. Valanis KC. Banding and stability in plastic materials. *Acta Mech*. 1989;79(1–2):113–41.
125. Rudnicki JW, Rice JR. Conditions for the localization of deformation in pressure-sensitive dilatant materials. *J Mech Phys Solids*. 1975;23(6):371–94.
126. Rice JR. The localization of plastic deformation. 1976;
127. Bigoni D, Hueckel T. Uniqueness and localization—I. Associative and non-associative elastoplasticity. *Int J Solids Struct*. 1991;28(2):197–213.
128. Altmeyer G, Abed-Meraim F, Balan T. Overview of the theoretical relations between necking and strain localization criteria *Abstract : Sci York*. 2013;1–8.
129. Lyapunov AM. The general problem of motion stability. *Ann Math Stud*. 1892;17.
130. Drucker DC. Some implications of work hardening and ideal plasticity. *Q Appl Math*. 1950;
131. Diouta NG, Shahrour I. A full 3-D material stability analysis of a classical elasto-plastic medium through a linear perturbation approach. *EPJ Appl Phys*. 2006;
132. Barbier G, Benallal A, Cano V. Relation théorique entre la méthode de perturbation linéaire et l'analyse de bifurcation pour la prédiction de la localisation des déformations. *Comptes Rendus l'Académie des Sci - Ser IIB - Mech*. 1998;
133. Benallal A. A note on ill-posedness for rate-dependent problems and its relation to the rate-independent case. *Comput Mech*. 2008;
134. Boudeau N, Lejeune A, Gelin J-C. Damage in sheet metal forming: prediction

- of necking phenomenon. *Rev Eur des Éléments Finis*. 2001;
135. Dudzinski D, Molinari A. Perturbation analysis of thermoviscoplastic instabilities in biaxial loading. *Int J Solids Struct*. 1991;
 136. Fressengeas C, Molinari A. Instability and localization of plastic flow in shear at high strain rates. *J Mech Phys Solids*. 1987;
 137. Dequiedt JL. Statistics of dynamic fragmentation for a necking instability. *Int J Solids Struct*. 2015;
 138. Abed-Meraim F, Balan T, Altmeyer G. Investigation and comparative analysis of plastic instability criteria: application to forming limit diagrams. *Int J Adv Manuf Technol*. 2014;71(5–8):1247–62.
 139. Altmeyer G. Theoretical and Numerical Comparison of Limit Point Bifurcation and Maximum Force Criteria. Application to the Prediction of Diffuse Necking. *Model Numer Simul Mater Sci*. 2013;
 140. Ben Bettaieb M, Abed-Meraim F. Investigation of localized necking in substrate-supported metal layers: Comparison of bifurcation and imperfection analyses. *Int J Plast*. 2015;
 141. Sancho R, Cendón D, Gálvez F. Mechanical Behaviour of Al2024-T3 Sheet Metal at Different Strain-rates and Temperatures. In: *Procedia Engineering*. 2017.
 142. Lesuer DR. Experimental investigations of material models for Ti-6Al-4V and 2024-T3. *Faa*. 1999;
 143. Rund M, Procházka R, Konopík P, Džugan J, Folgar H. Investigation of Sample-size Influence on Tensile Test Results at Different Strain Rates. In: *Procedia Engineering*. 2015.
 144. Larour P. Strain rate sensitivity of automotive sheet steels: influence of plastic strain, strain rate, temperature, microstructure, bake hardening and pre-strain. Aachen University. 2010.
 145. Hughes WJ. *Metallic Materials Properties Development and Standardization (MMPDS-10)*. Battelle Memorial Institute. 2015.
 146. Ananthan VS, Hall EO. Macroscopic aspects of Lüders band deformation in mild steel. *Acta Metall Mater*. 1991;
 147. Ray KK, Toppo V, Singh SB. Influence of pre-strain on the wear resistance of a plain carbon steel. *Mater Sci Eng A*. 2006;
 148. Dhatt G, Touzot G, Lefrançois E. Matrix Presentation of the Finite Element Method. In: *Finite Element Method*. 2013.

149. Zienkiewicz OC, Taylor RL, Zhu JZ. The Finite Element Method: Its Basis and Fundamentals: Its Basis and Fundamentals. Butterworth-Heinemann. 2005;132:1987–93.
150. Scheider I, Brocks W, Cornec A. Procedure for the Determination of True Stress-Strain Curves From Tensile Tests With Rectangular Cross-Section Specimens. J Eng Mater Technol. 2004;
151. Simulia 3DS. Abaqus Analysis User's Manual (version 6.12). University of Cambridge - Faculty of Mathematics. 2015.
152. Cogun F, Darendeliler H. Comparison of different yield criteria in various deep drawn cups. 2015;
153. Dizaji Sa. An Investigation Of Ductile Fracture Criteria For Sheet Metal Forming. Middle East Technical University. 2014.

APPENDICES

A. SAMPLE FINITE ELEMENT ANALYSIS VIEWS

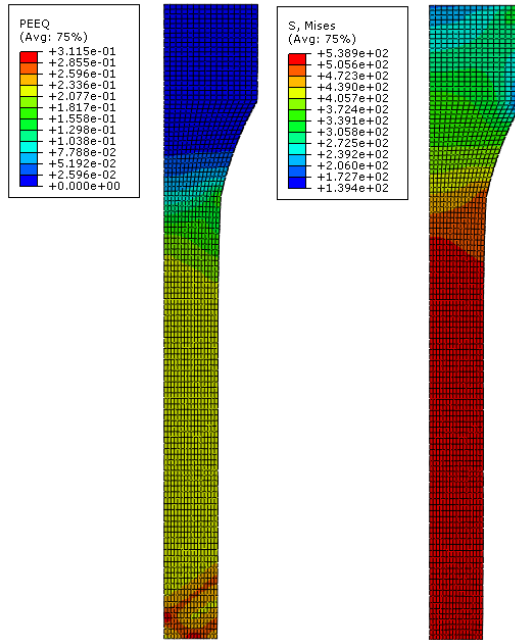


Figure 0.1. FE view of equivalent plastic strain and stress for TT-She-Al-Str

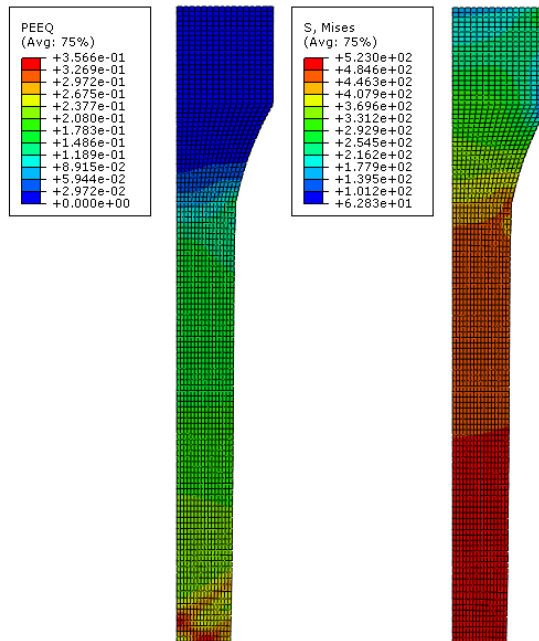


Figure 0.2. FE view of equivalent plastic strain and stress for TT-She-Al-Tpr

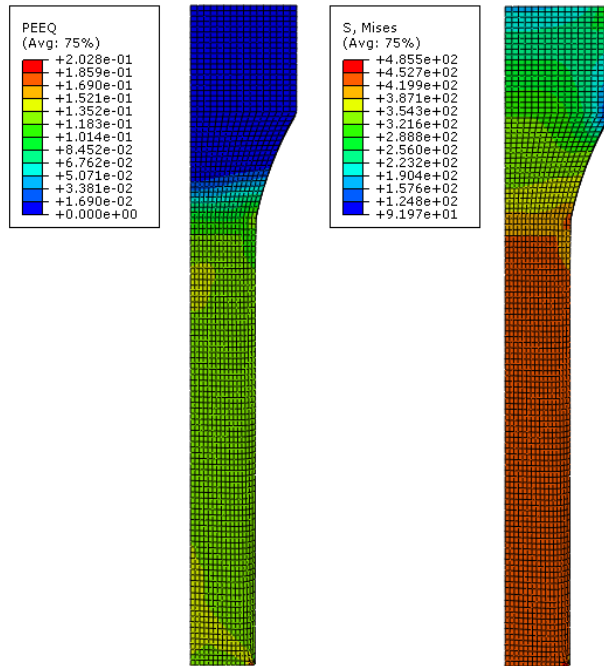


Figure 0.3. FE view of equivalent plastic strain and stress for TT-She-Al-Ntc

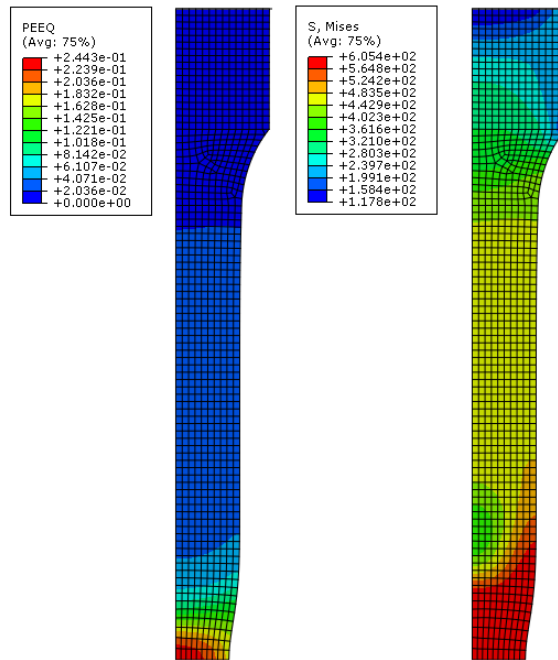


Figure 0.4. FE view of equivalent plastic strain and stress for TT-Ro-Al-Str

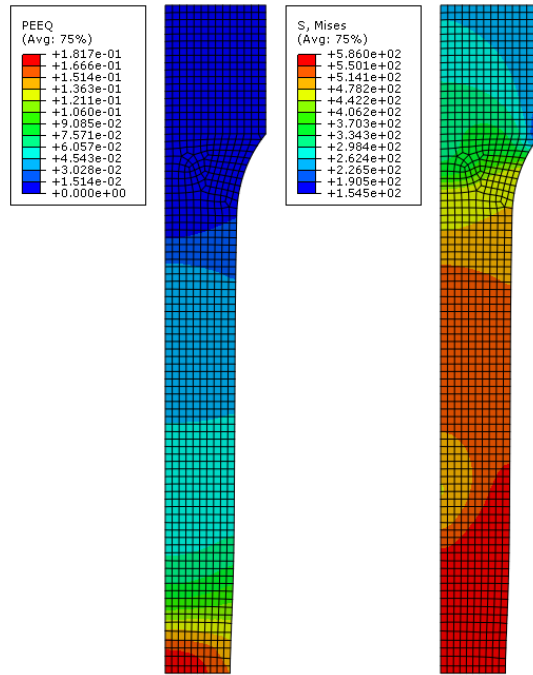


Figure 0.5. FE view of equivalent plastic strain and stress for TT-Ro-Al-Tpr

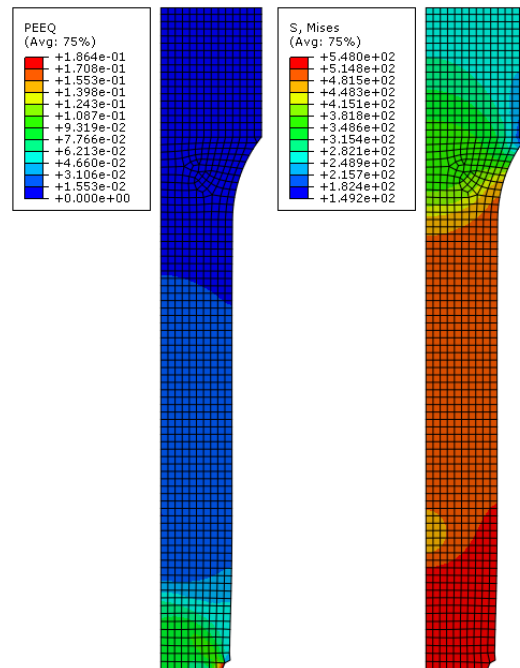


Figure 0.6. FE view of equivalent plastic strain and stress for TT-Ro-Al-Ntc

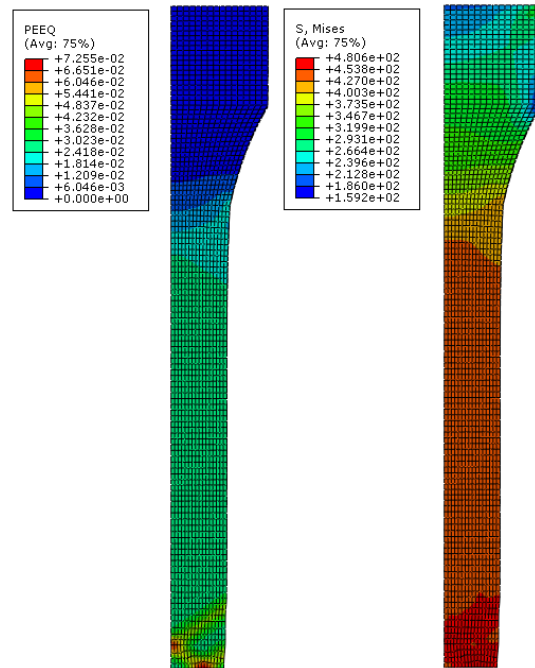


Figure 0.7. FE view of equivalent plastic strain and stress for TT-She-St-Str

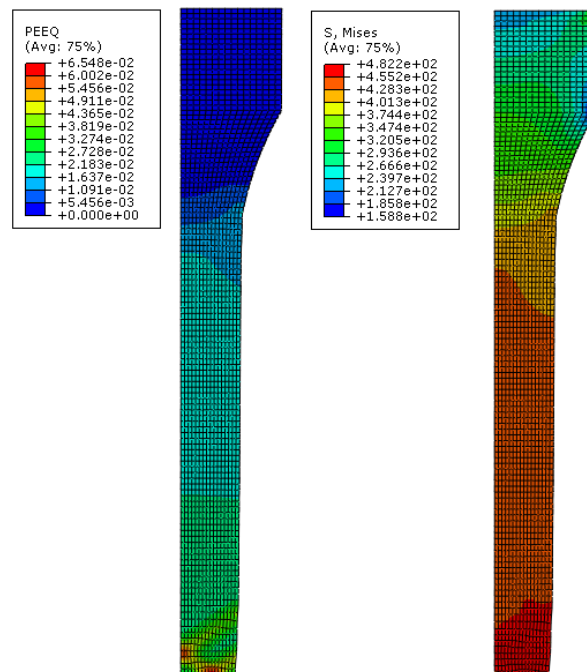


Figure 0.8. FE view of equivalent plastic strain and stress for TT-She-St-Tpr

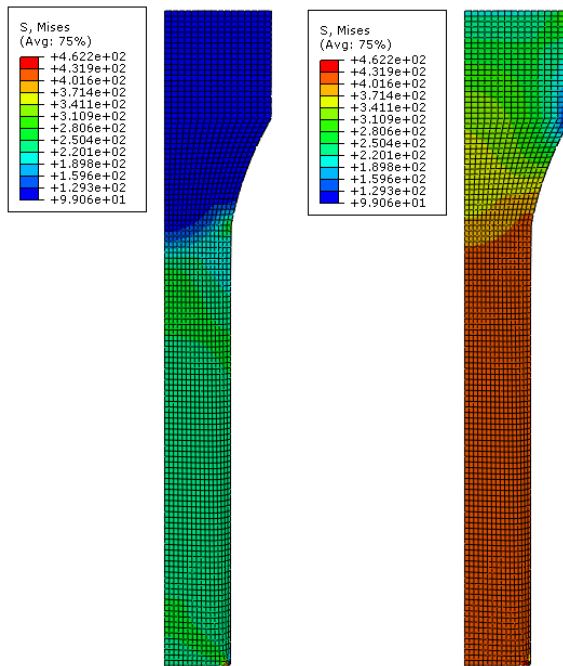


Figure 0.9. FE view of equivalent plastic strain and stress for TT-She-St-Ntc

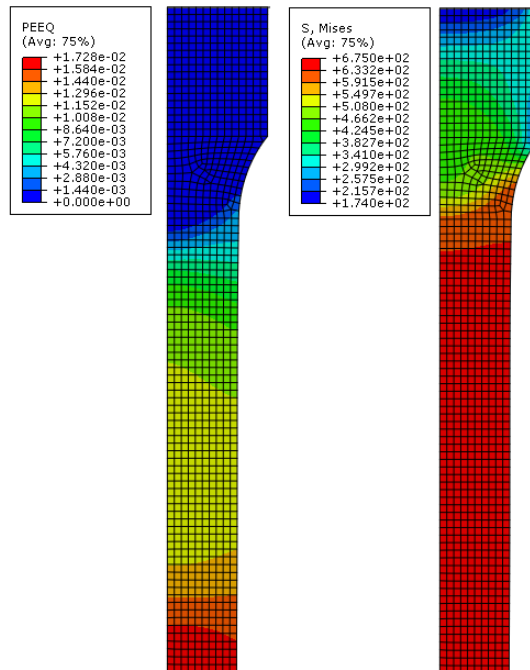


Figure 0.10. FE view of equivalent plastic strain and stress for TT-Ro-St-Str

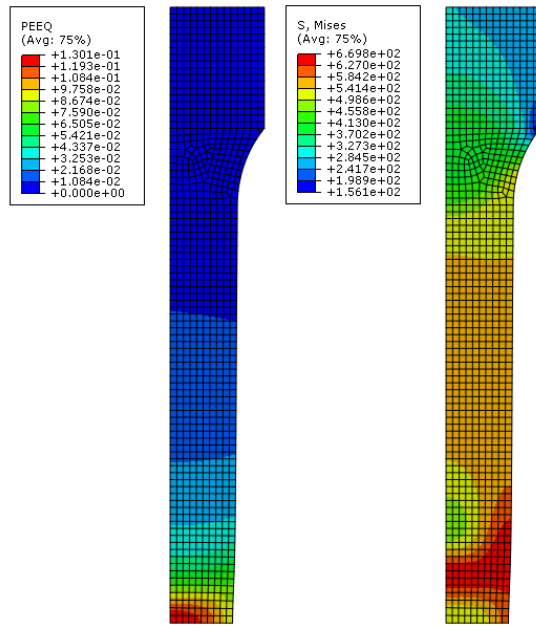


Figure 0.11. FE view of equivalent plastic strain and stress for TT-Ro-St-Tpr

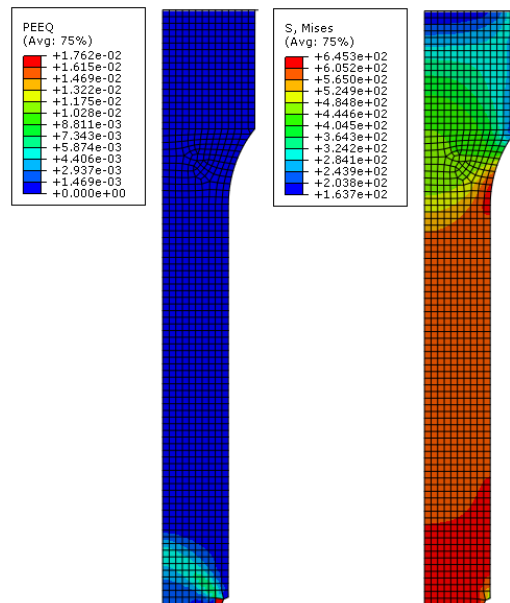


Figure 0.12. FE view of equivalent plastic strain and stress for TT-Ro-St-Ntc

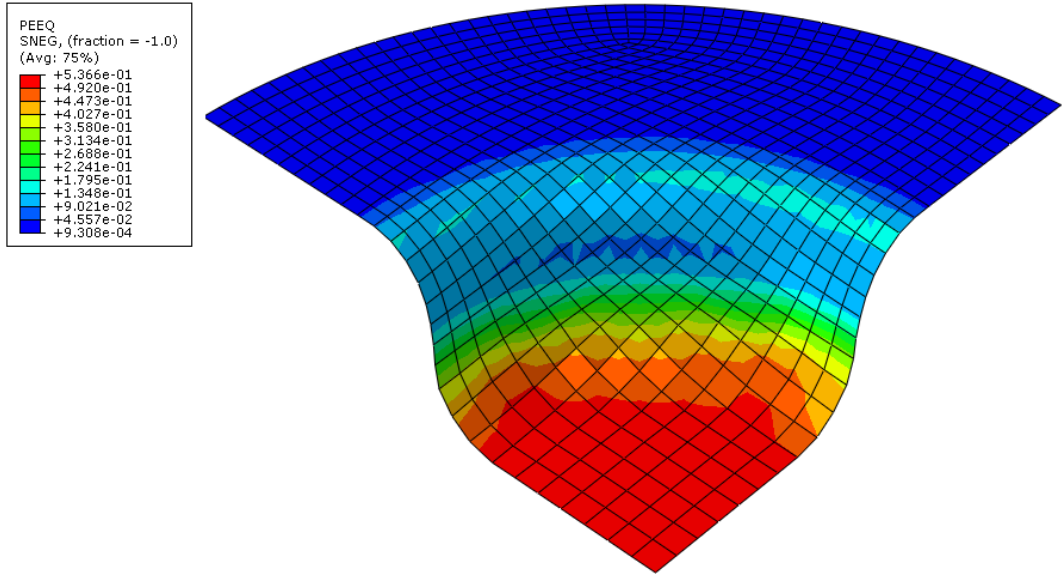


Figure 0.13. FE view of equivalent plastic strain for DDP-CC-Al

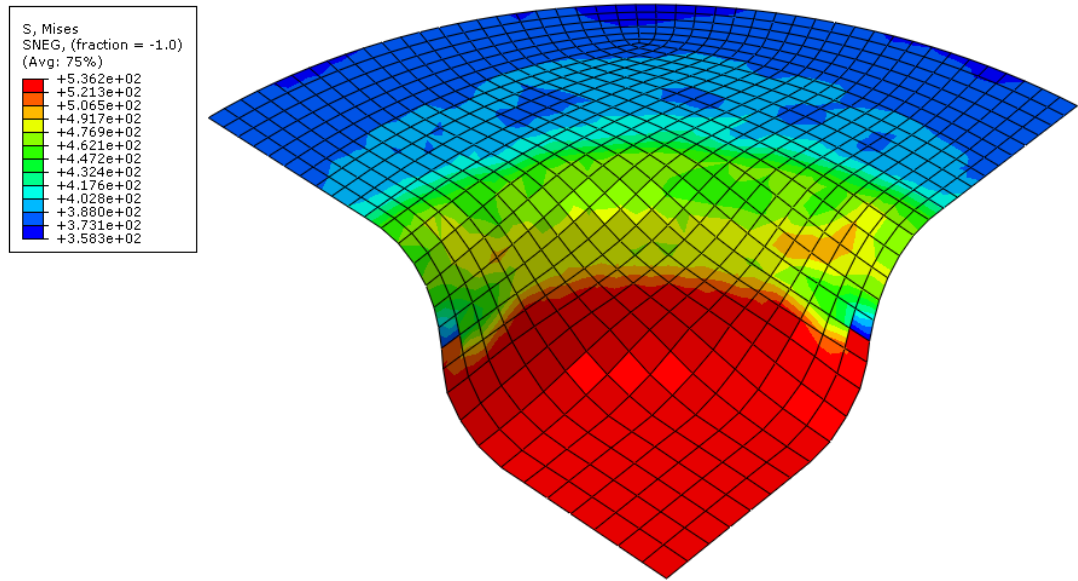


Figure 0.14. FE view of equivalent stress for DDP-CC-Al

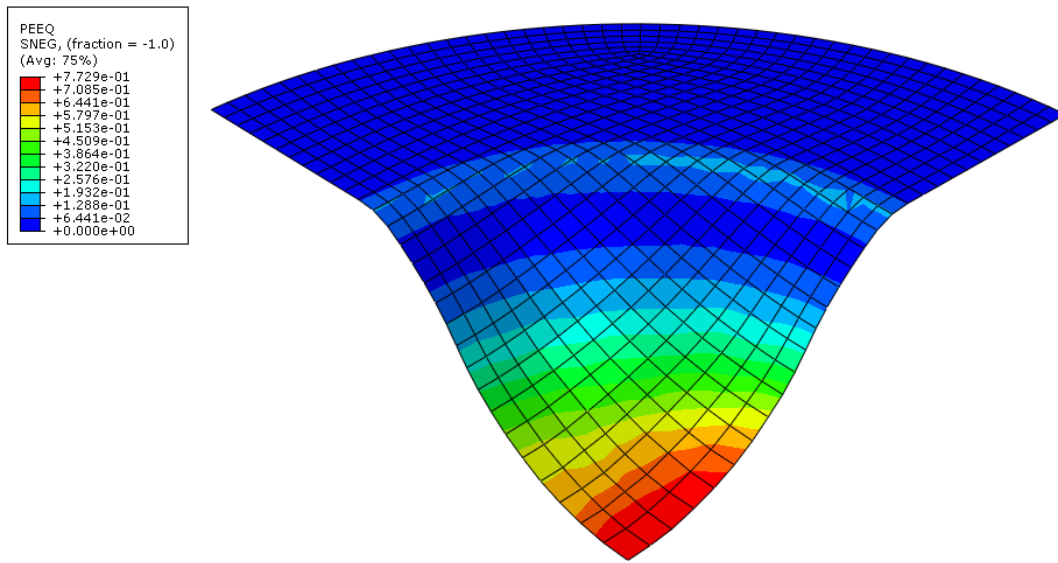


Figure 0.15. FE view of equivalent plastic strain for DDP-RB-AI

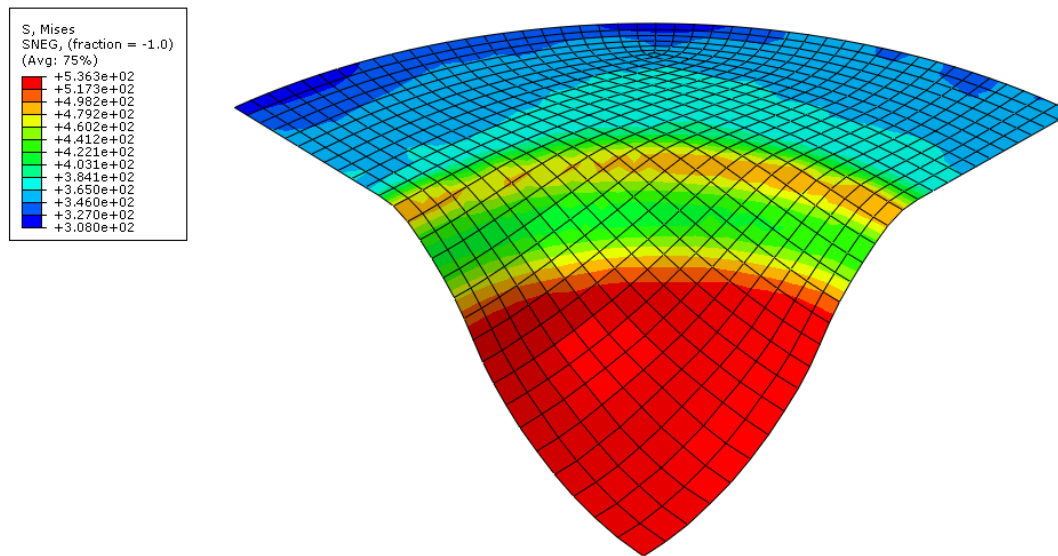


Figure 0.16. FE view of equivalent stress for DDP-RB-AI

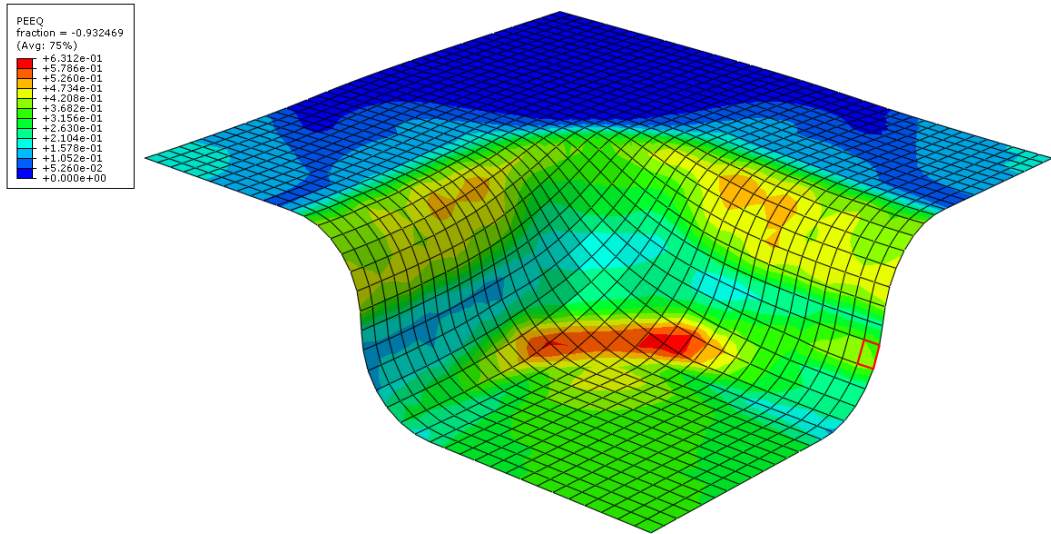


Figure 0.17. FE view of equivalent plastic strain for DDP-SC-AI

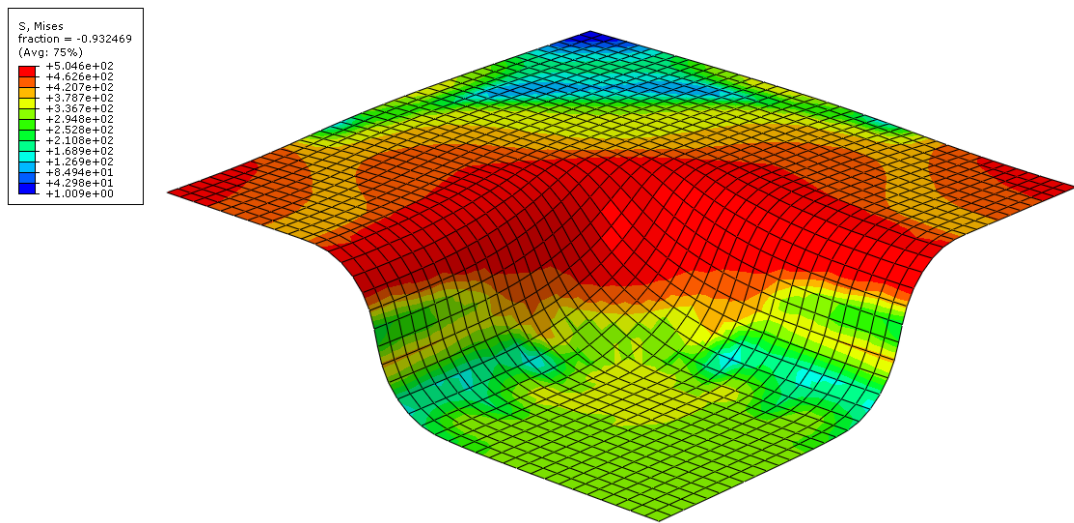


Figure 0.18. FE view of equivalent stress for DDP-RB-AI